INVESTIGATION OF THE RESPONSE OF GROUPS OF WAVE ENERGY DEVICES

A thesis submitted to the University of Manchester for the degree of
Doctor of Philosophy
in the Faculty of Engineering and Physical Sciences

2011

Sarah Bellew[1]

School of Mechanical, Aerospace and Civil Engineering

---

[1] née Thomas

Contents

Word Count: 64 468

Nomenclature

A	Added Mass, page 44
A_m	Wave Amplitude, page 38
A_{CsZ}	Cross-sectional area of the float in the vertical plane perpendicular to the direction of wave propagation , page 76
A_{WP}	Water-plane area, page 64
A_{ϑ}	Added mass which would be experienced after a phase shift, page 79
B	Radiation damping, page 44
B_{ϑ}	Radiation damping which would be experienced after a phase shift, page 79
C	Restoring coefficient, page 43
C_d	Drag coefficient, page 76
C_g	Group velocity, page 77
C_z	A set of terms used in the derivation of Equation (2.49), page 183
D_5	5 m Vertical circular cylinder draft, page 155
$D_{\%}$	The difference between the interaction factor for an array with R selected iteratively and an array with $R = diag(R_{opt})$, page 129
D_{10}	10 m Vertical circular cylinder draft, page 155
D_{15}	15 m Vertical circular cylinder draft, page 155
F	Excitation Force (simplified notation for F_e), page 46
$F^{[1]}$	Dimensional first-order excitation force, page 91
$F_{+}^{[2]}$	Dimensional second-order excitation force at sum frequency, page 92

$F_-^{[2]}$	Dimensional second-order excitation force at difference frequency, page 92
F_D	The total damping on an array of floats such that $F_D = R + B$, page 158
F_e	Excitation force, page 43
F_r	Radiation force, page 43
F_t	Time series of dimensional forces, page 92
F_{damp}	Mechanical damping force, page 43
F_{ext}	External driving force, page 43
F_{fd}	Viscous drag, page 76
F_{res}	Restoring force, page 43
$G(t)$	Arbitrary function of time only, page 36
$G(\theta, \psi_i)$	Function used to simplify Equation (2.45), page 50
H	Wave height, page 23
H_1	Initial height of radiated wave, page 78
H_2	Height of radiated wave at the channel wall, page 78
H_3	Height of wave at body centre after being radiated and reflected back from channel wall, page 78
H_s	Significant wave height, page 89
L	Wavelength, page 24
M	Body (dry) mass, page 43
M_m	The displaced mass of a float, page 62
M_{sup}	Supplementary mass on float, page 62
N	Number of bodies, page 34
N_R	Number of damping values considered in Method 1, page 120
P	Power, page 52
P_0	Power from an isolated device, page 110

$P_1(\omega)$	The maximum net power from the coarse net power range for which R values are determined during the iterative procedure of Method 2, page 122
P_c	Power in an arc of a circular wave radiated from a body, page 77
P_w	Power per unite length of wave crest, page 77
$P_{1it}(\omega)$	Individual power values determined to correspond to the greatest net power from a coarse net power range during the iterative procedure of Method 2, page 123
$P_{net}^{[C]}$	A discrete coarse range of net power values specified for use during the iterative procedure of Method 2, page 122
$P_{net}^{[F]}$	A discrete fine range of net power values specified for use during the iterative procedure of Method 2, page 123
Q	Normalised Interaction Factor, page 57
R	Mechanical damping coefficient, page 43
$R_{1it}(\omega)$	R values determined to correspond to the greatest net power from a coarse net power range during the iterative procedure of Method 2, page 123
R_{B0}	Radiation damping given relative to the maximum radiation damping on isolated device with $R = B$ and $M = 2M_m$ such that $R_{B0} = \frac{R}{\max B_0}$, page 115
R_{opt}	Mechanical damping calculated using the equation which gives the optimum mechanical damping value for an isolated device with fixed mass, page 117
S	Hydrostatic stiffness, page 44
S_1	Hydrostatic stiffness calculated using Equation (3.4), page 65
S_2	Hydrostatic stiffness calculated using Equation (3.5), page 65
S_b	The body surface, page 47
Sum	The sum over all wave frequencies and all floats, page 184
T	Wave period, page 23
T_p	Peak wave period, page 89

U	Velocity, page 35
U_b	The body velocity normal to the body surface, page 38
$X(t)$	Displacement of the body (variation of position with time), page 43
Z_1	Arbitrary complex variable, page 126
Z_2	Arbitrary complex variable, page 126
$\Im$	Imaginary part of a complex number, page 53
Ω_i	The total damping on float number i of the base array, page 158
Φ	Velocity Potential, page 35
Φ_e	Excitation velocity potential, page 41
Φ_e	Scattered velocity potential, page 41
Φ_i	Incident velocity potential, page 41
Φ_r	Radiation velocity potential, page 41
$\Re$	Real part of a complex number, page 53
$\Theta_i(D)$	The total radiation damping on float number i of the pair of cylinders with draft D, page 158
$\bar{X}$	Mean of all of the time averaged response amplitudes measured experimentally, page 65
$\breve{\sigma}$	stress tensor, page 35
$\breve{F}^{[1]}$	Non-dimensional first-order excitation force, page 91
$\breve{F}^{[2]}_{+}$	Non-dimensional second-order excitation force at sum frequencies, page 91
$\breve{F}^{[2]}_{-}$	Non-dimensional second-order excitation force at difference frequencies, page 91
$\delta\omega$	Frequency increments, page 90
$\delta\omega_F$	Frequency increment used to determine force amplitudes from the post-FFT force spectral density (independent of pre-FFT increments), page 96
$\delta\omega_{int}$	Frequency increments used in interpolated data, page 94

$\delta\psi$	Length of geometry panel in ψ direction, page 49
$\delta\theta$	Length of geometry panel in θ direction, page 49
$\dot{U}$	Float acceleration, page 78
ϵ	Small parameter used to expand velocity potential into a perturbation series, page 38
η	Equation of free surface, page 37
γ_1	A positive constant, page 43
γ_2	Coefficient used in Equation (2.44), page 49
γ_3	Coefficient used in Equation (2.44), page 49
γ_4	Constant, page 117
$\hat{}$	Complex amplitude, page 44
$\lvert X_z \rvert$	Response Amplitude, page 63
$\lvert d_z \rvert$	Response Amplitude Ratio, page 64
$\lvert d_z \rvert_{R=0}$	Free-float response amplitude ratio (calculated using Equation (3.1) with $R = 0$), page 147
$\lvert d_z^{[C]} \rvert$	Response amplitude ratio calculated numerically, page 71
$\lvert d_z^{[E]} \rvert$	Response amplitude ratio measured experimentally, page 71
μ	Viscosity, page 35
∇	The vector differential operator, del, page 35
ω_p	Frequency corresponding to Peak Period such that $\omega_p = \frac{2\pi}{T_p}$, page 100
ω_b	Frequency at which dimensional force amplitudes, calculated from interpolated non-dimensional forces, are given in the frequency domain, page 97
ω_{l1}	Lower limit to frequency bins used to determine the force amplitudes from the force spectral density, page 97
ω_{l2}	Upper limit to frequency bins used to determine the force amplitudes from the force spectral density, page 97

ω	Angular wave frequency, page 24
ω_0	Natural frequency, page 83
ω_m	The frequency at which the maximum ratio of second-order forces to first-order forces occurs within the restricted frequency range of $0.5 \leq \omega \leq 1.3$ rad/sec, page 101
ω_p	Peak period such that $\omega_p = \frac{2\pi}{T_p}$, page 89
ψ	The angle to the negative vertical (z) axis, page 47
ρ	Fluid density (≈ 1025 kg/m^3 for sea-water), page 35
θ	The angle to the positive horizontal (x) axis, page 47
$\tilde{P}$	Time averaged power loss, page 75
$\underline{n}$	The normal to the body surface pointing into the fluid domain, page 47
φ_A	Phase, page 92
ϑ	Phase difference of reflected radiated wave compared to originally radiated wave, page 78
ζ	Spectral density, page 89
$\zeta_F^{[1]}$	Spectral density of the first-order force, page 92
$\zeta_F^{[2]}$	Spectral density of the second-order force, page 92
*	Complex Conjugate (supersript), page 52
^{T}	The transpose of a matrix (superscript), page 53
a_1	Horizontal radius of experimental ellipsoidal floats, page 62
a_2	Vertical radius of experimental ellipsoidal floats, page 62
d	Water depth, page 23
g	Acceleration due to gravity $= 9.8$ m/s^2, page 35
k	Wavenumber, page 38
n_x	Normal to the body surface pointing into the fluid domain in the x (horizontal) direction, page 48

n_z	Normal to the body surface pointing into the fluid domain in the z (horizontal) direction, page 48
p	Pressure, page 35
q	Interaction factor, page 54
r_c	Radius of a circular wave, page 77
s	Float separation distance within an array (from one float centre to the adjacent float's centre), page 24
s_c	Half of the width of a channel, page 77
t	Time, page 35
v_φ	Vorticity, page 35
x	Horizontal Cartesian coordinate, page 34
y	Horizontal Cartesian coordinate, page 37
z	Vertical Cartesian coordinate, page 34
z_C	The calculated response amplitude ratio, page 184
z_E	The experimentally measured response amplitude ratio, page 184

Abstract

The University of Manchester
Sarah Bellew
Doctor of Philosophy
Investigation of the Response of Groups of Wave Energy Devices
September 2011

Placing wave energy devices within close proximity to each other can be beneficial as the costs of deployment, maintenance and infrastructure are reduced significantly compared to if the devices are deployed in isolation. A mathematical model is presented in this thesis which combines linear wave theory with a series of linear driven harmonic oscillators to model an array (group) of floating wave energy devices which move predominantly in heave (vertically) in a train of incident regular waves. Whilst similar mathematical models have been used previously to investigate interactions between fluids and groups of structures, much of the published work does not address array configurations or device constraints that are relevant to designers of structure-supported array devices.

The suitability of linear theory for application to closely spaced arrays is assessed in this thesis through comparison to small-scale experimental data and by evaluation of the magnitude of second-order hydrodynamic forces. Values of mechanical damping and mass are determined for each element of an array in order to achieve the maximum power from an array of floats without requiring the knowledge of the motion of every float within the array in order to apply the forces to any one float. Further to this, the analysis of floats of varying geometry is performed in order to assess the possibility of array optimisation through the variation of float geometries within a closely spaced array.

It is shown in this thesis that linear theory provides a reasonable prediction of the response of floats that are sufficiently close together to interact for most wave frequencies to which the arrays are likely to be subjected. Under the assumption of easily implementable mechanical damping, it is determined that the power output from an array of floats of equal geometry can be increased by specifying different magnitudes of mechanical damping on each float independently of the radiation damping. Variations in submerged float geometries for the purpose of manipulating array characteristics according to the incident wave frequency are best applied through the variation in draft of a single geometry. Variations in submerged float geometry which occur close to the free surface are found to be of the greatest significance. Where the float is uniform in cross-section, the most appropriate method to select float drafts within an array is found to be based on the evaluation of the total damping on each float.

Lay Abstract

The University of Manchester
Sarah Bellew
Doctor of Philosophy
Investigation of the Response of Groups of Wave Energy Devices
September 2011

Placing wave energy devices within close proximity to each other can be beneficial as the costs of deployment, maintenance and infrastructure are reduced significantly compared to if the devices are deployed in isolation. At such close proximity the devices will interact with each other in that devices will be subjected not only to the incident wave but also the waves which have been modified due to contact with other devices within the array. These interaction effects can be either beneficial or detrimental to the power production from the array depending on the precise wave conditions, device design and layout of array. This thesis addresses the modelling of groups (arrays) of wave energy devices which each use vertical (heaving) motion to generate electricity with a view to obtaining accurate predictions of their behaviour in different sea conditions as well as optimising their power output.

Declaration

No portion of the work referred to in the thesis has been submitted in support of an application for another degree or qualification of this or any other university or other institute of learning

Copyright Statement

i The author of this thesis (including any appendices and/or schedules to this thesis) owns certain copyright or related rights in it (the Copyright) and s/he has given The University of Manchester certain rights to use such Copyright, including for administrative purposes.

ii Copies of this thesis, either in full or in extracts and whether in hard or electronic copy, may be made only in accordance with the Copyright, Designs and Patents Act 1988 (as amended) and regulations issued under it or, where appropriate, in accordance with licensing agreements which the University has from time to time. This page must form part of any such copies made.

iii The ownership of certain Copyright, patents, designs, trade marks and other intellectual property (the Intellectual Property) and any reproductions of copyright works in the thesis, for example graphs and tables (Reproductions), which may be described in this thesis, may not be owned by the author and may be owned by third parties. Such Intellectual Property and Reproductions cannot and must not be made available for use without the prior written permission of the owner(s) of the relevant Intellectual Property and/or Reproductions.

iv Further information on the conditions under which disclosure, publication and commercialisation of this thesis, the Copyright and any Intellectual Property and/or Reproductions described in it may take place is available in the University IP Policy (see http://documents.manchester.ac.uk/DocuInfo.aspx?DocID=487), in any relevant Thesis restriction declarations deposited in the University Library, The University Librarys regulations (see http://www.manchester.ac.uk/library/aboutus/regulations) and in The Universitys policy on Presentation of Theses

Acknowledgement

I would like to express my sincere gratitude to my supervisors, Tim Stallard and Peter Stansby. Their encouragement, guidance and support from the initial to the final level helped me to develop a thorough understanding of the subject and enabled me to present my work at five international conferences and workshops throughout the course of the project.

I also would like to thank my husband, parents and colleagues for there continued support during the completion of the degree.

The Author

The author has previously completed a Master of Mathematics degree at The University of Leeds. During the course of the PhD project the author has published three conference papers as the first author (Thomas et al. (2008), Bellew et al. (2009) and Bellew and Stallard (2010)).

Chapter 1

Introduction

As the fossil fuel resources are depleting and the effects of global warming become more apparent, the desire to harness energy from renewable sources is ever increasing. Whilst 18% of the global electricity supply was formed from renewable energy in 2009, the wave energy industry is in its infancy with most devices currently still in the design and testing stages (REN21, 2010).

This thesis addresses the modelling of groups (arrays) of wave energy devices which each use vertical (heaving) motion to generate electricity with a view to obtaining accurate predictions of their behaviour in different sea conditions as well as optimising their power output.

This chapter begins with an overview of the different types of ocean wave energy devices which exist today (Section 1.1), followed by an explanation of why placing devices within close proximity to each other is of great interest to many device developers (Section 1.2).

There are many challenges to be overcome when designing a wave energy device (Section 1.3) and many stages to the development process before a full-scale commercial device is ready for grid connection (Section 1.4).

A numerical model is presented in this thesis to be applied to closely spaced arrays of wave energy devices. Some of the difficulties in modelling a real sea are discussed in Section 1.5. The fundamentals of the numerical model are then given in Section 1.6 (with a more complex mathematical description given in Chapter 2).

1.1 The Current Stage of the Industry

As the wave energy industry is still at the early stages of its development, there are many different methods currently being considered in order to extract the energy from the waves. Many of the device designs can be divided into the five categories of oscillating water columns (OWCs), overtopping devices, fully submerged oscillating bodies, bodies which oscillate about a hinged joint which is beneath the sea surface and floating oscillating bodies. This section gives a general description of each of these classifications together with details of some of the commercial devices which fall into them.

1.1.1 OWCs

An Oscillating Water Column (OWC) generally consists of a partially submerged structure, inside which air trapped above the free surface is forced through a turbine by the oscillatory motion of the free surface, thus driving an electricity generator. They can be located either at the shoreline by fixing them to a seabed or cliff, or offshore as floating devices which are moored to the seabed. Several full-scale, fixed devices have been installed around the world including the LIMPET in the UK (Boake et al., 2002) and the Pico Power plant in Azores (Brito-Melo et al., 2008). Fixed OWCs generally have a typical installed capacity of 60-500kW except for the OSPREY which had an installed capacity of 2mW, however that was destroyed by the ocean in 1995 (Falcão, 2010). The shoreline location of the fixed OWCs is a low energy environment but is beneficial for ease of installation and management. Several designs of floating OWCs exist including the Mighty Whale which was installed off the coast of Japan in 1998 (Washio et al., 2000), and the OE Buoy which has completed 2 years of $\frac{1}{4}$ scale sea trials in Ireland (OceanEnergy Ltd, 2011).

1.1.2 Overtopping Devices

An overtopping device allows the wave crests to flow over a dam into a raised reservoir where the water is allowed to flow back to sea-level through turbines. Notable overtopping devices include the Tapered Channel Wave Power Device (Tapchan) located at the shore fixed to a cliff (Clément et al., 2002), the Floating Wave Power Vessel fixed to the seabed by a multi-directional anchor system (Clément et al., 2002), Wave Dragon which focuses waves towards a ramp using large wave reflectors (Tedd and Kofoeda, 2009) and the Seawave Slot-Cone Generator (SSG) which includes a series of three reservoirs located above each other (Vicinanza and Frigaard, 2008).

1.1.3 Submerged Oscillating Bodies

Several devices have been suggested which would operate whilst fully submerged. The Bristol Cylinder comprises a submerged horizontal circular cylinder anchored to the seabed whose vertical and horizontal oscillations activate hydraulic pumps which are located within the anchors (Evans et al., 1979a) (McIver and McIver, 1995). The Edinburgh Mace (Salter et al., 2002) consists of a vertical spar with an enlarged head which oscillates about a hinge at the seabed, thus moving cables which attach the head to two points on the seabed, in the fore and aft positions of the prevailing wave direction. Whilst the Bristol Cylinder was tested at a small scale in an experimental wave tank with positive results, neither the Bristol Cylinder nor the Edinburgh Mace have been tested in the ocean. The Archimedes Wave Swing (AWS Ocean Energy Ltd, 2011) consists of a bottom air-filled cylindrical chamber which is fixed to the seabed and a floating upper cylindrical section which oscillates due to changes in pressure. Based on results of a full-scale prototype tested in 2004 (Prado et al., 2006) a modified version is currently under investigation.

1.1.4 Hinged Oscillating Bodies

Both the WaveRoller (AW-Energy Oy, 2011) and the Oyster (Whittaker et al., 2007) (Aquamarine Power, 2011) devices consist of flaps which are hinged to the seabed at one end, with the other end raising and lowering about the anchored point beneath the motion of the waves. This motion activates hydraulic rams on the sea bed thus pumping high pressured fluid to shore. The Oyster, whose flap is surface piercing, has undergone full-scale sea trials since 2009. A full-scale prototype of the WaveRoller, which is fully submerged and smaller than the Oyster, is currently under construction with a view to testing in the ocean in 2012. Both the Oyster and the WaveRoller are intended to operate in farms consisting of multiple devices. WRASPA is another hinged device which unlike the WaveRoller and the Oyster is not hinged on the seabed but on a fixed vertical base unit (Chaplin et al., 2009). It is still in the early stages of development hence has not undergone any sea trials.

1.1.5 Floating Pitching Devices

Pitching motion is the rotation about a transverse axis such as the rise and fall of a ship's hull under the motion of waves. Several devices make use of pitching motion to generate electricity from the waves. One of the more famous of the pitching devices is the Duck. In earlier designs it consisted of floating devices which pitched around spines which were aligned with the direction of incident waves (Jarvis, 1979). In later designs it consisted of an isolated floating device which pitched relative to a gyro (Salter, 1982). Many small scale experimental studies of the Duck were carried out, however no full-scale prototypes were ever built. Another famous pitching device is Pelamis which has already undergone a full-scale test of an array of three devices, each with an installed capacity of 750kW, 5km off the coast of Portugal. It is currently in the developmental stage of testing 27 full-scale devices between 1 and 10km off the coast of Scotland (Pelamis Wave Power Ltd, 2011). Two further devices which use the relative pitching of adjoining pontoons to generate electricity are the McCabe Wave Pump and the Raft (Falcão, 2010). A pitching device which has already undergone $\frac{1}{4}$ scale sea trials is Oceantec which consists of an elongated body that stays aligned with the wave fronts whilst using pitching motion relative to a gyroscopic device within it (Salcedo et al., 2009). Searev consists of a floating hull in which a hydraulic pump is activated by the relative movement of a large and heavy cylinder within the hull (Babarit and Clement, 2006). The PS Frog also uses the relative motion of an internal mass in a floating body, but it is set into motion by a submerged paddle (McCabe et al., 2006).

1.1.6 Floating Heaving Devices

Many wave energy devices use the heaving (vertical) motion of floats to generate electricity. This can be achieved using the heave motion relative to either the seabed, a second section of the float or a fixed structure.

Heave Relative to Sea-Bed Anchor

Several devices which used the heaving motion of a floating device relative to anchors on the seabed to generate electricity were developed by Budal between 1978 and 1983. The first device, the E-model, consisted of a vertical cylindrical float with a hemispherical bottom connected to the seabed by a pretensioned cable and used a piston pump. The second device, the M2-model, used a conical float with the broader part at the top which was connected to the seabed anchor by a steel rod and also used a piston pump. The third device, the N2-model, used a spherical float which was open at the lower end and connected to the seabed anchor by a steel rod and incorporated an OWC. All three models were experimentally tested at $\frac{1}{6} - \frac{1}{10}$ scale in a wave tank and the N2-model was also tested in the open sea (Falnes and Lillebekken, 2003).

More recently the the Wave Power Project Lysekil in Sweden has designed and tested an array of three full-scale devices consisting of heaving floats which are each anchored to the seabed and drive electrical generators on the seabed via cables but are designed to work in formation (Uppsala Univeritat, 2011) (Leijon et al., 2008) (Rahm, 2010).

Heave Relative to Secondary Section of Float

PowerBuoy (Draper, 2006) (Ocean Power Technologies Inc, 2011), Wavebob (Weber et al., 2009) (Wavebob Ltd, 2011), IPS Buoy (Falcão et al., 2009) (Interproject Service AB (IPS) and Technocean (TO) , 2011), Aegir Dynamo (Al-Habaibeh et al., 2010) (Ocean Navitas Ltd, 2011) and Aquabouy (Wacher and Neilsen, 2010) all use the heaving motion of a float relative to a secondary section of the float to generate electricity. Aquabouy for example consists of a large float with a large vertical shaft attached to its underside. The heaving motion of the float causes water to rush into the shaft which causes a piston located in the centre of the shaft to move. The movement of the piston then causes a hose to stretch resulting in water being pumped into a turbine which powers a generator. A $\frac{1}{5}$ scale Aquabouy device was deployed off the coast of Oregon in 2007.

Heave Relative to a Fixed Structure

Several heaving wave energy devices, not only place devices in close proximity to each other, but connect the devices to a common structure above the sea level. One such device is the Wavestar in which heaving floats are connected to a fixed platform via arms whose motion is transferred into the rotation of a generator (Wave Star A/S, 2011). Live sea trials on a $\frac{1}{10}$ scale device containing 40 hemispherical floats each of 1 m diameter began in 2006 with a 5.5 kW installed capacity. More recently a $\frac{1}{2}$ scale device with only 2 floats and a 600 kW installed capacity began sea trials in 2009 which has been connected to the grid since February 2010.

The Brazilian hyperbaric wave energy converter also comprises of several heaving floats connected on two sides of a common structure via arms. On each side of the platform the floats are not placed in a single line parallel to the structure as in the Wavestar, but are alternately placed in two lines parallel to the structure. The power take-off system uses hydraulic pumps activated by each arm together with a hyperbaric chamber to release a jet of water from a sealed circuit to activate a hydraulic turbine (Garcia-Rosa et al., 2009). Both $\frac{2}{13}$ and $\frac{1}{10}$ scale devices have been tested in large experimental wave-tanks in Brazil.

The Manchester Bobber is a device consisting of multiple floats each connected by a cable over pulleys to a counterweight so that the heaving motion of each float causes the rotation of a generator via a fly wheel (The University of Manchester, 2011). The device has been tested within an array in an experimental wave-tank at $\frac{1}{69}$ scale, with plans currently under-way to test a full-scale isolated float in open sea conditions.

The FO^3 Wave Energy Converter also consists of several heaving devices connected to a common platform, however the floats are connected to the platform by rigid rods instead of cables and the platform is floating (Taghipour and Moan, 2008). The FO^3 has been tested in the ocean with a single float and with an array of 4 floats at $\frac{1}{3}$ scale off the coast of Norway. The final design is intended to consist of 21 floats and have an installed capacity of 0.4 - 0.6 MW (Sustainable Economically Efficient Wave Energy Converter Project, 2011) (de Rouck and Meirschaert, 2009).

1.2 Closely Spaced Arrays

As the power output of most wave energy devices is small when deployed in isolation, (order of 1-2MW) commercial farms must comprise large numbers of individual devices. The devices which consist of heaving floats fixed to a common structure (described in Section 1.1.6) already incorporate this idea into their fundamental design.

Placing the devices within close proximity to each other can be beneficial as the costs of deployment, maintenance and infrastructure are reduced significantly compared to if the devices are deployed in isolation. At such close proximity the devices will interact with each other in that devices will be subjected not only to the incident wave but also the waves which have been modified due to contact with other devices within the array. These interaction effects can be either beneficial or detrimental to the power production from the array depending on the precise wave conditions, device design and layout of array.

Such devices are likely to be situated in the ocean at water depths (the distance from the undisturbed free surface to the seabed) of $d \sim 30$ m. The incident wave spectrum consists of several waves each of which have a period, T, (the time taken for two consecutive crests to pass a fixed point) and wave height, H, (the vertical distance between a crest and an adjacent trough). Within the incident wave spectrum the period of the wave which has the greatest energy is known as the peak period. Closely spaced arrays of wave energy devices are likely to be subjected to waves of peak periods in the range of 5 to 12 seconds. The wave frequency, ω, represents the flux of the wave crests, which is the number of wave crests passing a fixed point per unit time. It relates to the period of the wave such that $\omega = \frac{2\pi}{T}$. The wave frequency range corresponding to peak periods of 5 to 12 seconds to which the devices are likely to be subjected is 0.5 to 1.25 rad/s. Typical dimensions of the devices are radii of $a = 5$ m, and centre to centre separation distances of $s \sim 4a$.

1.3 Design Challenges for Wave Energy Devices

The immaturity of the wave energy industry is not due to the lack of potential, as ocean waves provide one of the most concentrated sources of renewable energy. With the exception of tidal waves, ocean waves are generated by the wind which is in turn generated by solar energy, and at each stage of the energy conversion the power becomes more concentrated. The concentration of wave power just below the sea surface is therefore approximately 5 times greater than the concentration of wind power 20 metres above the surface, and 20 to 30 times greater than that of solar power (Brooke, 2003). Ocean waves commonly have between 10 and 50 kW power per meter wave crest.

Wave power is dependent on the speed and duration of the wind and the distance over which the wind blows. In deep water the waves lose energy very slowly, allowing the waves to travel significant distances, becoming more regular in form as they move away from their origin. Coastlines which are exposed to prevailing winds therefore commonly have energetic wave-climates (Brooke, 2003). Only a fraction of the wave energy reaches the shores, however, as energy is lost due to interactions with the seabed when the waves reach shallow water, that is water with depths of less than half the wavelength (where the wavelength, L, is the horizontal distance between two wave-crests) (Cruz, 2008). Situating wave energy devices in close proximity to the shore is desirable to reduce the cost of deployment and maintenance. A compromise must therefore be sought between the high energy density of the deep waters and the low maintenance and infrastructure costs of the shallower waters when selecting a wave energy deployment site.

At any one location the power from the waves is inconsistent. It varies according to the season and the short term weather conditions and is variable from one wave to the next (Falnes, 2007). A key difficulty in effectively harnessing wave energy is creating a device which can operate in such an irregular source, producing electricity in a wide range of sea states.

A wave energy device must be able to withstand the harsh conditions of the sea. On a day to day basis this means it must be able to withstand the corrosive environment of the sea. The presence of dissolved oxygen and chloride ions in the seawater cause passive films to be simultaneously formed and broken down on metallic surfaces. Microbiological organisms living in the seawater attach themselves to structures resulting in the formation of a biofilm which can either accelerate or decelerate corrosion. There are numerous influential factors in the rate of corrosion of a structure such as the structural materials, the pH levels, oxygen content and temperature of the water and the fluid velocities (Shifler, 2005). Any parts of a device which remain above the seawater are exposed to the effects of wind and solar radiation as well as the corrosive effects of the seawater splashing upon them.

On a longer time span, the device must be sufficiently robust to survive extremes storms, storms which may only occur once or twice in the devices' lifetime. During such extreme storms the survivability of the device takes precedence over power capture, and so device designers must address two distinct design conditions, one for power capture and another for survivability in extreme storms. For example, Wavestar, a device which generates electricity from the motion of a group of floats, raises all of the floats out of the water during a severe storm, locking them in what the designers call "Storm protection mode", whereas the Manchester Bobber, which also generates electricity from the motion of a group of floats, has the ability to significantly reduce the floats' motion in extreme storms by applying only a small (~ 10 %) change in mass (Stallard et al., 2009b).

1.4 Research and Development Methods

It is expensive and time consuming to test devices at full-scale so it is vital that as much research as possible is carried out during the design stage. This research usually comprises of a combination of experimental and numerical modelling. Experimental modelling usually involves testing reduced geometric scale prototypes of the device in experimental wave tanks followed by either full scale or slightly reduced scale devices in the open sea. If the devices are to operate within groups, then an isolated device or a small proportion of the final number of the devices is usually tested in the open sea before the full group is deployed. Experimental modelling is time consuming and involves inaccuracies in the effects of scaling and approximations made in the model such as the use of a channel to model the open sea.

Numerical modelling uses assumptions to simplify the problem of the devices operating in the open sea to a manageable mathematical model. This can be a time effective method to test and modify device designs, however the validity of the assumptions must be confirmed when using the results of a numerical model for application to real sea conditions.

In this thesis an appropriate numerical model for closely spaced wave energy device arrays is determined and used to investigate optimum characteristics for arrays. Analysis of the model's limitations is performed using comparisons to small scale experimental studies and more complex numerical models.

1.5 Modelling Real Sea States

Whilst the ocean provides a strong source of energy, it is a harsh and sometimes unpredictable environment for the wave energy devices to operate in. Within the operational environment the devices are subjected to winds, waves and currents which vary from extreme storm to very calm conditions. Most devices are designed to operate in mid-weather conditions, but must have a system in place to ensure its survivability in the extreme storm conditions. The model within this thesis is only valid for devices in their operational state. The wind and current are not included in the models of this thesis. The effects of the wind are largely dependant on the precise device design, and the extent of the exposure above the water surface. The effects of current are known to change the forces and run-up in the wave-body interaction problem. These effects are studied in depth for isolated devices by different authors, originally in the frequency domain (e.g Grue and Palm (1984)), and more recently in the time-domain (e.g Liu et al. (2010), Liu and Teng (2010)). The inclusion of a small current in the current model could be implemented post analysis if required.

Ocean waves are irregular, meaning that the wave profile formed at any one position over a length of time is irregular, but can commonly be defined by summing regular sinusoidal waves which have different phases and amplitudes. Although it is not possible to determine precisely the characteristics of the individual component regular waves, a good approximation can be made using methods known as zero-upcrossing and zero-downcrossing. These methods partition the wave profile according to the points at which it crosses the mean water line (in the upwards or downwards direction respectively), so that the wavelength and wave-height can be determined for each component section, disregarding small fluctuations in the wave profile within each section. Irregular seas, by definition, vary irregularly with time so can only be directly analysed in the time domain which is complicated and computationally demanding for arrays of devices.

This thesis focuses on analysis in the frequency domain which means the analysis is performed for time-averaged regular waves and the corresponding time-averaged float characteristics. Understanding the limits to response in regular waves is a crucial step to forming an understanding in irregular waves, so although the results are not fully representative of a real sea state, they are highly informative. As the exact wave profile to which the devices will be subjected is not known in advance, the time-averaged frequency domain model is useful to determine how the devices are likely to react in the approximately predicted near future sea state. This could enable modifications and alterations to be made to the devices at regular time intervals in order to better extract power from the waves.

1.6 Hydrodynamic Modelling Techniques

In order to determine the forces, motions and power output of a wave energy device, both the workings of the device and the fluid within which it is placed must be effectively modelled. This section discusses the fundamentals of modelling the interaction between fluids and structures. A basic overview of these concepts is given in the following sections, with a more detailed mathematical description given in the next chapter (Chapter 2).

The most fundamental concept of the fluid model presented in this thesis is that the fluid is ideal (Section 1.6.1). This allows for a mathematical model of the fluid to be formed using boundary and radiation conditions. Applying the further assumption of small amplitudes of motion leads to linear wave theory (Section 1.6.2). Drag forces are not accounted for within the numerical model of this thesis as they should not be significant for the closely spaced arrays under investigation (Section 1.6.3).

Due to the proximity of the bodies to each other within the closely spaced arrays, modifications to the wave-field due to the presence of other bodies must be accounted for within the model. In some cases these interaction effects can result in significantly different forces and motions to a device in isolation (Section 1.6.4).

A model which accounts for the interaction effects can be time-consuming, particularly without the aid of computational modelling programmes such as WAMIT which is employed throughout this thesis. Several attempts have therefore been made in the past to simplify the model for wave interactions with groups of structures. Whilst analyses made using such approximation theories have sometimes produced remarkable results, they are not suitable for the analysis of closely spaced arrays of wave energy devices (Section 1.6.5) and so are not used within the model presented in this thesis.

1.6.1 Ideal Fluid

The equations of motion for a Newtonian fluid with constant viscosity are known as the Navier Stokes equations. Conservation of mass for an incompressible fluid requires that the volumetric dilation of the fluid is zero, which is expressed in the continuity (of mass) equation. Assuming the flow to be inviscid, that is, it has zero viscosity, reduces the Navier Stokes equations to the Euler equations.

If the flow is assumed to be irrotational then the curl of the velocity vector must be zero. A continuous, differentiable scalar function whose gradient automatically ensures that this is true is known as the velocity potential. If the flow is both incompressible and irrotational then the continuity equation can be written in terms of the velocity potential, an equation known as Laplace's equation.

Applying the assumption of irrotational flow to Euler's equations reduces them to one equation, the Bernoulli equation, a relation between the fluid velocity, velocity potential, pressure and gravity as well as time if the flow is unsteady.

If a velocity potential which satisfies Laplace's equation and conditions on all the fluid boundaries and a radiation condition at infinity is determined for an inviscid, irrotational and incompressible flow in which the velocity is known, Bernoulli's equation can be used to determine the fluid pressure.

1.6.2 Linear Wave Theory

The mathematical model of the fluid can be simplified by assuming the wave height is small when compared to the wavelength. This simplified version is known as linear wave theory, and was first suggested by Lamb in 1932 (Lamb, 1924, reprinted 1930). Using linear theory, it is possible to consider the flow beneath an irregular wave-field as the linear superposition of the flow beneath a number of regular wave components whose amplitudes are defined by the energy density of the irregular wave.

The velocity potential for a cylinder in a train of incident waves was first derived using linear theory by Havelock in 1940 (Havelock, 1940) for water of infinite depth, and later for finite water depth by McCamy and Fuchs in 1954 (McCamy and Fuchs, 1954). Since then linear theory has been used to find the velocity potentials of water in many situations, including in the vicinity of bodies of various geometries, and arrays of bodies.

1.6.3 Drag

When determining the loads on an offshore structure both potential flow effects and viscous effects may be important. When viscous forces are important, the Morison's equation can be used to calculate the force on a structure as the sum of a drag force component, typically proportional to the multiple of the fluid velocity and the absolute value of the fluid velocity, and an inertial force component proportional to the fluid acceleration. Viscous effects are usually deemed significant when the body diameter is small compared to the waveheight so that the flow is likely to separate.

The numerical model applied within throughout this thesis is applicable to closely spaced arrays of wave energy devices which are subjected to small amplitude waves. As the wave-heights are assumed small drag effects should be minimal, so Morison's equation is not required in the calculation of forces.

When a body diameter is large compared to the wavelength, the motion of the particles become small relative to the body dimension, hence the incident waves are modified after coming into contact with the body, a phenomenon known as diffraction. Diffraction effects are also significant for floating bodies and bodies which are in closely spaced arrays where interaction effects are significant.

As the focus of this thesis is closely spaced arrays of wave energy devices, diffraction effects must be accounted for in the model.

1.6.4 Trapped Waves

Trapped waves are oscillations of a fluid at a particular frequency which exist on the free surface in a localised region and so have finite energy, but have no radiation of energy to infinity. Trapped waves were initially discovered on a sloping beach in the form of a wave which propagates along the shoreline instead of perpendicular to it and has an amplitude which decays exponentially away from the shoreline (Stokes, 1846).

Trapped waves were later found to exist when a cylinder is placed on the centreline of an infinitely long channel (Stokes (1846), Jones (1953) and Ursell (1987)). A cut-off frequency is a frequency above which all waves will propagate to infinity, but below which the existence of discrete frequencies corresponding to trapped waves is possible

(Linton and Evans, 1992). The trapped waves in an infinitely long channel with a cylinder on its centreline have been shown to occur with wave frequencies just below the cut-off frequency (Evans and Linton (1991), Callan et al. (1991)).

Large wave loads have been found to occur on arrays of fixed vertical cylinders at specific wave frequencies which are comparable to trapped mode frequencies in a channel (Maniar and Newman, 1997). This phenomenon is explained by Maniar and Newman (1997) by describing planes normal to the centre-line of the array position, mid-way between the cylinders, as boundaries similar to channel walls.

The wave-loads determined on a long array of cylinders at a trapped wave frequency were found to be up to 35 times greater than those experienced by an isolated cylinder (Maniar and Newman, 1997). When analysed experimentally, the amplitude of free surface motion in the vicinity of fixed cylinders within an array was found to be less than the numerical predictions, but still significant (Kagemoto et al., 2002).

At certain wave frequencies it is therefore possible to experience much greater wave loads by placing devices in an array than in isolation which is a phenomena of keen interest to wave energy device researchers and developers.

1.6.5 Approximation Theories

Point absorber theory, first introduced by Budal (1977), and Plane Wave theory, first introduced by Simon (1982), are both approximation theories for analysing the response of arrays of devices. They are both developed using linear wave theory with the addition of the assumption that the inter-device spacing is large compared to the incident wave length plus one other assumption.

Point Absorber Theory

Point absorber theory, developed by Budal (1977), uses the assumption that the spacing between the bodies is large when compared to the diameters of the bodies together with the assumption that the far-field waves generated by each body within the array are not significantly disturbed by any of the other bodies or their generated waves. Budal partially optimized the power by defining a specific phase condition. He found that when the inter-device spacing is less than or equal to one wavelength, the power absorbed by a device within the array can be significantly greater than that of an isolated device. The average power absorbed by the bodies placed within a two-body array and a ten-body array was calculated to be a factor of 1.67 and 2.2 greater than when the same body was placed in isolation. For a theoretical, infinite array the maximum ratio of mean power absorption from a device within the array compared to a device in isolation was found to approach π when the devices are separated by a distance of one wavelength.

Evans (1979) and Falnes (1980) expanded on Budals work independently, to find a formula to calculate the optimum power output of an array of heaving point absorbers. They use the optimum value of the velocity amplitude for the devices (i.e. the value which gives the maximum value for power absorbed by the body). This is a complete and general optimisation, unlike Budal's whose phase condition only partially optimized the power in many cases. Their results were used by Thomas and Evans (1981) to determine the optimal wave-absorbing characteristics, displacements and power absorption of an optimally tuned array of 5 and 10 heaving semi-immersed spheres.

Plane wave theory

Simon (1982) developed a 'Plane Wave' approximation to the multiple scattering problem. The additional assumption in plane wave theory is that far from a structure the diverging waves can be approximated locally by plane waves. Based on this assumption the interactions only occur between plane waves, which simplifies the computations to a matrix equation.

Comparisons with linear wave theory have found plane wave theory (including a correction term) to be largely accurate for an array of bottom-mounted, surface piercing, vertical cylinders (McIver and Evans, 1984), and for a two element array of floating bodies (McIver, 1984), provided the spacing to wavelength ratio remains large. The theory has been shown to require minimal computational time but have a fairly high level of accuracy for the purpose of studying arrays of fixed, bottom-mounted, vertical cylinders, finding that Tension Leg Platforms experience large loads compared to isolated columns (Williams and Demirbilek, 1988).

Validity of Approximation Theories

The forces on a 5×1 array of floating circular cylindrical floats of radius a which are permitted to move vertically and in two horizontal directions have been shown to be nearly identical when calculated using plane wave theory to when calculated using full linear theory in the two horizontal directions, but noticeably different in the vertical (heave) direction (Mavrakos and McIver, 1997). This difference in heave force between the plane wave and multiple scattering theories is greater at the smaller spacing of $s = 5a$ than the larger spacing of $s = 8a$ due to the first assumption that the bodies are far apart. Comparison of the interaction factors (ratio of power within array to the power from the same number of devices in isolation) for the same array also found the results of the plane wave theory to be similar to those of full linear wave theory for both spacings provided the spacing to wavelength ratio is not too small.

Interaction factors calculated using Point Absorber Theory for the same array were also shown to be similar to those of full linear wave theory when the body radii are small compared to the wavelength. At higher body to wavelength ratios, the effects of scattering within the array become significant, making the approximation theory inaccurate.

The discrepancies in the heave force which have been found at $s = 5a$ for plane wave theory are likely to become even greater for the separation distance of $s = 4a$ considered in this thesis. As this is due to the assumption of wide spacing, which is also required in point absorber theory, neither theory is considered suitable for the closely spaced arrays considered here.

1.7 Synopsis

The aim of this Thesis is to quantify the influence of hydrodynamic interactions on the response and power output of closely spaced groups of wave devices. A numerical approach is employed based on the use of linear diffraction theory to facilitate analysis of a range of float- and array configurations. Linear analysis is conducted using the boundary element code WAMIT. An idealised model of an array is considered which comprises a coupled system of linear-spring-mass dampers. Details of the model are given in Chapter 2.

The suitability of linear wave theory for analysing arrays of wave devices has not been addressed in previous research. Comparison of the results of the numerical model to experimental measurements of undamped response and to second order sum- and difference-frequency irregular wave forces in Chapters 3 and 4 respectively provides a detailed assessment of the range of validity of the model.

A closely spaced array of fixed geometry floats in a fixed array layout is considered in Chapter 5 with a view to determining optimum mass and mechanical damping characteristics which can be realistically applied to the devices. Individual device geometry variations within a closely spaced array are considered in Chapter 6. Conclusions of both mathematical and engineering natures are drawn in the final chapter, Chapter 7, as well as a discussion on future projects leading on from the current research.

Chapter 2

Linear Modelling of an Array

In order to model the response or power output of a closely spaced array of wave energy devices, idealised models of both the wave field and the wave energy devices are typically used. In this chapter linear wave theory is introduced as an idealised model of the wave field, and a coupled system of N single-degree of freedom mechanical systems consisting of linear spring-mass dampers is used to model the wave energy device arrays. Particular attention is given to showing the resolution of the forces on floating bodies and consistency of the model with accepted studies of wave energy devices.

2.1 Modelling the Fluid

The flow past arrays of wave energy devices is assumed to be non-turbulent. Surface turbulence is likely to occur during extreme storms, however the model does not need to apply to this situation as in extreme storms survivability of the devices is prioritised over energy extraction. The flow is assumed to be two-dimensional in the vertical plane, with the horizontal and vertical coordinates, x and z respectively (see Figure 2.1).

2.1.1 Continuity Equations

A Newtonian fluid such as water must satisfy both a continuity Equation for mass and a conservation Equation for momentum. A continuity Equation is a partial differential Equation describing the transportation of a conserved quantity. The continuity Equation states that the rate at which mass enters a system is equal to the rate at which mass leaves the same system. This is written mathematically as

$$\frac{\partial \rho}{\partial t} + \nabla \cdot (\rho U) = 0, \tag{2.1}$$

where ρ is the fluid density, t is time, U is the velocity vector and ∇ represents the vector differential operator, del. The conservation Equation for momentum forms the Navier Stokes equations which are written in vector format as

$$\frac{\partial U}{\partial t} + U \cdot \nabla U = -\nabla \breve{\sigma} + \rho g, \tag{2.2}$$

where g is the acceleration due to gravity and $\breve{\sigma}$ the stress tensor (a set of 9 components, one for each of the 3 coordinate faces of an imaginary fluid element upon which stress acts and for each of the 3 directions in which the stress is directed).

2.1.2 Incompressible Fluid

All fluids are compressible to some extent, as the density changes due to differences in pressure and temperature. In water, however, the change in density is so small that it can be taken to be zero without loss of accuracy. When a fluid is assumed to be incompressible, the density of the fluid must not vary with time or position. The assumption that the fluid is incompressible reduces the continuity of mass equation to

$$\nabla \cdot U = 0. \tag{2.3}$$

The stress tensor for incompressible flows is also reduced to $\breve{\sigma} = \nabla p - \mu \nabla^2 U$, where p is the pressure and μ the viscosity, reducing the Navier Stokes equations to

$$\frac{\partial U}{\partial t} + U \cdot \nabla U = -\frac{1}{\rho}\nabla p + \mu \nabla^2 U + \rho g. \tag{2.4}$$

2.1.3 Irrotational Fluid

The fluid is assumed to be irrotational, meaning that its fluid particles are not rotating. Although this is rarely the case in reality, the effect of the rotation of the fluid is usually very small in non-turbulent water. When a fluid is irrotational the vorticity, v_φ, hence the curl of the fluid velocity is zero, $v_\varphi = \nabla \times U = 0$. This allows the fluid velocity to be expressed as the gradient of some scalar function, Φ, such that $U = \nabla \Phi$. The scalar function, Φ, which satisfies this equation is commonly known as the velocity potential. When $U = \nabla \Phi$ is substituted into the continuity of mass equation, Equation (2.3), the resulting condition on Φ is known as Laplace's Equation,

$$\nabla^2 \Phi = 0. \tag{2.5}$$

2.1.4 Inviscid Fluid

The fluid is further assumed to be inviscid, meaning it has zero viscosity ($\mu = 0$). Water has a low viscosity, so outside of boundary layers which are immediately adjacent to body surfaces its effects are negligible, justifying the inviscid approximation. The inviscid assumption simplifies the Navier Stokes equations (Equation (2.4)) to the following equation which is the vector form of Euler's equations,

$$\frac{\partial U}{\partial t} + U \cdot \nabla U = -\frac{1}{\rho} \nabla \left(p + \rho g z\right), \tag{2.6}$$

where p is the pressure and $-z$ the vertical distance below the free surface. In an irrotational, incompressible and inviscid flow, the condition of irrotationality can be used together with the velocity potential to reduce (2.6) to Bernoulli's equation,

$$\frac{\partial \Phi}{\partial t} + \frac{1}{2} \left(\nabla \Phi\right)^2 - gz + \frac{p}{\rho} = G(t), \tag{2.7}$$

where $G(t)$ is an arbitrary function of time only. By including the time dependence of G in the velocity potential, G can be a constant instead of a function.

Laplace's Equation can be solved subject to boundary conditions to find the velocity potential on a body (partly or fully) submerged in a fluid with surface waves, which can be used to determine the pressure distribution about the body using Bernoulli's equation, hence determine the forces on the body.

2.1.5 General Boundary Conditions

Resolution of forces on an immersed boundary requires solution of the flow problem together with boundary conditions on the body boundary, the free surface and the bottom boundary (see Figure 2.1) as well as a radiation condition.

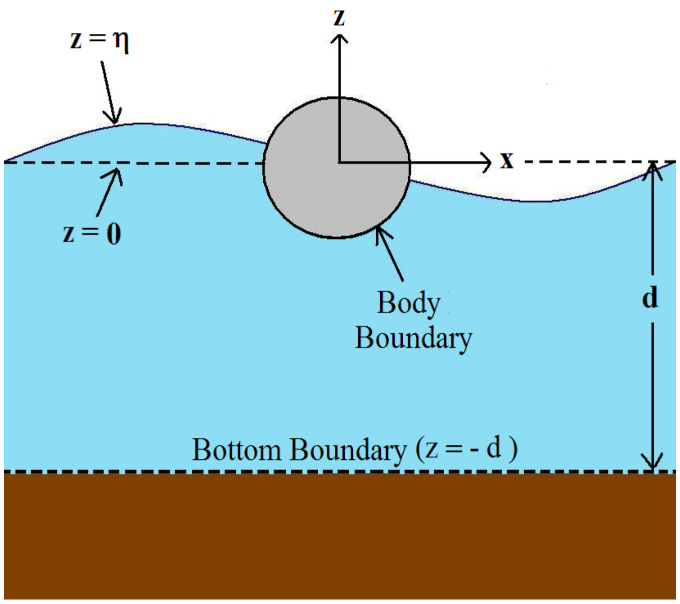

Figure 2.1: A body located at the free surface with coordinate system and boundaries labelled

The kinematic surface condition states that any particle which lies on the free surface must remain on the free surface, such that where $\eta(x, y, z, t)$ describes the free surface,

$$\frac{\partial \eta}{\partial t} + \frac{\partial \Phi}{\partial x}\frac{\partial \eta}{\partial x} + \frac{\partial \Phi}{\partial y}\frac{\partial \eta}{\partial y} - \frac{\partial \Phi}{\partial z} = 0 \qquad \text{on the free surface.} \tag{2.8}$$

The dynamic free-surface condition ensures that the pressure must remain constant across the free surface such that

$$\frac{\partial \Phi}{\partial t} + \frac{1}{2}(\nabla\Phi \cdot \nabla\Phi) + g\eta = \text{ constant} \qquad \text{on the free surface.} \tag{2.9}$$

The general free-surface condition is found by combining Equations (2.8) and (2.9) such that

$$g\frac{\partial \Phi}{\partial z} + \frac{\partial^2 \Phi}{\partial t^2} + 2\nabla\Phi \cdot \nabla\frac{\partial \Phi}{\partial t} + \frac{1}{2}\nabla\Phi \cdot \nabla(\nabla\Phi \cdot \nabla\Phi) = 0 \qquad \text{on the free surface.} \tag{2.10}$$

Normal components of the velocity of the solid body boundary must be impressed upon the fluid adjacent to it. The body surface boundary condition, where the body velocity normal to the body surface is U_b, is therefore given by

$$\frac{\partial \Phi}{\partial n} = U_b \qquad \text{on the body boundary.} \tag{2.11}$$

Similarly, the bottom boundary condition is given by

$$\frac{\partial \Phi}{\partial z} = 0 \qquad \text{on } z = -d. \tag{2.12}$$

At infinity (horizontally) the radiation condition ensures that only outgoing radiated waves exist. A formal, mathematical definition of the radiation condition is given in Section 2.1.8 as it requires terminology which is not defined at this stage.

Once the total velocity potential is known, Bernoulli's equation can be used to determine the pressure throughout the fluid. The forces on the body can then be found by integrating the pressure around the body. Determining the velocity potential can however be complicated.

2.1.6 Linear Theory and Boundary Conditions

A common simplification of the boundary conditions is obtained from the Stokes expansion method which is achieved using the assumption that the wave amplitude and hence wave height, H, are small compared to both the wavelength and the water depth. The wave amplitude, A_m, is the vertical distance from the undisturbed free surface to the peak, which for a sinusoidal wave is half of the wave height such that $A_m = \frac{H}{2}$. The density of the wave crests, i.e. the number of wave crests per unit distance, is known as the wavenumber, k, which relates to the wavelength such that $k = \frac{2\pi}{L}$.

The velocity potential can be expanded into a perturbation series for the small parameter, $\epsilon = \frac{kH}{2}$ as follows:

$$\Phi = \epsilon \Phi^{[1]} + \epsilon^2 \Phi^{[2]} + \cdots \tag{2.13}$$

On substituting Equation (2.13) into Laplace's and Euler's equations and the boundary conditions, N^{th}-order wave theory is formed by using only the terms of order ϵ^N or below. 1^{st}-order wave theory (in which all terms of order higher than ϵ are neglected) is commonly called Linear Wave Theory, and higher order wave theory is sometimes referred to as weakly non-linear wave theory to the N^{th}-order. The effects of including the second-order terms are considered in Chapter 4.

In linear wave theory, as the amplitude of the waves is small, the free-surface condition is applied at $z = 0$ instead of $z = \eta$ (see Figure 2.1). The linearised boundary conditions are therefore given by:

Linearised Kinematic Surface Condition:

$$\frac{\partial \eta}{\partial t} - \frac{\partial \Phi}{\partial z} = 0 \qquad \text{on } z = 0; \tag{2.14}$$

Linearised Dynamic Free-Surface Condition:

$$\frac{\partial \Phi}{\partial t} + g\eta = 0 \qquad \text{on } z = 0; \tag{2.15}$$

General Free-Surface Condition

$$g\frac{\partial \Phi}{\partial z} + \frac{\partial^2 \Phi}{\partial t^2} = 0 \qquad \text{on } z = 0, \tag{2.16}$$

with

$$\eta = -\frac{1}{g}\left(\frac{\partial \Phi}{\partial t}\right)_{z=0}; \tag{2.17}$$

Linearised Body-Surface Boundary Condition:

$$\frac{\partial \Phi}{\partial n} = U_b \qquad \text{on body surface;} \tag{2.18}$$

Linearised Bottom Boundary Condition:

$$\frac{\partial \Phi}{\partial z} = 0 \qquad \text{on } z = -d. \tag{2.19}$$

The radiation condition must also be satisfied ensuring only outgoing waves exist at infinity. A formal, mathematical definition of the radiation condition is given in Section 2.1.8.

Using the method of separation of variables to solve Laplace's Equation subject to the boundary conditions, the velocity potential can be determined to be

$$\Phi(x,z,t) = \frac{gH}{2\omega}\frac{\cosh\left(k(z+d)\right)}{\cosh(kd)}\cos(kx-\omega t). \tag{2.20}$$

In the calculation of Φ, the assumption that the wave is periodic in x is used. Equation (2.20) shows a linear relationship between the velocity potential and the wave height. This ensures that the velocity potentials of component waves can be summed together to determine the velocity potential of the resultant wave using the theory of superposition. Although sinusoidal waves are very rare in reality, many other more genuine waves shapes can be approximated by summing together a variety of different sinusoidal waves in this manner.

The pressure field can be determined using the linear velocity potential in a linearised form of Bernoulli's equation in which the quadratic terms are ignored:

$$\frac{\partial\Phi}{\partial t} - gz + \frac{p}{\rho} = G. \tag{2.21}$$

As the constant in Equation (2.7) is arbitrary it may be taken to be zero if required, so that the linear pressure is given by

$$p = \overbrace{\rho g z}^{StaticPressure} - \overbrace{\rho\frac{\partial\Phi}{\partial t}}^{DynamicPressure}. \tag{2.22}$$

2.1.7 Dispersion Relation

Substituting the derivatives of the velocity potential into the general free-surface condition (Equation (2.16)) at the free surface ($z = 0$) provides an important relation between the wave frequency, ω, and the wavenumber, k,

$$\omega^2 = gk\tanh(kd). \tag{2.23}$$

It is known as the linearised dispersion relation since, when written in terms of wave celerity, the speed at which a wave crest travels, it shows that at a given depth, waves with different wave numbers will travel at different speeds, a phenomenon known as dispersion.

2.1.8 Incident, Scattered and Radiated Waves

The set of equations which the velocity potential must satisfy, that is Laplace's Equation (Equation (2.5)), the boundary conditions (Equations (2.14) to (2.19)) and Bernoulli's equation (Equation (2.21)), is linear. This allows for the summation of component velocity potentials to form the total velocity potential, hence allows for the division of the wave problem into several sub-problems.

The wave body interaction problem is commonly divided into two sub-problems. The first is the radiation problem where there are no incident waves but the body is forced to oscillate with harmonic motion of specified frequency. The second is the excitation problem (sometimes referred to as the diffraction problem in other texts) where the body is subjected to a regular incident wave train whilst being restrained from oscillating. The corresponding waves have velocity potentials Φ_r and Φ_r respectively.

The excitation velocity potential, Φ_e, can be split into two constituent parts, the incident velocity potential, Φ_i, and the scattered velocity potential, Φ_s. The incident velocity potential represents the incident waves, undisturbed by the body (as if the body was not there). The excitation velocity potential represents the change in the incident wave field due to the presence of the body.

The total velocity potential is therefore written as

$$\Phi = \overbrace{\Phi_i + \Phi_s}^{\Phi_e} + \Phi_r. \tag{2.24}$$

The radiation condition applies only to the radiated waves, hence it is possible now to formally define the radiation condition for the radial ordinate R (Sarpkaya and Isaacson, 1981):

$$0 = \lim_{R \to \infty} \left[\frac{\partial \Phi_r}{\partial R} - ik\Phi_r \right]. \tag{2.25}$$

This condition at infinity ensures that the radiated waves must behave as outgoing plane waves far from the body (Wehausen and Laitone, 1960).

In order for the total velocity potential, Φ, to satisfy the body boundary condition given by Equation (2.18), the constituent velocity potentials must satisfy the following body boundary conditions:

$$\frac{\partial \Phi_r}{\partial n} = U \qquad \text{on the body surface,} \tag{2.26}$$

where $U =$ the forced body velocity, and

$$\frac{\partial \Phi_e}{\partial n} = 0 \qquad \text{on the body surface.} \qquad (2.27)$$

Since $\Phi_e = \Phi_i + \Phi_s$, the body boundary condition which Φ_i and Φ_s must both satisfy is given from Equation (2.27) by

$$\frac{\partial \Phi_i}{\partial n} = -\frac{\partial \Phi_s}{\partial n} \qquad \text{on the body surface.} \qquad (2.28)$$

The velocity potentials can be used to determine the pressure field using Bernoulli's equation (Equation (2.22)). Each of these pressure fields can be integrated around the body surface in order to determine the resulting forces on the body.

2.2 Modelling Wave Energy Converters

Due to the periodicity of the waves, a floating device can be modelled as a driven simple harmonic oscillator, which is similar to a simple harmonic oscillator except with damping and external forces also applied to the body.

2.2.1 Driven Harmonic Motion

Simple harmonic motion exists when the acceleration of a body is proportional to, but in the opposite direction to the displacement of the body from its mean position. In this way, as the body moves away from its mean position its displacement increases and its acceleration decreases until it eventually stops before returning to its mean position, whereupon it passes until it reaches its maximum displacement, and so the periodic motion is described. Mathematically, this is defined by the equation.

$$\frac{\mathrm{d}^2 X(t)}{\mathrm{d}t^2} = -\gamma_1 X(t),$$

where $X(t)$ is the displacement of the body (variation of position with time) and γ_1 is a positive constant. For an undamped body undergoing simple harmonic motion, the total force must satisfy Newton's second law and Hooke's law. Newton's second law states that the acceleration of a body is parallel and directly proportional to the net force and inversely proportional to the mass. Hooke's law states that for relatively small deformations of an object, the displacement or size of the deformation is directly proportional to the deforming force or load. Allowing the constant, γ_1, to be of the form $\gamma_1 = \frac{C}{M}$ where C is a constant and M the mass of the body, allows the force to be written as

$$F_{TOT} = M\frac{\mathrm{d}^2X(t)}{\mathrm{d}t^2} = -\overbrace{CX(t)}^{F_{res}}. \tag{2.29}$$

The right-hand side of Equation (2.29) represents a restoring force, F_{res} , with restoring coefficient, C. For a simple harmonic oscillator, this is the only force acting on the body. Adding a mechanical damping force, F_{damp}, proportional to the velocity of the body with damping coefficient, R, into this equation gives the equation of a damped harmonic oscillator,

$$F_{TOT} = M\frac{\mathrm{d}^2X(t)}{\mathrm{d}t^2} = -\overbrace{R\frac{\mathrm{d}X(t)}{\mathrm{d}t}}^{F_{damp}} - \overbrace{CX(t)}^{F_{res}}.$$

If an external driving force, F_{ext}, is also present then the body becomes a driven harmonic oscillator described by the equation

$$F_{TOT} = M\frac{\mathrm{d}^2X(t)}{\mathrm{d}t^2} = F_{ext} - \overbrace{R\frac{\mathrm{d}X(t)}{\mathrm{d}t}}^{F_{damp}} - \overbrace{CX(t)}^{F_{res}}.$$

This can be rearranged to give the equation

$$F_{ext} = M\frac{\mathrm{d}^2X(t)}{\mathrm{d}t^2} + \overbrace{R\frac{\mathrm{d}X(t)}{\mathrm{d}t}}^{F_{damp}} + \overbrace{CX(t)}^{F_{res}}. \tag{2.30}$$

2.2.2 Application to Wave Energy Devices

Wave energy devices are subject to external forces from the waves, namely the excitation force, F_e, from the incident and scattered waves and the radiation force, F_r, from the radiated waves, as well as a hydrostatic restoring force, F_{res}, and damping from the power take-off system and friction, F_{damp}. The forces are therefore described by

$$F_{TOT} \;=\; M\frac{\mathrm{d}^2X(t)}{\mathrm{d}t^2} = \overbrace{F_e + F_r}^{F_{ext}} + F_{damp} + F_{res}. \tag{2.31}$$

If it is now assumed that the mechanical damping force varies linearly with velocity such that $F_R = -R\frac{\mathrm{d}X(t)}{\mathrm{d}t}$ where R is the mechanical damping coefficient, and the hydrostatic restoring force varies linearly with displacement such that $F_{res} = -SX(t)$ for constant S (known as the hydrostatic stiffness) then the wave energy device can be described as a driven harmonic oscillator with equation

$$F_{TOT} \;=\; M\frac{\mathrm{d}^2X(t)}{\mathrm{d}t^2} = \overbrace{F_e + F_r}^{F_{ext}} - \overbrace{R\frac{\mathrm{d}X(t)}{\mathrm{d}t}}^{F_{damp}} - \overbrace{SX(t)}^{F_{res}}.$$

Now, as the forces and motions are all periodic, the complex amplitudes can be considered (see Appendix B) to simplify the calculus so that

$$\hat{F}_{TOT} \;=\; Mi\omega\hat{U} = \overbrace{\hat{F}_e + \hat{F}_r}^{\hat{F}_{ext}} - \overbrace{R\hat{U}}^{\hat{F}_{damp}} + \frac{i}{\omega}\overbrace{S\hat{U}}^{\hat{F}_{res}}, \tag{2.32}$$

where a hat symbol, $\hat{}$, denotes the complex amplitude and U is the velocity of the body.

2.2.3 Radiation Force and Velocity

The radiation force, F_r, can be split into the sum of two forces, the first is linear with acceleration and the second is linear with body velocity. In this way the radiation force can be written as

$$F_r = -\left(B\frac{\mathrm{d}X(t)}{\mathrm{d}t} + A\frac{\mathrm{d}^2X(t)}{\mathrm{d}t^2}\right), \tag{2.33}$$

where B is known as the radiation damping and A the added mass. In terms of complex amplitudes this can be written as

$$\hat{F}_r = -(B + i\omega A)\,\hat{U}, \tag{2.34}$$

so Equation (2.32) can be rewritten as

$$\hat{F}_{TOT} = Mi\omega\hat{U} = \hat{F}_e + \left(-(B+R) - i\omega A + \frac{i}{\omega}S\right)\hat{U}. \tag{2.35}$$

The body velocity can therefore be defined as

$$\hat{U} = \frac{\hat{F}_e}{\left((B+R) + i\omega\left(M + A - \frac{S}{\omega^2}\right)\right)}. \tag{2.36}$$

2.3 Parameters

An unconstrained body is able to move in six possible directions, known as degrees of freedom (see Figure 2.2). For an isolated device whose motion is restricted to i degrees of freedom (where $1 \leq i \leq 6$ as in Figure 2.2), the added mass (A), mechanical damping (R), radiation damping (B) and hydrodynamic stiffness (S) are square matrices of length i, and the excitation force (F_e) is a vector of length i.

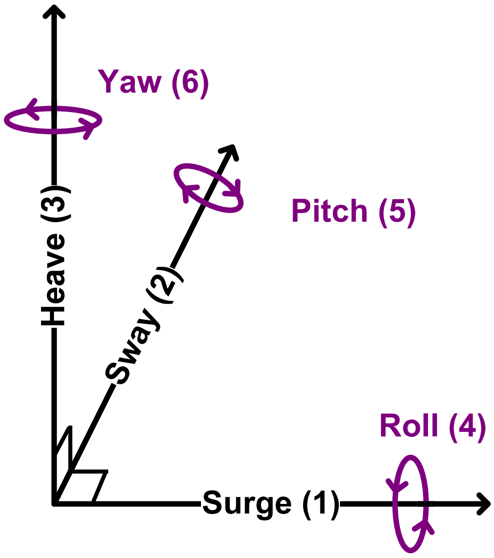

Figure 2.2: Diagram of the three dimensional axes showing the 6 degrees of motion for a floating body

A single body that is only able to move in heave, which is the focus of this thesis, will have single values for A, B, R, S, and F_e.

For an array of devices, the forces on each float will differ from those on an isolated float due to scattering of the waves by all devices in the array. For an N element array of bodies the square matrix and vector lengths (for A, R, B, S and F_e) are increased to $I \times N$. Where an array of N bodies are each restricted to motion in heave, the focus of this thesis, the radiation damping component, $B_{i,j}$ represents the radiation damping on body i due to the radiation caused by an oscillation of body j with unit amplitude. Similarly for components of the matrices (A, B and S). The excitation force component $(F_e)_i$ represents the excitation force on body i.

2.4 Calculating Body Forces

The pressure due to the incident and scattered waves is determined using the excitation velocity potential, determined by solving Laplace's Equation together with the boundary conditions, in Bernoulli's equation. This pressure can be integrated around the body to determine the excitation force, F_e. From herein, the excitation force will be referred to as F to simplify the notation. Analytic solutions exist for the excitation force for certain body geometries but, for arbitrary geometries, numerical solutions are typically obtained using methods such as the boundary element method. Numerical solutions can be readily obtained using computational analysis programmes such as WAMIT. In this Section, the excitation force for a basic geometry is derived for a range of wave frequencies and compared to the solution obtained using an approximation theory known as Froude-Krylov theory.

2.4.1 WAMIT

WAMIT is a program for computational analysis of the diffraction and radiation of waves due to the interaction of surface waves with offshore structures. It can solve the boundary value problem using either linear wave theory or second-order wave theory. Both finite and infinite depths are permitted, as are fixed and floating bodies and arrays of multiple bodies.

The boundary value problem is solved using an integral Equation method including Greens functions together with a panel method. Further details of the theory used can be found in Lee (1995). Geometries can be input into the program either as a series of coordinates which form the vertices of panels which tessellate to form the surface, or as analytically defined smooth, continuous surfaces known as patches.

WAMIT is able to compute many quantities such as the hydrostatic stiffness coefficients, added mass coefficients, radiation damping coefficients, excitation forces, pressures and free surface elevation. All outputs from WAMIT are non-dimensional complex amplitudes. Details on dimensionalising the output values are given in the manual (WAMIT, Inc, 2008).

2.4.2 Froude-Krylov Theory

Froude Krylov theory can be used to approximate the excitation force on a small body by multiplying the force due to the incident waves alone by a constant. When a body is small compared to the wavelength, the velocity field on the body induced by the incident waves can be assumed to be constant over the body such that $\Phi_s =$ constant. Condition (2.28) becomes $\frac{\partial \Phi_e}{\partial n} = \frac{\partial \Phi_i}{\partial n} = 0$, suggesting that under these circumstances, the excitation force can be approximated by the incident waves alone. This small body approximation is known as the Froude-Krylov approximation, hence the approximate excitation force is called the Froude-Krylov force, F_{FK}, given by integrating the pressure field around the body surface S_b due to the incident wave only. The incident velocity potential is given by Equation (2.20), hence the dynamic pressure due to the incident waves alone is determined using Bernoulli's equation (Equation (2.22)) as

$$p_i = -\rho \frac{gH}{2} \frac{\cosh\left(k(z+d)\right)}{\cosh(kd)} \sin(kx - \omega t).$$

Integrating this around the body surface, S_b, gives the incident force

$$F_i = \iint_{S_b} p_i \, \underline{n} \mathrm{d}S_b,$$

where $\underline{n}$ represents the normal to the body surface pointing into the fluid domain. Therefore

$$F_i = -\frac{\rho\, g\, H}{2\cosh(k\, d)} \iint_{S_b} \left(\, \cosh(k(d+z))\ \sin(k\, x - \omega\, t)\right)\ \underline{n} \mathrm{d}S_b. \tag{2.37}$$

2.4.3 Application to a Hemispherical Float

The vertical (mode 3 in Diagram 2.2) force is now calculated for a hemispherical floating body of radius a using the Froude-Krylov method and compared to the force obtained using full Linear Theory through the application of the computer analysis program WAMIT. The angle to the positive horizontal (x) axis is θ and the angle to the negative vertical (z) axis is ψ (see Figure 2.3).

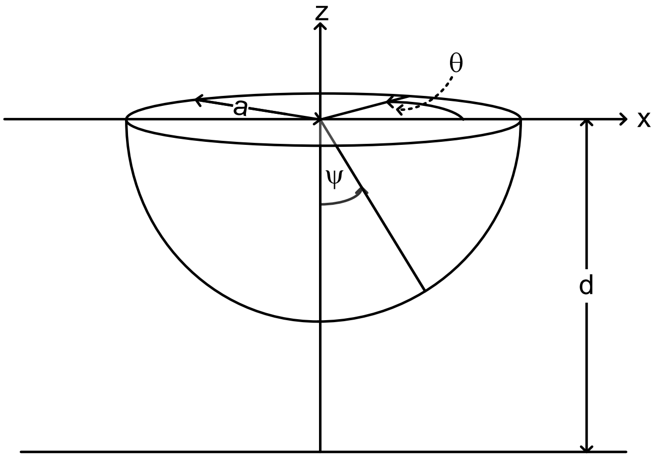

Figure 2.3: Diagram to show coordinate system for hemispherical body of radius a located at the free surface, in water of depth d

The x and z coordinates are given by

$$x = a \sin\psi \cos\theta \tag{2.38}$$

and

$$z = -a \cos\psi \tag{2.39}$$

respectively, the elemental area, $\mathrm{d}S$, is given by

$$\mathrm{d}S_b = a^2 \sin\psi \mathrm{d}\theta \mathrm{d}\psi \tag{2.40}$$

and the the normals to the body surface pointing into the fluid domain in the x and z directions are given by

$$n_x = \sin\psi \, \cos\theta \tag{2.41}$$

and

$$n_z = \cos\psi \tag{2.42}$$

respectively. The vertical component of the Froude-Krylov force on the hemispherical body is therefore

$$F_{FK_z} = \frac{\rho\, g\, H a^2}{2\cosh(k\, d)} \int_0^{\pi/2}\!\!\int_0^{2\pi} \left(\begin{array}{c} \cosh(k(d - a\cos\psi)) \\ \times \cos(k\, a \sin\psi \cos\theta - \omega\, t) \end{array} \right) \cos\psi \sin\psi \mathrm{d}\theta \mathrm{d}\psi. \quad (2.43)$$

These surface integrals can either be solved analytically or numerically. Both methods are shown here for comparison.

Analytic Solution of Froude-Krylov Forces on Hemispherical Float

The double integrals in Equation (2.43) can be solved analytically using the Bessel function of the first kind and some well known identities (see Appendix D) to give

$$F_{FK_z} = \frac{\pi \rho\, g\, H a^2}{\cosh(k\, d)} \left(\gamma_2 \cosh\left(kd\right) + \gamma_3 \sinh\left(kd\right)\right), \quad (2.44)$$

where

$$\gamma_2 = \left(\begin{array}{l} 1 + \frac{a^2k^2}{8} - \frac{a^4k^4}{576} + \frac{a^6k^6}{46080} - \frac{a^8k^8}{5160960} + \frac{a^{10}k^{10}}{796262400} - \frac{29a^{12}k^{12}}{78033715200} \\ + \frac{a^{14}k^{14}}{249707888640} - \frac{53a^{16}k^{16}}{337105649664000} + \frac{a^{18}k^{18}}{6742112993280000} - \frac{a^{20}k^{20}}{148326485852160000} \end{array} \right)$$

and

$$\gamma_3 = \left(\begin{array}{l} - 6758061133824000\, ak + 39070080\, a^{11}k^{11} \\ - 868224\, a^{13}k^{13} + 19152\, a^{15}k^{15} - 42\, a^{17}k^{17} + a^{19}k^{19} \end{array} \right) \cdot \frac{1}{10137091700736000}.$$

Numerical Calculation of Froude-Krylov Forces on Hemispherical Float

Equation (2.43) can alternatively be evaluated numerically using the composite trapezoidal rule twice.

To do this, the angles θ and ψ must be divided into n Sections of size $\delta\theta$ and m Sections of size $\delta\psi$ respectively such that

$$\begin{aligned} \overrightarrow{\theta} &= [0, \delta\theta, 2\delta\theta, \cdots, (\theta_{n-2})\delta\theta, 2\pi] \\ \text{and } \overrightarrow{\psi} &= [0, \delta\psi, 2\delta\psi, \cdots, (\psi_{m-2})\delta\psi, \frac{\pi}{2}\delta\psi]. \end{aligned}$$

The Froude-Krylov force can then be calculated (see Appendix E) as

$$F_{FK_z} = \frac{\rho\, g\, H a^2}{2\cosh(k\, d)} \left(\left(\frac{1}{2} \left(G\left(\theta, \psi_0\right) + G\left(\theta, \psi_n\right)\right) + \sum_{i=1}^{m-1} G\left(\theta, \psi_i\right) \right) \delta\psi \right), \qquad (2.45)$$

where

$$G\left(\theta, \psi_i\right) = \left(\frac{1}{2} \left(I\left(\theta_0, \psi_i\right) + I\left(\theta_n, \psi_i\right)\right) + \sum_{j=1}^{n-1} I\left(\theta_j, \psi_i\right) \right) \delta\theta.$$

The aspect ratio of each panel (formed from the division of θ and ψ) is given by the ratio of the largest side to the shortest side of the panel. When MATLAB is used to determine the Froude-Krylov force, convergence occurs fastest when the aspect ratio is unity (i.e. when $m = n$). To minimize computational time, a panel aspect ratio of unity is therefore used.

Comparison of Froude-Krylov and Linear Theory Forces

In order to compare the Froude-Krylov force to the full excitation force a free floating hemispherical body of radius $a = 5$ m, in water of depth $d = 7a$ is considered in a train of incident waves of constant wave frequency ω. The body is analysed in frequencies of $0.49 \leq \omega \leq 2.3$ rad/s with increments of 0.02 rad/s.

The black solid line in Figure 2.4 shows the dimensional excitation force as calculated using linear wave theory through the application of WAMIT. As the frequency of the incident waves are increased, the magnitude of the excitation force is decreased.

The grey solid and black dashed lines in Figure 2.4 represent the incident wave force as calculated by Froude Krylov theory using analytical and numerical integrations respectively.

The analytical solution is determined from Equation (2.44), where the infinite series is expanded to the order of 10 and the numerical solution is determined using Equation (2.45) with panels sizes determined so as achieve converged values.

The analytical solution is truncated such that $(ka)^n$ for large n is excluded. Whilst this is acceptable for small values of ka, the effect of the truncation is clearly visible for larger values where the force calculated differs considerable from the force calculated numerically.

According to Froude-Krylov theory this force multiplied by a constant value, C_{FK}, should be representative of the entire excitation force, provided the body is small compared to the wavelength. This restricts the theory to small values of ω, where the effect of the scattered waves should be minimal. A coefficient of $C_{FK} = 1.1$ has been shown to be appropriate for hemispherical geometries for values of $ka < 0.8$ which corresponds to $\omega = 1.25$ rad/s here (American Society of Civil Engineers Task Committee on Hydrology Handbook, 1996). In agreement with this published value, the mean coefficient calculated in this Section within the same frequency range is 1.14 for both the numerical and analytical methods. At higher frequencies the ratio of Froude-Krylov force to excitation force is not constant, and varies between the numerical and analytical calculations of the Froude-Krylov force. Froude-Krylov theory is not applicable at these higher wave frequencies however as the assumption of large wavelength compared to the body size is invalid.

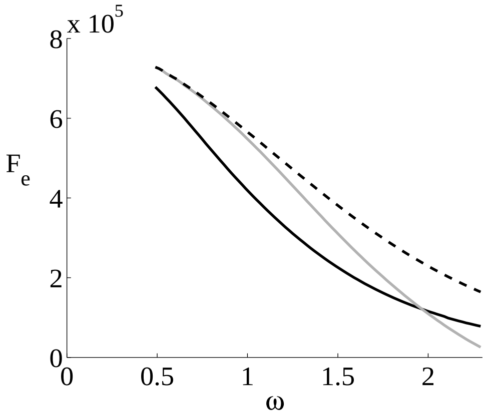

Figure 2.4: Excitation force on a free-floating hemispherical float restricted to heave motion only with radius $a = 5$ m, in water of depth $d = 7a$, subject to a train of incident waves of constant wave frequency ω
KEY:
Solid black line, Full excitation Force force (calculated using WAMIT);
Dashed black line, Froude-Krylov force calculated analytically;
Solid, grey line, Froude-Krylov force calculated numerically

2.5 Power

In the preceding Sections a model has been derived which combines linear wave theory with driven harmonic oscillators to model floating bodies in a train of incident waves. It has been shown how this model can be used to calculate the velocity potential, pressures and hence forces on the bodies. Equations have been derived which connect the forces on the body to the velocity of the body. Based on these equations together with an understanding that the mechanical power of a moving body is given by the product of force and velocity, this Section gives a derivation of the power that can be absorbed by the floating bodies. These power equations are then used to define measures of the performance of individual devices within arrays.

2.5.1 Derivation of the Power Equations

The mechanical power, P, of a moving body is a function of the external force, F_{ext}, on the body multiplied by the body's velocity, U, such that

$$P(t) = F_{ext}(t)U(t). \tag{2.46}$$

Using this relationship the time averaged power can be written in terms of the complex amplitudes of F_{ext} and U (see Appendix F) as

$$P = \frac{1}{2}\Re\left\{\hat{F}_{ext}^{*}\hat{U}\right\}, \tag{2.47}$$

in which the superscript symbol, '$*$', represents the complex conjugate. The external force comes from the waves and so is the sum of the excitation force, F_e, and radiation force, F_r, (see Section 2.2.2), so its complex amplitude can be written (using Equation (2.34)) as

$$\hat{F}_{ext} = \hat{F}_e^{*} - \hat{U}^{*}\left(B - i\omega\hat{A}\right). \tag{2.48}$$

Substituting Equation 2.48 into Equation 2.47 results in the following equation for time averaged power (see Appendix F for full derivation):

$$P = \frac{1}{8}\hat{F}_e^{*}B^{-1}\hat{F}_e - \frac{1}{2}\left(\hat{U} - \frac{1}{2}B^{-1}\hat{F}_e\right)^{*} B\left(\hat{U} - \frac{1}{2}B^{-1}\hat{F}_e\right). \tag{2.49}$$

Using Equation (2.32), the external force from the waves could alternatively be written as

$$\hat{F}_{ext} = \left(-i\omega\left(M + \frac{S}{\omega^2}\right) + R\right)\hat{U}. \tag{2.50}$$

Substituting Equation 2.50 into Equation 2.47 results in an alternative Equation for power,

$$P = \frac{1}{2}\left(\Re\{U\}^T R^T \Re\{U\} + \Im\{U\}^T R^T \Im\{U\}\right), \tag{2.51}$$

where the superscript symbol, 'T' , represents the transpose of the matrices and $\Re$ and $\Im$ represent the real and imaginary parts respectively. For an array of N devices A, B, R, M and S are $N \times N$ matrices, F is a vector of length N resulting in P representing the net power, a single value for the whole array (see Section 2.3). Equation 2.51 can be re-written in terms of the components of the U and R matrices such that

$$P = \frac{1}{2}\left(\sum_{i=1}^{N}\sum_{j=1}^{N}\Re\{U_i\}R_{i,j}^{T}\Re\{U_j\} + \sum_{i=1}^{N}\sum_{j=1}^{N}\Im\{U_i\}R_{i,j}^{T}\Im\{U_j\}\right). \tag{2.52}$$

In the specific case where R is a diagonal matrix transposing the matrix has no effect such that $R^T = R$ and $R_{i\neq j} = 0$. This reduces Equation (2.52) to

$$P = \sum_{i=1}^{N} P_i R_{i,i} \text{ for } P_i = \frac{1}{2}R_{i,i}|U_i|^2 \text{ (iff } R_{i\neq j} = 0 \ \forall \ 1 \leq i,j \leq N). \tag{2.53}$$

As the mechanical damping on an isolated device has only a single element, elements with $R_{i\neq j}$ do not exist, so Equation (2.53) is true also for an isolated device.

Whilst Equation (2.49), given in (Thomas and Evans, 1981), is the most general Equation to calculate the net power, it does not indicate how much power is absorbed by each individual device within an array. If the specific condition that the mechanical damping matrix is diagonal is met, it is therefore beneficial to use Equation (2.53). Equation (2.53) is also a more simple Equation to work with than (2.49), making it the preferable Equation to calculate the power from an isolated device.

2.5.2 Optimal Power

Power output is maximum when the second term of Equation (2.49) vanishes (i.e. when $U = \frac{1}{2}B^{-1}F$). This is satisfied only when the force and velocity are in phase (i.e. $S = (M + A)\,\omega^2$) and when the mechanical damping matrix R is identical to the dense radiation damping matrix B (Thomas and Evans, 1981) so that

$$P_{max} = \frac{1}{8}\hat{F}_e^{*}B^{-1}\hat{F}_e. \tag{2.54}$$

2.6 Interaction Factors

2.6.1 Conventional Interaction Factor, q

The response of each float is dependent on both the excitation force due to the diffracted wave-field and forcing due to waves radiated by the oscillation of the devices. It is widely known that these interactions cause both the response and power output of a float within an array to differ from the same device in isolation. A measure of the effect of the hydrodynamic coupling between devices is commonly given by the interaction factor q which is defined as:

$$q = \frac{\text{Net power from array}}{N \times \text{Power from same device in isolation}} \tag{2.55}$$

An interaction factor of $q = 1$ indicates that the devices within the array are producing the same amount of overall power as if the same number of devices are in isolation, whereas factors greater- or less-than one indicate constructive- or destructive interactions. The interaction factor is therefore an important measure of the performance of closely spaced arrays and it is particularly useful for developers to understand the limiting values applicable to real systems.

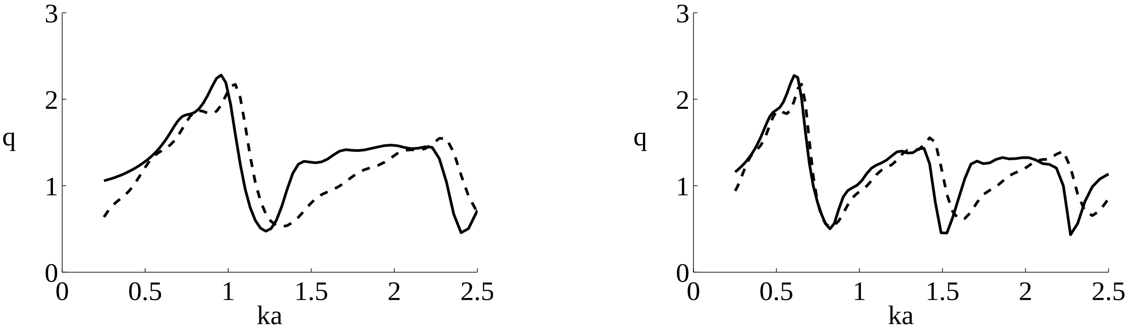

(a) $s = 5a$

(b) $s = 8a$

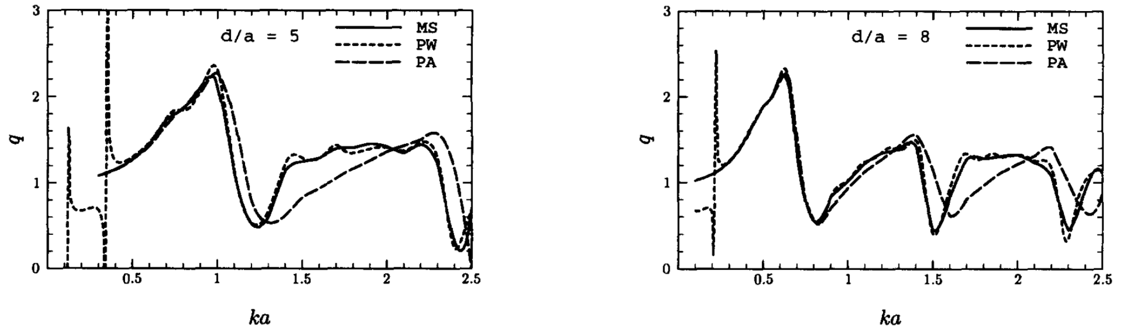

(c) (Mavrakos and McIver, 1997) $s = 5a$
NB: dotted line represents alternative approximation theory known as Plane Wave Theory (discussed in Section 1.6.5) which is not calculated here

(d) (Mavrakos and McIver, 1997) $s = 8a$
NB: dotted line represents alternative approximation theory known as Plane Wave Theory (discussed in Section 1.6.5) which is not calculated here

Figure 2.5: Interaction factor, q, against ka where k is the wavenumber and a the float radius for a 5×1 array of circular cylinders with draft=radius, separation distance, s, in water of depth $8a$
KEY:
Solid line, Calculated using full linear wave theory using WAMIT;
Dashed line, Calculated using Point Absorber theory

Figure 2.5 shows the optimal interaction factor as calculated using Equation (2.55) together with Equation (2.54) using the excitation force vectors and radiation damping matrices as given by the wave analysis program, WAMIT. The data is shown for a 5×1 array of heaving vertical cylindrical floats of radius a and draught a in water of finite depth, $d = 8a$ for two separation distances, $s = 5a$ and $s = 8a$, to allow for comparison to the published Figure (Mavrakos and McIver, 1997, Figure 7). The similarity between the published results of Mavrakos and McIver (1997) and those determined using the WAMIT parameters is clearly visible.

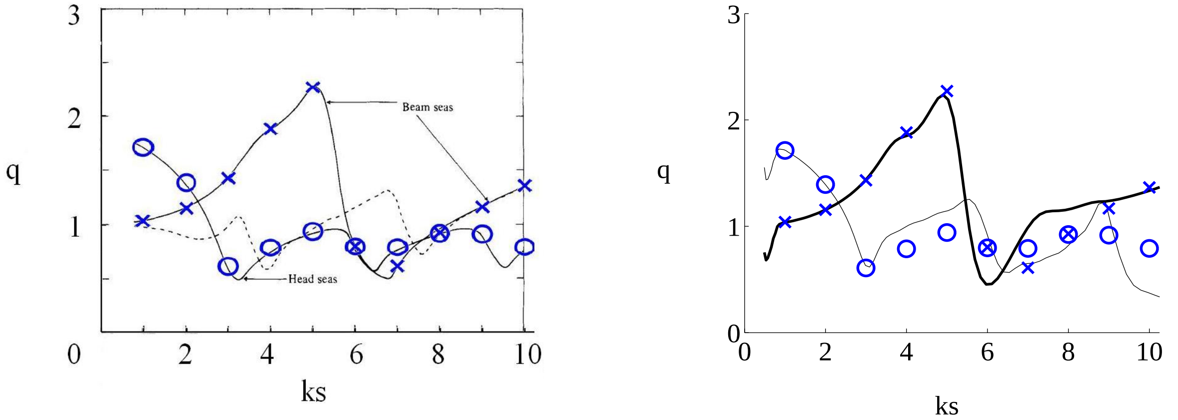

(a) Black lines, Fixed $k = \frac{0.4}{a}$, varied s, directly from (Thomas and Evans, 1981)
NB: dotted line represents alternative wave direction (45^o to the line of the array) which is not considered in this thesis

(b) Solid lines, varied k and fixed $s = 4a$ (Thick line, Beam seas and Thin line, head seas)

Figure 2.6: Interaction factor, q, for a 5×1 array of hemispherical floats in water of infinite depth where ks is varied by varying k, the wavenumber, compared to Figure a overlaid onto Figure 2 from Thomas and Evans (1981) and to an array where ks is varied by varying s, the float separation distance
KEY:
×, Beam seas as calculated using WAMIT results with fixed $k = 0.4/a$;
o , Head seas as calculated using WAMIT results with fixed $k = 0.4/a$

Much of the research in this thesis is presented for hemispherical floats and so the interaction factor for an optimally tuned (as described in Section 2.5.2) 5×1 array of heaving hemispherical floats of radius a is shown in Figure 2.6. Beam seas represents the seas in which the train of incident waves propagates perpendicular to the line of the array and head seas represents seas in which the train of incident waves propagates along the line of the array. The markers show the optimal interaction factors determined using WAMIT coefficients for an array in which ks is varied by changing the separation distance, s, but keeping a fixed wave frequency and hence wavenumber, k, such that $ka = 0.4$. It can be seen in Figure 2.6a that the resulting interaction factors are the same as those published for the same array by (Thomas and Evans, 1981).

It could however be difficult to implement an array in which the separation distance is varied according to the incident wave frequency. This thesis therefore focuses on arrays in which the separation distance is fixed and the wave frequency is varied. The solid lines in Figure 2.6b show the optimal interaction factors from such an array whose spacing is fixed ($s = 4a$) in trains of incident waves of varying frequencies. The ratio of device radius to wavelength varies over the range $0.2 < ka < 2.5$ in this fixed spacing array. The two cases are therefore only directly comparable for $ks = 1.6$. As the value of ks decreases for the fixed spacing array, the amplitude of the wave-field scattered by each device reduces.

The research presented in this report is predominantly in water of finite depth whereas the data in Figure 2.6 is for an array in water of infinite depth. Using a finite water depth presents a slight shift in the interaction factor curves shown in Figure 2.6 towards higher values of ks, although this is only significant at low ks values.

2.6.2 Normalised Interaction Factor, Q

The interaction factor, as given by Equation (2.55), is calculated relative to the power of an isolated device, which is dependent on the damping applied to the isolated device together with its mass. When comparing methods to vary the mass and mechanical damping matrices for an array of devices, the interaction factor, or q-factor, although widely used, can be misleading as the isolated devices to which the arrays are being compared in the q-factor, are different. It can be more informative to compare the power from an array of devices to the maximum power from the same number of isolated devices with set mass and mechanical damping values:

$$Q = \frac{\text{Net power from array}}{N \times \left(\begin{array}{c} \text{Maximum power from an isolated device} \\ \text{with a fixed mass and damping value} \end{array} \right)} \tag{2.56}$$

In this thesis Q uses a comparison to an isolated device having a mass of twice its dry weight ($M_0 = 2M_m$) and mechanical damping equal to the radiation damping ($R_0 = B_0$). Figure (2.7) shows both types of interaction factor (q and Q) for two five element arrays, one in which the float masses are each $1.5M_m$, and one in which they are $2M_m$ (where M_m is the displaced mass of fluid). Comparison of the q-factors (Figure (2.7a)) shows that the performance within an array compared to in isolation is better for the lighter floats than the heavier floats. This could however be misleading, as this does not mean that the array of lighter floats is performing better than the array of heavier floats, only that the interactions within the array are greater. As the Q-factor instead gives the performance of both arrays relative to a fixed power value, the comparison of the performance of both arrays relative to each other becomes much clearer. It can be seen in Figure 2.7b that the heavier array (for which the individual floats have a natural frequency of 1.07 rad/sec) is able to absorb significantly greater power than the lighter array (for which the individual floats have a natural frequency of 1.21 rad/sec) for all frequencies below $\omega = 1.08$ rad/sec, even though the q factor is larger for the lighter array in this same frequency range.

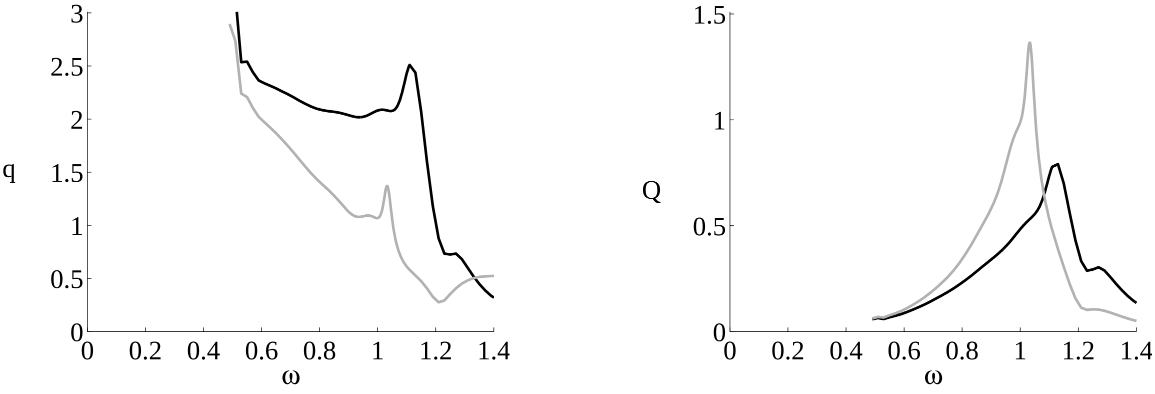

(a) The interaction factor, q (b) The Normalised interaction factor, Q

Figure 2.7: The interaction factor, q, and Normalised interaction factor, Q, for 5×1 arrays of hemispherical floats of radius $a = 5$ m with separation distance of $s = 4a$ in head seas with mechanical damping $R = B$ and float masses of either $M = 1.5M_m$ or $M = 2M_m$; q-factor given relative to same devices in isolation at each frequency, Q-factor given relative to the maximum power from an isolated device with mass equal to twice its dry weight ($M_0 = 2M_m$) and mechanical damping equal to the radiation damping ($R_0 = B_0$):
KEY:
Black line, $R = B$ and $M = 1.5M_m$; Grey line, $R = B$ and $M = 2M_m$

Both the q-factor (Equation (2.55)) and the Q-factor (Equation (2.56)) are used in this thesis in order to measure the effects of interaction within arrays of devices.

2.7 Chapter Summary

A mathematical model is presented which combines linear wave theory with a series of linear driven harmonic oscillators to model an array of floating wave energy devices in a train of incident regular waves. The calculation of forces using the model is investigated including comparisons for an isolated device to the Froude-Krylov force in which scattered waves are not considered.

Two equations are derived in order to calculate the net power from the waves. It is shown that the equation which is commonly used to calculate power for an isolated device can also be used to calculate the individual power values within an array, provided the mechanical damping matrix is diagonal.

Two different measures are presented to establish how much power a device can absorb within an array compared to if it was in isolation. The first measure is the commonly used interaction factor, q, for which comparisons are made with published data. The second interaction measure, the Normalised Interaction Factor, Q, allows for comparison between arrays of devices with different properties.

Chapter 3

Comparison to Experiment

Linear hydrodynamic analysis has been widely used to study the response of either individual floating bodies or arrays of floating structures such as wave energy devices. It has been shown that this approach is sufficient to determine the wave induced force on fixed geometries and to predict the response of isolated floating geometries to regular waves. However, there have been few studies which evaluate the accuracy of this approach for predicting the response of the shallow draft floats that are generally of interest for wave energy devices.

In this chapter the validity of linear theory is considered for predicting response due to regular waves by comparing linear theory predictions of a line of five floats to experimental measurements. The floats considered are shallow draft and arranged at a separation distance of two diameters centre to centre.

3.1 Introduction

Experimental data for the forces on isolated devices of basic geometries have been shown to be in close agreement with linear theory provided the wave amplitude remains small compared to the body diameter (Evans et al. (1979b) and Chakrabarti and Tam (1973)). Several experimental studies have been published of the response of isolated floats that are based on designs for wave energy devices that are presently in development (Count (1978), Greenhow et al. (1982), Vantorre et al. (2004) and Stallard et al. (2009b)). Rigid structures which include small arrays of cylindrical bodies such as Tension Leg or Gravity Based platforms and floating airports have prompted experimental studies into the wave-structure interaction, finding large wave elevations in the vicinity of the cylinders under certain wave conditions and array layouts (Swan et al. (1997), Ohl et al. (2001) and Kagemoto et al. (2002)). However, there are few published studies concerning experimental studies of arrays of floating wave energy devices. Those that have been published have generally focused on comparison to either predictions of optimal response (e.g. Budal et al. (1979)) or on specific device configurations.

One of the earliest notable experimental studies of arrays of wave energy converters was conducted by Budal et al. (1979) who reported measurements of the free-response amplitude and power absorption of a (rigidly connected) pair of hemispherical ended floats (radius $a = 0.075$ m , draft = a+0.1 m). The floats were located in a two-element array across the width of a 1.01 m wide flume such that the centre of each float was located 0.25 m from a side wall. This was intended to represent an infinitely long line of tuned devices (with a natural frequency equal to the wave frequency) at $s = 6.66a$ spacing aligned with the wave crest. The measured power captured by the devices confirmed predictions of point absorber theory in that the interaction factor (q-factor) increases linearly toward π as the device spacing approaches the wavelength.

At a similar time, tests were conducted at the University of Edinburgh on behalf of the UK Central Electricity Generating Board (Count, 1980). Interaction factors were obtained for two linear arrays comprising two devices at non-dimensional spacing $ks = 7.48$ and ten devices at $ks = 4.99$. Both cases show reasonable agreement with point absorber predictions. Although some findings from this study have been documented, detailed reports and measurements seem to be lost (Stallard et al., 2008).

In recent years, various device developers have conducted experiments to understand the power output from prototype systems. This includes developers such as the WaveStar which has had an array of 1:10 scale device in the sea from 2006 to 2010 and a full scale array the sea since 2009 (Marquis, 2010) and the FO^3 device array which has been tested in the ocean with a single float and with an array of 4 floats at $\frac{1}{3}$ scale (de Rouck and Meirschaert, 2009). The variation of averaged power (excluding losses in the power take-off) with significant wave height has been found to follow the same trend at $\frac{1}{3}$ scale in the sea as those determined for the $\frac{1}{40}$ scale experimental wave tank model. A large amount of scatter was, however, found to be present in the results from the sea trials which is thought to be due to the variations in wave directions and periods which were not accounted for in the experimental wave tank (Frigaard and Lyke Anderson, 2008). Experimental data has been released for the AquaBuOY device however these are based on a distinct and unusual power take off system involving a large, vertical accelerator tube attached to the base of the float (Wacher and Neilsen, 2010).

The purpose of the present study is to compare predictions of the response of a closely spaced array of floats obtained using linear analysis to experimental measurements of a comparable system. Each float is the same geometry and mass and mechanical damping is minimised such that the response amplitude is maximised. By neglecting mechanical damping, which is usually applied via a power take-off system, large response amplitudes tend to occur. The most onerous conditions for linear theory, which is based on the assumption that motion amplitudes are small, are therefore provided by neglecting mechanical damping.

The closely spaced array considered is comprised of heaving floats which are each connected to a counterweight via a cable which is supported by a pulley system attached to a fixed structure located above the waterline. This is a similar set-up to the device analysed by Stallard et al. (2009b), except here multiple identical devices are arranged in a closely spaced array and the float geometry is simplified to a uniform vertical cylinder with a semi-ellipsoidal base. The level of mechanical damping applied to the float can be specified using a dynamometer system which is an inherent part of the experimental model. For the purpose of measurements reported in this study, friction in the drivetrain is compensated for, thus float motion can be considered as mechanically undamped. Further details regarding the dynamometer and its operation can be found in Weller (2010).

3.2 Experimental Set-Up and Measured Response

The experimental equipment is described in Thomas et al. (2008) and details of the experimental arrangement and procedures are given by Weller (2009). All experiments were run as part of a PhD programme which was run in parallel to the research of this thesis (Weller, 2010). Tests were conducted in a 5 m wide flume with a flat bed of length 18.5 m from paddles to mid-beach. In all of the array tests, the middle float was located at the centre-line of the flume (i.e. 2.5 m from both flume walls) and 3.6 m from the wave-paddles. Each float has a cylindrical section with an ellipsoidal base with circular cross section of radius $a_1 = 0.076$ m, draft radius (of the ellipsoidal section) of $a_2 = 0.065$ m and mass 1.2 kg.

The displaced mass of the float, M_m, was 0.8 kg with a supplementary mass, M_{sup}, of 0.8 kg, split into two sections; 0.4 kg added to the float, and 0.4 kg as a counterweight supported by a pulley in a similar manner to the approach used in (Vantorre et al., 2004). In this way the total system mass was $M = 2M_m$ without changing the submerged geometry of the float. When in still water, the free surface was located at the top of the ellipsoidal base. Experiments were conducted at $\frac{1}{66}$ geometric scale of the linear analysis conducted in WAMIT, for which the cross section radius was 5 m and the draft radius was 4.28 m. Wave periods and system masses were obtained such that Froude similarity was maintained. For the experimental set-up described in this section, Froude-scaling was applied with a geometric scale factor of 66.

The float-counterweight pulley system was chosen over a strut support system to minimise mechanical friction. Although this mechanism allowed each float to undergo some motion in surge, horizontal motion observed was small relative to the incident wavelength and so pulley rotation was a reasonable approximation to the vertical displacement (Weller, 2010). Angular pulley displacements were measured using a digital encoder on each device. Vertical float displacements were obtained by multiplying the angular pulley displacements by the radius of the pulley, 0.0175 m. Six capacitance-type wave gauges were used to record time varying wave amplitudes. For all tests, the wave amplitude was specified as 0.013 m, equivalent to 0.86 m full-scale, and wave frequencies in the range $0.75 - 1.75$ Hz were generated. The response amplitude ratios reported were normalised relative to the measured wave amplitude.

For reference purposes, the floats are numbered from 1 to 5 as shown in Figure 3.1.

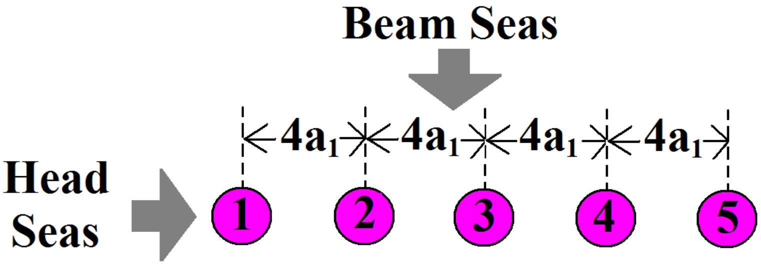

Figure 3.1: Diagram of 5×1 array of hemispheres of radius a with a centre to centre separation distance of $s = 4a_1$; beam and head sea directions are also indicated

The experimentally measured response amplitude ratios are represented by markers in Figures 3.2 and 3.4 for beam seas (where waves propagate perpendicular to line of array) and in Figures 3.3 and 3.5 for head seas (where waves propagate along the line of the array).

3.3 Numerical Prediction of Response

The response amplitude, $|X_z|$, of a body oscillating in heave due to an incident wave of angular frequency ω can be obtained by integrating the float velocity as given by

Equation (2.36), such that

$$|X_z| = \frac{\hat{F}}{i\omega(R+B) - \omega^2(M + A - \frac{S}{\omega^2})}. \tag{3.1}$$

The study in this chapter concerns the response of mechanically unconstrained devices as discussed in Section 3.1, such that mechanical damping, B, in Equation (3.1) is zero. This assumes that mechanical friction is zero and hence power generation is zero. Small amplitude motion is assumed and so hydrostatic stiffness S is typically expressed in terms of water plane area, A_{WP}, such that

$$S = \rho g \cdot A_{WP}. \tag{3.2}$$

It is straightforward to include linear mechanical damping in the model if required. The response amplitude relative to the wave amplitude ($\frac{1}{2}H$) is known as the response amplitude ratio, $|d_z|$, and is given by

$$|d_z| = \frac{2\,|X_z|}{H}. \tag{3.3}$$

Linear theory predictions with zero mechanical damping and stiffness calculated using Equation (3.2) with the water plane area calculated when at rest (defined to be stiffness calculation S_1 in Section 3.3.1) are shown by the solid black lines in Figures 3.2 and 3.3. In general, agreement away from the peak of the predicted response appears to be reasonable, although the measured response amplitude curve is shifted slightly towards lower wave frequencies, with an apparent under-prediction of the response at low frequencies. Near the peak frequency, the measured response is somewhat smaller than predicted. Also, for beam seas, the predicted symmetry of response is not seen in the experimental data (Float 2 different to 4).

3.3.1 Modified Stiffness & Damping

In this section two variations on the calculation of hydrostatic stiffness are considered as well as a possible improvement in the agreement between the linear theory and experimental results which could be achieved by including a small amount of additional damping in the calculations. The four variations in the linear theory calculations are represented by different lines in Figures 3.2 to 3.5.

Modified Hydrostatic Stiffness

For a device with a constant horizontal cross-sectional area such as a vertical cylinder, the water-plane area is constant. A float with a non-uniform horizontal cross-sectional area has a water-plane area which is dependent on draft. One of the fundamental assumptions in linear wave theory is that the amplitudes of all oscillations are small. In the initial calculation of hydrostatic stiffness, the variation of water-plane area due to the heave motion of the float was therefore assumed to be negligible such that

$$S_1 = \rho g \cdot A_{WP}\left(X = 0\right). \tag{3.4}$$

When evaluated at the mean water line the radius is a_1 but response amplitude ratios up to $0.6a_1$ were observed during experiments. Over this range of displacement, the water plane radius varies from $0.71a_1$ to a_1 over this range. A more appropriate calculation of stiffness should therefore account for this variation. The mean of the maximum and minimum water-plane areas when the float oscillates with the mean response amplitude measured experimentally (for all floats) is

$$S_2 = \rho g \cdot \left(\frac{\min\left(A_{WP}\left(\bar{X}\right)\right) + \max\left(A_{WP}\left(\bar{X}\right)\right)}{2} \right). \tag{3.5}$$

$\bar{X}$ represents the mean of all of the time averaged response amplitudes measured experimentally such that

$$\bar{X} = \frac{\sum_{i=1}^{N_\omega} \sum_{j=1}^{N} X_j\left(i\right)}{N_\omega \cdot N}, \tag{3.6}$$

where N_ω is the number of frequencies tested experimentally and N is the number of floats. In beam seas, $\bar{X} = 1.61$ m and in head seas $\bar{X} = 1.49$ m. The response amplitude ratios calculated using S_2 are plotted on Figures 3.2 and 3.3.

Equation (3.5) is only intended to give an indication of the effect of hydrostatic stiffness on response. It does not give an exact representation of the mean hydrostatic stiffness on the floats as any phase differences between the wave and float responses are neglected.

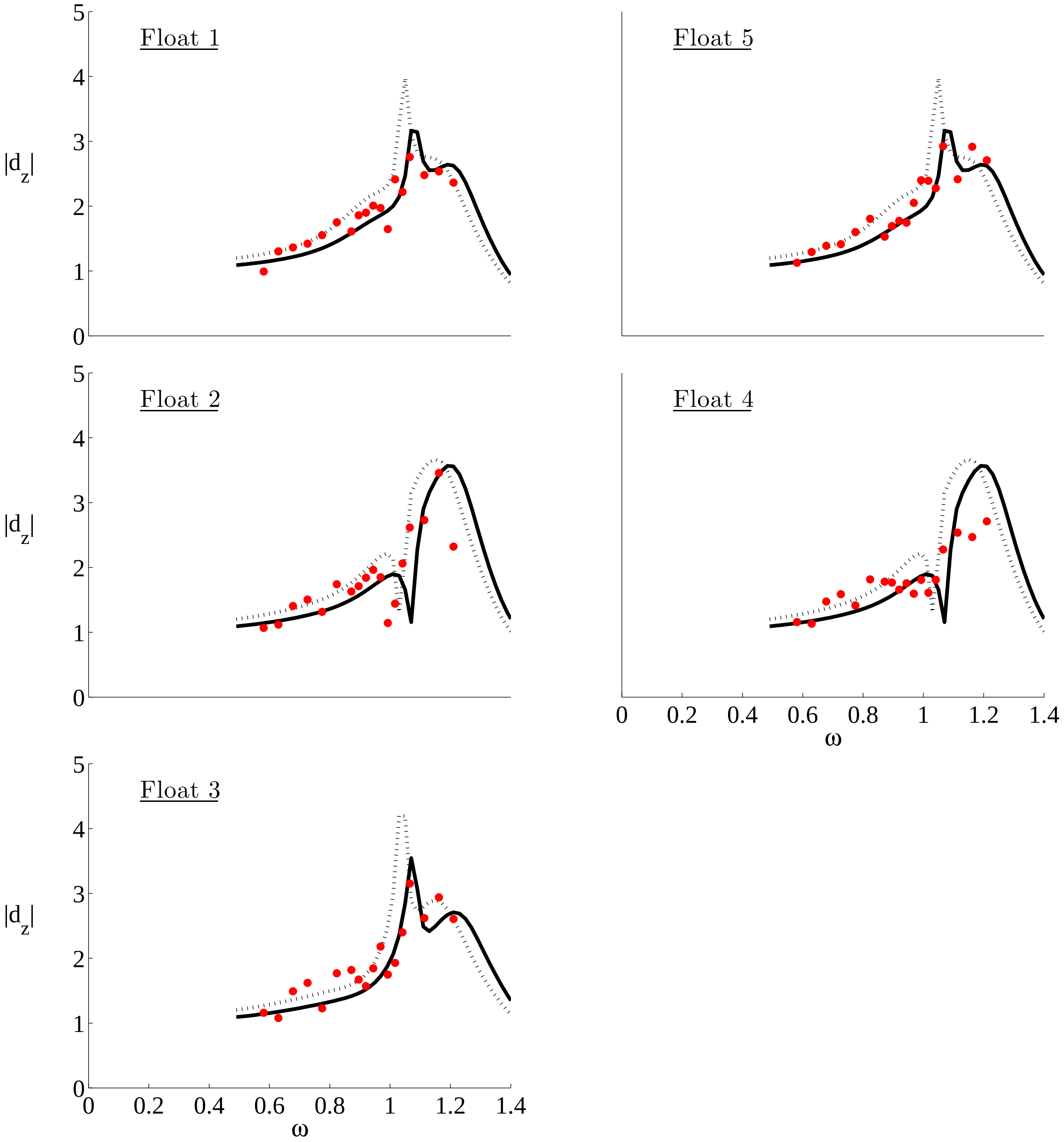

Figure 3.2: Response amplitude ratio, $|d_z|$, for each float within a 5 × 1 array of hemispherical floats of radius a_1 with centre to centre separation distance of $s = 4a_1$ in BEAM seas.

KEY: Markers, experimental data;

Solid black line, Calculations with $S = S_1$ (Equation (3.4)) and $R = 0$;

Dotted black line, Calculations with $S = S_2$ (Equation (3.5)) and $R = 0$

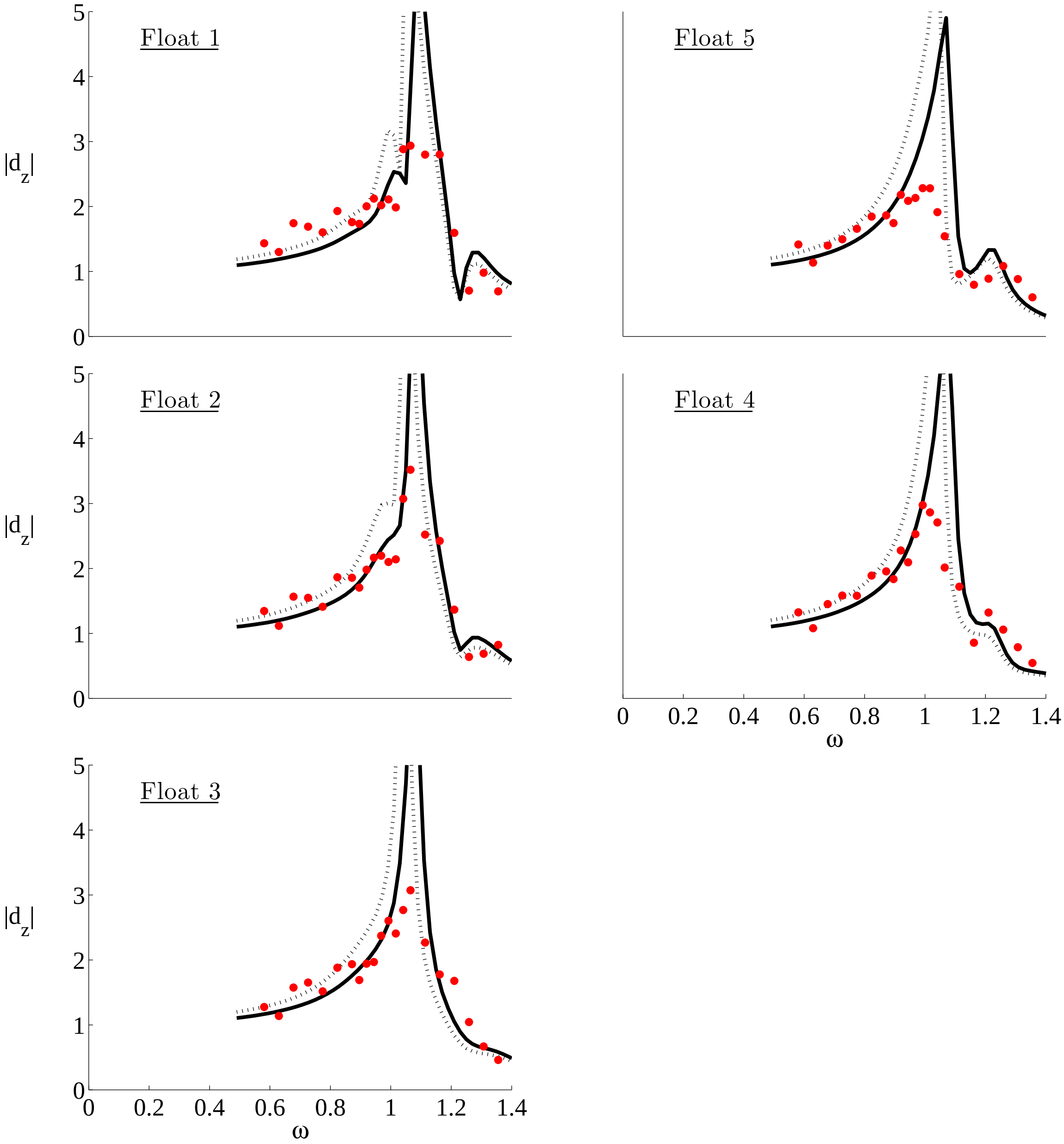

Figure 3.3: Response amplitude ratio, $|d_z|$, for each float within a 5 × 1 array of hemispherical floats of radius a_1 with centre to centre separation distance of $s = 4a_1$ in HEAD seas.
KEY: Markers, experimental data;
Solid black line, Calculations with $S = S_1$ (Equation (3.4)) and $R = 0$;
Dotted black line, Calculations with $S = S_2$ (Equation (3.5)) and $R = 0$

Additional Damping

As the experimental model does not include any power take-off systems applying a damping force to the floats, the initial linear theory predictions were made using an assumption of zero additional damping. The root mean square of the difference between the numerical predictions and experimental data can however be reduced by including a small amount of additional damping in the numerical model.

The root mean square error ($RMSE$) is commonly used to give a measure of the quality of the fit of numerical data to actual data, where a small $RMSE$ indicates a good fit (Salkind, 2010). It is described in more detail in Section 3.4 with a mathematical definition given by Equation (G.6).

To determine the magnitude of the additional damping which, when applied to all floats for all wave frequencies, reduces the root mean square of the difference between the numerical predictions and experimental data, an iterative method is developed. Values of additional damping from 0 to 100 kNs/m which are multiples of 10 kNs/m are considered in the iterative procedure.

The iteratively selected additional damping values are shown in Table 3.1. Using the iterative procedure a greater value of additional damping is determined to be necessary (in the numerical model) in the head seas array compared to the beam seas array in order to reduce the difference between the experimental and numerical data. This is also the case for when the hydrostatic stiffness is calculated using S_2 (Equation (3.5)) compared to when it was calculated using S_1 (Equation (3.4)). The resulting response amplitude ratios can be seen in Figures 3.4 and 3.5 as solid grey lines for stiffness calculations, S_1, and as black dashed lines for stiffness calculations, S_2.

	Beam	Head
S_1	$R = 20$ kNm/s	$R = 40$ kNm/s
S_2	$R = 30$ kNm/s	$R = 60$ kNm/s

Table 3.1: Additional damping values selected iteratively to include in the numerical model to minimise the root mean square difference between the numerical predictions and the experimental data when the hydrostatic stiffness in the numerical model is calculated using S_1 (Equation (3.4)) and S_2 (Equation (3.5))

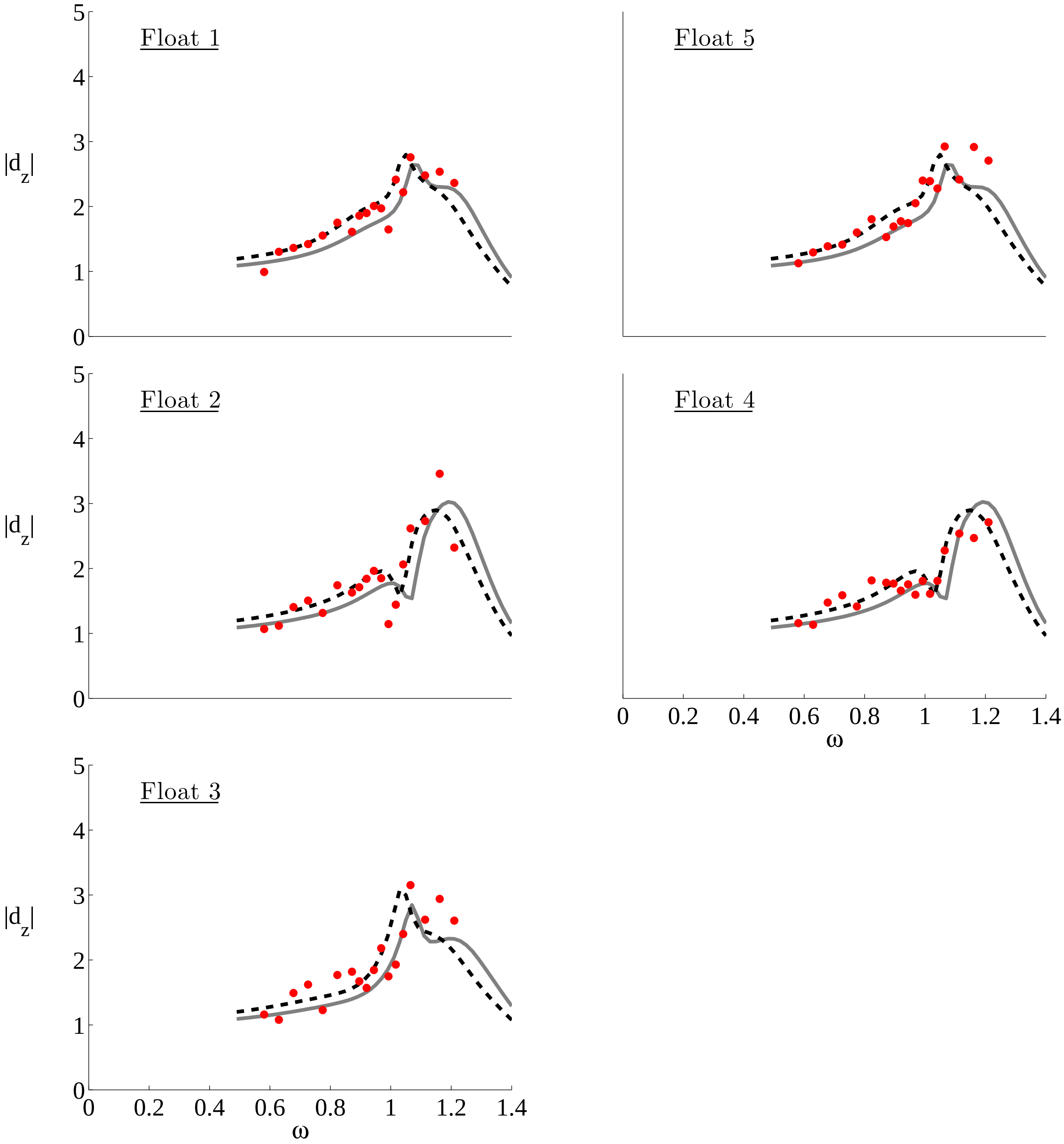

Figure 3.4: Response amplitude ratio, $|d_z|$, for each float within a 5×1 array of hemispherical floats of radius a_1 with centre to centre separation distance of $s = 4a_1$ in BEAM seas.

KEY: Markers, experimental data (same as in Figure 3.2);
Solid grey line, Calculations with $S = S_1$ (Equation (3.4)) and $R = 20$ KNms^{-1};
Dashed black line, Calculations with $S = S_2$ (Equation (3.5)) and $R = 30$ KNms^{-1}

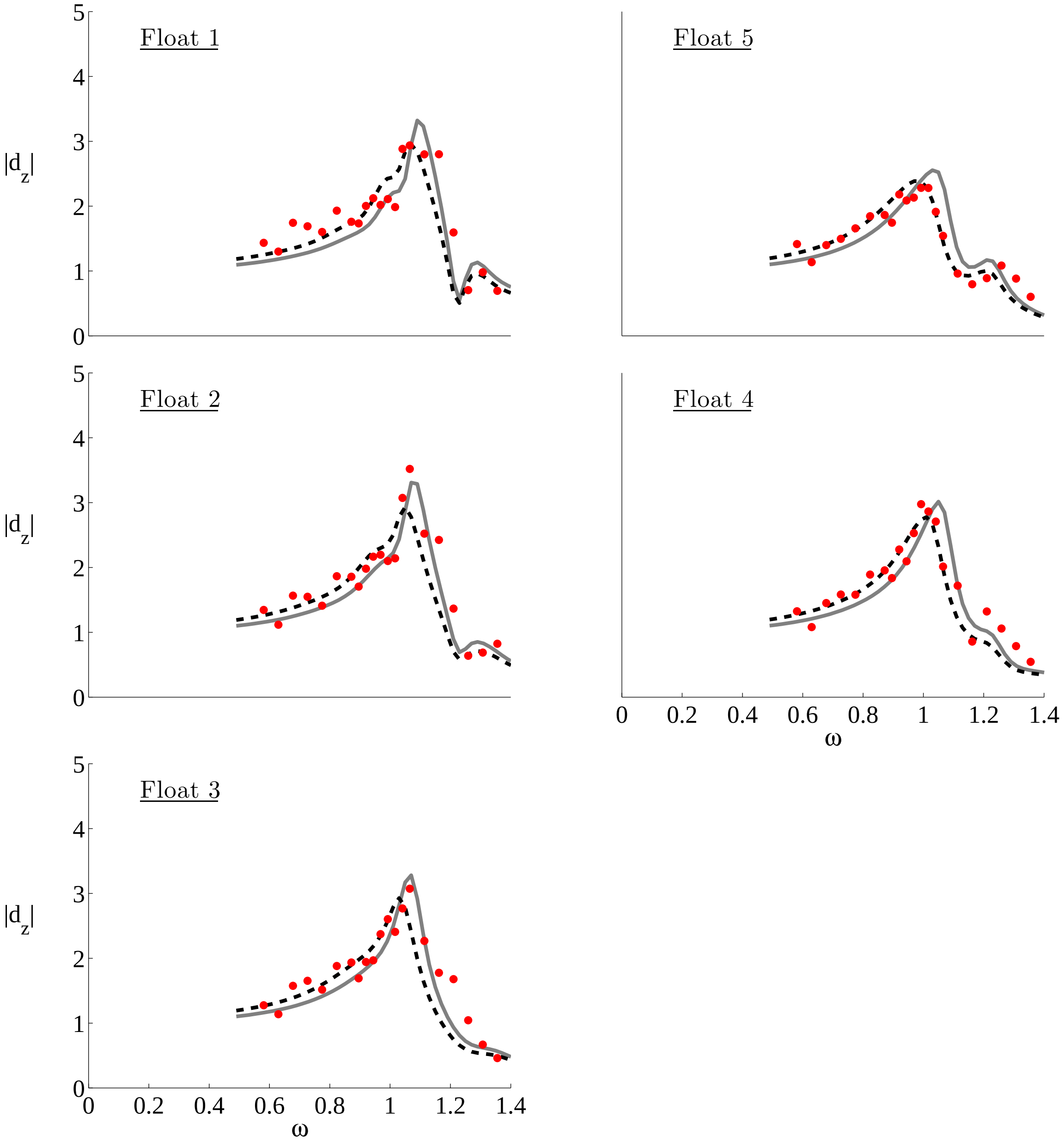

Figure 3.5: Response amplitude ratio, $|d_z|$, for each float within a 5×1 array of hemispherical floats of radius a_1 with centre to centre separation distance of $s = 4a_1$ in HEAD seas.
KEY: Markers, experimental data (same as in Figure 3.3);
Solid grey line, Calculations with $S = S_1$ (Equation (3.4)) and $R = 40$ KNms^{-1};
Dashed black line, Calculations with $S = S_2$ (Equation (3.5)) and $R = 60$ KNms^{-1}

3.4 Statistical Comparison of Methods

There are many different methods which can be used to validate a model by comparing its predictions to the real world. A model can be shown to be invalid by its failure according to a statistical test, however it cannot be shown to be valid as an inability to show significant difference between the predictions of a numerical model and the real world data may only be due to the power of the statistical test in that particular application (Mayer and Butler, 1993). Any one statistical measure may be reliant on rigid assumptions, so that if any one of the assumptions is not valid then the results of the statistical test cannot be relied upon (Loague and Green, 1991). It is therefore more thorough to consider a variety of different statistical measures together with a subjective assessment of the data in a graphical format.

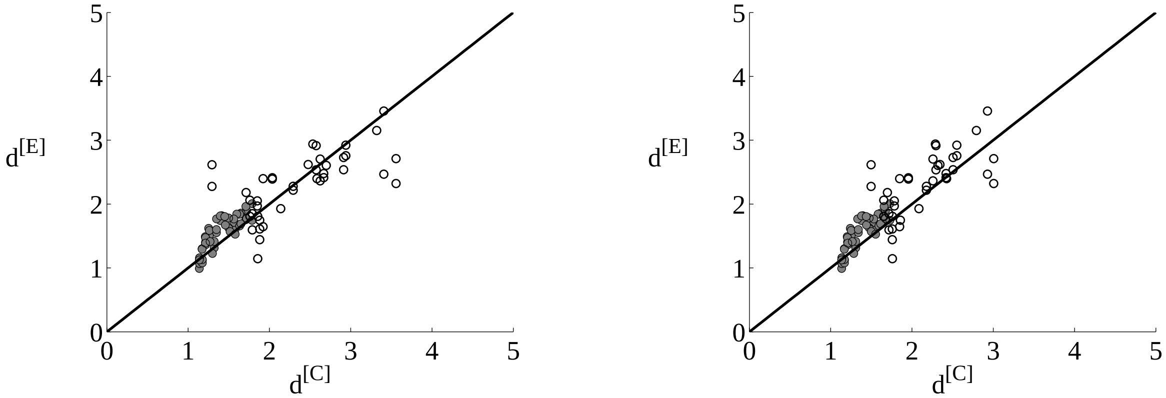

(a) $S = S_1$ (Equation (3.4)) and $R = 0$

(b) $S = S_1$ (Equation (3.4)) and R as given by Table 3.1

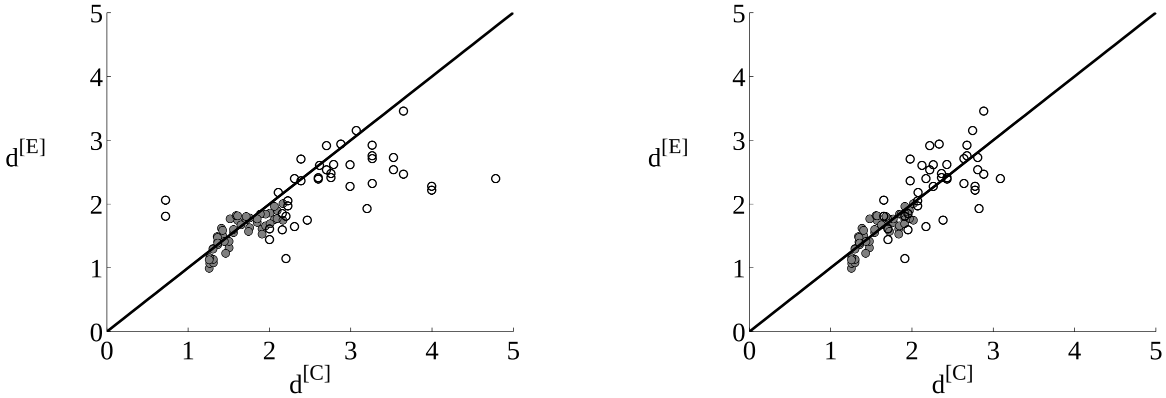

(c) $S = S_2$ (Equation (3.5)) and $R = 0$

(d) $S = S_2$ (Equation (3.5)) and R as given by Table 3.1

Figure 3.6: Response amplitude ratio, $|d_z|$, for each float within a 5 × 1 array of hemispherical floats of radius a_1 with centre to centre separation distance of $s = 4a_1$ in BEAM seas as measured experimentally $\left(\left|d_z^{[E]}\right|\right)$ and numerically $\left(\left|d_z^{[C]}\right|\right)$. The solid lines mark the line $|d_z^{[E]}| = |d_z^{[C]}|$. Numerical models use stiffness, S, and additional damping, R, as given in figure captions
KEY:
Solid grey circular markers, $\omega \leq 0.94$ rad/s; Empty circular markers , $\omega > 0.94$ rad/s
Figures correspond to:
(a) solid black lines in Figure 3.2; (b) solid grey lines in Figure 3.4; (c) dotted lines in Figure 3.2; (d) dashed lines in Figure 3.4

Mayer and Butler (1993) suggest that the accuracy of a model can be visualised more easily when the actual data is plotted against the model data directly. Figures

3.6 and 3.7 demonstrate this for each of the four numerical models, with the data for the lower half of the wave frequencies ($0.49 \leq \omega \leq 0.94$ rad/sec) shown by solid circles and the data for the higher half of the frequencies ($0.94 < \omega \leq 1.39$ rad/sec) which are close to the peak with the empty circles. In these figures it is only the relationship between the experimental and calculated values which is shown, and not the variation with incident wave frequency or float position within the array.

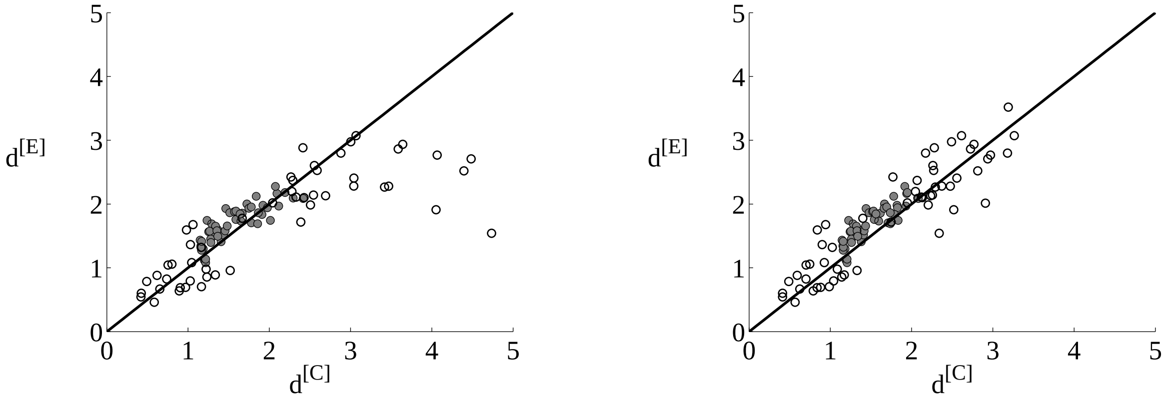

(a) $S = S_1$ (Equation (3.4)) and $R = 0$

(b) $S = S_1$ (Equation (3.4)) and R as given by Table 3.1

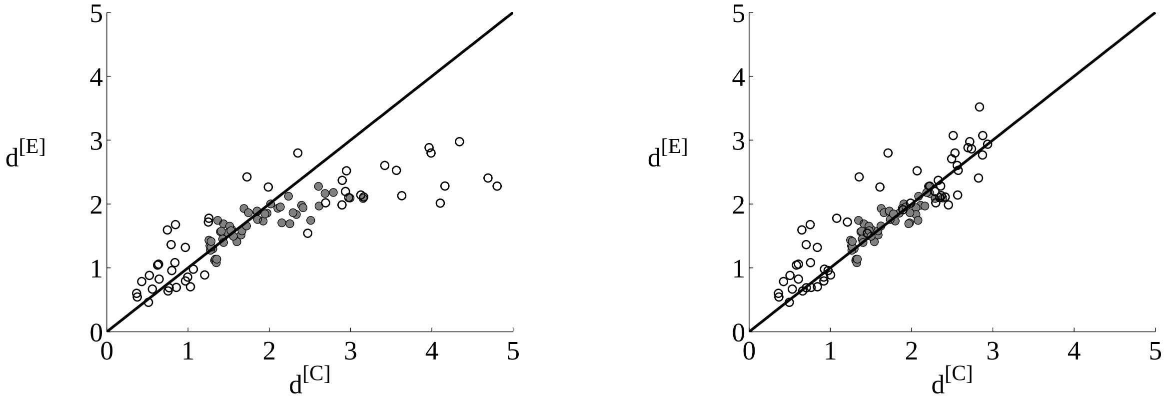

(c) $S = S_2$ (Equation (3.5)) and $R = 0$

(d) $S = S_2$ (Equation (3.5)) and R as given by Table 3.1

Figure 3.7: Response amplitude ratio, $|d_z|$, for each float within a 5×1 array of hemispherical floats of radius a_1 with centre to centre separation distance of $s = 4a_1$ in HEAD seas as measured experimentally $\left(\left|d_z^{[E]}\right|\right)$ and numerically $\left(\left|d_z^{[C]}\right|\right)$. The solid lines mark the line $|d_z^{[E]}| = |d_z^{[C]}|$. Numerical models use stiffness, S, and additional damping, R, as given in figure captions
KEY:
Solid grey circular markers, $\omega \leq 0.94$ rad/s; Empty circular markers , $\omega > 0.94$ rad/s
Figures correspond to:
(a) solid black lines in Figure 3.3; (b) solid grey lines in Figure 3.5; (c) dotted lines in Figure 3.3; (d) dashed lines in Figure 3.5

In all cases significantly greater scatter can be seen about the line of perfect model fit $\left(|d_z^{[E]}| = |d_z^{[C]}|\right)$ at frequencies near the peak compared to the low frequencies away from the peak. The improved agreement when additional damping is included in the numerical model (Figures 3.2 to 3.5), can be seen by the reduction in scatter of the higher frequency data in Figures 3.6 and 3.7.

There are several statistical measures which can be used to determine which numerical model provides the most similar results to the experimental data (see Appendix G for mathematical definitions).

Variable Name	Ideal Value	S_1		S_2	
		$R = 0$	R as in Table 3.1	$R = 0$	R as in Table 3.1
MAE	0	0.24	0.24	0.34	**0.21**
$MAPE$	0	12.6 %	12.6 %	18.0 %	**11.3 %**
$MAEPM$	0	12.7%	12.9 %	18.2 %	**11.3 %**
$RMSE$	0	0.34	0.31	0.55	**0.29**
$RMSPE$	0	23.7 %	21.6 %	38.1 %	**20.8 %**
$RMSEPM$	0	18.2 %	16.6 %	29.1 %	**15.5 %**
CRM	0	0.03	0.09	-0.12	**-0.01**
PDV	0	- 0.41	**0.14**	-1.15	0.18
ME	0	1.32	1.12	2.38	**0.90**
CD	1	0.70	**1.05**	0.43	1.21
EF	1	0.60	0.66	-0.04	**0.70**

Table 3.2: Statistical measures of suitability of numerical models based on linear theory for application to experimental data for arrays in $BEAM$ seas. Numerical models have hydrostatic stiffness calculated as S_1 (Equation (3.4)) or S_2 (Equation (3.5)), and additional damping is either excluded (such that $R = 0$) or included with values as given in Table 3.1; Statistical definitions are given in Equations (G.5) to (G.15) in Appendix G; the best numerical model is indicated by bold font for each statistical measure

Table 3.2 shows that of the four numerical models, the most appropriate in beam seas is the use of linear theory with the hydrostatic stiffness calculated using S_2 (Equation (3.5)) and additional damping included such that $R = 30$ kNm/s (as given by Table 3.1). Nine out of the eleven statistical measures found this model favourable, with the only exception being PDV and CD indicating that the linear theory model with the inclusion of additional damping but stiffness calculated using S_1 (Equation (3.4)) provided a closer variance to the experimental data than the other three models.

Table 3.3 shows that in head seas the linear theory models including additional damping are preferable over those which do not include any, with five statistical measures indicating that calculating the stiffness with S_2 is preferable, and six indicating that stiffness calculation S_1 is preferable. The statistical measures for both models including additional damping are similar in all eleven cases.

The selected models (in beam and head seas) predict data with means at most 5% different to the experimental data and variances at most 14% different from the experimental data. A perfect fit would result in an EF value of 1, and a poor fit in an EF value below zero, so EF values around 0.8 as given by the selected models indicate a relatively good overall fit. A maximum response amplitude ratio error of around 0.9 is however determined in both head and beam seas by the selected models, which is around 50% of the mean experimental value, showing that the numerical models are good for giving an indication of the expected response amplitude ratio, but not the exact value particularly close to the peak wave frequency.

Variable Name	Ideal Value	S_1		S_2	
		$R = 0$	R as in Table 3.1	$R = 0$	R as in Table 3.1
MAE	0	0.44	0.25	0.71	**0.22**
$MAPE$	0	24.6 %	15.9 %	34.4 %	**13.7 %**
$MAEPM$	0	25.0 %	14.3 %	41.0 %	**12.5** %
$RMSE$	0	0.79	**0.31**	1.27	0.32
$RMSPE$	0	54.6 %	**23.5 %**	80.0 %	23.7 %
$RMSEPM$	0	45.2 %	17.6 %	72.7 %	**18.1 %**
CRM	0	-0.12	0.06	-0.30	**0.05**
DVR	0	-2.16	**-0.05**	-5.34	-0.10
ME	0	3.76	**0.89**	5.48	1.09
CD	1	0.31	**0.92**	0.14	0.89
EF	1	-0.48	**0.78**	-2.83	0.76

Table 3.3: Statistical measures of suitability of numerical models based on linear theory for application to experimental data for arrays in *HEAD* seas. Numerical models have hydrostatic stiffness calculated as S_1 (Equation (3.4)) or S_2 (Equation (3.5)), and additional damping is either excluded (such that $R = 0$) or included with values as given in Table 3.1; Statistical definitions are given in Equations (G.5) to (G.15) in Appendix G; the best numerical model is indicated by bold font for each statistical measure

3.5 Discussion of Model Discrepancies

The large over-prediction in peak response determined using linear theory with the basic stiffness calculation and zero additional damping is expected to be due to a combination of factors. In this section an estimate is obtained of the magnitude of damping or stiffness variation due to experimental processes and due to the modelling assumptions. The intention is to understand which of the assumptions has the greatest influence on response.

3.5.1 Mechanical Friction

The first factor is friction within the additional components of the dynamometer system. Although power was not extracted from the devices during the experiments, the float-pulley-counterweight system was still connected to the power take-off system. Calibration of the experimental dynamometer outside of the flume determined a value of current equivalent to the static friction in the rotating system, which was programmed into the circuit board as an offset current. Small variations in static friction were found to exist due to variations in various factors including temperature and device usage. To account for these variations, a calibration process was adopted involving deceleration tests of the drivetrain in order to compensate for friction in the system. These small variations in static friction were typically around 2 mA which is equivalent to a power loss of 0.0017W (Weller, 2010). With a Froude Scaling factor of 66, this corresponds to a power loss of $\tilde{P} = 0.0017 \times 66^3 = 3.97$ kW.

Assuming harmonic motion , this power loss can be written as a function of float velocity and damping using Equation (2.53). The time averaged power can be calculated from Equation (2.53) at frequency ω (corresponding to period, T) such that

$$\tilde{P} = \frac{1}{2T} \int_0^T R\dot{X}_z \mathrm{d}t. \tag{3.7}$$

So, assuming periodic motion

$$X_z = |X_z| \cos(\omega t),$$

hence the velocity is given by

$$\dot{X}_z = \omega \left| X_z \right| \sin\left(\omega t\right).$$

Substituting this back into Equation (3.7) gives

$$\tilde{P} = \frac{R \left| X_z \right|}{2T} \int_0^T \left(\frac{2\pi}{T}\right) \sin\left(\omega t\right) \mathrm{d}t,$$

where the frequency ω has been replaced with $\frac{2\pi}{T}$ and the R is taken to be the time averaged mechanical damping. This can be integrated to give

$$\tilde{P} = \frac{\pi^2 \left| X_z \right|}{T^2} R,$$

which can be rearranged to give

$$R = \frac{T^2}{\pi^2 \left| X_z \right|} \tilde{P} = \frac{4}{\omega^2 \left| X_z \right|} \tilde{P}. \tag{3.8}$$

Using Equation (3.8), the maximum unaccounted friction force at full scale due to a power loss of $\tilde{P} = 3.97$ kW is calculated to be 4825.9 kNm/s. Although this is relatively large, it is subject to uncertainties in scaling (see Section 3.5.5).

3.5.2 Viscous Drag

The second factor is viscous drag, F_{fd}, an alternative form of drag experienced by the float. This is defined as $F_{fd} = \frac{1}{2} C_d U^2 A_{CsZ}$ where C_d is the drag coefficient, U the float velocity and A_{CsZ} the cross-sectional area of the float in the vertical plane perpendicular to the direction of wave propagation. As the area does not change significantly, $A_{CsZ} \approx \pi \times 5 \times 4.28 = 33.59\text{m}^2$ (since float radii are 5 and 4.28 m), the maximum viscous drag must occur when the velocity is maximum. The velocity can be determined as the multiple of the complex amplitude of the response and $i\omega$. As only the absolute amplitude and not the complex amplitude of the response is known for the experimental array, the multiplication with ω indicates an approximate velocity. The maximum velocity is approximately 3.4 m/s in beam seas and 3.2 m/s in head seas at full scale. A spherical body with a velocity of 3.4 m/s is expected to have a drag coefficient of the order of 5 (Massey, 1975). The maximum viscous drag in beam seas is therefore $F_{fd} = \frac{5}{2} \times 3.4^2 \times \pi \times 5 \times 4.2763 = 1.9413$ kNm/s. This corresponds to only 6.5 % of the required 30 kNm/s.

3.5.3 Flume Walls

All numerical calculations are based on hydrodynamic parameters calculated for 33m water depth (equivalent to 0.45m depth at the geometric scale considered) for the open sea case. It is recognised that the hydrodynamic parameters for a body in a narrow channel may differ from those in the open sea.

The excitation force and pressure field on arrays of fixed vertical cylinders has been found to be significantly different in a channel when compared to the open sea, even when the channel width is large compared to the array dimensions (Butler and Thomas, 1993). However for floating bodies, it is the variation of radiation force due to the channel walls which is more likely to contribute to the observed difference between theoretically predicted and measured maximum response amplitudes. It has been shown that a body restricted to heave only which is located on the centre line of a channel of width $2s_c$ will have a different absorption length to that of the open sea case except in specific spacing to wavelength ratios (Bjarte-Larsson et al., 2006). The absorption length is defined to be the power absorbed by a body divided by the power available per unit crest width.

Maximum power absorption (given by Equation (2.54)) is a function of excitation force and radiation damping, so the difference in maximum absorption between the open sea and channel cases corresponds to a variation in the relationship between the excitation force and radiation damping. This could therefore indicate a difference in the radiation damping from the open sea to the channel.

The magnitudes of such a variation in radiation damping have not been investigated, particularly not for free-float response, however they are not expected to be the main contributors to the requirement of the additional damping in the linear theory predictions as the experimental channel width considered here is significantly greater than the array dimensions, hence the time taken for waves to reflect from the channel walls to the array in order for the radiated wave to be affected is quite large.

The power per unit length of wave crest is given by $P_w = \frac{1}{8}\rho g H^2 C_g$ where C_g is the group velocity. Assuming that waves radiate uniformly from a body placed at the centre of the channel, circular waves are generated. Consider an arc of such a circular wave subtending an infinitesimally small angle, $\delta\theta$, at a distance r_c from the body such that its length is $\delta\theta r_c$. The power in this wave arc is constant and independent of its distance from the body and given by $P_c = P_w \times \delta\theta r_c = \frac{1}{8}\rho g H^2 C_g \delta\theta r_c$. As ρ, g, π and

C_g are also independent of r_c, the wave height must be inversely proportional to the square-root of the distance from the body such that $H \propto \frac{1}{\sqrt{r_c}}$. If the body is placed at the centre of a flume of width $2s$, then the wave must travel a distance, $s - a_1$ from the body surface to the channel wall. If the initial wave height is H_1, then at the flume wall the wave height is given by $H_2 = \frac{1}{\sqrt{s}} H_1$. Assuming the wave is perfectly reflected at the channel wall, then the reflected wave must travel a distance of s back to the centre of the float (the point at which the radiation damping force is measured), at which its wave height is

$$H_3 = \frac{1}{\sqrt{2s - a_1}} H_1. \tag{3.9}$$

In the experiments discussed in this section the flume was 5 m in width such that $s = 2.5$ m, and the body has a horizontal radius of $a_1 = 0.076$ m, so

$$H_3 = 0.45 H_1. \tag{3.10}$$

The total radiation force is formed from the sum of the radiation force due to the radiation of a wave of unit amplitude and the force due to the reflected wave of amplitude 45 % of the originally radiated wave. After travelling a distance of $(2s - a_1)$, the reflected wave has a phase difference of $\vartheta = \frac{(2s - a_1)}{L} \times 2\pi$ compared to the original radiated wave.

The radiation force can be written using Equation (2.33) as

$$-F_r = BU + A\dot{U}, \tag{3.11}$$

where B is the radiation damping, A the added mass, U the float velocity and $\dot{U}$ the float acceleration. This ordinarily represents the radiation force due to an oscillation of unit amplitude. According to Equation (3.10), when the reflection of the radiated wave reaches the origin, its wave height is 45 % of the original wave height. If there is zero phase difference between the originally radiated wave and the reflected radiated wave at the centre of the origin, the radiation damping and added mass coefficients are therefore 45% of those originally calculated. These must therefore be summed together with the originally calculated coefficients to give the actual added mass and radiation damping coefficients.

The wavelength of the radiated wave varies according to the incident wave frequency however, whilst the distance the wave must travel before returning to the origin is fixed. A phase shift (ϑ) between the original and radiated waves will therefore be experienced at most frequencies. The added mass and radiation damping are known before the phase shift is implemented. Before the phase shift of ϑ, the velocity can be written as $U = |U| \cos(\omega t - \vartheta)$ and the acceleration as $\dot{U} = -\omega |U| \sin(\omega t - \vartheta)$. The radiation force can thus be rewritten as

$$-F_r = B\,|U| \cos(\omega t - \vartheta) + A\,|U| \left(-\omega \sin(\omega t - \vartheta)\right). \tag{3.12}$$

Using trigonometric identities this can be rearranged such that the force is written in the form of Equation (3.11) in terms of the velocity, $U = |U| \cos(\omega t)$, and acceleration, $\dot{U} = -\omega |U| \sin(\omega t)$, after the phase shift of ϑ. The radiation damping and added mass which would be experienced after the phase shift can therefore be written as

$$B_\vartheta = \cos(\vartheta)\, B + \omega \sin(\vartheta)\, A \tag{3.13}$$

$$\text{and} \quad A_\vartheta = -\frac{1}{\omega} \sin(\vartheta)\, B + \cos(\vartheta)\, A \tag{3.14}$$

respectively. The magnitude of the phase shift between the originally radiated wave and the reflected wave therefore determines the magnitude of the variation in added mass and radiation damping.

In head seas (at full scale), float 1 achieved the greatest Response Amplitude Ratio at $\omega = 1.09$ rad/sec (corresponding to a wavelength of $L = 51.79$ m). This corresponds to a small-scale wavelength of $L = 0.79$ m which corresponds to a phase shift of $\vartheta = 6.25 \times 2\pi = 12.5 \times \pi = 0.5\pi$. Applying this to Equation (3.13) results in a variation in radiation damping of $B_{0.5\pi} = 0$. At this wave frequency the calculated radiation damping is therefore not affected by the reflected wave (although the added mass is affected).

The phase difference is however highly dependent on the precise frequency. Consider for example the frequency of $\omega = 1.09$ rad/sec at full scale (only one increment lower than the peak Response Amplitude Ratio frequency of 1.09 rad/sec). This corresponds to a small-scale wavelength of $6.49\,(2s - a_1)$ hence a phase shift of $\vartheta = 6.0287 \times 2\pi = 12.0574\pi$. At this wave frequency the sum of the first row of the calculated radiation damping matrix is 122.99 kNs/m and the sum of the first row of the calculated added mass matrix is 113970 kg. The radiation damping due to the reflected wave is therefore $B_{0.9838\pi} = \cos(12.0574 \times \pi) \times 0.45 \times 122990 + \sin(12.0574 \times \pi) \times 0.45 \times 113970 = 63.6$

kNs/m. Similarly at $\omega = 1.11$ rad/sec (full scale) the radiation damping due to the reflected wave is -48 kNs/m.

These calculations indicate that the variation in radiation damping within the experiments due to reflected waves could account for the majority of the discrepancy between the numerical and experimental data at certain wave frequencies. The calculations are only indicative however and the magnitude by which the radiation damping is modified within the experiments is highly sensitive to the wave frequency.

3.5.4 Variations in Spacing

Variations in spacing along the array due to oscillations in surge were visible during the experiments, particularly in head seas. The large peak in the linear model is sensitive to the phase of the excitation force and so may be inhibited by small variations in float spacing caused by oscillations in surge. At rest the devices had a centre to centre spacing of $s = 4a$ which is the spacing used in the numerical calculations. The movement of floats noticed during the experiments was less than a float radius. That is, the instantaneous spacing between floats when oscillating in surge reduced by about 1 radius. This could correspond to a change of mean spacing, $\delta s << a$.

A phase shift caused by the variation in spacing would result in a greater radiation damping due to the inclusion of parts of both the undisturbed radiation damping and added mass according to Equation (3.13). The phase shift is given by $\vartheta = 2\pi\frac{\delta s}{L}$ where δs is the change in spacing and L the wavelength.

In head seas (at full scale), the greatest Response Amplitude Ratio at $\omega = 1.09$ rad/sec ($L = 51.79$ m) occurred on float one. At this frequency, the sum of the first row of the radiation damping matrix is given by $B\left(x - \delta x\right) = 118.56$ kNs/m and the sum of the first row of the radiation damping matrix is given by $A\left(x - \delta x\right) = 110910$ kg. A shift in mean body position of $\delta x = 0.5a$ would result in a phase shift $\vartheta\left(0.5a\right) = 0.61$. The radiation damping therefore becomes $B(x) = 166.33$ kNs/m, an increase of 47.8 kNs/m compared to the calculated radiation damping. This increase in radiation damping due to the change in spacing is greater than the additional damping that was required in head seas when the basic hydrostatic stiffness calculation was used ($R = 40$kN/s).

3.5.5 Scaling Approximations

Each of the five experimental floats were hand-made to the same specifications, however discrepancies of up to 0.5 mm are inherent in the float major and minor axis.The proportions of the body were assumed to remain unchanged when scaled, however if the dimensions of the experimental floats were larger than intended in one direction and smaller than intended in another then this could result in the proportions of the bodies being changed, causing the added mass and radiation damping of the experimental body to differ from those of the numerical calculations. If the discrepancies occurred in the float dimensions such that their proportions remained intact then the Froude scaling factor would be in the range $65.4 < SF \leq 66.2$, causing the full scale mass to be 0.66 % greater or smaller than that used in the calculations (in which a scaling factor of $SF = 65.8$ was used). The calculation of the hydrostatic stiffness was based on the full scale water-plane area which was 5 m irrespective of any discrepencies in the experimental float measurements so would not experience a variation due to the errors. The variation in the mass due to the scaling factor discrepancy means that the natural frequency of an isolated float could have been over- or underestimated by 0.02 rad/s, which is half of the difference between the natural frequencies calculated with the two different stiffness calculations, S_1 and S_2.

3.6 Chapter Conclusion

Predictions of free float response for a 5×1 array of free-floating hemispherical floats made using linear wave theory are compared to experimental data scaled up to full-scale from a $\frac{1}{66}$ scale test array. Power take-off is not considered so that large response amplitude ratios occur. This provides a more stringent test for linear wave theory than an array in which float motion is subject to mechanical damping.

Four possible cases are considered using linear wave theory such that the stiffness is either calculated by assuming negligible change in water-plane area or by accounting for the vertically non-uniform geometry by using a mean water-plane area, as well as either including or excluding additional damping. In the cases where additional damping is applied, the same amount is applied on all floats at all wave frequencies with its value selected iteratively so as to minimise the root mean square error of the numerical calculations to the experimental data.

A range of statistical measures are calculated to assess the fit of each of the four numerical models to the experimental measurements. As a general rule (in both beam and head seas) calculations made using linear theory in which a small amount of additional damping is included and the stiffness is calculated using the mean water-plane area (so as to account for the non-uniform cross-sectional area of the floats) are determined to be in closest agreement with the experimental data. In head seas however, linear theory calculations including additional damping and hydrostatic stiffness calculated assuming negligible change in water-plane area are also found to be in close agreement with the experimental data.

The experimental response amplitude ratios are found to be consistently close to 1.5 at low frequencies but form a peak at high frequencies with response amplitude ratios of up to 3.52. The selected numerical models provide response amplitude ratios with the same general trend as the experimental data. The selected numerical models have a Root Mean Square Error in response amplitude ratio of around 0.3 and Modelling Efficiency values (for which one indicates a perfect fit and zero a poor fit) of between 0.7 and 0.78 indicated a good overall agreement with the experimental data. The agreement between the experimental and numerical data is found to be consistently good at frequencies far from the peak, with the largest discrepancies found close to the peak frequency.

The improved fit between the experimental data and linear model simulations in which a small amount of additional damping was included, can be explained by phenomena observed in the small-scale experiments which were not accounted for in the numerical model. These phenomena include influence of mechanical friction and small differences between the actual and modelled float geometries which become significant when Froude scaling is applied. In addition, it is shown that the linear radiation damping force used in numerical predictions may differ from the actual radiation damping. These discrepancies may occur due to the presence of flume walls and due to small changes of the mean spacing between individual floats. The latter is particularly important for the head seas array in which change of spacing was observed during the experiments.

Chapter 4

Second Order Forcing

It was explained in Chapter 2 that the total velocity potential, Φ, can be expressed as a perturbation series of the wave-slope parameter, $\epsilon = \frac{kH}{2}$, where k is the wavenumber and H is the wave height, such that

$$\Phi = \epsilon\Phi^{[1]} + \epsilon^2\Phi^{[2]} + \epsilon^3\Phi^{[3]} + \cdots \tag{4.1}$$

The first-order problem, used in the numerical models of Chapter 3, is only able to account for loads and forces at frequencies within the incident wave spectrum. When second-order terms are considered, the velocity potential also includes components at the sums- and differences of pairs of component frequencies of the incident wave spectrum. These sum and difference frequencies are often not part of the incident wave spectrum. Second-order effects are therefore greatest at small and large frequencies relative to the peak frequency of the spectrum (corresponding to difference and sum frequencies respectively). This can become important if the sum or difference frequency coincides with the natural frequency of a body, or if the damping or restoring forces at that frequency are small (Kim and Yue, 1989).

The natural frequency of a heaving float, ω_0, is a function of hydrostatic stiffness, S, (proportional to the water-plane area), the added mass, A, and the system mass, M, such that $\omega_0 = \sqrt{\frac{S}{A+M}}$. Wave energy devices commonly have a natural frequency which is higher than the peak frequency of the most common sea-states at the planned deployment site. This allows for smaller devices (with smaller water-plane areas hence smaller hydrostatic stiffness) and provides suitable circumstances for control systems such as latching to be implemented where necessary (Babarit et al. (2004) and Falcão (2008)). Since the natural frequencies of wave energy devices are typically high, it is possible that second-order effects at sum frequencies could be significant close to the natural frequency of the devices. Since wave spectra may be broad banded, second-order effects at difference frequencies may also be important at the frequency which corresponds to double the natural period of the device (i.e. $\omega_0/2$), particularly for high wave periods.

The aim of this chapter is to gain an understanding of the magnitude of first- and second-order forces on a small, closely spaced, array of wave energy devices. Different sea-states (defined in Section 4.3) are considered with a view to determining a relationship between the frequencies at which second-order effects are important within a closely spaced array and the significant wave height and peak period of the incident wave spectrum.

A short review of the published research to date on second-order effects is given in Section 4.2 with a discussion on how this relates to second-order effects in arrays of wave energy devices. Section 4.4 describes the method used in this chapter to compare the first- and second-order forces using wave amplitudes calculated from wave spectra to dimensionalise the force given by the computer analysis program, WAMIT. As the calculation of non-dimensional second-order forces using WAMIT is computationally demanding, a coarse frequency increment is initially used to obtain the non-dimensional forces. Section 4.5 provides a study to show the convergence of the dimensional forces using decreasing frequency increments of interpolated non-dimensional forces. The ratio of second to first-order forces is then analysed in detail in Section 4.6 using the interpolated data for the different sea-states.

4.1 Second Order Solution Methods

To obtain second-order contributions to the velocity potential, a boundary value problem is typically solved. This is more complicated than the first-order boundary value problem (Section 2.1.6) since the free-surface boundary condition is inhomogenous. The inhomogeneous part of the condition consists of quadratic products of the first-order potential together with a term containing the second-order potential. There are two main approaches for solving the second-order problem, a direct approach and an indirect approach.

The indirect approach avoids the direct calculation of the second-order potential by defining an additional radiation potential. In this way, the second-order forces and the distribution of wave pressures on a body can be determined (Eatock Taylor et al., 1989). This approach does not require calculation of the complete second-order velocity potential and so does not calculate the free-surface elevation at field points or the wave run-up on a structure (Mavrakos and Chatjigeorgiou, 2009a). Even though this method avoids the direct calculation of the second-order potential, the numerical effort is not reduced significantly (Newman, 2001). Published research on the indirect method include Lighthill (1979), Molin (1979), Eatock Taylor and Hung (1987), Masuda et al. (1986), Masuda et al. (1987), Abuk-Azm and Williams (1988a), Abuk-Azm and Williams (1988b), Abuk-Azm and Williams (1989a) and Abuk-Azm and Williams (1989b).

The direct approach to solving the second-order boundary value problem requires the direct integration of the pressure over the body surface. This is more computationally complex than the indirect method but results in the calculation of the second-order diffraction potential and so allows for the calculation of local flow features away from the body such as the pressure field or the free-surface elevation. The second-order free-surface elevation consists of a part due only to the second-order velocity potential and two parts which are due only to the first-order velocity potential. The parts which are due to the first-order potential consist of quadratic functions of the first-order velocity potential. Published research on the direct method include Kim and Yue (1989), Chau and Eatock Taylor (1988), Kriebel (1990), Chau and Eatock Taylor (1992), Newman (1990b), Huang (1996a), Eatock Taylor and Huang (1997a), Eatock Taylor and Huang (1997b), Malenica et al. (1999), Mavrakos and Chatjigeorgiou (2006) and Mavrakos and Chatjigeorgiou (2009b).

An approximation theory based on the direct approach with the assumption of large depth has been developed which does not attempt to satisfy the radiation condition or the boundary condition on the body surface. It has been found to give similar results for the second-order vertical force acting on a truncated surface piercing circular cylinder at low frequencies to those obtained numerically using the complete direct method with finite depth, but exceeds the numerical computations by 10-20 % at high frequencies (Newman, 1990a).

A semi-analytical method of solution for the second-order diffraction problem in which integrals are analysed both numerically in a finite domain containing the body (or bodies), and analytically in an outer region extending to infinity in the horizontal plane is commonly used in both the application of the indirect method (Ghalayini and Williams, 1991) and direct method (Kim and Yue, 1989).

In this chapter the direct approach is applied via the wave analysis program, WAMIT, however an option to use the indirect approach does also exist in WAMIT.

Within WAMIT, the free surface integral is evaluated numerically in the inner integral domain, and analytically in the (evanescent-wave free) outer domain by means of expanding the Green function and the asymptotes of the first-order potentials in Fourier-Bessel series (see the WAMIT theory manual for further details (Lee, 1995)).

4.2 Second Order Effects

Both the indirect and direct methods have received much attention since the 1970s, however much of the published research is focused on the development of methods as opposed to the results of the application of the methods. Most of the results concerning the application of the second-order models to bodies have focused on the application to isolated bodies, however limited research on second-order effects in multi-body problems does exist. Second-order effects including wave run-up, pressure and forcing on moving bodies has received extremely limited research. The following sections give a brief overview of the results which have been published to date concerning second-order effects on both isolated bodies and arrays of fixed and oscillating bodies.

4.2.1 Fixed Isolated Bodies

The approximation theory based on the direct approach with the assumption of large depth has been used to show that the second-order pressure is inversely proportional to depth. At large depths, second-order contribution to pressure is larger than the first-order component (Newman, 1990a). This implies that the second-order potential decreases more slowly with depth than the first-order potential.

The second-order body forces, pressure distributions and wave amplitudes have been calculated for a bottom mounted uniform vertical cylinder and a truncated but motionless conical island using an explicitly obtained second-order velocity potential Kim and Yue (1989). The second-order effects are amplified in the case of the bottom-mounted cone, and are greater than the first-order effects at certain phase differences for steep incident waves.

Using a semi-analytical direct method, the second-order free-surface elevation around a bottom mounted cylinder has been shown to be significantly different to that predicted by linear wave theory (Eatock Taylor and Huang, 1997a), and the first- and second-order free-surface elevation for a fixed truncated cylinder has been shown to be very similar to that of a bottom mounted cylinder (Huang, 1996a). The location of the maximum free-surface elevation has also been shown to be dependent on the order to which it is calculated (Huang, 1996a).

In the case of a bottom mounted circular cylinder, a direct semi-analytical method has been used to show that a significant increase in wave run-up can occur if the maximum second-order and first-order wave components are in phase (Eatock Taylor and Huang, 1997b). Using a fully analytical direct method, the inclusion of second-order effects on a bottom mounted circular cylinder has been shown to increase the maximum wave crest run up by 50 % and the forces by 10 - 20 % compared to linear theory (Kriebel, 1990).

Arrays of Fixed Bodies

The indirect (semi-analytical) method has been applied to arrays of bottom-mounted vertical cylinders with cylindrical and elliptical cross-section, at two different spacings (Ghalayini and Williams, 1991), finding that for spacings of $5a$ and $3a$ (where a is the radius of the floats) the increase in the magnitude of the force due to second-order effects is between 20 and 30 %.

Bottom -mounted cylinder arrays have also been analysed using a semi analytical direct approach to determine second-order wave elevation and forces (Malenica et al., 1999). The second-order surge force and pitch moment are considered on a 2×1 array, a triangular array and a 2×2 array of cylinders separated by $s = 6a$ in water of depth $3a$. Even though the second-order forces on individual cylinders within the array are larger than those of an isolated cylinder for almost all of the frequency range considered, it has been shown that the total array averaged second-order force is sometimes not large due to phase differences between the cylinders.

Arrays of four cylinders in a 2×2 layout with separation distances of $s = 4a$ and $s = 3.333a$ have also been considered by the same authors (Malenica et al., 1999). At the frequencies at which linear near-trapping (see Section 1.6.4) has been shown to occur, both the first-order elevations and the individual components of the second-order elevation are large, but due to the phase differences between the second-order components, the total second-order elevation is small. When the incident wave frequency is half of the linear near-trapping frequency however, the wave elevation at first-order, and at second-order due to the quadratic components of the first-order potential only (see Section 4.1) were found to be unremarkable, whereas the component of the second-order wave elevation due to the second-order potential was large, hence the total second-order elevation was large. This suggests that second-order near-trapping occurs when the double frequency associated with the second-order incoming wave coincides with the linear near-trapping frequency (Malenica et al., 1999). The increase in second-order wave elevation at the second-order near-trapping frequency was found to be much more pronounced (more than twice the magnitude in certain places) when the separation was reduced from $s = 4a$ to $S = 3.333a$.

Malenica et al. (1999) results were extended by Newman (2001) to the case of truncated but fixed vertical cylinders located at the free surface with $s = 4a$, and to the case where pontoons of width a join the bases of the truncated cylinders, both in infinite water depth. Unlike the floats considered in this thesis, Newman (2001) considered floats which were unable to oscillate. It was found that that by using truncated cylinders in infinite water depth the maximum second-order run-up (at the second-order near-trapping frequency) was reduced by about one third compared to that of the bottom-mounted surface piercing array of Malenica et al. (1999). At the linear near-trapping frequency however, there was very little difference between the two arrays as the first-order velocity field is above the bottoms of the truncated cylinders. The effects of the pontoon was also found to be significant at second-order, resulting in a reduction of only about a sixth compared to the bottom mounted case.

Oscillating Bodies

Very limited research has been published on second-order effects for moving bodies. A complex, isolated, moving body consisting of two concentric cylinders which move relative to each other like a piston forming a 'moon pool' (a separate inner fluid domain) between them has been analysed using a semi-analytical direct method (Mavrakos and Chatjigeorgiou, 2009b). The inclusion of a moon pool has been shown previously to result in extreme amplifications of the hydrodynamic loading due to resonances in the inner fluid domain. The second-order forces were found to have a significant effect at these resonant frequencies. First-order resonance frequencies were further determined to stimulate resonances on both horizontal and vertical forces at double the incident wave frequency.

4.3 Sea State Description

A wave energy device will be subject to a range of incident wave frequencies. As linear forces occur at the same frequency as the incident wave frequency, analysis of linear forces can be performed directly at the incident wave frequencies. Second-order forces however occur at the sum and difference frequencies of pairs of incident wave frequencies. In order to compare the magnitude of the second-order forces in relation to first-order forces at a specific frequency, the amplitudes of the component waves are needed. The likely amplitude of waves which occur at each of the incident wave frequencies can be determined using a wave spectrum.

Analysis of random sea waves can be performed by assuming they consist of an infinite number of waves which have different frequencies and directions. Spectra are formed by plotting the distribution of energy from these infinite number of waves against either frequency and direction (two-dimensional spectra) or just frequency (one-directional spectra). Several formulae have been developed based on real wave data to produce one-directional frequency spectra (Sarpkaya and Isaacson, 1981).

The Bretschneider spectrum is a well known spectrum which is dependent on both peak wave period, T_p, and significant wave height, H_s. The significant wave height is the mean wave height of the highest third of the wave heights, and the significant wave period is the period of the wave which has the greatest energy. The frequency which corresponds to the peak wave period is here termed ω_p such that $T_p = \frac{2\pi}{\omega_p}$. At wave frequency, ω, the Bretschneider spectrum is calculated (when including modifications) as (Goda, 2000, pg. 28)

$$\zeta(\omega) = 0.3223 H_s^2 \left(\frac{2\pi}{\omega_p}\right)^{-4} \left(\frac{\omega}{2\pi}\right)^{-5} e^{-1.2915\left(\frac{\omega}{\omega_p}\right)^{-4}}. \tag{4.2}$$

An increase in significant period leads to a shift in the peak spectral density towards the lower wave frequency and an increase in the value of the peak spectral density. An increase in significant wave height results in an increase in spectral density. There are many methods other than the Bretschneider spectrum to describe the distribution of energy density. For example; a widely used empirical function includes the Jonswap spectrum. The bandwidth of the spectral density, that is the range of frequencies over which the spectral density is large, is dependent on the choice of spectral definition (e.g Bretschneider or Jonswap), hence the corresponding frequency bandwidths of the forces at sum and difference frequencies is also dependent on this parameter.

Using Equation (4.2), the spectral density, $\zeta\left(\omega\right)$, can be plotted against frequency using a discrete range of wave frequencies. When the spectral density is calculated based on a range of frequencies whose increment is $\delta\omega$ the absolute amplitude of the waves can be determined as

$$\left|\hat{A}_m(\omega)\right| = \sqrt{2\zeta(\omega)\delta\omega}, \tag{4.3}$$

where $\delta\omega$ is the frequency increment. The absolute value of the wave amplitude at a specific wave frequency determined in this way is therefore dependent on the frequency increment of the range of frequencies from which the spectral density was calculated.

For this study, data from a hind-cast model is employed to select a mean H_s and maximum H_s for each value of T_p (Table 4.1). Each combination of H_s and T_p represents a different sea state. The data used for the analysis in this chapter is based on a hind-cast model for the combined time periods of January 1977 to December 1979 and January 1989 to December 1994 for the West Shetland Shelf (latitude 61.373°N, longitude 0.670°W) for which an average annual frequency distribution of significant wave height and spectral peak period is given (GEOS, 2001). Waves near the Shetlands are extremely energetic so these conditions are expected to be fully developed.

The steepness of the waves can be calculated as

$$\text{steepness} = \left\{ \frac{H}{L} \right\}. \tag{4.4}$$

Waves become unstable when the wave steepness approaches 0.147 (Woodroffe, 2002) such that linear theory would not be able to sufficiently model them. In order to analyse the suitability of linear theory for application to the sea states considered, the wave steepness is calculated for a wave which has $H = H_s$ and $L = L_p$ for each sea state where L_p is the wave length corresponding to the peak period, T_p. L_p is calculated as

$$L_p = \frac{2\pi}{k_p} \tag{4.5}$$

where k_p is the wave number corresponding to wave frequency ω_p. k_p is calculated using the dispersion equation (Equation (2.23)) with a depth of $d = 30$ m (as discussed in Section 1.2). The wave steepness for the waves with $H = H_s$ and $L = L_p$ do not exceed the limit of 0.142 in any of the 16 sea states considered. It is recognised, however, that some waves will exist in each sea state which have higher wave heights than the significant wave height. Even if each sea state includes waves with $H = 2H_s$, the steepness of these waves only exceeds the upper limit of 0.147 in one of the 16 sea states, where $T_p = 5.5$ seconds and H_s is maximum (12 m).

T_p/s	ω_p/rad/s	L_p/m	Mean H_s/m	Max H_s/m	$\left(\frac{\text{Mean } H_s}{L_p}\right)$	$\left(\frac{\text{Max } H_s}{L_p}\right)$
5.50	1.14	47.17	1.33	3.75	0.03	0.08
6.50	0.97	65.73	1.61	3.75	0.02	0.06
7.50	0.84	86.63	1.93	4.75	0.02	0.06
8.50	0.74	108.75	2.20	5.25	0.02	0.05
9.50	0.66	130.93	2.50	6.25	0.02	0.05
10.50	0.60	153.14	3.00	7.75	0.02	0.05
11.50	0.55	173.94	3.56	12.00	0.02	0.07
12.50	0.50	198.41	4.24	12.00	0.02	0.06

Table 4.1: Maximum and mean significant wave heights, H_s, as calculated using wave data for the West Shetland Shelf for the peak wave periods, T_p, specified; ω_p and L_p are the wave frequency and wave length (Equation (4.5)) respectively which correspond to the peak period; $\left(\frac{\text{Mean } H_s}{L_p}\right)$ and $\left(\frac{\text{Max } H_s}{L_p}\right)$ are the steepnesses of the waves with mean and maximum wave height respectively.

4.4 Calculating Dimensionalised Forces

WAMIT produces the complex amplitudes of the excitation forces which are non-dimensional and represented here by $\breve{F}^{[1]}$ for the first-order forces and $\breve{F}_{+}^{[2]}$ and $\breve{F}_{-}^{[2]}$ for the second-order forces at sum and difference frequencies respectively. The first-order forces can be dimensionalised to give $\hat{F}^{[1]}$ by multiplying by the water density, ρ, the gravitational acceleration, g, and the complex amplitude of the wave, $\hat{A}_m$ such that

$$\hat{F}^{[1]}\left(\omega, t\right) = \breve{F}^{[1]}\left(\omega\right) \rho g \hat{A}_m \left(\omega, t\right), \tag{4.6}$$

where the complex amplitudes of the waves are of the form

$$\hat{A}_m(\omega, t) = \left|\hat{A}_m(\omega)\right| e^{i(\omega t + \varphi_A)}, \tag{4.7}$$

where φ_A is the phase of the wave and $|\hat{A}_m(\omega)|$ its absolute amplitude. The second-order forces can be dimensionalised by multiplying by ρ, g, the complex amplitude of the first component wave and either the complex amplitude of the second component wave for sum frequencies or its complex conjugate (denoted by *) for difference frequencies such that

$$\hat{F}_+^{[2]}\left(\omega_1+\omega_2,t\right)=\breve{F}_+^{[1]}\left(\omega_1+\omega_2\right)\rho g\hat{A}_m\left(\omega_1\right)\hat{A}_m\left(\omega_2\right) \tag{4.8}$$

$$\text{and}\quad \hat{F}_-^{[2]}\left(\omega_1-\omega_2,t\right)=\breve{F}_-^{[1]}\left(\omega_1-\omega_2\right)\rho g\hat{A}_m\left(\omega_1\right)\hat{A}_m\left(\omega_2\right)^* \tag{4.9}$$

where, for difference frequencies, $\omega_1>\omega_2$.

Selecting the phase at random such that $0\le\varphi_A\le 2\pi$, the dimensionalised complex amplitudes of the excitation forces can be calculated for each frequency, ω, at a specific time, t, using Equations (4.6), (4.8) and (4.9). The summation of these forces across the frequency range then gives the excitation force at time t. Evaluation over $0\le t\le t_{max}$ yields a time series of the excitation force:

$$F_t^{[1]}(t)=\sum_{\omega=0}^{\omega_{max}}\hat{F}\left(\omega,t\right) \tag{4.10}$$

$$F_t^{[2]}(t)=\sum_{\min(\omega_i+\omega_j)}^{\max(\omega_i+\omega_j)}\hat{F}_+^{[2]}\left(\omega_i+\omega_j,t\right)+\sum_{\min(\omega_i-\omega_j)}^{\max(\omega_i-\omega_j)}\hat{F}_-^{[2]}\left(\omega_i-\omega_j,t\right). \tag{4.11}$$

A time series can be transformed back into the frequency domain using an FFT (Fast Fourier Transform). The FFT is applied using Welch's averaged modified periodogram method of spectral estimation, applied through the 'Pwelch' function in MATLAB. Welch's averaged modified periodogram method applies windows to the time domain. The windows work as smoothing functions which weight the frequencies so that peak in the middle of the window and decrease to zero at the edges. This reduces the effects of any discontinuities which result from using a finite time signal. The discontinuities are known as spectral leakage which primarily result from the finite length of the time signal containing fractions of periods.

This results in the calculation of the spectral density of the first- and second-order forces ($\zeta_F^{[1]}$ and $\zeta_F^{[2]}$ respectively). The amplitudes of the dimensional second-order forces are then obtained in the frequency domain from these force spectral densities using the following equations:

$$\left|F^{[1]}(\omega)\right| = \sqrt{2\zeta_F^{[1]}(\omega)\delta\omega} \tag{4.12}$$

$$\left|F^{[2]}(\omega)\right| = \sqrt{2\zeta_F^{[2]}(\omega)\delta\omega}. \tag{4.13}$$

The resolution of the resultant spectrum is therefore dependent on the frequency increment $\delta\omega$ in Equations (4.12) and (4.13). It is however independent of $\delta\omega$ in Equation (4.3) allowing for a convergence in this parameter (section 4.5).

The process (Figure 4.1) of calculating the dimensional force spectrum from the non-dimensional WAMIT forces and wave spectrum becomes

$$F(\omega, t) \rightarrow F(t) \rightarrow \zeta_F(\omega) \rightarrow F(\omega) \tag{4.14}$$

for $\omega \in 0 : \delta\omega : \omega_{max}$ and $t \in 0 : \delta t : t_{max}$.

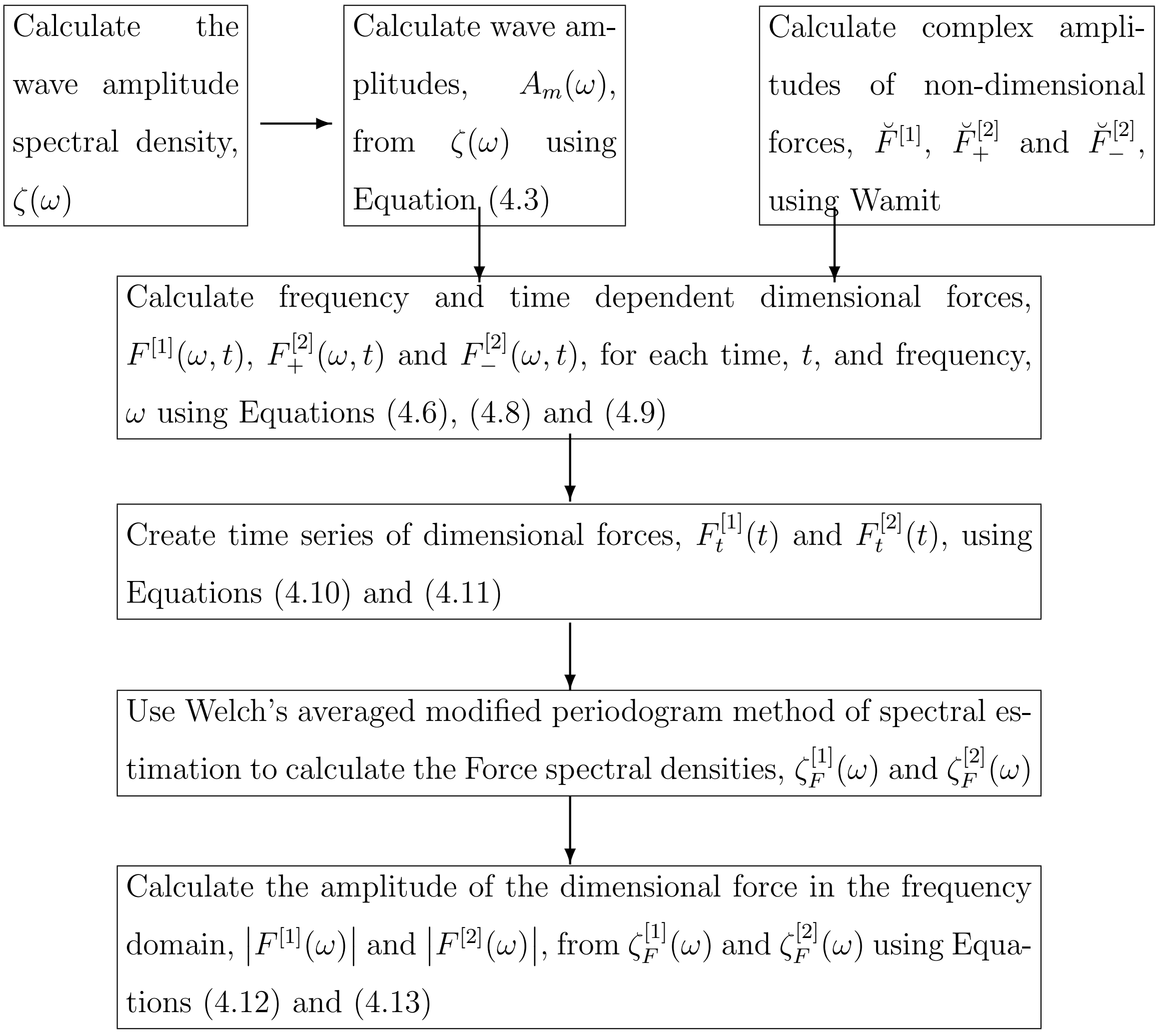

Figure 4.1: Flow chart showing process used to obtain dimensional excitation force amplitudes in the frequency domain

4.5 Interpolation

As the calculation of second-order forces using WAMIT is computationally demanding, the frequency range for which the non-dimensional forces are determined in WAMIT is fairly coarse. For improved accuracy, it is desirable to use interpolated non-dimensional forces to determine the dimensional forces. This section provides a convergence study on the frequency increment to which the non-dimensional forces are interpolated. it is necessary for the dimensional force amplitudes determined from the interpolated non-dimensional forces to be independent of the choice of this frequency increment for the first-order forces and converge for decreasing magnitude of this frequency increment for the second-order forces.

Prior to interpolation, the non-dimensional force data is given in the frequency range $0.2 \leq \omega \leq 2.8$ rad/s with a frequency increment of 0.2 rad/sec (written 0.2 : 0.2 : 2.8 rad/s). The non-dimensional forces are interpolated to obtain data within the same frequency range at finer frequency increments of $\delta\omega_{int} = 0.05, 0.01$ rad/sec such that the interpolated frequency range is $0.2 : \delta\omega_{int} : 2.8$ rad/s. The interpolation of the non-dimensional forces is performed using a one-dimensional cubic interpolation for the first-order forces and a two dimensional cubic interpolation for the second-order forces since they are functions of one and two frequencies respectively (see Figures 4.2 and 4.3).

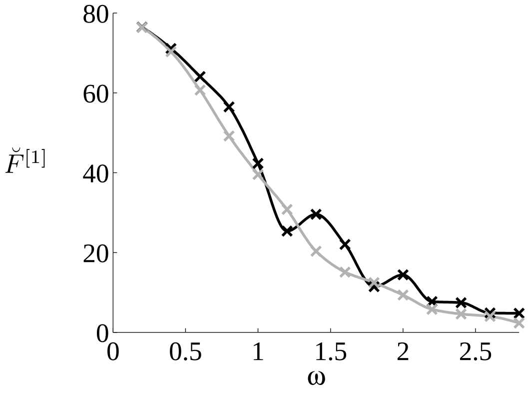

Figure 4.2: First-order non-dimensional wave forces, $\breve{F}^{[1]}$, on a 2×1 array of hemispherical floats in head seas; The component waves are in the range $0.2 \leq \omega \leq 2.8$ rad/s with the original data given at frequency increments of 0.2 rad/sec (crosses) and the (cubic) interpolated data given at increments of 0.01 rad/sec (solid lines);
KEY:
Black, Front float (float 1); Grey, Back float (float 2)

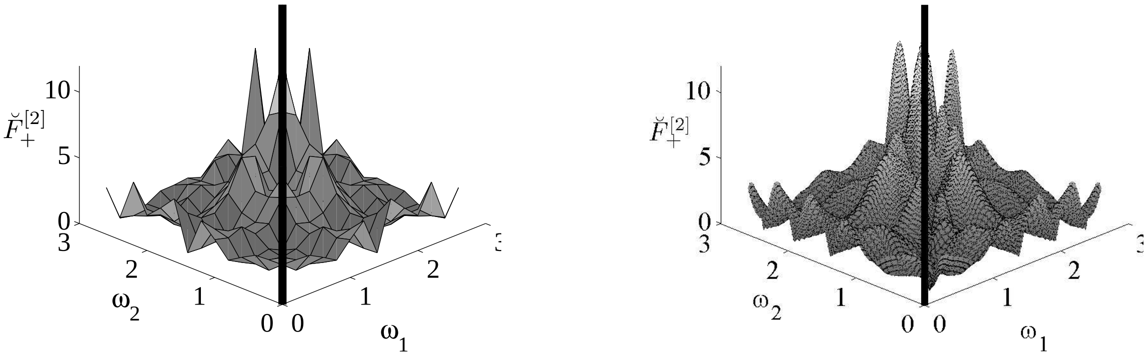

(a) $\breve{F}_+^{[2]}$ at original component frequencies (b) $\breve{F}_+^{[2]}$ at interpolated component frequencies

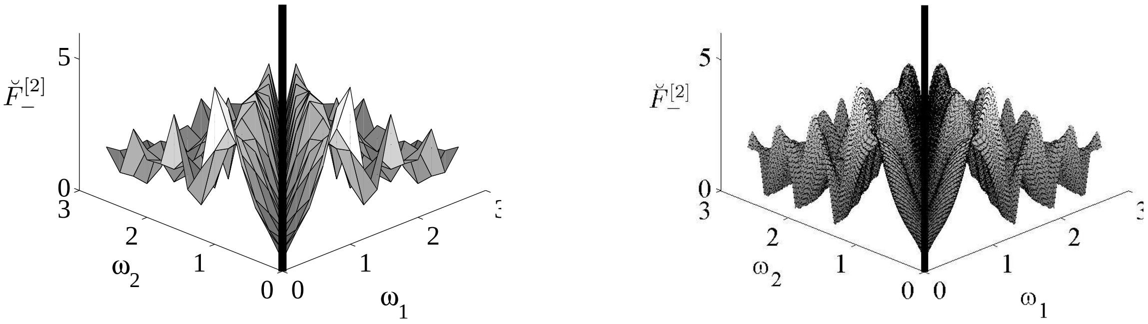

(c) $\breve{F}_-^{[2]}$ at original component frequencies (d) $\breve{F}_-^{[2]}$ at interpolated component frequencies

Figure 4.3: Second-order non-dimensional wave forces, $\breve{F}_+^{[2]}$ and $\breve{F}_-^{[2]}$, at the sum and difference frequencies respectively of the component waves ω_1 and ω_2 on a 2×1 array of hemispherical floats in head seas; The component waves are in the range $0.2 \leq \omega \leq 2.8$ rad/s with the original data given at frequency increments of 0.2 rad/sec and the (cubic) interpolated data given at increments of 0.01 rad/sec; Solid vertical lines represent $\omega_1 = \omega_2$

A significant period of $T_s = 6.14$ seconds and a significant wave height of $H_s = 3.75$ m is used in Equation (4.2) to form the wave amplitude frequency spectrum (Figure 4.4a). The absolute amplitude of the waves is calculated from the spectral density (see Figure 4.4b) using Equation (4.3) with $\delta\omega = \delta\omega_{int}$ such that

$$\left|\hat{A}_m(\omega)\right| = \sqrt{2\zeta(\omega)\delta\omega_{int}}. \tag{4.15}$$

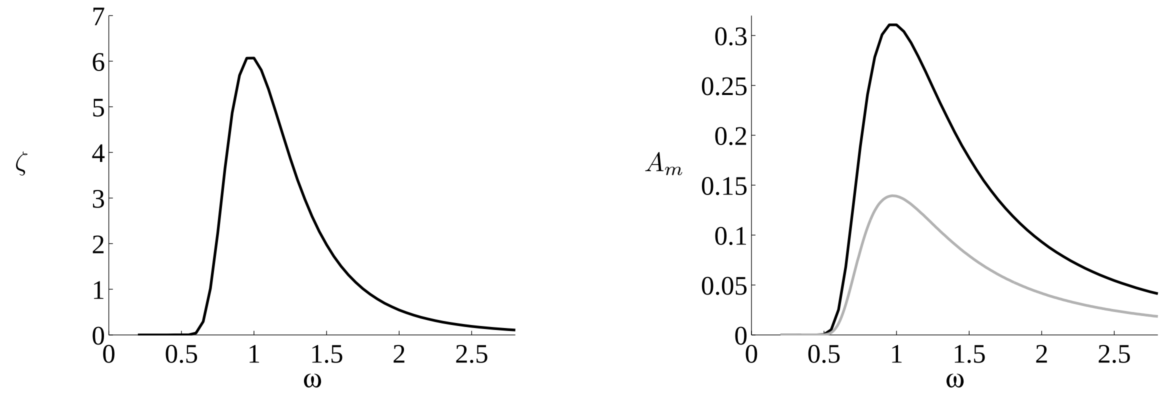

(a) Spectral density of wave amplitude

(b) Wave amplitude calculated with

KEY Black, $\delta\omega = \delta\omega_{int} = 0.05$ rad/sec;

Grey, $\delta\omega = \delta\omega_{int} = 0.01$ rad/sec

Figure 4.4: The spectral density, ζ, of the wave amplitudes as calculated using the Bretschneider spectrum with a significant period of $T_s = 6.14$ seconds; and a significant wave height of $H_s = 3.75$ m and the corresponding wave amplitudes, $|A_m|$, on float 2 calculated from the spectral density using Equation (4.3) with frequency increment $\delta\omega = \delta\omega_{int} = 0.05$ and 0.01 rad/sec

Using the process discussed in Section 4.4, the spectral densities, $\zeta_F^{[1]}$ and $\zeta_F^{[2]}$, of the forces are determined. The amplitudes of the forces which can be obtained from these force spectral densities is dependent on the frequency increment used within Equations (4.12) and (4.13). In order to compare the forces obtained using different values of $\delta\omega_{int}$, the $\delta\omega$ in Equations (4.12) and (4.13) must be constant and independent of $\delta\omega_{int}$. This constant value is $\delta\omega_F = 0.05$ rad/s such that

$$\left|F^{[1]}(\omega)\right| = \sqrt{2\zeta_F^{[1]}(\omega)\delta\omega_F} \tag{4.16}$$

$$\text{and} \quad \left|F^{[2]}(\omega)\right| = \sqrt{2\zeta_F^{[2]}(\omega)\delta\omega_F}. \tag{4.17}$$

The terms $\zeta_F^{[1]}(\omega)\delta\omega_F$ and $\zeta_F^{[2]}(\omega)\delta\omega_F$ in Equations (4.16) and (4.17) are achieved using trapezoidal numerical integration of the spectral densities over frequency regions of size $\delta\omega_F$. The force spectral density must therefore be divided into discrete sections, or bins, of size $\delta\omega_F$.

The force spectral density is however created from the time series, which is created from data at frequency increments of $\delta\omega_{int}$. The force spectral density therefore already contains frequency bins of width $\delta\omega_{int}$ centred on each of the frequencies in the range $0.2 : \delta\omega_{int} : 2.8$ rad/s (Figures 4.5a and 4.5b). These bins of width $\delta\omega_{int}$ must not be divided when creating the bins of width $\delta\omega_F$.

Where the desired frequency is ω, the corresponding bin of size $\delta\omega_F$ must therefore be specified such that it contains frequencies ω_j in the range

$$\omega_{l1} \leq \omega_j \leq \omega_{l2}, \tag{4.18}$$

where the limit frequencies are given by

$$\omega_{l1} = (\omega - 0.5\delta\omega_F - 0.5\delta\omega_{int}) \tag{4.19}$$

$$\text{and} \quad \omega_{l2} = (\omega + 0.5\delta\omega_F - 0.5\delta\omega_{int}). \tag{4.20}$$

In this way (Figure 4.5d) the original (pre-FFT) bins of size $\delta\omega_{int}$ are not subdivided (as they are in Figure 4.5c), and the final bins are of size $\delta\omega_F$ regardless of the magnitude of $\delta\omega_{int}$. This allows the spectral densities formed using input data of different frequency increments to be directly compared to each other. The horizontal centre of each such bin of width $\delta\omega_F$ is then used as the output frequency, ω_b, such that

$$\omega_b = \omega - 0.5\delta\omega_{int} \tag{4.21}$$

which is close to, but not equal to the desired frequency, ω. The amplitudes of the dimensionalised forces are therefore given by

$$\left|F^{[1]}(\omega_b)\right| = \sqrt{2\int_{\omega_1}^{\omega_2} \zeta_F^{[1]}(\omega)\mathrm{d}\omega} \tag{4.22}$$

$$\text{and} \quad \left|F^{[2]}(\omega_b)\right| = \sqrt{2\int_{\omega_1}^{\omega_2} \zeta_F^{[2]}(\omega)\mathrm{d}\omega} \tag{4.23}$$

where the integral is performed using the trapezoidal rule (as described in Appendix E).

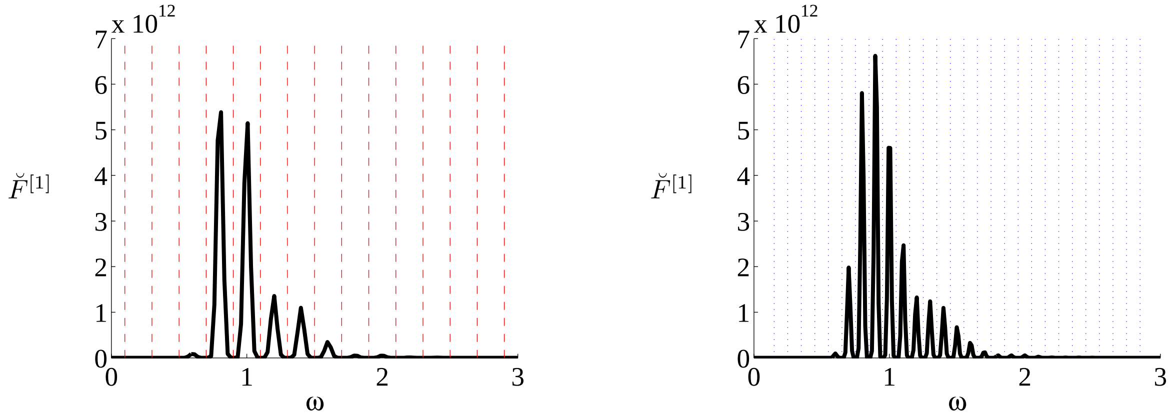

(a) $\zeta_F^{[1]}$ with pre-FFT frequency increment, $\delta\omega_{int} = 0.2$ rad/sec; Vertical lines represent limits of bins of width $\delta\omega_{int}$ centred on frequencies $0.2 : \delta\omega_{int} : 2.8$ rad/sec

(b) $\zeta_F^{[1]}$ with pre-FFT frequency increment, $\delta\omega_{int} = 0.1$ rad/sec; Vertical lines represent limits of bins of width $\delta\omega_{int}$ centred on frequencies $0.2 : \delta\omega_{int} : 2.8$ rad/sec

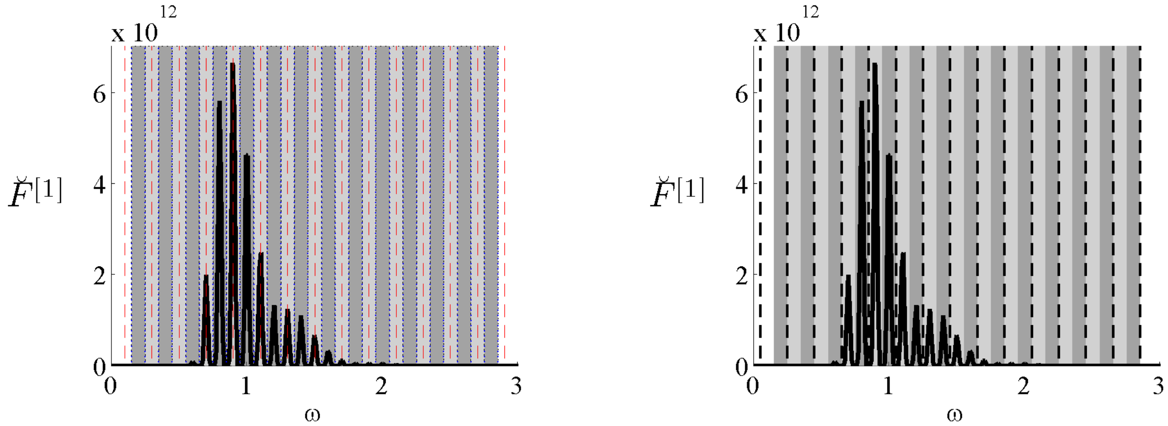

(c) $\zeta_F^{[1]}$ with pre-FFT frequency increment, $\delta\omega_{int} = 0.1$ rad/sec; Dotted vertical lines represent limits of bins (shown in alternate shades of grey) of width $\delta\omega_{int}$ centred on frequencies $0.2 : \delta\omega_{int} : 2.8$ rad/sec; Dashed vertical lines represent limits of bins of width $\delta\omega_F = 0.2$ rad/sec centred on frequencies $0.2 : \delta\omega_F : 2.8$ rad/sec

(d) $\zeta_F^{[1]}$ with pre-FFT frequency increment, $\delta\omega_{int} = 0.1$ rad/sec; Bins coloured in n alternate shades of grey are of width $\delta\omega_{int}$ centred on frequencies $0.2 : \delta\omega_{int} : 2.8$ rad/sec; Dashed vertical lines represent limits of bins of width $\delta\omega_F = 0.2$ rad/sec centred on frequencies given by Equation (4.21)

Figure 4.5: First-order force spectral density on a 2×1 array of hemispherical floats in head seas produced using Welch's averaged modified periodogram method of spectral estimation on time series. The frequency increment of the data used to form the time series is $\delta\omega_{int}$ and the frequency increment which is used to obtain the Force Amplitudes from these force spectral densities is $\delta\omega_F$

The linear dimensional forces determined in this manner are shown in Figure 4.6b. For comparison, Figure 4.6a also shows the first-order forces calculated using Equation (4.22) with $\delta\omega_F = \delta\omega_{int} = 0.05, 0.01$ rad/sec. It is clear from Figure 4.6 that the magnitude of the final dimensionalised excitation force is dependent on $\delta\omega_F$ and not on $\delta\omega_{int}$. The second-order force (Figure 4.7) converges with decreasing frequency increment as required.

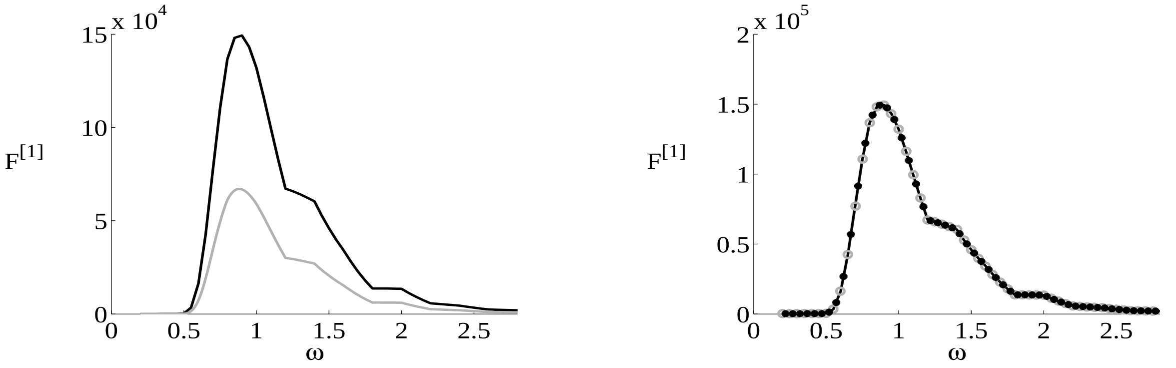

(a) Grey, $\delta\omega_{int} = \delta\omega_F = 0.05$ rad/s;
Black, $\delta\omega_{int} = \delta\omega_F = 0.01$ rad/s

(b) Solid line, $\delta\omega_{int} = \delta\omega_F = 0.2$ rad/s (original WAMIT results without interpolation);
Grey o markers, $\delta\omega_{int} = 0.05$ rad/s and $\delta\omega_F = 0.05$ rad/s;
Black * markers, $\delta\omega_{int} = 0.01$ rad/s and $\delta\omega_F = 0.05$ rad/s

Figure 4.6: First-order interpolated excitation force on front float of 2 × 1 array of hemispherical floats, dimensionalised using amplitudes as given from Bretschneider spectrum with significant period $T_s = 6.14$ seconds and significant wave height $H_s = 3.75$ m; The WAMIT data is interpolated so that it is defined at frequency intervals of $\delta\omega_{int}$, transformed to a spectral density in the frequency domain using an FFT, then evaluated at frequency intervals of $\delta\omega_F$

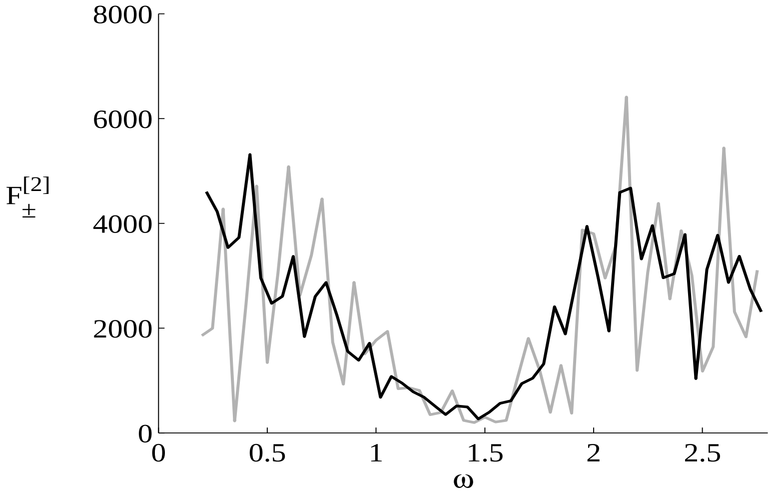

Figure 4.7: Second-order excitation force on front float of 2 × 1 array of hemispherical floats calculated at both sum and difference frequencies; The WAMIT data is interpolated so that it is defined at frequency intervals of $\delta\omega_{int}$, transformed to a spectral density in the frequency domain using an FFT, then evaluated at frequency intervals of $\delta\omega_F$
KEY:
Grey, $\delta\omega_{int} = 0.05$, rad/s $\delta\omega_F = 0.05$ rad/s;
Black, $\delta\omega_{int} = 0.01$, rad/s $\delta\omega_F = 0.05$ rad/s

The smallest increment of $\delta\omega_{int} = 0.01$ is used to perform the second-order analysis from herein as this results in the smoothest variation with frequency. The final increment from herein is small ($\delta\omega_F = 0.01$) so as to achieve the greatest level of accuracy.

4.6 Variation of Forces with H_s and T_p

Interpolated forces are used in this section using WAMIT data with frequency increments of 0.2 rad/sec in the range $0.2 \leq \omega \leq 2.8$ rad/sec, and a frequency increment of $\delta\omega_{int} = \delta\omega_F = 0.01$ rad/sec for the interpolated forces (see Section 4.5). A range of different sea-states based on the Bretschneider spectrum (Equation (4.2)) are used to determine the spectral density of the wave amplitudes by which the forces are dimensionalised. Sea-states are defined with peak wave periods, T_p, in the range 5.5 - 12.5 seconds. For each peak period two significant wave heights, H_s, are considered based on the mean and maximum heights that are predicted to occur for each period (see 4.3).

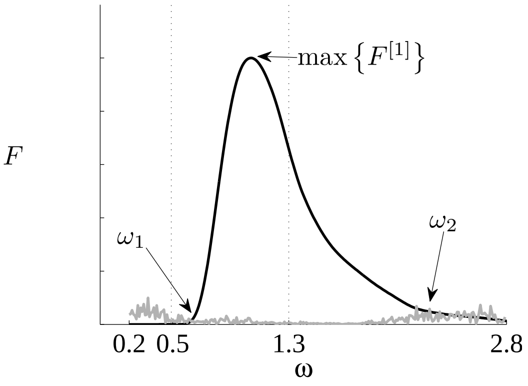

Figure 4.8: Indicative graph showing variation with wave frequency of first-order forces (solid black line) and second-order forces (solid grey line) as dimensionalised using the Bretschneider spectrum with frequencies in the range $0.2 \leq \omega \leq 2.8$ rad/sec for the back float (float 2) of a 2×1 array of hemispherical floats in head seas; vertical dotted lines are shown to indicate the frequency range of interest to closely spaced arrays ($0.5 \leq \omega \leq 1.3$ rad/sec); also shown are the maximum first-order force $\left(\max\left\{F^{[1]}\right\}\right)$ and the frequencies ω_1 and ω_2 where $F^{[2]} > F^{[1]}$ for $\omega \leq \omega_1 < \omega_p$ and $\omega_p \leq \omega_2 < \omega$ (where $\omega_p = \frac{2\pi}{T_p}$)

The general trend of the first- and second-order dimensionalised forces is shown in Figure 4.8. The first-order force forms a curve with a peak at a wave frequency slightly less than the frequency corresponding to the peak wave period. This frequency difference occurs since the non-dimensional force increases with decreasing wave frequency. There is negligible energy content for frequencies that are less than $\frac{\omega_p}{2}$ or greater than $3\omega_p$ and hence first-order forces are also negligible over these ranges. The second-order forces occur at the sum and difference frequencies of component waves. The difference frequencies are therefore predominantly less than the peak frequency and the sum frequencies greater than the peak frequency. Second-order forces are most significant where the amplitudes of both component waves are large. This occurs when both component wave frequencies are close to ω_p, hence their sum is large and their difference is small. Second-order forces are therefore of small magnitude close to the peak frequency.

The frequency range over which the second-order force is greater than the first-order force is identified as $\omega_1 < \omega < \omega_2$ (see Figure 4.8). The values of ω_1 and ω_2 are listed in Table 4.2 for all 16 of the sea states considered. The purpose of this chapter is to determine whether second-order forces need to be considered when analysing closely spaced arrays. The ratio of second to first-order forces in the likely operational frequency range for closely spaced arrays of wave energy devices is therefore of most importance. The maximum ratio of second-order forces to first-order forces within the restricted frequency range of $0.5 \leq \omega \leq 1.3$ rad/sec (Section 1.2) is therefore shown in Table 4.2. The frequency at which this maximum ratio occurs is called ω_m. Only frequencies for which the first-order forces are at least 1 % of the maximum first-order force are considered within this range. This restriction eliminates excessively large ratios of second to first-order forces at frequencies at which the first-order force is close to zero. In particular, this restriction is applicable to low wave frequencies where the peak period is low.

T_p/s	ω_p rad/s	H_s/m	ω_1	ω_2	ω_m	$\frac{F^{[2]}(\omega_m)}{F^{[1]}(\omega_m)}$
5.5	1.1424	1.33	0.62	-	0.64	0.52
6.5	0.9666	1.61	0.52	2.52	0.54	0.97
7.5	0.8378	1.93	0.45	2.21	0.52	0.13
8.5	0.7392	2.2	0.4	2.14	0.53	0.03
9.5	0.6614	2.5	0.36	2	1.3	0.05
10.5	0.5984	3	0.32	1.95	1.25	0.08
11.5	0.5464	3.56	0.3	1.93	1.25	0.19
12.5	0.5027	4.24	0.27	1.75	1.18	0.21

(a) Mean H_s, as calculated using wave data for the West Shetland Shelf for the peak periods, T_p

T_p/s	ω_p rad/s	H_s/m	ω_1	ω_2	ω_m	$\frac{F^{[2]}(\omega_m)}{F^{[1]}(\omega_m)}$
5.5	1.1424	3.75	0.66	2.36	0.63	3.54
6.5	0.9666	3.75	0.55	2.1	0.53	1.39
7.5	0.8378	4.75	0.47	2.05	0.51	0.48
8.5	0.7392	5.25	0.42	1.83	0.5	0.07
9.5	0.6614	6.25	0.37	1.77	1.27	0.13
10.5	0.5984	7.75	0.33	1.64	1.3	0.26
11.5	0.5464	12	0.31	1.43	1.3	0.46
12.5	0.5027	12	0.28	1.36	1.26	0.53

(b) Maximum H_s, as calculated using wave data for the West Shetland Shelf for the peak periods, T_s

Table 4.2: Comparison of second-order to first-order excitation forces for a 2×1 array of hemispherical floats of radius $a = 5$ m with separation $s = 4a$ in head seas with wave spectra calculated using the Bretschneider spectrum with peak period, T_p, (with corresponding peak frequency ω_p) and significant wave height, H_s with waves in the range $0.2 \leq \omega \leq 2.8$ rad/sec; ω_1 and ω_2 are the limit frequencies (in rad/sec) such that $F^{[2]} > F^{[1]}$ for $\omega \leq \omega_1 < \omega_p$ and $\omega_p \leq \omega_2 < \omega$; ω_m is the frequency at which $\max\{F^{[2]}(\omega)/F^{[1]}(\omega)\}$ occurs within the restricted frequency range $0.5 \leq \omega \leq 1.3$ rad/sec (with the restriction $\frac{F^{[1]}(\omega)}{\max(F^{[1]})} > 0.01$)

When T_p is large, the largest component amplitudes occur at low wave frequencies, hence significant second-order forces are experienced at sum frequencies which are low enough to be in the upper end of the operational range for closely spaced wave energy devices. The ratio of second to first-order forces can be significant at these higher frequencies since the peak in the first-order wave force occurs at much lower wave frequencies for high T_p values (Figures 4.9c, 4.9d, 4.10c and 4.10d). It is only when the peak period is small (Figures 4.9a and 4.10a), that large magnitudes of second-order forces occur at difference frequencies which are large enough to be within the range of interest. When the peak period occurs such that the peak in the first-order force is located in the middle of the frequency range of interest to closely spaced arrays, the second-order forces are not significant in the same range (Figures 4.9b and 4.10b).

An increase in significant wave height causes an increase in the spectral density of the component wave amplitudes. As the second-order forces are due to two component waves but the first-order forces are a result of only one wave, this increase in spectral density causes a more significant increase in the amplitudes of the second-order forces than the first-order forces (Figure 4.9d and 4.10d).

For all sea states considered, the magnitude of the second order forces is small at all wave frequencies when compared to the magnitude of the first order force at the peak frequency. For the sea state with $T_p = 12.5$ seconds, $\omega_p = 0.74$ rad/sec and maximum H_s ($H_s = 12$ m) for example (Figure 4.9b), the maximum second order force occurs at $\omega = 2.18$ rad/sec on both floats and is 5 and 6 % of the maximum first order force (which occurs just lower than the peak frequency at $\omega = 0.69$ rad/sec) on the first and second order floats respectively.

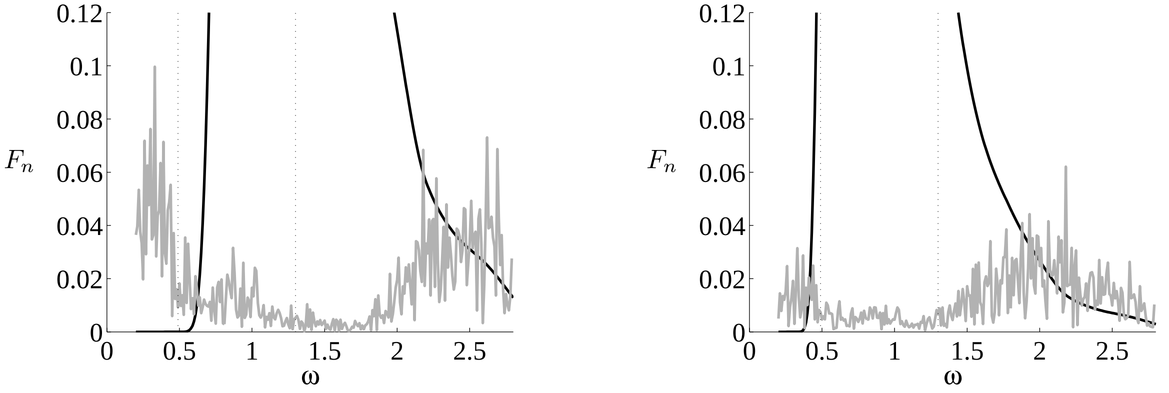

(a) $T_p = 5.5$ seconds, $H_s =$ maximum

(b) $T_p = 8.5$ seconds, $H_s =$ maximum

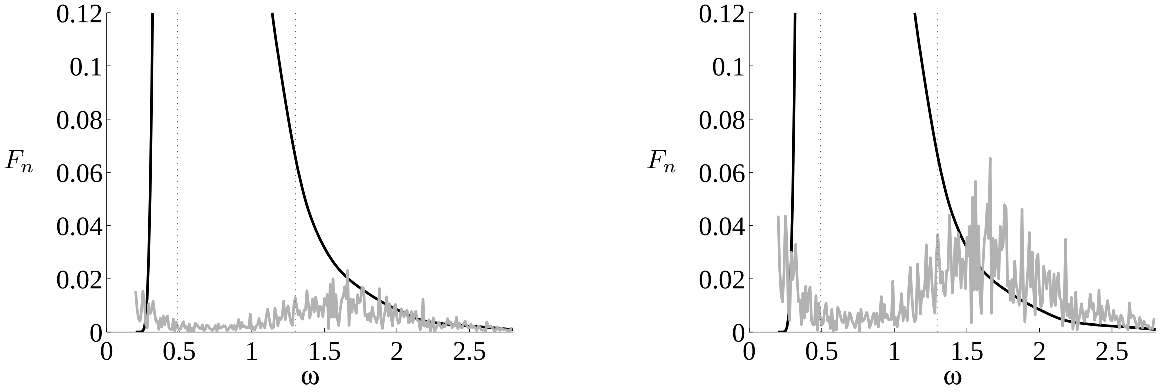

(c) $T_p = 12.5$ seconds, $H_s =$ mean

(d) $T_p = 12.5$ seconds, $H_s =$ maximum

Figure 4.9: First- and second-order wave forces on the front float of a 2×1 array of hemispherical floats in head seas. All forces are normalised by a fixed value which is the maximum first-order force amplitude on an isolated hemispherical float, dimensionalised using wave amplitudes as calculated using the Bretschneider spectrum (Equation (4.2)) with significant wave period $T_s = 0.95T_p$ and significant wave height, H_s
KEY:
Black, First-order; Grey, Second Order

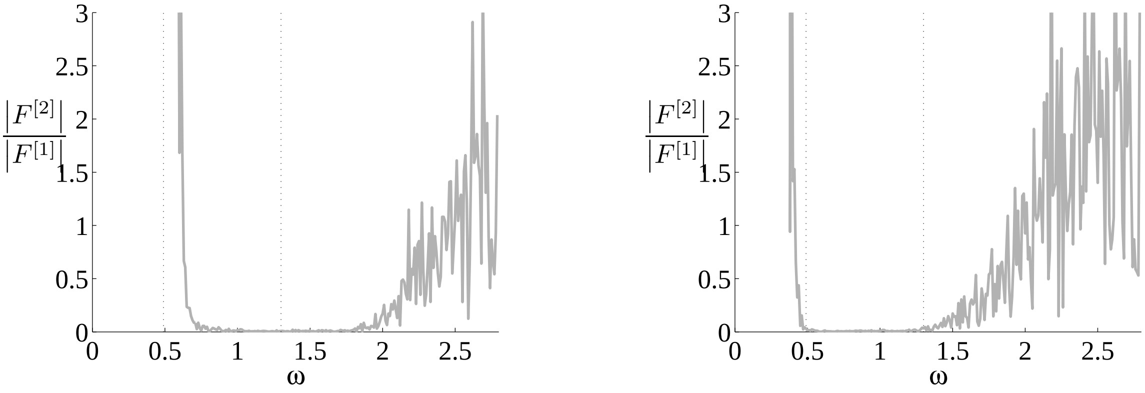

(a) T_p = 5.5 seconds, H_s = maximum

(b) T_p = 8.5 seconds, H_s = maximum

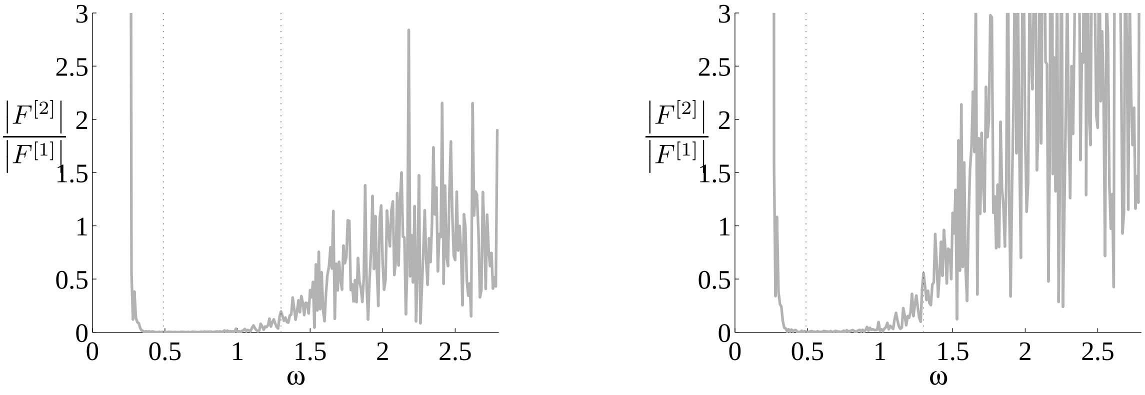

(c) T_p = 12.5 seconds, H_s = mean

(d) T_p = 12.5 seconds, H_s = maximum

Figure 4.10: Ratio between second and first-order wave forces on the back float of a 2×1 array of hemispherical floats in head seas dimensionalised using wave amplitudes as calculated using the Bretschneider spectrum (Equation (4.2)) with significant wave period $T_s = 0.95Tp$ and significant wave height, H_s

A strong correlation is present between the frequency ranges for which the second-order forces are at least 10 % of the first-order forces, the significant wave height and the significant wave period. Let $\omega_i \leq \omega \leq \omega_j$ represent the wave periods for which the second-order forces are more than 10 % of the first-order forces, and $\omega < \omega_i$ and $\omega > \omega_j$ the ranges where the second-order forces are at least 10 % of the first-order forces. Implementing a least square best fit to H_s and T_p simultaneously results in the following quadratic equations for the position of the limit frequencies for the sixteen spectra considered:

$$\omega_i = a_i + b_i T_p + c_i T_p^2 + d_i H_s + e_i T_p H_s + f_i H_s^2 \tag{4.24}$$

where

$$\begin{aligned} a_i &= 1.63, \\ b_i &= -2.26 \times 10^{-1}, \\ c_i &= 9.86 \times 10^{-3}, \\ d_i &= 4.48 \times 10^{-2}, \\ e_i &= -4.45 \times 10^{-3}, \\ \text{and} \quad f_i &= 6.49 \times 10^{-4} \end{aligned}$$

and

$$\omega_j = a_j + b_j T_p + c_j T_p^2 + d_j H_s + e_j T_p H_s + f_j H_s^2 \tag{4.25}$$

where

$$\begin{aligned} a_j &= 3.57, \\ b_j &= -3.15 \times 10^{-1}, \\ c_j &= 1.08 \times 10^{-2}, \\ d_j &= -8.59 \times 10^{-2}, \\ e_j &= 3.50 \times 10^{-3}, \\ \text{and} \quad f_j &= 1.59 \times 10^{-3}. \end{aligned}$$

The ω_i and ω_j limit frequencies for all sixteen sea-states are shown in Figure 4.11. For each significant wave period, an increase in significant wave height represents an increase in ω_i and a decrease in ω_j. Equations (4.24) and (4.25) are used to form lines of best fit which are also shown in figure 4.11.

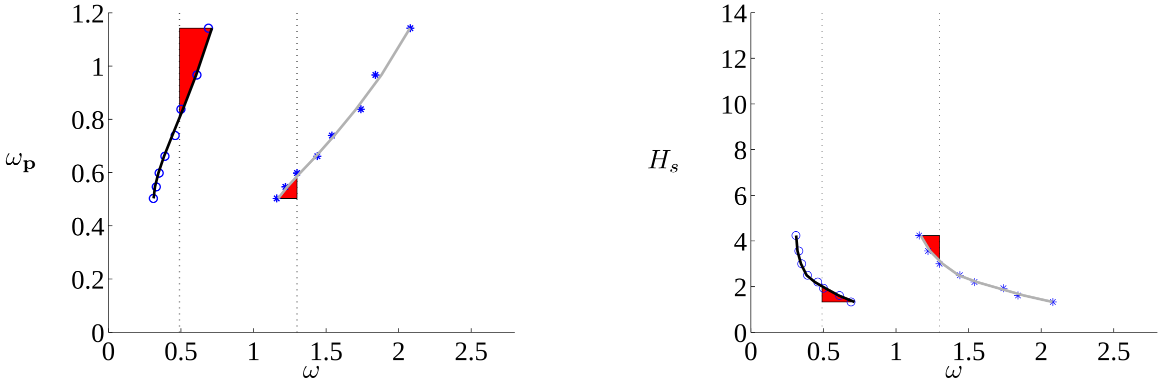

(a) Variation of ω_i and ω_j with peak frequency when H_s = mean (see Table 4.1)

(b) Variation of ω_i and ω_j with Significant wave height when H_s = mean(see Table 4.1)

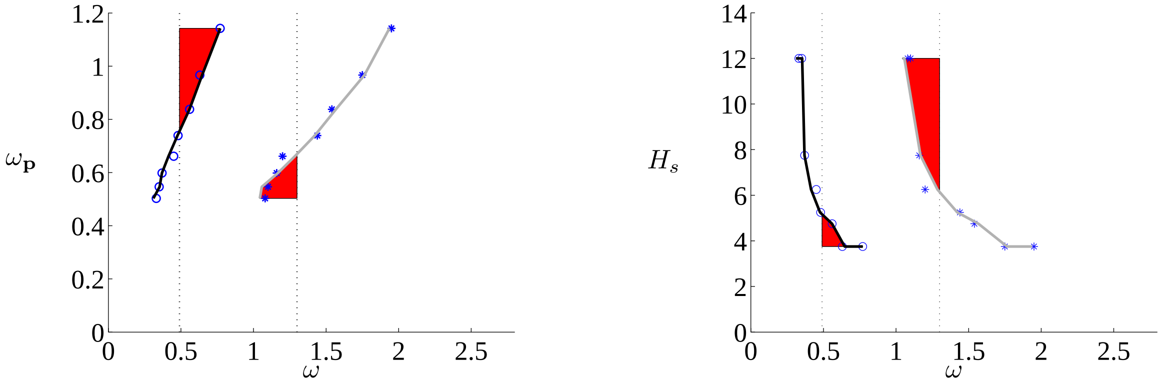

(c) Variation of ω_i and ω_j with peak frequency when H_s = maximum (see Table 4.1)

(d) Variation of ω_i and ω_j with Significant wave height when H_s = maximum (see Table 4.1)

Figure 4.11: Limits, ω_i and ω_j, of the wave frequency ranges ($0.2 \leq \omega \leq \omega_i$ rad/sec and $\omega_j \leq \omega \leq 2.8$ rad/sec) over which the second-order forces are at least 10% of the first-order forces on at least one float of a 2×1 array of hemispherical floats in head seas
KEY:
circle markers (o), ω_i; star markers (*), ω_j;
Solid lines, quadratic line of best fit as given by Equations (4.24) and (4.25);
Vertical dotted lines indicate operational frequency range for closely spaced arrays ($0.5 \leq \omega \leq 1.3$ rad/sec);
Shaded sections indicate regions where second-order forces are at least 10 % of first-order forces within the likely operational frequency range for closely spaced wave energy devices

It is found that second-order wave forces are insignificant within a frequency range, but are greater than or equal to 10 % of the first-order forces at frequencies above and below this range. When the peak frequencies are large ($\omega_p \geq 0.8378$ rad/sec, $T_p \leq 7.5$ seconds) second-order forces are significant (≥ 10 % of first-order) in the lower frequencies. When the peak frequency is small ($\omega_p \leq 0.5464$ rad/sec, $T_p \geq 11.5$ seconds), second-order forces are significant (≥ 10 % of first-order) in the higher frequencies. An increase in significant wave height increases the ratio of second to first-order forces such that this upper limit is reduced to $\omega_p \leq 0.6614$ rad/sec ($T_p \geq 9.5$ s).

The natural frequency of a neutrally buoyant hemispherical float with a 5 m radius is 1.44 rad/sec ($T = 4.36$ s). In sea states with peak periods greater than 9.4 seconds and significant wave heights greater than 2.47 m, or sea states with peak periods greater than 8.4 seconds and significant wave heights greater than 5.2 m, second-order forces would be at least 10 % of the magnitude of the first-order forces at the natural frequency. Since this natural frequency is higher than the range of wave conditions that are expected at wave energy sites, systems with larger mass are of interest. The system considered in Chapters 3 and 5 comprises a float with mass equal to double the displaced mass. The natural frequency is 1.08 rad/sec ($T = 5.82$ s), which is within the likely operational frequency range for closely spaced arrays. For this system, second-order forces would be greater than 10% of first-order forces at the natural frequency in sea states for which the peak period is greater than 11.3 seconds and the significant wave height is greater than 11.3 m.

4.7 Chapter Conclusion

The magnitude of second-order sum- and difference-frequency forces on a heaving float have been evaluated for a range of sea-states that are representative of a wave energy site. First- and second-order forces are compared on a 2×1 array of hemispherical floats in head seas. Non-dimensional forces are calculated using the wave analysis program, WAMIT, which are then dimensionalised using wave amplitudes calculated using the Bretschneider spectrum. To minimise computational cost, non-dimensional second-order forces are calculated at coarse frequency increments and bi-cubic interpolation employed to obtain values at finer increments. A convergence study is performed for a single spectrum, showing the effect of this process on the resultant spectrum of total force. Based on this study, interpolated first- and second-order non-dimensional forces are dimensionalised using wave amplitudes calculated for sixteen different sea-states. Each spectrum is defined according to the empirical Bretschneider function. Peak periods and significant wave heights are selected based on a hind-cast model of the sea-states occurring at a representative site. Both mean and maximum significant wave heights are considered for each wave period.

It is found that second-order wave forces are insignificant within a large frequency range, but are greater than or equal to 10 % of the first-order forces at frequencies above and below this range. Quadratic equations for the limit frequencies of the frequency range over which second-order effects are less than 10 % of the first-order forces are presented in terms of the significant wave height and the peak period. The operational frequency range for closely spaced wave energy devices is limited. It is therefore only when the peak period is either small or large that second-order effects are significant ($\geq$ 10 % of first-order) in the frequency range of interest for closely spaced arrays. When the peak period is $\leq$ 7.5 seconds, second-order forces are significant in the lower frequencies, and when the peak period is $\geq$ 11.5 seconds (or $\geq$ 9.5 seconds when the significant wave height is large), second-order forces are significant in the higher frequencies within the likely operational frequency range for closely spaced arrays.

Chapter 5

Optimisation of Fixed Geometry Arrays

A numerical model in which the fluid is modelled using linear wave theory and the wave energy devices are modelled as driven harmonic oscillators has been defined in Chapter 2. The suitability of this model for predicting the response amplitude of shallow draft floats arranged at close spacing was evaluated in Chapters 3 and 4. The experimental comparison of Chapter 3 suggests the model provides a reasonable prediction of response providing that response amplitudes are small. The second-order force analysis of Chapter 4 suggests that, although second-order forcing does exist in the frequency range of interest, it is small enough to exclude from the model without loss of accuracy.

In this chapter the numerical model is used in order to determine appropriate values for parameters that can feasibly be adjusted to modify the response of devices within closely spaced arrays. The arrays considered are of fixed geometry and layout for all wave frequencies considered and the objective is to select mechanical parameters such that net power output from the array of devices is maximised.

5.1 Introduction

For an isolated device the time-averaged power output, P_0, (where the suffix, 0, indicates an isolated device), can be written using Equation (2.53) in which the velocity is given by Equation (2.36) such that

$$P_0 = \frac{1}{2}R\left\|\frac{F(\omega)}{(R+B(\omega))+i\omega\left(M+A(\omega)-\frac{S}{\omega^2}\right)}\right\|^2 . \tag{5.1}$$

For a known wave frequency (ω) therefore, the power output P_0 from an individual device can be modified by changing the float form to adjust the excitation force, the radiation damping, B, the added mass, A or the hydrodynamic stiffness, S. For a float of predefined immersed geometry, as considered in this chapter, the power output can only be modified by varying the float mass or the mechanical damping applied to the float. The optimum power output for a fixed geometry float is given by applying a mechanical damping equal to the radiation damping, $R = B$, and selecting a float mass such that $M = -A(\omega) + \frac{S}{\omega^2}$. A large variation of mass is not straightforward to achieve however and, for the case of neutrally buoyant devices, a change of mass would also result in a change of immersed geometry. It is possible to keep a constant immersed geometry by using a float-counterweight-pulley system such as that described in Section 3.

Within an array, the hydrodynamic terms (radiation damping and added mass) can also be modified by altering the inter-float spacing and layout of the array. Several studies have considered the influence of float spacing, configuration and array orientation on power output. However, it will not necessarily be straightforward to alter device spacing or array configuration during operation and so it is important to understand how the power output of arrays of predefined configuration can be modified. Modification of power output by variation of immersed geometry of individual floats is considered further in Chapter 6. In this chapter arrays of fixed float geometries in fixed layouts are considered in which either the mechanical damping, R, or the total mass of the floats, M, can be adjusted to achieve greater power. Although varying R is not the most effective way to manipulate the power absorbed by an isolated device, it may have a significant impact on the response and hence power within a closely spaced array since the forcing on other floats due to radiated waves will be modified.

5.1.1 Optimising Array Power Output

A theoretical array which is optimally tuned would have frequency dependent mechanical damping and mass specified such that $R(\omega) = B(\omega)$ and $M(\omega) = \frac{S}{\omega^2} - A(\omega)$, however unlike for an isolated device this would require the use of dense matrices. The off-diagonal elements of these matrices represent the application of an external force to each float that is dependent on the velocity and acceleration of all other bodies in the array and so are not straightforward to develop in a real system. This idealised system is studied by (Fitzgerald and Thomas, 2007), (Falnes, 1980), (Thomas and Evans, 1981) and (Mavrakos and McIver, 1997). For a linear array of five heaving semi-immersed spheres of radius a in incident waves with wavenumber $k = 0.4/a$, Fitzgerald and Thomas (2007) showed that a pentagonal configuration can attain an interaction factor of up to $q = 2.77$. For the same device size and wavenumber but for a linear array, which is the focus of this chapter, Thomas and Evans (1981) calculated a maximum interaction factor of $q = 2.25$ over a range of device spacings. Whilst these interaction factors are seemingly impressive, this requires specification of an external force on each float that is a function of the motion of all other floats in the array. A more easily implementable system is sought in this chapter in which the device spacing does not need to be varied to match each incident wave frequency.

A more practical design approach would be to apply a certain amount of mass and damping to each float irrespective of the motion of any other floats within the array. A system in which the device spacing does not need to be varied to match each incident wave frequency would also be more easily implementable. Several authors have considered arrays with sub-optimal mechanical damping and mass matrices to represent a feasible engineered system.

In regular seas, the diagonal mass and damping matrices which result in the greatest net power have been sought by Justino and Clément (2003). The diagonal elements of the matrices were defined by multiplying the diagonal elements of the corresponding fully optimised dense matrices by constant values within the range 0.8 to 1.2. They determined that when calculating diagonal R and M matrices in this manner, the greatest power could be achieved by using constant value of 1. In order to achieve the greatest power in different irregular wave spectra, sub-optimal diagonal damping matrices were iteratively selected for a fixed mass array by Cruz et al. (2009) and sub-optimal diagonal damping and mass matrices were selected by de Backer et al. (2009) using the theory of linear superposition. Greater interaction factors were found when each diagonal element of the damping matrix was selected individually than if they were all set to be equal to one value (either selected to give greatest power or set equal to the radiation damping of an isolated device).

The purpose of this chapter is to calculate the greatest power which can be achieved in regular seas by a sub-optimal closely-spaced array whose mass and mechanical damping arrays are diagonal matrices. The effects in irregular waves are not considered here as it remains unclear whether superposition of interaction factors derived assuming steady state response is a valid approach. A 5×1 array of semi-immersed spheres of radius a whose masses are constant and equal to twice the displaced mass of the water is considered with centre to centre separation distances of $s = 4a$ and a water depth of $d = 7a$. The two incident wave train directions, beam and head seas, are shown in diagram 5.1 together with the float numbering.

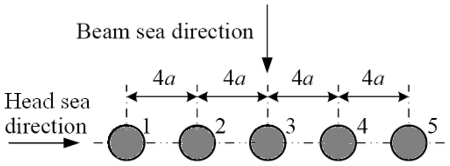

Figure 5.1: Diagram of 5×1 array of hemispheres of radius a with a centre to centre separation distance of $s = 4a$; beam and head sea directions are also indicated

The influence of the form of the mass and damping matrices on power output and interaction factor is shown in Section 5.2. Methods to calculate the optimum diagonal mechanical damping elements are explained in Section 5.4. An iterative method to select the diagonal matrix elements is described in Section 5.3. The result of using the iterative method to select the diagonal elements of the mechanical damping and mass matrices is then discussed in Sections 5.5 and 5.6 respectively.

5.2 Basic Approaches to Selecting Diagonal M and R Matrices

The system mass matrix, M, (which excludes the added mass, A) and the mechanical damping matrix, R, can be varied in order to manipulate the net power from an array. When both the optimum dense mass and optimum dense damping matrices are used such that the net power can be calculated using Equation (2.54), the net power, and hence Q is maximised at all wave frequencies (thin dotted line in Figure 5.2b). In practice, a dense mass matrix is difficult to achieve since the off-diagonal elements of the mass matrix represent a force that is dependent on the acceleration of all floats. This section considers several methods for calculating diagonal mass and damping matrices and evaluates the influence of these diagonal matrices on the response of a closely spaced line array of five devices. Both the interaction factor, q, and the Normalised interaction factor, Q, are shown in Figure 5.2 for five element arrays in which the mass and mechanical damping matrices are varied. The relevant isolated parameters are shown in Figure 5.3. The following sections discuss the differences in q and Q between these arrays in more detail.

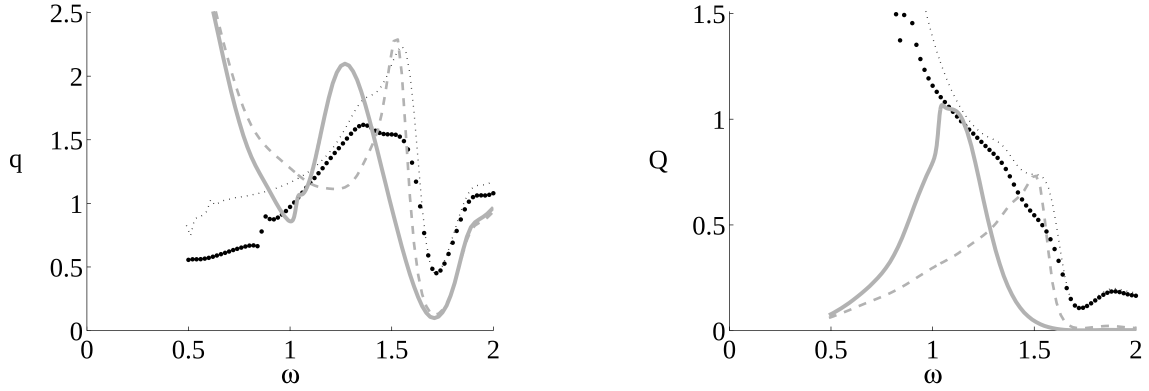

(a) q-factor, Varied M, $R = B$

Thin dotted black line, $M = \left(\frac{S}{\omega^2} - A\right)$;

Thick dotted black line, $M = diag\left(\frac{S}{\omega^2} - A\right)$;

Thin Dashed grey line, $M = I(5) \times M_m$;

Thick solid grey line, $M = I(5) \times 2M_m$

(b) Q, Varied M, $R = B$

Thin dotted black line, $M = \left(\frac{S}{\omega^2} - A\right)$;

Thick dotted black line, $M = diag\left(\frac{S}{\omega^2} - A\right)$;

Thin Dashed grey line, $M = I(5) \times M_m$;

Thick solid grey line, $M = I(5) \times 2M_m$

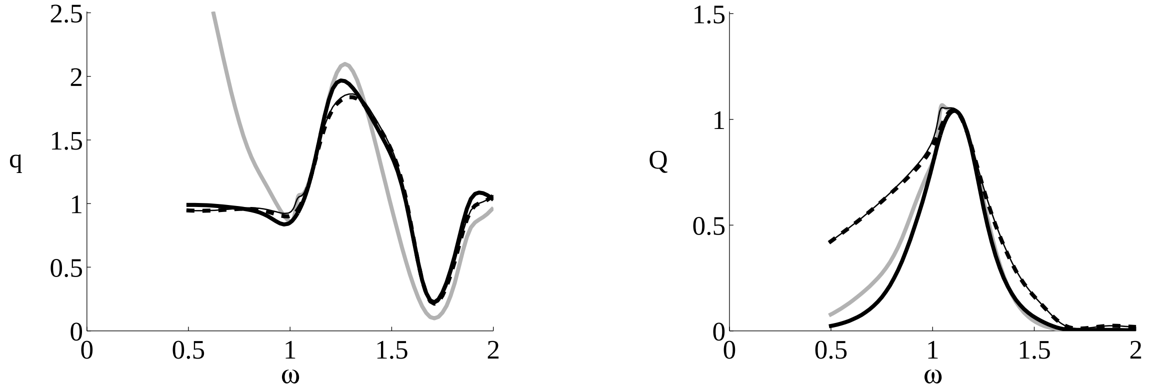

(c) q-factor, $M = 2M_m$, Varied R:

Thick solid grey line, $R = B$;

Thick solid black line, $R = diag(B)$;

Thin solid black line, $R = R_{opt}$;

Thick dashed black line, $R = diag(R_{opt})$

(d) Q, $M = 2M_m$, Varied R:

Thick solid grey line, $R = B$;

Thick solid black line, $R = diag(B)$;

Thin solid black line, $R = R_{opt}$;

Thick dashed black line, $R = diag(R_{opt})$

Figure 5.2: Interaction factor, q, and Normalised interaction factor, Q, (as given by Equation (2.56)) for 5×1 array of hemispheres in beam seas ($M = 2M_m$ represents the diagonal matrix $M = I(5) \times 2M_m$ where $I(5)$ represents the 5×5 identity matrix)

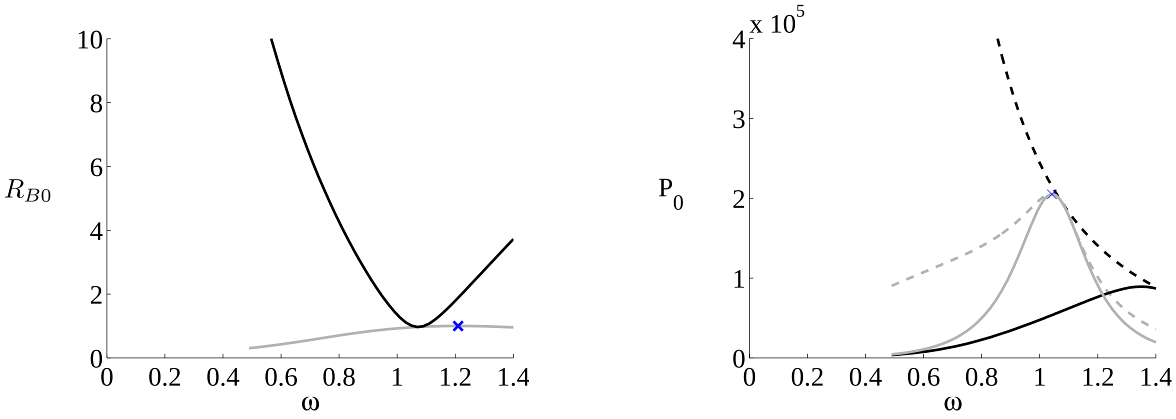

(a) Mechanical Damping:
Grey line, $R = B_0$ & $M = 2M_m$;
Black line, $R = R_{opt}$ & $M = 2M_m$;
×, $R = \max(B_0)$ & $M = 2M_m$

(b) Power:
Black dashed line, $R = B_0$ & $M = \frac{S}{\omega^2} - A$;
Solid black line, $R = B_0$ & $M = M_m$;
Solid grey line, $R = B_0$ & $M = 2M_m$;
Grey dashed line, $R = R_{opt}$ & $M = 2M_m$;
×, $R = \max(B_0)$ & $M = 2M_m$

Figure 5.3: Mechanical damping and power for an isolated heaving hemispherical float (Radiation damping given relative to the maximum radiation damping on isolated device with $R = B$ and $M = 2M_m$ such that $R_{B0} = \frac{R}{\max B_0}$)

5.2.1 Variable Mass Array with $R = B$

Consider the application of a diagonal mass matrix, whose diagonal elements are dependent on both the wave frequency and the float position within the array, and a dense mechanical damping matrix equal to the radiation damping matrix. Perhaps the most straightforward method to select a diagonal mass matrix would be to replace the off-diagonal elements of the optimal matrices with zeros, $M(\omega) = diag(M_{opt})$ where $M_{opt} = \frac{S}{\omega^2} - A(\omega)$. By applying this diagonal matrix instead of the optimal mass matrix, the interaction factors are reduced considerably but the power follows a similar trend to the fully optimised array (see thick dotted black line in Figure 5.2). The maximum interaction factor for this case is around 1.5 in contrast to 2.3 when a dense mass matrix is applied.

Whilst these interaction factors are informative for selecting appropriate dimensions for a device, it is important to note that this range of factors cannot represent the behaviour of a real system since, after design and installation, the mass of most wave energy devices can only be modified over a modest range. A modification to the mass of each device at each wave frequency could also prove difficult to implement. It is therefore relevant to consider an array in which the device masses do not vary with frequency.

5.2.2 Fixed Mass Array with $R = B$

Consider now the application of a diagonal mass matrix, whose diagonal elements are constant, and a dense mechanical damping matrix equal to the radiation damping matrix. Interaction factors are shown for two fixed mass systems in Figure 5.2 representing an array of neutrally buoyant floats ($M = M_m$) with $R = B$ and an array of floats of double this mass ($M = 2M_m$) and $R = B$. This represents a system in which each float is connected to a supplementary mass as considered by (Stallard et al., 2009a) and (de Backer et al., 2009). Clearly the fixed and variable mass systems exhibit very different interaction factor trends to each other. At their maxima, the q-factors for fixed mass arrays exceed the optimal system at the same frequency, particularly for the heavier constant mass (thick solid grey line). It is important to note that this only occurs because the factors are defined relative to the same device in isolation; for the optimal array, the isolated device mass varies with frequency whereas for the constant mass array the isolated device has constant mass.

The increase in mass from M_m to $2M_m$ significantly reduces the wave frequency at which the peak in net power occurs. For typical hemispherical floats of radius 5 m, float masses of $1.88M_m \leq M \leq 11.76M_m$ would put the natural frequency of the floats within the desired frequency range 0.5 to 1.25 rad/sec (as discussed in Section 1.2), however from an engineering perspective it is desirable for the masses to be as small as possible. Small mass systems are generally advantageous since this reduces cost, particular of installation and, in the case of structure supported devices, reduces structural requirements. Herein an array of equal mass floats of mass $2M_m$ is considered in which each float drives an independent linear damper which applies a force in phase with the velocity of that float only. The mass and mechanical damping matrices are therefore both diagonal, with all of the diagonal elements of the mass matrix equal to $2M_m$ at all wave frequencies. For this system, it is not straightforward to determine the mechanical damping for each float that would maximise net power output from the array of floats. Approaches based on the radiation damping matrix and an iterative method are considered.

5.2.3 Fixed Mass Array with $R = diag(B)$

Consider now the application of a diagonal mass array with constant diagonal values, together with a diagonal mechanical damping matrix. Perhaps the most straightforward selection of a diagonal mechanical damping matrix is to apply the diagonal elements of a dense damping matrix, $R = diag(B)$. A similar approach has been investigated by Justino and Clément (2003) who showed that application of the diagonal of the intrinsic impedance matrix $(B + i\omega(M + A))$ maximised the power output from an array of fully-immersed spheres for a given wave frequency. This approach can only be applied if both mass and damping are modified with wave frequency. A similar analysis, but with constant mass, $M = 2M_m$, and different range of constant multiplier values is shown here in Figure 5.4 for a 5 × 1 array of heaving, semi-immersed spheres in beam seas. A similar conclusion to Justino and Clément (2003) can be drawn in that maximum power is obtained from this fixed mass array by applying a diagonal damping matrix whose elements are all exactly equal to the radiation damping elements.

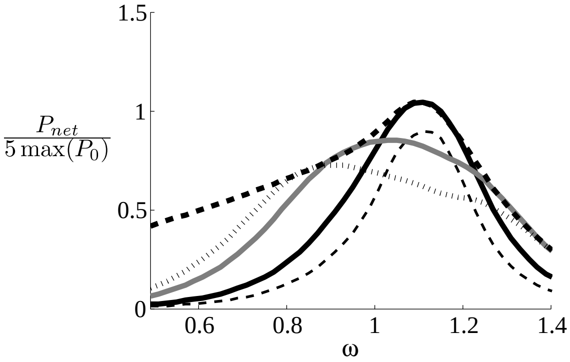

Figure 5.4: Comparison of P_{net} values obtained for a 5 × 1 array of hemispheres in beam seas by varying the choice of R matrix such that either $R = diag\,(R_{opt})$ or $R = \gamma_4 diag(B)$ for different values of constant γ_4:
KEY:
Thick dashed line, $R = diag\,(R_{opt})$; Thick dotted line, $R = 5diag(B)$; Solid grey line, $R = 3diag(B)$; Solid black line, $R = diag(B)$; Thin dashed line, $R = 0.5diag(B)$

5.2.4 Fixed Mass Array with $R = diag(R_{opt})$

An alternative approach to select the diagonal elements of the mechanical damping matrix is based on the output of an isolated device. Equation 5.1 gives the power which can be absorbed by a mechanical damper applying a damping force R to an isolated device. The differential with respect to R of equation 5.1 can be equated with zero to determine R_{opt}; the value of R which results in the greatest power for an isolated device (equation 5.2) (Falnes, 1980).

$$R_{opt} = \sqrt{B^2 + \omega^2 \left(A + M - \frac{S}{\omega^2}\right)^2} \tag{5.2}$$

By substituting matrices A, B, M and S to equation 5.2 in place of the intended scalars a (nearly) optimum dense damping matrix can be obtained for an array. This approach is not expected to give the maximum attainable power output but does account for use of a fixed mass matrix.

5.2.5 Comparison of Fixed Mass Arrays with $R = diag(B)$ and $R = diag(R_{opt})$

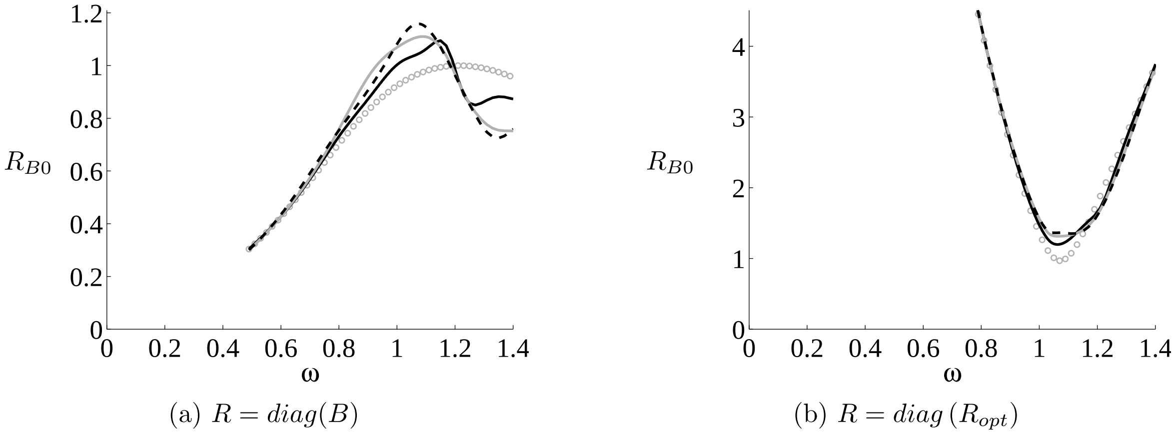

(a) $R = diag(B)$ (b) $R = diag\left(R_{opt}\right)$

Figure 5.5: Mechanical damping, R, calculated as $R = diag(B)$ and $R = diag\left(R_{opt}\right)$ and normalised by the maximum radiation damping on the isolated hemisphere ($\max(B_0)$) for a 5×1 array of hemispheres in beam seas:
KEY:
Solid black line, float 1 (and 5); Solid grey line, float 2 (and 4); Dashed line, float 3; Grey circular markers = damping on isolated device

.

Figure 5.5 shows the frequency variation of both $R = diag(B)$ and $R = diag(R_{opt})$ for each element of a 5×1 beam seas array, together with the damping on an isolated device such that $R = B$ and $R = R_{opt}$ respectively. The elements of the damping matrices follow a similar trend to the damping on the isolated device, however a greater variation in damping can be seen in the array with $R = diag(B)$. The two damping matrices (and isolated damping curves) have opposing trends with wave frequency.

Applying the damping matrices $R = diag(R_{opt})$ or $R = diag(B)$ to the arrays results in net powers and hence Q which form a parabola when plotted against frequency (as shown in Figure 5.2) with a peak at $\omega = 1.1$ rad/sec in beam seas and $\omega = 1.02$ rad/sec in head seas. At frequencies away from the peak, the damping matrix $R = diag(R_{opt})$ results in a greater net power than $R = diag(B)$. At frequencies near the peak in beam seas both matrices result in an equal net power whereas in head seas $R = diag(B)$ results in a greater net power than $R = diag(R_{opt})$.

Interaction factors resulting from these mechanical damping configurations are also shown in Figure 5.2. Note that these are normalised to a different isolated device, with the interaction factors for arrays with $R = diag(R_{opt})$ and $R = diag(B)$ calculated relative to an isolated device whose mechanical damping values are given by $R = R_{opt}$ (by applying Equation (5.2)) and $R = B$ respectively.

Applying the $R = diag(B)$ and $R = diag(R_{opt})$ damping values to the array in beam seas results in an interaction factor greater than one (indicating positive interaction) for $1.062 \leq \omega \leq 1.57$ rad/sec and $1.06 \leq \omega \leq 1.59$ rad/sec respectively and also for very high frequencies. In head seas the resulting interaction factors are predominantly below 1 (indicating negative interaction within the array) for all frequencies with $R = diag(R_{opt})$ and higher frequencies ($\omega \geq 1.032$ rad/sec) with $R = diag(B)$.

Within the range of interest for closely spaced arrays ($0.5 \leq \omega \leq 1.25$ rad/sec) therefore, positive interaction is seen in beam seas only for high frequencies ($1.06 \leq \omega \leq 1.25$ rad/sec) for arrays with either $R = diag(B)$ or $R = diag(R_{opt})$, and in head seas only for the array with $R = diag(B)$ for $0.49 \leq \omega \leq 1.032$ rad/sec.

It is unclear whether either of these diagonalisation approaches yield the maximum net power output from the array and so it is useful to determine whether float-specific values of mechanical damping can improve power output.

5.3 Diagonal Damping Matrix Selection Procedure

In this Section, unique damping values are identified for each float such that the net power output from the array is maximised. To individually select the diagonal elements of the diagonal mechanical damping matrix, R, which will result in the greatest net power, two different methods are applied and compared for a discrete range of wave frequencies, ω. Both methods produce similar damping values to each other with the resulting net power values within 0.6 % of each other. Both methods are described here in detail.

5.3.1 Method 1

A discrete range of possible R values is defined and at each wave frequency the net powers resulting from applying every combination of these values as diagonal elements of the R matrix is calculated (as shown in Figure 5.6 for a 2-element array). At each wave frequency the combination which results in the greatest net power is selected (as shown by the circular markers in Figure 5.6 for a 2-element array). For a two-element array this method allows a visual representation of the power attainable from all possible combinations of damping values showing that there is only one peak in power at each wave frequency (Figure 5.6). The uniqueness of the selected optimal damping values cannot be visualised for larger arrays however.

Using this method, the damping values are selected in a clear manner, however the computational cost is high and so the size of the discrete range of wave frequencies and possible R values are limited by the computational memory. Using a computer with a 3.19 GHz Processor and 2 GB RAM, the optimal damping matrix for a two element array can be calculated in 61 seconds from a range of 500 damping values, and 272 seconds from a range 1000 damping values. For a larger, N-element array the number of required calculations at each wave frequency would be increased from $(N_R)^2$ to $(N_R)^N$ where N_R is the number of damping values considered.

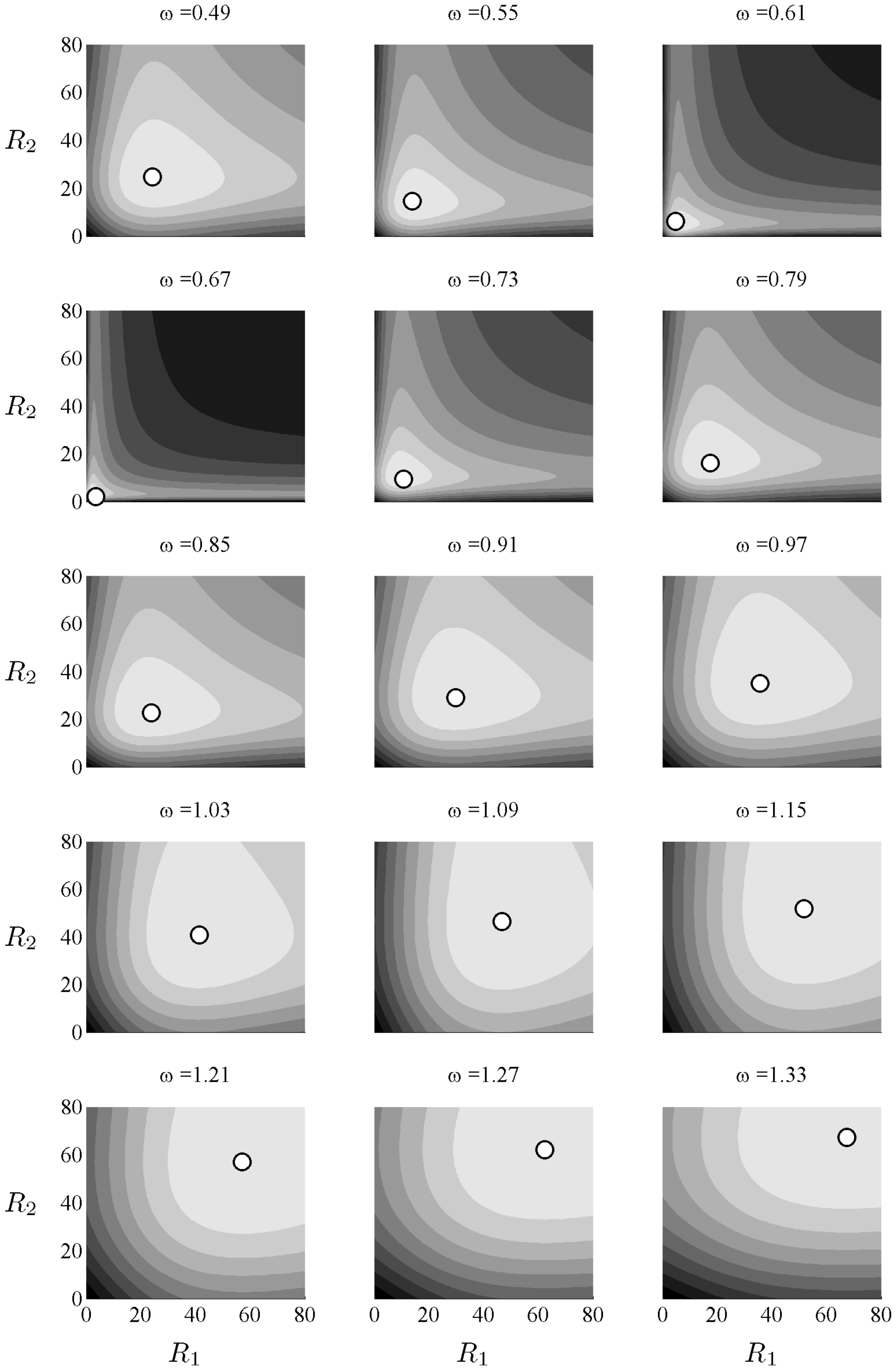

Figure 5.6: Surface Plots showing power absorbed by 2 × 1 array of cylinders in beam seas with float masses $M = 2M_m$ and a diagonal mechanical damping matrix, R, whose diagonal elements, R_{11} and R_{22}, are varied; the greater the resulting net power, the lighter the colour on the surface plot; damping values are given relative to the maximum radiation damping on an isolated cylinder with the same specifications such that $R_1 = \frac{R_{11}}{\max(B_0)}$ and $R_2 = \frac{R_{22}}{\max(B_0)}$; written directly above each surface plot is the wave frequency, ω,in rad/sec to which it corresponds; circular markers show the combination of damping values which result in the maximum power at each wave frequency

5.3.2 Method 2

The second method is an iterative method which uses an inbuilt MATLAB function to apply the Levenberg-Marquardt algorithm. A discrete range of net power values is specified, and the algorithm is applied to determine the values of R and individual power values from continuous domains which result in net power to within 10^{-10} of the specified net power. The greatest net power value at each ω for which R values are obtained is then stored.

The Levenberg-Marquardt algorithm is a least squares algorithm which uses an iterative approach to determine the mechanical damping values. Whilst Method 1 requires the calculation of power for every combination of damping values in the specified frequency range, Method 2 calculates only the values which it determines necessary using the least squares approach. The computational cost of Method 2 is therefore much less than method 1 allowing for an application to a much wider range of mechanical damping values (an infinite range) and application to more wave frequencies.

To minimise computational time, the iterative procedure is first run with a large but coarse net power range of $0.4\max(P_{net}(R = diag(B))) \leq P_{net} \leq 1.3\max(P_{net}(R = diag(B)))$ with 100 power increments ($I = 0.9\max(P_0)/100$) within this range. At each wave frequency, ω, the maximum net power from this range for which R values are determined is called $P_1(\omega)$. The iterative procedure is then completed for a second time using the results of the first iterative procedure such that the discrete power range is reduced to $P_1(\omega) \leq P_{net} \leq (P_1(\omega) + 4I)$ with 400 finer increments in this range. The mechanical damping values selected in the initial iterative procedure are used as initial values in the second iterative procedure.

The entire procedure to determine the optimal diagonal mechanical damping matrix is therefore given by

1 A discrete coarse range of net power values, $P_{net}^{[C]}$, is specified as $0.4\max(P_{net}(R = diag(B))) \leq P_{net} \leq 1.3\max(P_{net}(R = diag(B)))$ with 100 power increments ($I = 0.9\max(P_0)/100$) within this range

2 At each ω,

   (a) For each $P_{net} \in P_{net}^{[C]}$, elements of R and individual power values from continuous domains which result in net power values within 9 decimal places of P_{net} are obtained using the Levenberg-Marquardt algorithm. The initial starting value for each R element is the maximum radiation damping on an isolated device, $\max(B_0)$, and the initial starting value of each individual power value is $\frac{P_{net}}{N}$ where N is the number of elements within the array.

(b) The greatest P_{net} value for which R values are obtained is then stored and called $P_1(\omega)$, and the corresponding vectors of R and individual power values are called $R_{1it}(\omega)$ and $P_{1it}(\omega)$ respectively.

(c) A finer discrete range of net power values, $P_{net}^{[F]}$, is specified as $P_1(\omega) \leq P_{net} \leq (P_1(\omega) + 4I)$ with 400 finer increments in this range

(d) For each $P_{net} \in P_{net}^{[F]}$, elements of R and individual power values from continuous domains which result in net power values within 9 decimal places of P_{net} are obtained using the Levenberg-Marquardt algorithm. The initial starting values for the R elements are given by $R_{1it}(\omega)$, and the initial starting values of the individual power values are given by $P_{1it}(\omega)$.

(e) The greatest P_{net} value for which R values are obtained is then stored together with the corresponding optimal diagonal R matrix.

The iterative method is restricted by the discrete range of net power values for which damping values are sought. As a result, float-specific values are determined within the range $0.49 \leq \omega \leq 1.35$ and so covers a representative range of operational wave conditions, as outside of this range lower net power values are required.

5.3.3 Comparison of Methods

The two methods are compared in this section for a two element array of cylindrical floats (represented by the surface plot in Figure 5.6 for Method 1) and a five element array of hemispherical floats for the frequency range, $0.49 \leq \omega \leq 2.3$ rad/sec with increments of 0.02 rad/sec.

For the two element array, the frequency range over which a large amount of power is absorbed by the array (the bandwidth) is small. If Method 2 is applied by considering net power values which are at least 40 % of the maximum net power achieved when $R = diag(B)$ as defined in Section 5.3.2, suitable damping values are only attained for the peak frequency ($\omega = 0.65$ rad/sec) and directly adjecent frequencies ($\omega = 0.63$ and 0.67 rad/sec). In order to increase the range of frequencies over which the two methods can be compared, net powers are sought instead which are at least 10 % of the maximum net power achieved when $R = diag(B)$. With this increased range of net power values considered, Method 2 determines suitable damping matrices for all frequencies in the range $0.49 \leq \omega \leq 0.75$ rad/sec.

The same net power is calculated using both methods (less than 0.1 % difference) at all frequencies except the peak frequency. The net power determined using method 2 however is 2 % less than that determined using method 1 at the peak frequency ($\omega = 0.65$ rad/sec).

The mechanical damping values which are selected using each method follow the same trend (Figure 5.7a). The damping values selected, however, do vary by up to 110 % at the peak frequency and 6 % at all other frequencies. The damping values selected by both methods are minimal on both floats at the peak frequency. The variation in damping values of 110 % between methods at the peak frequency therefore corresponds to only a small variation in magnitude of damping.

When the damping and power values selected by Method 2 are set as initial values for the iterative procedure of Method 1, damping values are determined which result in 0.3 % greater net power than that determined by Method 2. This corresponds to an increase of 2.5 % compared to the net power determined using the generic initial values as specified in Section 5.3.2. Although there exists a clear dependence of Method 2 on the initial values, a descrepency below 3 % it is not considered significant enough to void its results.

The computational time to compute the optimal diagonal mechanical damping matrix using method 1 is 40 % greater than that of method 2 for the two-element array. For larger arrays the computational inefficiency of Method 1 makes it unrealistic for it to be used to determine the initial conditions for Method 2. Although there exists a clear dependence of Method 2 on the initial values, it is able to produce similar net power values to Method 1 when using generic initial values with significantly reduced computational time.

The two methods are compared for a 5 × 1 array of hemispherical floats in beam seas. For the purpose of comparison, additional conditions are placed in Method 2 to restrict the discrete R range such that $0.5 \max(B_0) \leq R_{i,i} \leq 8 \max(B_0)$. As with the two element array, the mechanical damping values selected using both methods in order to achieve greatest power are found to follow the same trend. As the range of R values is discrete in the first method and continuous in the second method, different damping values are determined with each method although this is less than 7.2 % difference for all but one frequency. The difference in the resulting net power values however is found to be less than 0.6 % for all wave frequencies.

In order to allow for efficient analysis of arrays of five or more bodies, Method 2 is used from herein to determine the optimal diagonal damping matrices.

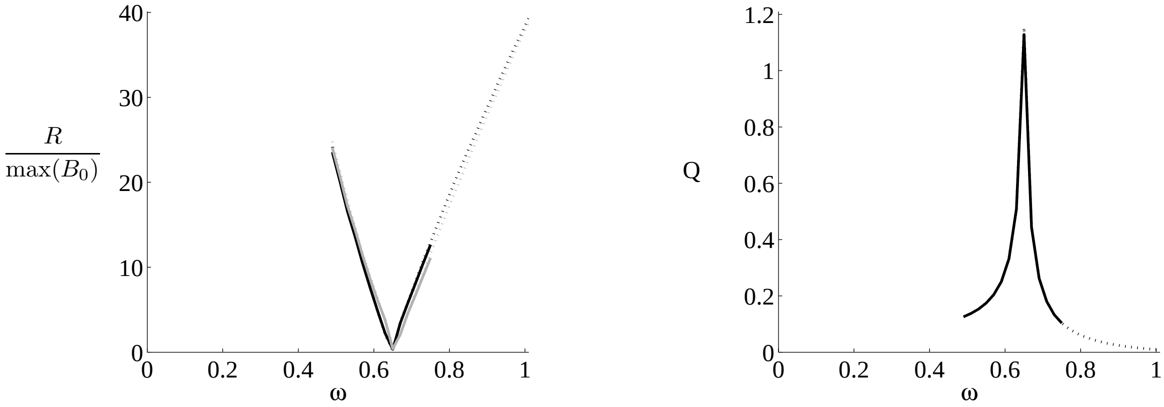

(a) Mechanical damping

(Black, float 1; Grey, float 2)

(b) Q-factor

Figure 5.7: Elements of the optimal diagonal mechanical damping matrix elements relative to the maximum radiation damping on an isolated device and their corresponding optimal Q-factors (determined using Equation (2.56) where the isolated body has the same specifications as the bodies within the array) for a 2×1 array of cylindrical floats with radius = draft = $a = 5$ m, $s = 4a$, and $M = 2M_m$
KEY:
Dotted lines, Method 1 (see Section 5.3.1); Solid lines, Method 2 (see Section 5.3.2)

If there is only one peak value then it could be possible to differentiate the power equation with respect to matrix R in order to determine the optimal mechanical damping matrix. The method of differentiation is discussed further in the next section.

5.4 Direct Sub-Optimal R Matrix Calculation

For an isolated device, the mechanical damping value which will result in the greatest power is given by R_{opt} (Equation (5.2)) which is identified as the zero of the differential of power with respect to mechanical damping ($\frac{\mathrm{d}P_0}{\mathrm{d}R} = 0$). Theoretically, the same method could be used to determine the mechanical damping matrix which will result in the greatest power from an array of devices by differentiating Equation (2.49) with respect to the matrix R and equating with zero. This procedure is discussed in this section.

Prior to differentiation of Equation (2.49) the velocity given by Equation (2.36) must be substituted into (2.49). This must then be expanded using the rules of complex matrix multiplication to give power, P, in terms of the matrices constituent elements, $R_{i,j}$, $B_{i,j}$, $A_{i,j}$, $S_{i,i}$, $M_{i,i}$, $\Re\{F_i\}$, $\Im\{F_i\}$ as well as ω.

Using the chain rule P can be written as:

$$\frac{dP}{dR} = \frac{\partial P}{\partial U}\frac{\partial U}{\partial R}. \tag{5.3}$$

P is a single value and U a vector, so the first partial differential equation can be written as

$$\frac{\partial P}{\partial U} = \begin{bmatrix} \frac{\partial P}{\partial U_1} & \frac{\partial P}{\partial U_2} & \cdots \end{bmatrix}. \tag{5.4}$$

U is a vector and R a matrix, so the second partial differential in Equation (5.3) can be written as

$$\frac{\partial U}{\partial R} = \begin{bmatrix} \frac{\partial U}{\partial R_{11}} & \frac{\partial U}{\partial R_{21}} & \cdots \\ \frac{\partial U}{\partial R_{12}} & \frac{\partial U}{\partial R_{22}} & \cdots \\ \vdots & \vdots & \vdots \end{bmatrix}. \tag{5.5}$$

Using Equations (5.3) together with Equations (5.4) and (5.5) therefore gives

$$\frac{dP}{dR} = \begin{bmatrix} \left(\frac{\partial P}{\partial U_1}\frac{\partial U}{\partial R_{11}} + \frac{\partial P}{\partial U_2}\frac{\partial U}{\partial R_{12}} + \cdots\right) & , & \left(\frac{\partial P}{\partial U_1}\frac{\partial U}{\partial R_{21}} + \frac{\partial P}{\partial U_2}\frac{\partial U}{\partial R_{22}} + \cdots\right) & , & \cdots \end{bmatrix}. \tag{5.6}$$

Both the net power, P, given by Equation (2.49) and the velocity, U, given by Equation (2.36) are complex. The differentiation is therefore further complicated by the differentials of complex numbers. The Cauchy-Riemann Formula for the derivative of a complex variable $Z_1 = Z_1^{\Re} + iZ_1^{\Im}$ with respect to another complex variable $Z_2 = Z_2^{\Re} + iZ_2^{\Im}$ is

$$\frac{\partial Z_1}{\partial Z_2} = \frac{\partial Z_1^{\Re}}{\partial Z_2^{\Re}} + i\frac{\partial Z_1^{\Im}}{\partial Z_2^{\Re}}. \tag{5.7}$$

Equation (5.7) must be used to expand each term of equation (5.6) to determine the differential of the power with respect to the mechanical damping matrix. Each of the N^2 elements can then be equated with zero to determine N^2 equations which define the optimal mechanical damping values. Assuming the mechanical damping matrix to be diagonal, reduces this to a system of N equations. Each of these equations forms a relationship between the diagonal damping elements, $R_{i,i}$, and the known hydrodynamic parameters, $B_{i,j}$, $A_{i,j}$, $S_{i,i}$, $M_{i,i}$, $\Re\{F_i\}$, $\Im\{F_i\}$ and ω.

This method is long and complicated even for a two element array, and impractical for larger arrays. The more efficient iterative method discussed in Section 5.3 is therefore used from herein to determine optimal array characteristics.

5.5 Iteratively-Selected Mechanical Damping

In this section the iterative approach described in Section 5.3.2 (Method 2) is applied to a 5×1 and a 5×2 array of hemispheres in both beam and head seas for two cases

1 any value of mechanical damping ($|R_\infty| \leq \infty$) can be applied and

2 mechanical damping in the range $0 \leq R \leq 2\max(B_0)$ can be applied.

The first case ($R \leq \infty$) corresponds to the maximum power output for the array under consideration. However, the magnitude of mechanical damping required to achieve these power values may not be practical and so the limited R case represents the power attainable if mechanical damping is restricted to a finite range of less than twice the radiation damping on an isolated device. This is a somewhat subjective upper limit but demonstrates the effect of limiting damping. Interaction factors for the array with iteratively-selected float-specific mechanical damping values are calculated relative to an isolated device with the optimum mechanical damping value for a fixed mass device as calculated using Equation (5.2). Therefore, interaction factors presented in the following sections are directly comparable to those for an array with $R = diag(R_{opt})$ shown in Figure 5.2. Note that all damping values in this chapter are given relative to the maximum radiation damping coefficient for an isolated device, which for a hemispherical float of mass $2M_m$ and radius 5m is 97 kNs/m.

Frequencies are considered in the range $0.49 \leq \omega \leq 2.3$ rad/sec. To obtain a smoother variation of values with frequency, a finer resolution of wave frequencies is used for the frequency range near the peak frequency, that is the frequency at which greatest power is achieved. Therefore, within the ranges $0.99 \leq \omega \leq 1.15$ rad/sec in beam seas and $0.95 \leq \omega \leq 1.05$ rad/sec in head seas, the frequency increment is 0.002 rad/sec and for lower and higher wave frequencies outside of this range the frequency increment is 0.02 rad/sec.

5.5.1 Application to One-dimensional Rectangular Arrays

In this section the iterative selection procedure is applied to a 5×1 array. Note that the horizontal axes of the figures in this section do not begin at zero.

In beam seas the maximum power attained when the diagonal mechanical damping values are selected iteratively from an unlimited and restricted range occur at $\omega = 1.072$ rad/sec and $\omega = 1.146$ rad/sec respectively. The reduction in net power at these frequencies compared to an equivalent array in which both the mass and mechanical damping matrices are dense and fully optimal are 2.66 % and 3.4 % respectively. In head seas, the reduction in power compared to the fully optimal array (at $\omega = 0.982$ rad/sec) is 17.7 %.

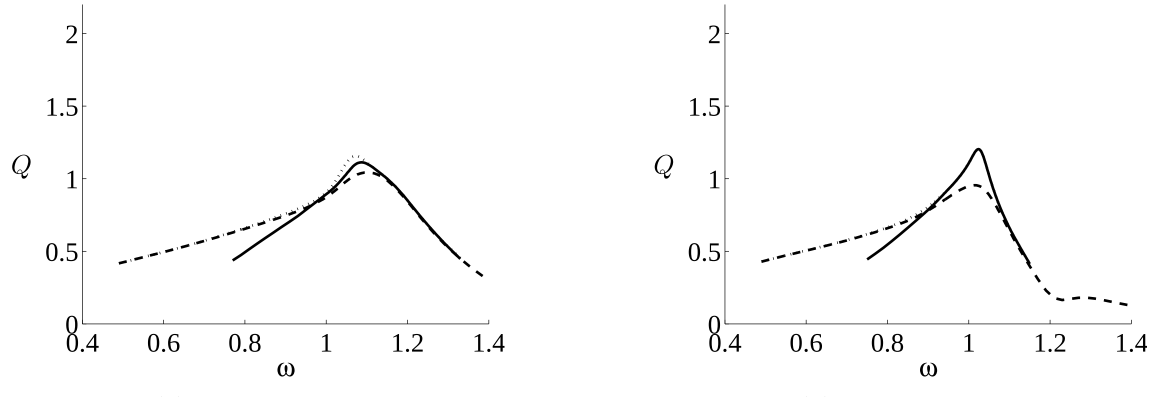

(a) Beam seas

(b) Head seas

Figure 5.8: Q, the ratio of net power, P_{net}, to the maximum power from an isolated device (as given by Equation (2.56)) for a 5×1 array of hemispheres with mass $M = 2M_m$ and values of the diagonal mechanical damping matrix, R, selected so as to give the maximum P_{net} at each wave frequency, ω:
KEY:
Dashed line, $R = diag\,(R_{opt})$ (shown for comparison);
Dotted line, R selected iteratively from an unlimited range of values, $(R \leq \infty)$;
Solid line, R selected iteratively from the range $0 \leq R \leq 2\max{(B_0)}$

For both of the 5×1 array orientations considered here, application of float-specific values of mechanical damping derived using the iterative method increases power output relative to the application of $R = diag(R_{opt})$ over a range of wavenumbers just above $\omega = 1$ (Figure 5.8). Maximum increases in interaction factors are 12.3 % in beam seas and 26.5 % in head seas, corresponding to interaction factors of $q = 1.18$ and $q = 1.2$ respectively (Figures 5.9 and 5.10). Limiting the magnitude of mechanical damping to less than $2\max(B_0)$ reduces the interaction factors in beam seas but, in head seas, the same increase of interaction factors is observed when mechanical damping is limited. At low wavenumbers ($\omega \leq 0.95$ rad/sec in beam seas and $\omega \leq 0.87$ rad/sec in head seas), interaction factors are within 2.5 % of those obtained by applying R_{opt} and are close to unity. If high mechanical damping values are not applied at these low frequencies however, power output is reduced significantly.

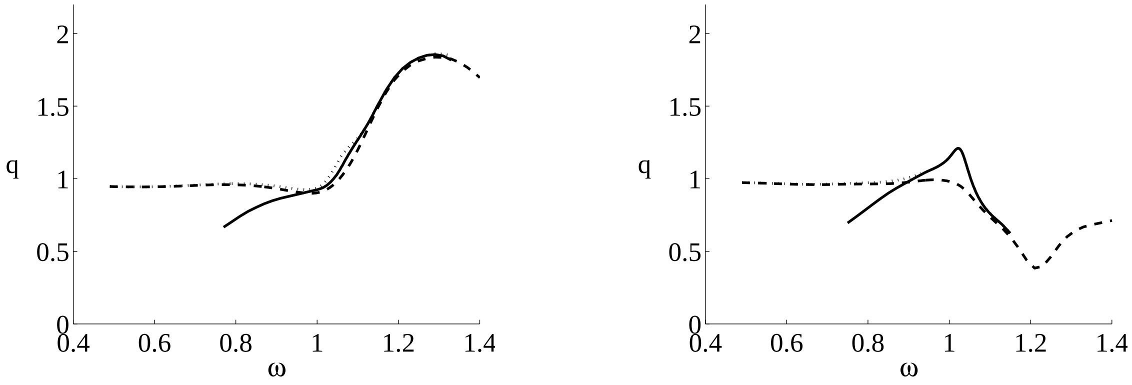

(a) Beam Seas interaction factor

(b) Head Seas interaction factor

Figure 5.9: q-Factor given relative to an isolated hemisphere with $R = R_{opt}$ and $M = 2M_m$ for a 5×1 array of hemispheres with masses $2M_m$ and diagonal mechanical damping, R, calculated as:
KEY:
Dashed line, $R = diag\left(R_{opt}\right)$ (shown for comparison);
Dotted line, R selected iteratively from an unlimited range of values, $(R \leq \infty)$;
Solid line, R selected iteratively from the range $0 \leq R \leq 2\max\left(B_0\right)$

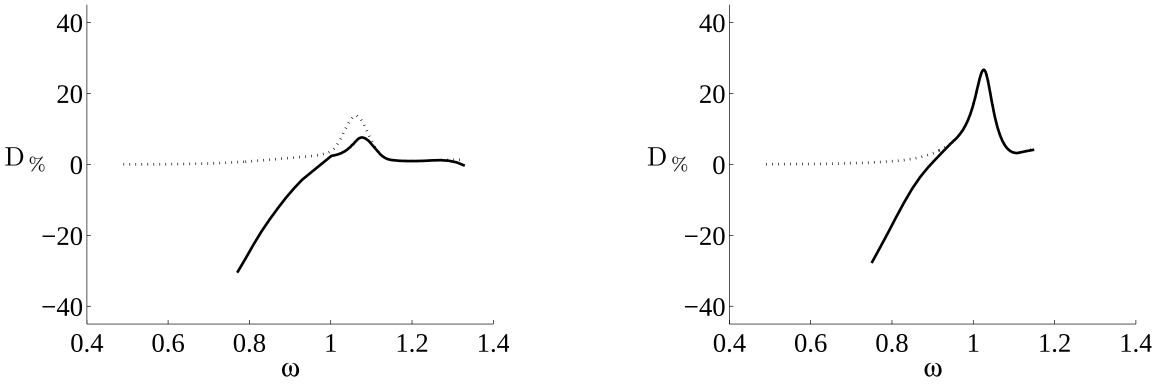

(a) Beam Seas difference in interaction factors

(b) Head Seas difference in interaction factors

Figure 5.10: $D_{\%}$, the difference between the interaction factor for a 5×1 array of hemispheres with $M = 2M_m$ and R selected iteratively (Dotted and solid lines in Figure 5.9), and the interaction factor for the same array with $R = diag(R_{opt})$ (Dashed line in Figure 5.9):
KEY:
Dashed line, $R = diag\left(R_{opt}\right)$ (shown for comparison);
Dotted line, R selected iteratively from an unlimited range of values, $(R \leq \infty)$;
Solid line, R selected iteratively from the range $0 \leq R \leq 2\max\left(B_0\right)$

On inspection of the mechanical damping values that are applied in order to achieve these increases in interaction factors (Figure 5.11), it is clear that in beam seas high- and low-damping is applied to alternate floats. Much lower damping is applied to the middle and end floats (1, 3 and 5) than the intermediate floats (2 and 4). This implies that the maximum power output is attained when only alternate floats oscillate and the others remain nearly stationary. Even-numbered floats clearly require large values of damping (up to $5\max(B_0)$) and so the damping on these floats is reduced by limiting the applied mechanical damping to $2B_0$ and this reduces the interaction factor to $q = 1.13$. In head seas the variation of mechanical damping with float number is similar to that of R_{opt} in that damping increases with float number ($R_i < R_{i+1}$) for $ks < 0.994$ and decreases with float number for $ks > 1.07$.

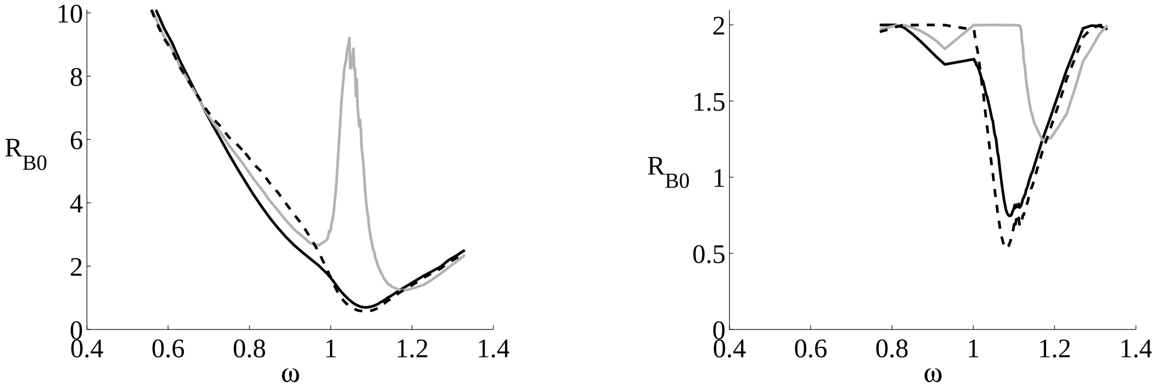

(a) $R \leq \infty$, Beam Seas

(b) $R < 2\max(B_0)$, Beam Seas

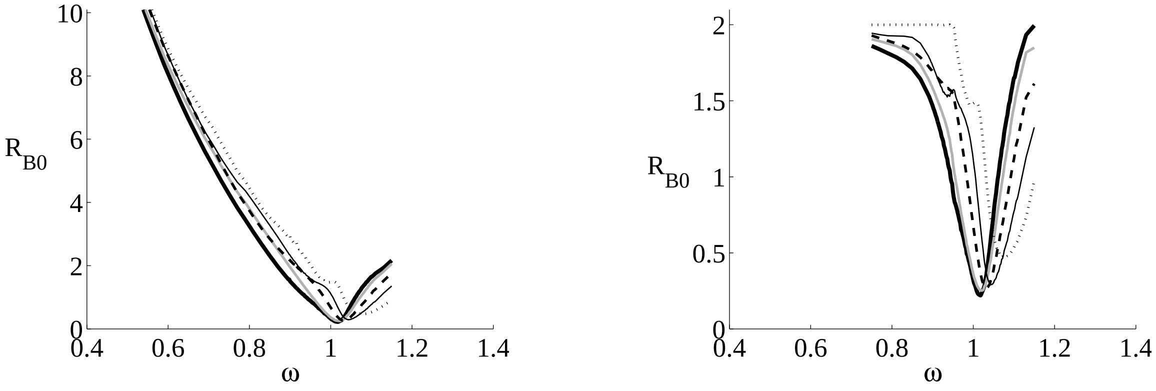

(c) $R \leq \infty$, Head Seas

(d) $R < 2\max(B_0)$, Head Seas

Figure 5.11: Mechanical damping values relative to the maximum radiation damping on isolated device with $R = B$ and $M = 2M_m$ such that $R_{B0} = \frac{R}{\max B_0}$ chosen in order to give the maximum P_{net} value at each wave frequency for a 5×1 array of hemispheres.
KEY:
Thick solid black line, float 1 (and 5 in beam seas); Solid grey line, float 2 (and 4 in beam seas); Dashed line, float 3; Thin solid black line, float 4 (in head seas); Dotted black line, float 5 (in head seas)

5.5.2 Application to Two-dimensional Rectangular Arrays

5.5.3 5×2 array, R variation

Applying the same approach to obtain float-specific mechanical damping values for each float in a 5 x 2 array yields the Q- and q-factors shown in Figures 5.12 and 5.13 respectively. For both array orientations, interaction factors are increased (compared to the array with $R = diag\left(R_{opt}\right)$) over a wider wavenumber range than for the 5×1 array. Peak increases in interaction factor are 37.1 % in beam seas and 20.6 % in head seas, corresponding to interaction factors of $q = 1.02$ and $q = 1.2$ respectively (Figure 5.14).

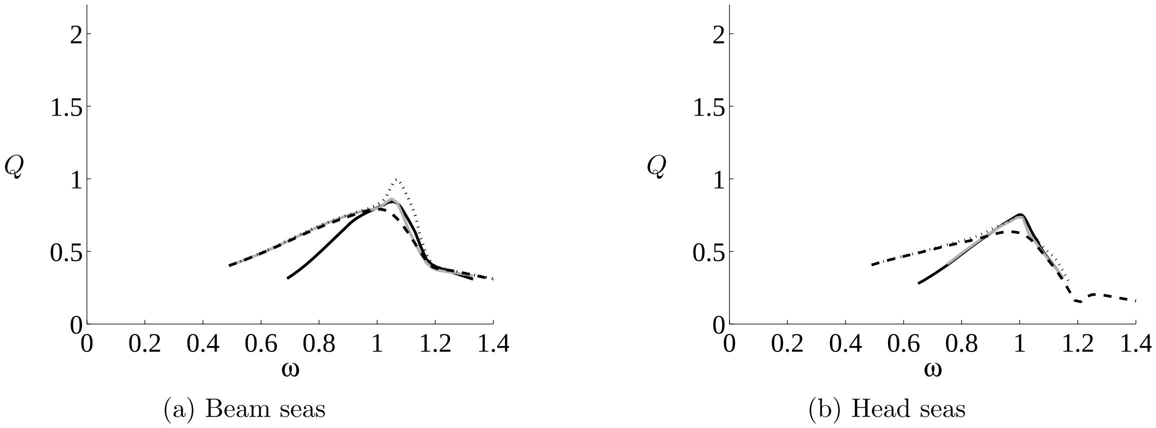

(a) Beam seas

(b) Head seas

Figure 5.12: Q, the ratio of net power, P_{net}, to the maximum power from an isolated device (as given by Equation (2.56)) for a 5×2 array of hemispheres with mass $M = 2M_m$ and values of the diagonal mechanical damping matrix, R, selected so as to give the maximum P_{net} at each wave frequency, ω:

KEY:

Dashed line, $R = diag\left(R_{opt}\right)$ (shown for comparison);
Dotted line, R selected iteratively for 5×2 array, $R \leq \infty$;
Solid black line, R selected iteratively for 5×2 array, $R < 2\max(B_0)$;
Grey line, R selected iteratively for 5×1 array and applied to each row of 5×2 array

In beam seas, the peak increase in interaction factor when compared to the base case occurs at a slightly higher value than for the 5×1 array in the same sea conditions, whereas in head seas the maximum increase occurs at a slightly lower wave frequency than for the 5×1 array. It is interesting to note that marginally higher interaction factors are observed in head seas if negative mechanical damping is applied to some floats. Increases of up to 2.8 % are observed due to the application of negative mechanical damping in the range $1.052 \leq \omega \leq 1.13$ rad/sec relative to the data shown in Figure 5.13. In effect, these floats are forced to oscillate hence inputting power rather than absorbing power.

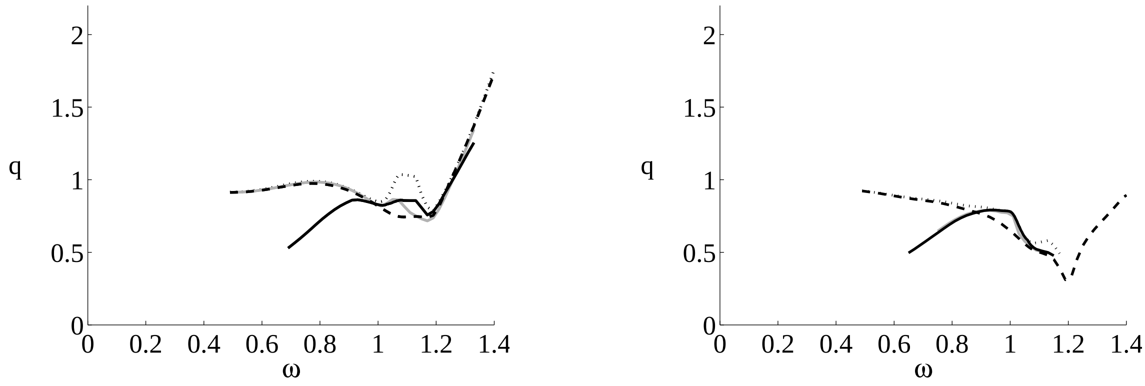

(a) Beam Seas interaction factor

(b) Head Seas interaction factor

Figure 5.13: Interaction Factor for a 5 × 2 array of hemispheres with:
KEY:
Dashed line, $R = diag\left(R_{opt}\right)$ (shown for comparison);
Dotted line, R selected iteratively for 5 × 2 array, $R \leq \infty$;
Solid black line, R selected iteratively for 5 × 2 array, $R < 2\max(B_0)$;
Grey line, R selected iteratively for 5 × 1 array and applied to each row of 5 × 2 array

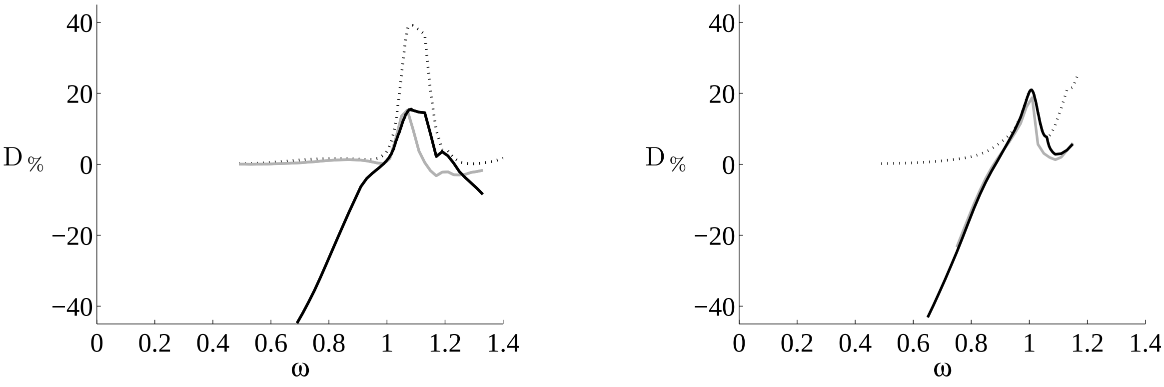

(a) Beam Seas difference in interaction factors

(b) Head Seas difference in interaction factors

Figure 5.14: $D_{\%}$, the difference between the interaction factor for a 5 × 2 array of hemispheres with $M = 2M_m$ and R selected iteratively (Dotted and solid black lines in Figure 5.13), and the interaction factor for the same array with $R = diag(R_{opt})$ (Dashed line in Figure 5.13):
KEY:
Dashed line, $R = diag\left(R_{opt}\right)$ (shown for comparison);
Dotted line, R selected iteratively for 5 × 2 array, $R \leq \infty$;
Solid black line, R selected iteratively for 5 × 2 array, $R < 2\max(B_0)$;
Grey line, R selected iteratively for 5 × 1 array and applied to each row of 5 × 2 array

In beam seas the general trend of damping values on both rows is similar to that of the 5×1 array but with higher damping applied to floats on the front row (Figure 5.15). On both rows, maximum interaction factors occur when high damping is applied to floats 2 and 4 whilst relatively low values are applied to the odd-numbered floats. This indicates that greater power is obtained when two floats on each row are held nearly stationary. In head seas (not shown here) the iteratively-selected damping values for the 5×2 array are similar to those of the base case at low ks values, with an increase in damping along each row as in the 5×1 array. For larger ks values there is no obvious trend to the frequency variation of damping along each row.

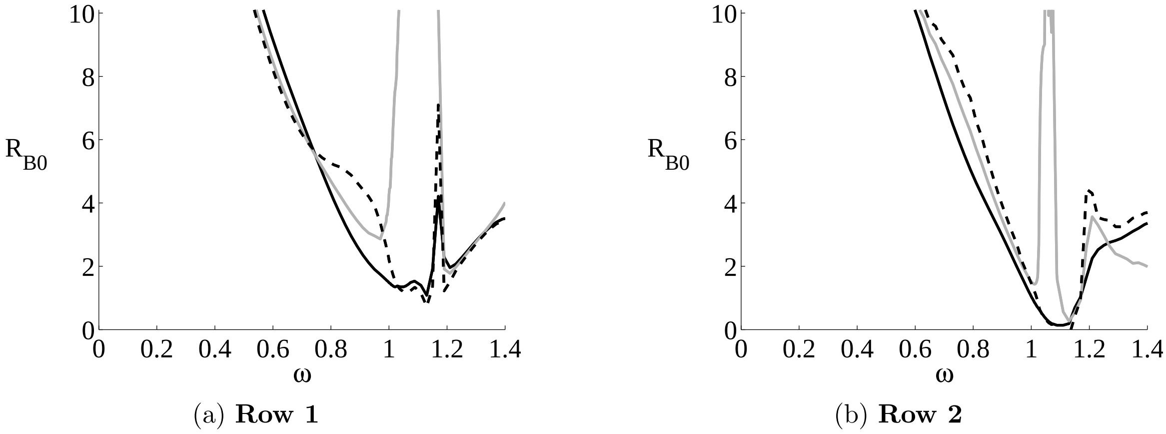

(a) **Row 1** (b) **Row 2**

Figure 5.15: $R_{B0} = \frac{R}{\max B_0}$ with R values chosen such that $R > 0$ in order to give the maximum P_{net} value at each wave frequency for a 5×2 array of hemispheres in beam seas (see dotted line in Figure 5.13 for resulting q-factors); Each row is numbered from 1 to 5 as in Figure 5.1:
solid black line = floats 1 and 5 ;
solid grey line = floats 2 and 4;
dashed line = float 3

An increase in interaction factor, although less than that of the 5×2 iteration, can still be seen when the 5×1 results are applied to each row of the 5×2 array (grey line in Figures 5.12 and 5.13). The damping values required to achieve maximum power in the 5×2 array are symmetric between rows in head seas, and dependent on the row in beam seas. As a result, the float-specific values which are selected iteratively to attain greatest power for a 5×1 array are a much better approximation to those selected for each row of the 5×2 array in head seas than in beam seas.

5.5.4 Response Amplitude Ratios

If a buoy loses contact with the free surface it can experience high hydrodynamic forces known as slamming forces as it re-enters the water. Slamming forces are not included in the current numerical model. The hemispherical floats have a radius of $a = 5$ m hence lose contact with the free surface when the response amplitude ratio $|d_z| > \frac{a}{A_m}$ for wave amplitude A_m. In water of depths of approximately 35 m at which closely spaced arrays are likely to be located, significant wave heights of approximately 2 m are common, with individual wave cycles having heights in the range $0.5 \leq H \leq 6$ m.

With a wave height of 2 m (hence wave amplitude of $A_m = 1$ m) slamming forces are likely to occur when $|d_z| > 5$.

The response amplitude ratios corresponding to the arrays with the iteratively-selected float-specific damping applied can be seen in Figures 5.16 and 5.17, where response amplitude ratio is the ratio of the absolute response of the float to the wave amplitude. In all cases, the effect of the large damping values at low and high frequencies is simply achieving a response amplitude of approximately 1 on all floats. In both incident wave directions of the 5×1 and 5×2 array float 3 attains the greatest response amplitude. In beam seas, the peak in damping on the intermediate floats of the 5×1 array and the second row of 5×2 array (2,4,7 and 9) in the range of the peak net power, results in a reduction in response amplitude on these floats.

In the peak net power frequency range there is a reduction in damping applied to the second row of the 5×2 array in beam seas compared to the first row. As a result, the response amplitudes are much greater on the floats in the second row compared to the first row, reaching response amplitudes up to 4.6 on float 3. This means that the absolute response of the float (in m) is 4.6 times the amplitude of the wave. With such a high response amplitude ratio, slamming forces are likely to occur when $H > 2 \times \left(\frac{5}{4.6}\right) = 2.17$ m. This includes all waves close to the approximate expected significant wave height of $H_s = 2$ m so is highly probable. The large increase in interaction factor of 37.1 % with an interaction factor of $q = 1.02$ compared to the base case for which $q = 0.75$ as calculated for the fixed mass 5×2 array in beam seas is therefore not necessarily attainable for the specified floats.

The greatest response amplitudes required for the 5×1 array in beam seas is only 3.2. The neglection of slamming forces in the model is therefore inappropriate when $H > 3.13$ m. The large interaction factors (up to $q = 1.2$) calculated for this array are consistent with the assumptions made in the calculation method for wave heights close to the expected significant wave height of 2 m. A similar argument confirms the validity of the response amplitude ratios for the 5×2 array in head seas, however this only results in an interaction factor less than one.

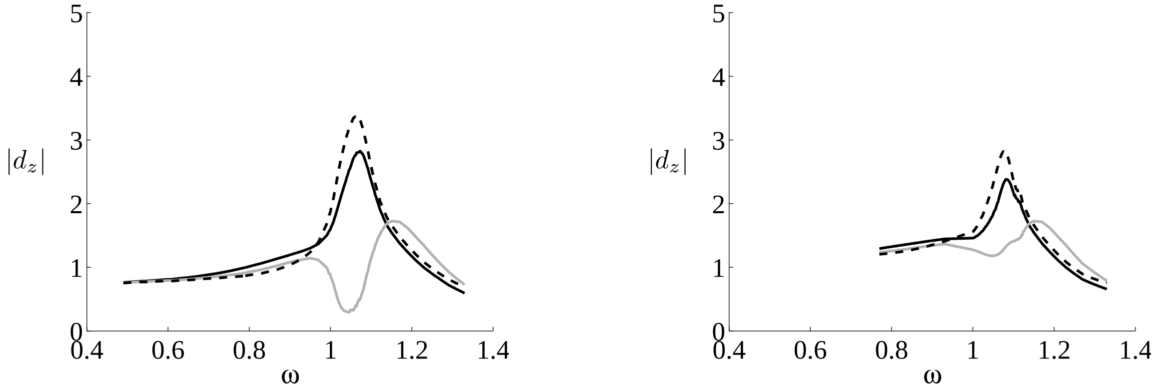

(a) $R \leq \infty$, **Beam** seas: solid black line = float 1 and 3; solid grey line = float 2 and 4; dashed black line = float 3

(b) $R < 2\max(B_0)$, **Beam** seas: solid black line = float 1 and 3; solid grey line = float 2 and 4; dashed black line = float 3

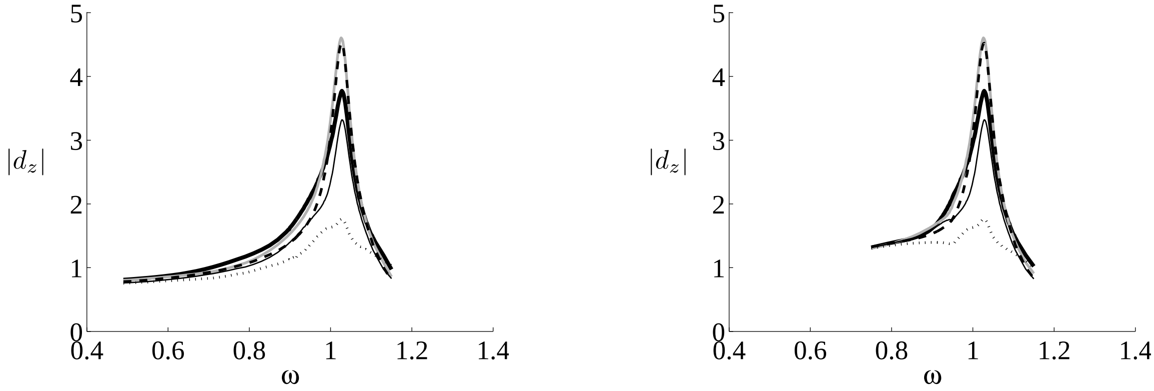

(c) $R \leq \infty$, **Head** seas: thick solid black line = float 1; solid grey line = float 2; dashed black line = float 3; thin solid black line = float 4; dotted black line = float 5

(d) $R \leq \infty$, **Head** seas: thick solid black line = float 1; solid grey line = float 2; dashed black line = float 3; thin solid black line = float 4; dotted black line = float 5

Figure 5.16: Response Amplitude Ratio, $|d_z|$, for a 5×1 array of hemispheres whose R matrix is diagonal and selected iteratively

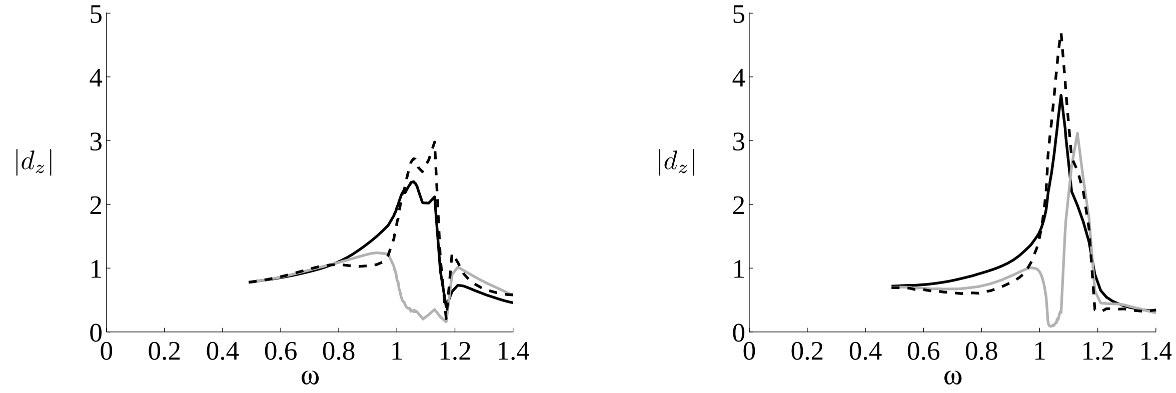

(a) **Row 1**

solid black line = floats 1 and 5 ;

solid grey line = floats 2 and 4;

dashed line = float 3

(b) **Row 2**

solid black line = floats 1 and 5 ;

solid grey line = floats 2 and 4;

dashed line = float 3

Figure 5.17: Response Amplitude Ratios, $|d_z|$, on each float when R is chosen in order to give the maximum P_{net} value at each wave frequency for a 5×2 array of hemispheres in beam seas

Thomas and Evans (1981) considered restricting the amplitude of the motion of the floats to be below a fixed multiple of the wave amplitude thus restricting the response amplitude ratio. When considering a 5×1 array of hemispheres with variable spacing in a single incident wave frequency they found that restricting the response amplitude ratio to be less than 2 resulted in a negative interaction factor except at near optimum spacing, but less than 3 resulted in interaction factors much closer to the optimally tuned array across the range of spacings considered. Their analysis allowed for dense mass and damping matrices, whereas only diagonal mass and damping matrices are considered here. No restrictions are placed on the response amplitudes here.

5.6 Iteratively-Selected Mass

The mass of the floats in the damping analysis in Section 5.5 was chosen to be twice the displaced mass, enabling the peak in the net powers to occur within the frequency range of interest to closely spaced wave energy devices. A decrease in float mass would result in a shift in net power towards the higher frequencies. A similar analysis to the last section is carried out in this section to iteratively determine the frequency dependent diagonal mass and damping combinations which result in the greatest net power for a given frequency. For simplicity, it is assumed that mass can be varied without variation of float draft such that the hydrodynamic parameters do not vary with mass. This represents a system similar to the experimental arrangement of Section

3. Clearly this is not possible with all devices since implementation would require an external force (non-buoyancy) to support the additional mass. Even if this is available, an unlimited variation of mass is clearly impractical. Figure 5.18 shows the resulting Q when the total mass is restricted to the range $1.75M_m \leq M \leq 2.25M_m$. As the mass is not constant, a comparison to arrays of equal mass floats in which the mass is equal to the limit mass values ($M = 1.75M_m$ or $2.25M_m$) is employed.

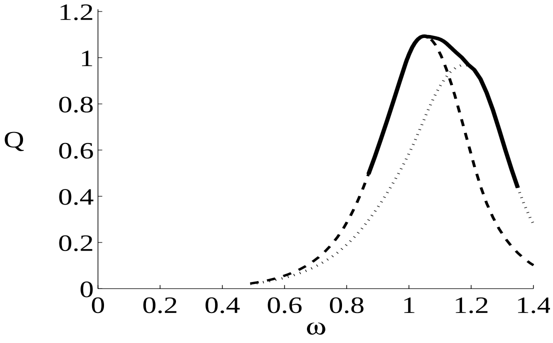

Figure 5.18: Q, the ratio of net power, P_{net}, to the maximum power from an isolated device (as given by Equation (2.56) with an isolated device with $M = 2M_m$) for a 5×1 array of hemispheres in BEAM seas with $R = diag(B)$ and mass values selected so as to give the maximum P_{net} at each wave frequency, ω:
KEY:
Dashed line, $M = 2.25M_m$ (shown for comparison); Dotted line, $M = 1.75M_m$ (shown for comparison); Thick solid line, M values iteratively selected from the range $1.75M_m \leq M \leq 2.25M_m$

The maximum mass ($M = 2.25M_m$) is required for all frequencies below the peak frequency of the maximum mass power curve. Similarly, at frequencies above the peak frequency of the minimum mass power curve, the maximum Q is achieved by applying the minimum mass on all floats. At frequencies between these two peaks, by applying a variation in mass along the array with individually selected mass values, Q values can be attained between the maximum values attained by applying the maximum and minimum mass values (Figure 5.19).

At the frequency corresponding to the maximum power for an array of equal mass floats with $M = 2M_m$, an increase in Q of nearly 4 % is found using the iteratively-selected mass values which are dependent on float position within the array.

The increase in Q obtained by increasing the mass from the minimum to the maximum mass values is about 12 %. This is similar in magnitude to the increase in Q (13 %) found by using iteratively-selected float dependent mechanical damping values for the 5×1 fixed mass array in beam seas instead of the diagonal matrix $R = diag\left(R_{opt}\right)$ (see Figure 5.8).

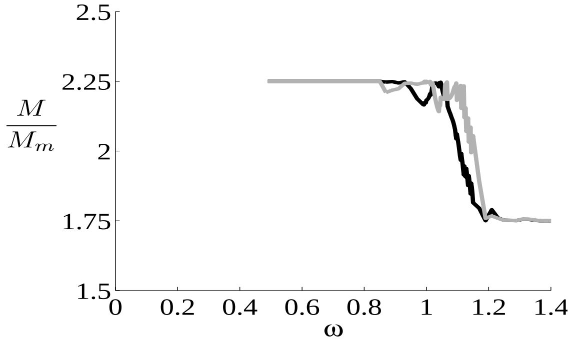

Figure 5.19: Mass values between 1.75 M_m and 2.25 M_m chosen to give the maximum P_{net} value at each wave frequency for a 5×1 array of hemispheres in beam seas with $R = diag(B)$ (see thick solid line in Figure 5.18 for resulting Q values):
KEY:
Solid black line, float 1 (and 5); Solid grey line, float 2 (and 4); Dashed line, float 3

5.7 Chapter Conclusion

Although it has been shown that large interaction factors (> 2) may occur in regular waves at certain ratios of device spacing to wavelength, much of the existing work does not address array configurations or device constraints that are relevant to designers of structure-supported array devices. Specifically, much of the published work addresses relatively large inter-device spacing and optimal mass and damping matrices are typically applied.

An array of floats each of which are restrained by an independent linear damper is considered in this chapter. The system considered is intended to represent the behaviour of a realistic closely spaced array in which float mass cannot be significantly altered between sea-states and damping is applied to only the heave oscillation of each float. The damping force on each float is specified such that it does not depend on the motion of other floats within the array, thus forming a diagonal mechanical damping matrix. The maximum power and hence interaction factor that is achievable in regular seas by such an array is determined.

This chapter has investigated whether an appropriate diagonal mechanical damping, R, matrix can be applied to an equal mass array of floats in order to achieve maximum net power over a range of wave frequencies.

Differentiating the absolute value of net power with respect to the matrix R and equating with zero would determine the damping matrix which would result in the maximum net power output for a fixed mass array. The equations resulting from this analysis however have been shown in this chapter to be highly complicated, even for a basic two element array.

Three approaches for obtaining a diagonal damping matrix have instead been considered based on i) the radiation damping matrix, ii) the optimal damping equation for an isolated device and iii) an iterative approach. For a particular frequency, the values of mechanical damping required on each float within the array that maximise net power output do not appear to be directly related to the diagonal elements of the radiation damping matrix ($R = diag(B)$).

Over most of the frequency range, the diagonal of the optimal damping matrix for a fixed mass system provides maximum net power. In this case there is minimal difference between the damping of each float. However, close to the maximum power output from an isolated device, greater net power can be obtained by using damping values that are determined by an iterative approach. Here a Levenberg-Marquardt algorithm is employed for the iteration, however other methods could be used. For a 5×1 array of hemispherical floats, application of a diagonal damping matrix whose elements are selected iteratively is found to increase the net power by up to 12 % in beam seas and 18 % in head seas compared to when the diagonal elements of the damping matrix are selected according to the optimal damping equation for an isolated device. When a restriction, $R \leq 2 \max B_0$, is placed on the range of R values permitted in the iterative procedure, the peak increase reduces to ~ 7 % in beam seas.

The interaction factors for an array with an optimal (dense) mechanical damping matrix differ considerably from those for an array with individual mechanical damping on each float (diagonal damping matrix).

For the array in beam seas, increased power output only occurs when alternate floats are nearly stationary and, if this is not possible, power output is similar to that obtained by applying mechanical damping similar to the hydrodynamic damping of each float. In head seas, maximum power output is obtained at low wavenumbers if mechanical damping is increased with row number. In contrast, at high wavenumbers, net power output is maximum when damping is greatest on the front float.

The optimal damping values iteratively selected to achieve maximum power in a 5×2 array are symmetric between rows in head seas, and dependent on the row in beam seas. Peak increases in interaction factor (compared to when the diagonal elements of the damping matrix are selected according to the optimal damping equation for an isolated device) are 37.1 % in beam seas and 20.6 % in head seas for the 5×2 array. These increases correspond to interaction factors of $q = 1.02$ and $q = 1.2$ in beam and head seas respectively. An increase in interaction factor, although less than that of the

5×2 iteration, can be seen when the 5×1 results are applied to each row of the 5×2 array. The application of these 5×1 values to each row of the 5×2 array is a much closer approximation to the values actually selected to achieve the greatest power for the 5×2 array in head seas than in beam seas.

A similar iterative approach has also been used to determine a unique mass for each float in order to maximise net power. A system by which both the mass and the damping could be varied within limited ranges would allow for even greater manipulation of the power output. Using the current method to determine such M and R values however would require numerous iterations, and would be computationally inefficient.

At the frequency corresponding to the maximum power for an array of equal mass floats with $M = 2M_m$, an increase in Q of nearly 4 % is found using the iteratively-selected mass values which are dependent on float position within the array. Assuming mechanical damping to be equal to the diagonal of the radiation damping matrix, similar increases of net power are found if the mass of each float is varied from $1.75M_m$ to $2.25M_m$ on all floats as the increase found by using iteratively-selected float dependent mechanical damping values for the 5×1 fixed mass array in beam seas instead of the diagonal matrix $R = diag\,(R_{opt})$.

Chapter 6

Optimisation of Geometries

Mechanical damping values have been determined in Chapter 5 which could be applied directly to each float within a linear array with fixed geometries and spacing in order to achieve the greatest power. In some cases impractically high values of mechanical damping were deemed necessary. As the radiation damping is dependent on the submerged geometry, the total damping (consisting of the radiation and mechanical damping) could also be varied by varying the submerged geometries of the floats within the array, thus reducing the amount of mechanical damping required to achieve the maximum power (at a given frequency).

This chapter considers the possibility that a reduction in required mechanical damping could be achieved by using alternative float geometries without reducing the net power from the array. It is assumed that the hydrodynamic parameters are known for all geometries considered. A method to select the most appropriate geometry from a selection of geometries is required. The calculation of power requires a mechanical damping force to be applied. As the range of geometries considered could be large, and the range of possible mechanical values infinite, the method to select geometries must not depend on the calculation of power for each possible geometry.

Two geometry selection criteria are considered for a range of geometries. The first considers only the magnitude of radiation damping on each float with a view to achieving a specific (optimal) magnitude of total damping. As well as the radiation damping, the added mass, excitation force and in some cases the hydrostatic stiffness and float mass are all dependent on the submerged float geometry. For certain groups of geometries, the variation of all of these hydrodynamic parameters is significant, hence must be accounted for when selecting a geometry. The free-float response amplitude ratio is therefore considered as a second selection criterion as it incorporates all of these hydrodynamic parameters but not mechanical damping.

The geometry selection criterion which accounts only for the variation in radiation damping would require the variation in all other hydrodynamic parameters with geometry to be minimal. The geometry which would require the least mechanical damping to achieve a specific total (radiation plus mechanical) damping would be selected. The desired total damping would be determined for a specific base geometry using the iterative method described in Chapter 5. For free-float response to be an appropriate measure there must be a correlation between the geometries which achieve the greatest free-float response and those which achieve the greatest power under the application of a mechanical damping force.

To select the most suitable geometry for each position within an array, knowledge of the interaction of that float geometry with all of the other float geometries is required. If the size of the array is large, then this would require knowledge of many combinations of the floats in order to select the most appropriate float geometry for each position within an array. Section 6.1 presents an argument for using only the knowledge of the interaction of each float with the float directly adjacent to it within a large linear array to determine the most appropriate geometry for each position within the array.

Whilst several independent geometries are considered, it is recognised that simply varying the draft of a float of fixed overall geometry results in a variation in submerged geometry, hence allows for the manipulation of hydrodynamic parameters according to the current wave conditions. An investigation into the use of both radiation damping and free-float response amplitude ratio as draft selection methods is presented in Section 6.2 for several geometries placed in isolation.

A method to select the most appropriate draft to operate over a range of wave frequencies is considered in Section 6.3 and applied to a specific complex geometry, ConTop.

Section 6.4 considers a small array of basic and equal geometry floats for which the optimal diagonal mechanical damping matrix (determined using the optimisation procedure of Chapter 5) is known. Based on the findings of the isolated device in Section 6.2, an appropriate method is used to determine at which frequencies the mechanical damping could be reduced by varying the draft of the floats (equally) without reducing the total power from the array.

6.1 Direct Neighbour Coupling

This chapter investigates the selection of a float geometry (from a range of geometries) which is most appropriate for a particular position within a linear array according to either the total damping matrix or the free float response. Both of these selection methods require the calculation of hydrodynamic parameters for each of the geometries considered. Interaction effects within arrays have been shown throughout this thesis to be significant in certain wave conditions. The hydrodynamic parameters are therefore dependent on the float geometries at every position within the array, so must be calculated for every combination of float geometries within the array. For large arrays, or when the range of geometries considered is large, the number of calculations required is large.

This section considers whether the hydrodynamic parameters for each pair of possible geometries could alone be used to determine the most appropriate geometry for each position in a large array. Considering only the interactions of floats with the floats which are located directly adjacent to it within a linear array is here termed Direct Neighbour coupling. Disregarding the interaction of floats located further away within the array in this way would reduce the number of required computations significantly.

The off-diagonal elements of the radiation damping matrix are generally largest when they are located directly adjacent to a diagonal element within the matrix. This is indicated by Table 6.1a for the 5×1 array of hemispherical floats where the maximum elements of the radiation damping matrix directly adjacent to the diagonal elements are up to 91% of the value of diagonal elements, whereas those which are the furthest from a diagonal damping element are a maximum of 22% of the diagonal damping element.

B	j=1	j=2	j=3	j=4	j=5
$i = 1$	1.00	0.90	0.66	0.33	0.22
$i = 2$	0.91	1.00	0.91	0.67	0.33
$i = 3$	0.67	0.91	1.00	0.91	0.67
$i = 4$	0.33	0.67	0.91	1.00	0.91
$i = 5$	0.22	0.33	0.66	0.90	1.00

(a) max $\left(\frac{B_{ij}}{B_{ii}}\right)$ for radiation damping matrix B

A	j=1	j=2	j=3	j=4	j=5
$i = 1$	1.00	0.29	0.21	0.16	0.14
$i = 2$	0.31	1.00	0.28	0.23	0.17
$i = 3$	0.21	0.28	1.00	0.28	0.21
$i = 4$	0.17	0.23	0.28	1.00	0.31
$i = 5$	0.14	0.16	0.21	0.29	1.00

(b) max $\left(\frac{A_{ij}}{A_{ii}}\right)$ for added mass matrix A

Table 6.1: The maximum ratio of off-diagonal elements of each row of the radiation damping and added mass matrices to the diagonal element in the same matrix row (row i) for a 5×1 array of hemispherical floats in beam seas

This suggests that float geometries within an array could be selected based on only the coupling between directly adjacent floats. This would require knowledge of the hydrodynamic parameters corresponding to each combination of two geometries from a discrete range regardless of the overall size of the array.

The ratio between the off-diagonal and diagonal added mass elements is generally smaller than that of the radiation damping matrix, with the off diagonal elements corresponding to between 14 % and 31 % of the diagonal elements for the 5×1 array of hemispherical floats in beam seas. As with the radiation damping matrix, Table 6.1b indicates that this is focused mainly on the elements directly adjacent to the diagonal elements, supporting the argument for the use of Direct-Neighbour Coupling.

6.2 Draft Variation of Isolated Body

Before the direct coupling of different geometry floats is considered, it is useful to obtain an understanding of the effect of the variation of draft of isolated floats. The magnitude of variation of radiation damping with float geometry compared to the magnitude of variation of other hydrodynamic parameters should give an indication of whether the radiation damping can be used as an indicator of which draft is most appropriate (where knowledge of the optimal total damping is known). A correlation between the free-float response and the maximum power under the application of different mechanical damping values would indicate the free-float response amplitude ratio as an effective selection criterion.

The free-float Response Amplitude Ratio of the floats (given by Equation (3.3)) combines the added mass, radiation damping and excitation force together with hydrostatic stiffness, which is independent of draft of the vertical circular cylinder, and the float mass. The objective is to understand the relationship between free float response amplitude $|z_a|$ and the power output of the same float P when subject to mechanical damping, R. To do this comparison it is necessary to a) understand variation of hydrodynamic parameters with draft, b) specify mass (two types considered) and c) calculate response and power (as per figure 6.4).

The hydrostatic stiffness is dependent on the cross-sectional area of the float at the water plane (see Section 3). A draft variation for a float for which the water-plane area remains constant allows for a variation in submerged float geometry without varying the hydrostatic stiffness, thus reducing the parameters to consider.

Three float geometries are considered in this section at different depths (see Figure

6.1). The simplest of these three geometries is the flat-based cylinder which has a uniform cross-section, hence has a constant hydrostatic stiffness at all drafts (see Figure 6.1a). The flat-based cylinder has commonly been used in published research on wave-body interactions and is predefined explicitly in WAMIT (as discussed in Appendix C). The second geometry considered is a hemispherical-based cylinder (see Figure 6.1b). This is only analysed at drafts at which the hemispherical base is fully submerged, hence the hydrostatic stiffness remains constant. By comparison to the flat based cylinder, the hemispherical based cylinder allows for an analysis of how geometry changes below the free surface affect the hydrodynamic parameters. The third, and most complex, geometry is called ConTop in this chapter and consists of a uniform vertical cylinder, below which is a conical section, below which is another uniform vertical cylinder, below which is a curved section (see Figure 6.1c). This is analysed for both drafts in which the hydrostatic stiffness remains constant (such that the free-surface is located at the middle straight section) and at a selection of drafts over which the hydrostatic stiffness varies. The analysis of ConTop enables the scope of the conclusions drawn from the more simplistic geometries to be verified.

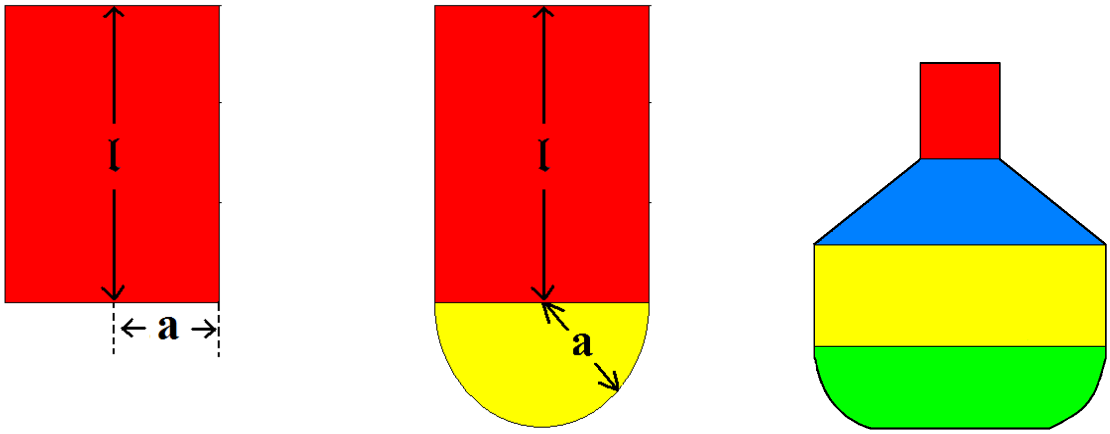

(a) Flat-Based Cylinder

(b) Hemispherical-Based Cylinder

(c) ConTop

Figure 6.1: Flat-based cylinder with radius a and draft l and Hemispherical-based cylinder with a straight section with radius a and draft l and a hemispherical base with radius a; $a = 5$ m and $l = 5$, 10 or 15 m

6.2.1 Effect of Submerged Geometry Variations

The variation of added mass, excitation force, and radiation damping with draft is shown in Appendix I for all three geometries. As the draft of both the flat-based and hemispherical based cylinder is increased, the radiation damping and excitation force are decreased, and the added mass is decreased at lower frequencies and increased at higher frequencies.

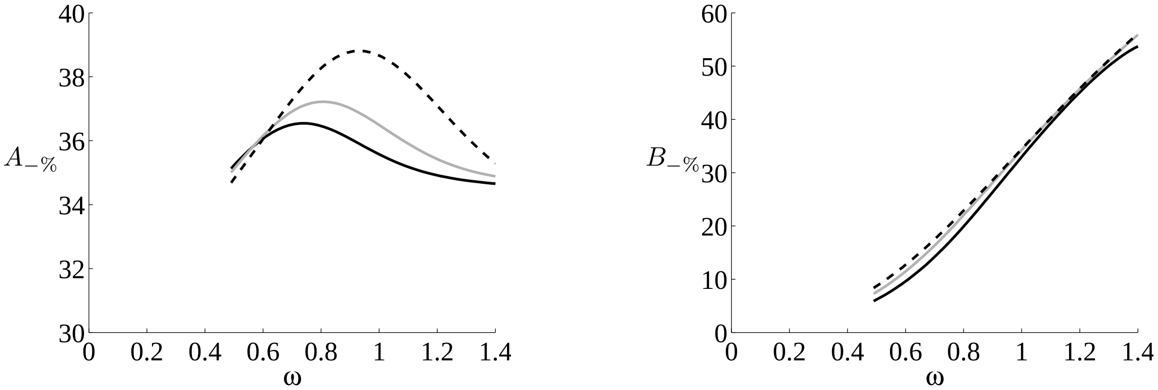

(a) Added Mass: $A_{-\%} = 100 - 100\frac{|A_h|}{|A_f|}$ (b) Radiation Damping: $B_{-\%} = 100 - 100\frac{|B_h|}{|B_f|}$

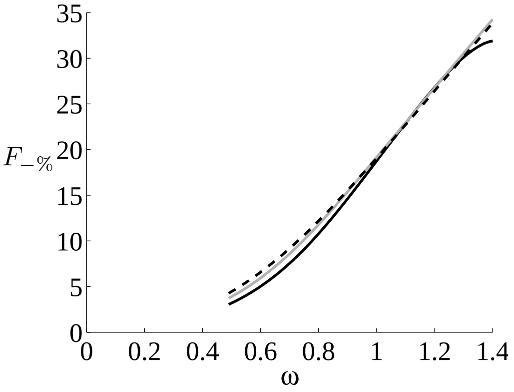

(c) Excitation Force: $F_{-\%} = 100 - 100\frac{|F_h|}{|F_f|}$

Figure 6.2: Percentage reduction in hydrodynamic parameters from the flat based cylinder of radius $a = 5$ m and draft l (see Figures 6.1a and I.1) to the hemispherical-based cylinder of radius a and straight section length l (see Figures 6.1b and I.2); A_f, B_f and F_f are the flat-based cylinder's added mass, radiation damping and excitation force respectively, and A_h, B_h and F_h are the hemispherical-based cylinder's added mass, radiation damping and excitation force respectively:
KEY:
Solid black line, $l = 3a$; Grey line, $l = 2a$; Dashed black line, $l = a$

Comparison of the hydrodynamic parameters at different drafts for the flat and hemispherical based cylinders with equal length straight sections is shown in Figure 6.2. The effect of including a hemispherical base to the straight cylinder is to decrease the added mass by 35 to 40% at all frequencies and decrease the radiation damping and excitation force with increasing frequency with a maximum decrease of 57 % and 35 % respectively at high wave frequencies. The decrease in all three hydrodynamic parameters due to the inclusion of the hemispherical base is more significant for the shallower draft floats (such that the dashed line is greater than the grey and black soild lines in figure 6.2) over the majority of the frequency range. This indicates that geometry variations close to the free surface are of greatest importance in float designs.

6.2.2 Radiation Damping as a Geometry Selection Criterion

The radiation damping is the parameter which varies the greatest between drafts for both the flat based and hemispherically based cylinders (see Appendix Sections I.1.1 and I.1.2). Similarly, changes of ConTop draft for which the free surface remains at the middle vertical straight edge of the geometry results in only minor variations in added mass and excitation force compared to large variations in radiation damping (see Appendix I.1.3). This indicates that selecting drafts based on the damping alone could be sufficient to select the most appropriate float draft from a range of drafts with constant hydrostatic stiffness.

The added mass, excitation force and radiation damping all vary considerably however between drafts of ConTop which have different hydrostatic stiffness values (see Appendix I.1.3). Selecting drafts from a selection of drafts in which the water-plane area varies therefore requires a more complex criteria than the radiation damping alone.

6.2.3 $|d_z|_{R=0}$ as a Geometry Selection Criterion

Although less than the radiation damping in some cases, the added mass and excitation force do vary with draft so a measure which accounts for the variation in all three parameters would be preferable. The free-float response amplitude ratio ($|d_z|_{R=0}$) connects all three parameters (Equation (3.1) with $R = 0$), however in order for power to be absorbed a mechanical damping force must be applied, thus varying the float response. This section determines whether free-float response can be used as an indicator of which float draft will absorb the most power over a given frequency range when different values of mechanical damping are applied.

Three sets of geometries are considered. The first set consists of three drafts of flat based cylinder with l = 5 m, 10 m and 15 m; the second set consists of 6 drafts of ConTop for which the free-surface is located along the middle uniform cylindrical section, hence the water-plane area and hydrostatic stiffness remain constant; and the third set consists of 6 drafts of ConTop over which the hydrostatic stiffness is varied.

Both the $|d_z|_{R=0}$ and power require the mass of the floats to be specified. Two different mass cases are considered within each geometry set such that the floats are neutrally buoyant with a draft dependent mass equal to the displaced mass ($M = M_m$) or have a constant mass which is independent of draft. The constant masses considered are equal to the displaced mass of each the drafts within the set.

The power further requires that a mechanical damping value be specified. Two cases of mechanical damping are considered within each geometry set such that it is either optimal for the float mass considered ($R = R_{opt}$ using Equation (5.2)) or is constant and independent of float draft. The constant mechanical damping values considered are equal to the maximum radiation damping on each of the drafts within each set.

The natural frequency, ω_0, of the floats is dependent on the added mass, hydrostatic stiffness and mass of the floats such that

$$\omega_0 = \sqrt{\frac{S}{M + A\left(\omega_0\right)}}. \tag{6.1}$$

Draft Dependent Mass

When the mass of the devices is allowed to vary according to the draft ($M = M_m$), the larger the draft the larger the mass, hence the lower the natural frequency (Figure 6.3) and larger the peak in free-float response (Figure J.1a). The peaks in the power curves for each draft are found close to their natural frequencies, resulting in the range of wave frequencies over which each draft results in the greatest power being very similar to those of greatest free-float response (Figure J.1c) for all three geometry sets and all mechanical damping values considered.

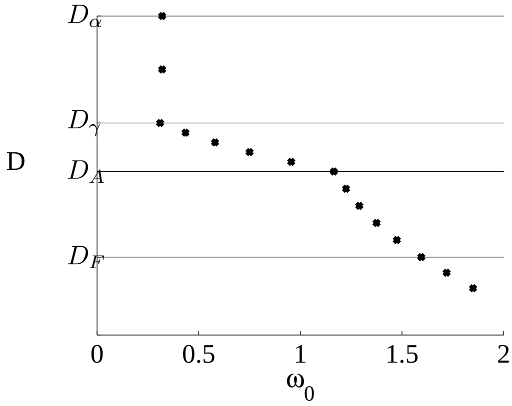

Figure 6.3: Natural frequency (ω_0) of each draft of ConTop (to the nearest 0.2 rad/s) when its mass is equal to its displaced mass of fluid ($M = M_m$) calculated using Equation (6.1)

In both sets of ConTop drafts (with constant and variable hydrostatic stiffness) there is a minor exception to this correlation at low wave frequencies when $R = R_{opt}$. At these low frequencies the greatest power is achieved by the deepest draft float (Figure J.2c) whereas the greatest free-float response is achieved by the shallowest draft float (Figure J.2a). The variation with draft of both the free-float response and power with $R = R_{opt}$ is however small in this frequency range, such that selecting the draft which achieves the greatest free-float response (the shallowest draft) would result in only a small decrease in power compared to the deepest draft float.

In the set of ConTop drafts with varying stiffness, an extremely large peak in free-float response is calculated at a low wave frequency for the draft for which the free surface is located at the upper-inclined surface (Figure J.3a). This peak does not, however, translate to a large power output for any mechanical damping value (Figure J.3c). This extreme peak could be due to motion trapped modes which are coupled oscillations of the body and the fluid which would not decrease with time in the absence of viscosity (McIver and McIver, 2007). The extreme peak is predicted as a result of the limited radiation damping calculated close to the natural frequency. In practice, the extreme peak would not occur however due to the additional forces which would be present for these drafts due to sloshing, wave breaking and viscous effects which are not included within the linear model (Stallard et al., 2009b).

Constant Mass and Constant Stiffness

For the two geometry sets over which the hydrostatic stiffness is constant, when all drafts within the set have the same mass the natural frequencies are very similar, differing only due to the slight difference in added mass. For both sets of drafts, the shallowest draft float achieves the greatest free-float response amplitude ratio for frequencies away from the natural frequency, with different geometries achieving greatest power close to the natural frequency (Figures J.1b and J.2b).

For the flat based cylindrical drafts, the free float response of the constant mass floats decreases as the draft increases at low and high frequencies but increases with increasing draft near the peaks. Small variations in natural frequency can be seen when the constant mass is small. This is because a small mass corresponds to a high natural frequency, which is where the variation of added mass with draft is greatest (see Figure I.1a). The variation in free-float response with draft close to the peaks does not correspond to the power achieved. The shallowest draft float absorbs the greatest power over the entire frequency range when the mechanical damping is constant and over most of the frequency range when the mechanical damping is optimal such that $R = R_{opt}$ (figure J.1d).

For the ConTop drafts of constant mass and stiffness, the shallowest draft float also achieves greatest power when the mechanical damping is constant and large or is optimal (Figure J.2d). When the mechanical damping is small however, there is no obvious method to select the float draft which will result in the greatest power. A comparison of the constant mechanical damping values and the optimal mechanical damping values can provide an explanation of how the magnitude of the constant mechanical damping affects which drafts achieve the greatest power (see Appendix J).

Constant Mass and Draft Dependent Stiffness

Even when the mass remains constant, the natural frequency (see Equation (6.1)) varies between drafts due to large differences in hydrostatic stiffness and variations in added mass.

The greatest power is achieved by different drafts at different wave frequencies (Figure J.3b). There is no obvious correlation between the regions over which each draft achieves the greatest free-float response and the regions over which it achieves the greatest power, regardless of the choice of fixed mass or damping value (Figure J.3d).

The only exception to this is the large peak in free-float response for draft D_ϵ corresponds to a large peak in power at the same frequency when the optimal damping is used ($R = Ropt$). As discussed earlier however, this is unlikely to occur in practice due to additional forces which would be present for this draft which are not accounted for in the linear theory model.

Where the constant mechanical damping value is large, the shallowest draft float does result in the greatest power for a significant proportion of the frequency range but not the entire frequency range (Figure J.3d). There is therefore no obvious method to select drafts to achieve the greatest power when the mass and mechanical damping values are constant and independent of draft.

Summary for all Geometries

When the mass is dependent on the draft such that $M = M_m$, due to the variations in natural frequency with draft, the ranges of frequencies over which each draft achieves the greatest power is indicated by the free-float response and is largely independent of the choice of mechanical damping values (except for low frequencies when $R = R_{opt}$).

Where the mass and hydrostatic stiffness are constant and independent of float draft and the mechanical damping large, the smallest draft float will commonly result in the greatest power for most wave frequencies, but not necessarily the greatest free-float response, particularly close to the natural frequency.

Where the hydrostatic stiffness varies between drafts and the mass is constant, there is no obvious correlation between the regions over which each draft achieves the greatest free-float response and the regions over which it achieves the greatest power

6.3 Optimal Draft: ConTop

The ConTop geometry (defined in Appendix H) allows for a large variation in power with small variations in mass hence draft. It was shown in Section 6.2.2 that the radiation damping alone does not provide a sufficient criterion by which drafts should be selected to achieve greatest power, where the range of drafts considered involves variations in the water-plane area hence stiffness. Further to this it was shown in Section 6.2.3, that the free-float response is also not a sufficient draft selection procedure where the hydrostatic stiffness varies between drafts but the mass does not.

Where the ConTop float is neutrally buoyant at each draft however, it was demonstrated in Section 6.2.3 that the draft which results in the greatest power at a particular wave frequency can be determined from the free-float response, $|d_z|_{R=0}$, without prior knowledge of the magnitude of mechanical damping. The only exception to this is at frequencies where the variation in $|d_z|_{R=0}$ between drafts is negligible, however the variation in power at these frequencies is also negligible.

Sections 6.2.2 and 6.2.3 focused on methods to select drafts so as to achieve greatest power when an unknown quantity of mechanical damping is applied. In contrast, this section considers the selection of draft to achieve greatest power when the power which would be achieved by each draft at each wave frequency is known. In practice, it is likely that the device will be subjected to a range of frequencies in a short period of time. Varying the draft of the float to match every wave is not practical. The ideal selection procedure should allow for the greatest power capture from a device over a likely range of wave frequencies.

When the mechanical damping is optimal ($R = R_{opt}$) and the floats are neutrally buoyant, large variations in float draft from one frequency to the next are required to achieve the greatest power at each wave frequency (Figures 6.4a and 6.4b). When $R = R_{opt}$ and the mass is constant however, large variations in the selected float drafts are seen at higher frequencies, even though the difference in power due to the draft variation is minimal (Figures 6.4c and 6.4d).

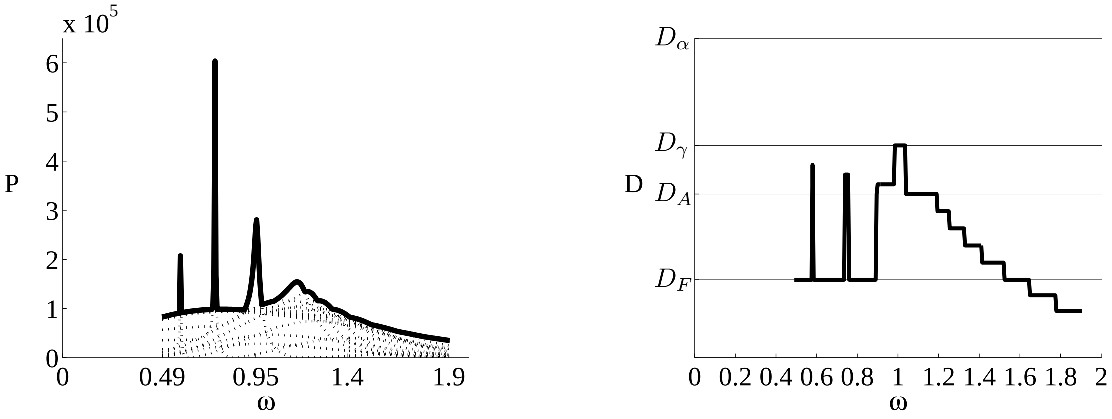

(a) Draft-dependent mass, $M = M_m$

Dotted lines, Power extracted by each draft of ConTop

Thick solid line, Maximum Power achieved at each wave frequency

(b) Draft-dependent mass, $M = M_m$

Drafts of ConTop selected so as to obtain the maximum power at each wave frequency

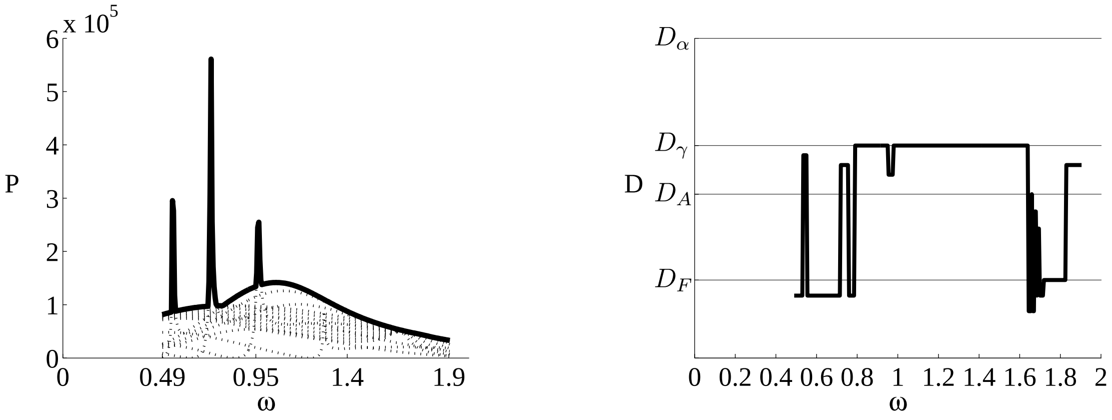

(c) Fixed mass, $M = M_m(D_F) = M_{D_F}$

Dotted lines, Power extracted by each draft of ConTop

Thick solid line, Maximum Power achieved at each wave frequency

(d) Fixed mass, $M = M_m(D_F) = M_{D_F}$

Drafts of ConTop selected so as to obtain the maximum power at each wave frequency

Figure 6.4: Drafts of ConTop geometry from the range D_α to D_H as defined in Figure H.2 which result in the greatest power at each wave frequency when the mechanical damping is optimal such that $R = R_{opt}$ and either the floats are neutrally buoyant (so that the mass is equal to the displaced mass of fluid) such that $M = M_m$ or the mass is constant for all floats and equal to the displaced mass of the draft D_F float such that $M = M_m(D_F) = M_{D_F}$

It could therefore be preferable to select a draft based on a combination of its bandwidth and magnitude so as to achieve a large amount of power over a range of wave frequencies. Bandwidth is measured by Falnes (2002) as the frequency range over which the kinetic energy is greater than half of the maximum kinetic energy. Here, a new measure, χ, is defined which combines the mean and standard deviations of power for a body. The use of power and the two common statistical measures of mean and standard deviation is used instead here to follow on more fluently from other common measures in the industry such as the interaction factor. The most suitable float geometry to absorb power for a range of frequencies will have the lowest value of χ where χ is defined to be

$$\chi(l) = \overline{P} \times Std(P), \tag{6.2}$$

where $\overline{P}$ is the mean power across the frequency range, and $Std(P)$ is the standard deviation of power over the range of frequencies.

Figure 6.5 shows the results of using χ to select ConTop drafts for three different frequency ranges. Whilst the drafts selected to maximise χ do not give the greatest power at all frequencies within the range, they do achieve a large and consistent amount of power which could be preferable when frequencies are expected to vary within a certain range. In particular, there is very little reduction in power in the range $1.4 \leq \omega \leq 1.9$ rad/sec as a result of using draft D_δ which is selected by χ (Figures 6.5c and 6.5d) instead of using the large range of drafts (from D_H to D_γ) which give the greatest power at different frequencies within this frequency range (Figures 6.4c and 6.4d).

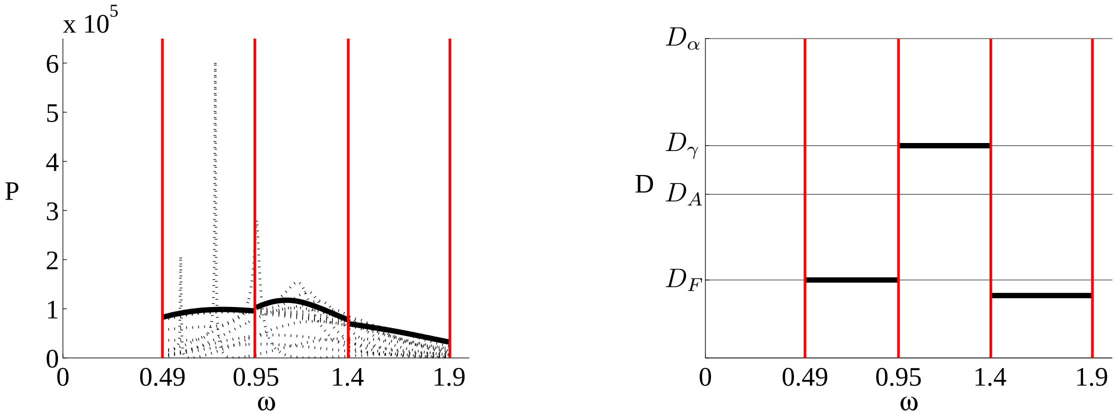

(a) Draft-dependent mass, $M = M_m$

Dotted lines, Power extracted by each draft of ConTop

Thick solid lines, Power extracted by drafts of ConTop selected using Equation (6.2) for each frequency range

(b) Drafts of ConTop selected using Equation (6.2) for each frequency range; Draft-dependent mass, $M = M_m$

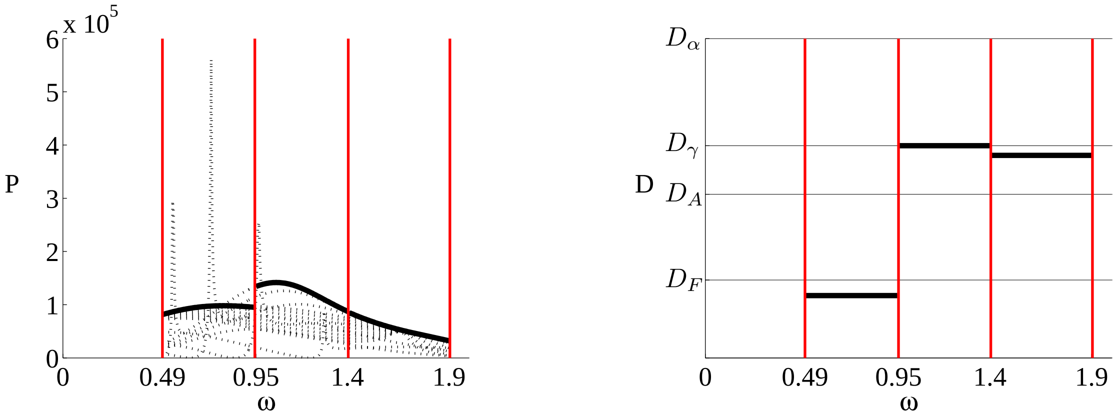

(c) Fixed mass, $M = M_m\left(D_F\right) = M_{D_F}$

Dotted lines, Power extracted by each draft of ConTop

Thick solid lines, Power extracted by drafts of ConTop selected using Equation (6.2) for each frequency range

(d) Drafts of ConTop selected using Equation (6.2) for each frequency range; Fixed mass, $M = M_m\left(D_F\right) = M_{D_F}$

Figure 6.5: Most suitable drafts of ConTop from the range D_α to D_H as defined in Figure H.2 for power extraction (with optimal mechanical damping, $R = R_{opt}$) in three separate frequency ranges according to the χ measure given by Equation (6.2); vertical lines indicate limits of frequency ranges such that:
Frequency range 1: $0.49 \leq \omega < 0.95$;
Frequency range 2: $0.95 \leq \omega < 1.4$;
Frequency range 3: $1.4 \leq \omega \leq 1.9$;

It is recognised that the drafts D_γ to D_η for which the upper inclined surface is located at the free surface are likely to experience additional forces in practice, so the linear theory calculations are not entirely applicable for these drafts. For the purpose of studying the method of draft selection however, they are included in the current section.

6.4 Draft Variation Within an Array

Section 6.1 demonstrated that the radiation damping and added mass on adjacent floats decays with float separation. For linear arrays the damping on nearest neighbours is approximately twice as large as on the next-nearest float. This suggests that the influence of floats at greater than $4a$ spacing could be neglected when evaluating the influence of interactions on array response.

Section 6.2 considered the variation of draft of several geometries determining that the hydrodynamic parameters can be varied significantly with geometry changes close to the free surface having the greatest effect. Frequency ranges corresponding to the greatest free-float response have been shown to predominantly correlate with the frequency ranges of greatest power regardless of the choice of mechanical damping, provided the mass of the floats varies in relation to the draft. Where the mass and hydrostatic stiffness are constant, the radiation damping was determined in Section 6.2.2 to vary significantly between drafts compared to the added mass or excitation force, suggesting radiation damping could provide an efficient draft selection criterion.

This section looks again at the basic vertical circular cylinder (as shown in Figure 6.1a) to determine how they interact with each other in pairs to enable a method to be determined by which pairs could be selected according to the incident wave frequency. Individual wave frequencies are considered at this stage so float drafts are obtained to maximise power output at a single wave frequency rather than obtaining steady power across a range of wave frequencies as considered in Section 6.3.

Three 2×1 arrays of vertical circular cylinders in head seas are considered here in which both floats have equal submerged geometry with drafts $D_5 = 5$ m, $D_{10} = 10$ m or $D_{15} = 15$ m, and are separated by a centre to centre distance of $4a$ where $a = 5$ m is the radius of the float.

6.4.1 Variation in Hydrodynamic Parameters

As with the isolated devices, the variation with draft is much greater for the radiation damping (Figure 6.6) than the excitation force or added mass (Figure I.5 in Appendix I). The off-diagonal elements of the radiation damping matrices are much larger in relation to the diagonal elements than those of the added mass matrix. This supports theory that a measure based on the radiation damping matrix alone could be sufficient as a method to select drafts to be placed within an array.

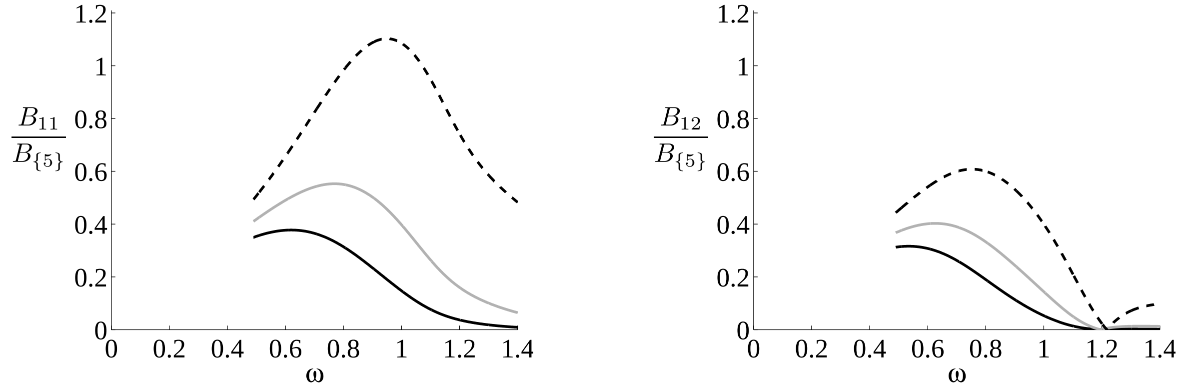

(a) Diagonal Radiation Damping Elements where $B_{\{5\}} = \max(B_0(D_5))$

(b) Off-Diagonal Radiation Damping Elements where $B_{\{5\}} = \max(B_0(D_5))$

Figure 6.6: Radiation damping, B, for three pairs of equal draft flat-based cylindrical floats of radius $a = 5$ m in head seas
KEY:
Solid black line, drafts $= 3a$;
Grey line, drafts $= 2a$;
Dashed black line, drafts $= a$;

For all three drafts considered, the diagonal elements of the added mass and radiation damping matrices vary from the isolated float values by less than 1.12% (Figures I.6a and I.6b). The excitation forces on the array floats vary from the isolated float values by less than 20% (Figures I.6e and I.6f). Whilst the off-diagonal elements of the added mass matrices are negligable (less than 1% of the isolated float values) the off diagonal elements of the radiation damping matrix are up to 90% of the isolated float values (Figures I.6b and I.6d). The use of isolated float values alone to determine properties of the array which depend on the radiation damping is therefore not appropriate.

Figures 6.7c and 6.7d show the comparison between the response amplitude ratio of the floats in the array and the response amplitude ratio of the same float in isolation (with a fixed mass). The response amplitude ratios are significantly different from that of the isolated floats, and even different from one float to the next within each array. This is to be expected from the large interaction effects present in the off-diagonal elements of the radiation damping matrix and the large interaction factors presented for larger arrays in Chapter 5. It further supports theory that floats cannot be selected in order to achieve the greatest response amplitude ratio within arrays based on their performance in isolation.

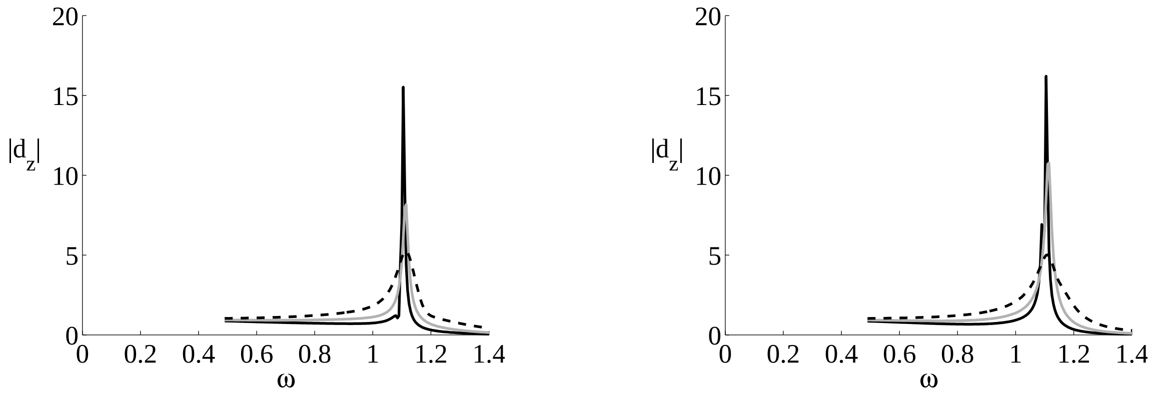

(a) Float 1 (b) Float 2

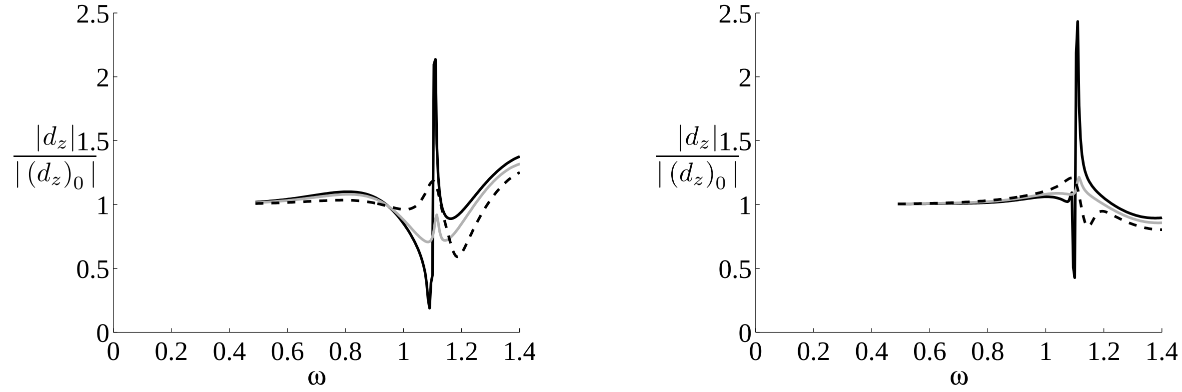

(c) Float 1 (d) Float 2

Figure 6.7: Response Amplitude Ratio, $|d_z|_{R=0}$ (simplified to $|d_z|$ in axes labels), and the free-float response amplitude ratio relative to an isolated device, for three pairs of identical vertical circular cylinder of radius $a = 5$ m with a flat base and varying drafts, including the free-float response when all floats have a mass equal to the displaced mass of fluid from the float with draft $D_5 = 5$ m:
KEY:
Solid black line, both drafts $= 3a$;
Grey line, both drafts $= 2a$;
Dashed black line, both drafts $= a$;

6.4.2 Selecting Geometries Within an Array

An iterative method was developed in Chapter 5 to determine the diagonal mechanical damping matrix which will result in the greatest net power from a fixed mass array at a specific wave frequency. When the diagonal damping matrix elements were selected from an unlimited range they were impractically large at certain frequencies. This section considers whether the amount of mechanical damping which is iteratively selected so as to achieve greatest power could be reduced by decreasing the float draft, thus increasing the radiation damping, without reducing the power absorbed. Floats considered in this section have constant hydrostatic stiffness and mass that are independent of draft.

The initial (base) array for which the iteratively determined optimal diagonal mechanical damping matrix is determined is a 2 × 1 array of equal draft flat-based cylinders. Whilst several alternative drafts can be considered to replace the base array, the selection method must require as few calculations as possible. For the selection of drafts with equal hydrostatic stiffness and mass, the radiation damping has been shown to vary significantly more with draft than the added mass or excitation force. The use of the radiation damping alone to determine the most appropriate draft of cylinder at each wave frequency is therefore considered in this section.

The base array have drafts of $3a$ where the radius $a = 5$ m. Two alternative drafts of $2a$ and a are considered. The radiation damping generally increases with decreasing draft.

The total damping on an array of power absorbing floats is given by the sum of the mechanical and radiation damping matrices such that $F_D = R + B$. As R is a 2×2 diagonal matrix and B a 2×2 dense matrix, the total damping on each float of the base array for unit response is given as the sum of each row of F_D which is written as

$$\Omega_i = R_{i,i} + B_{i,i} + B_{i,j} \tag{6.3}$$

for $i, j \in 1, 2$. All elements of $\Omega_i = R_{i,i} + B_{i,i} + B_{i,j}$ are known, since the matrix, R, is the iteratively selected mechanical damping matrix. For every draft, D, (including the base array and each alternative draft pair) the sum of the i^{th} row of the radiation damping matrix is known and defined as

$$\Theta_i(D) = B_{i,i} + B_{i,j}. \tag{6.4}$$

For each draft, the mechanical damping elements, $R_{i,i}$, can be calculated such that

$$R_{i,i}(D) = \Omega_i - \Theta_i(D). \tag{6.5}$$

$R_{i,i}(D)$ represents the total damping on float i of the base array minus the total radiation damping on float i of the pair of floats with draft D.

For the base array this will result in the iteratively selected mechanical damping values, whereas for the alternative draft pairs it will result in new mechanical damping values. The purpose of selecting a draft is to minimise the mechanical damping required without reducing the power. Applying negative mechanical damping to floats is likely to reduce the net power absorbed however. At each frequency, only the drafts for which $R_{i,i}$ is non-negative on both floats will therefore be considered. The mechanical damping for each draft, D, is therefore given by

$$R_{i,i}(D) = \begin{cases} \Omega_i - \Theta_i(D) & \text{if} \quad \Omega_i \leq \Theta_i(D) \\ NaN & \text{if} \quad \Omega_i > \Theta_i(D) \end{cases} \tag{6.6}$$

where NaN (Not-a-Number) represents an invalid entry (see Figure 6.8). It is the net mechanical damping which must be minimised, which is given for each draft, D, by

$$\sum_{i=1}^{2} R_{i,i}(D) = \begin{cases} \sum_{i=1}^{2} (\Omega_i - \Theta_i(D)) & \text{if} \quad \Omega_i \leq \Theta_i(D) \quad \text{for both of } i = 1, 2 \\ NaN & \text{if} \quad \Omega_i > \Theta_i(D) \quad \text{for either of } i = 1, 2 \end{cases} . \tag{6.7}$$

The criterion by which the pair of floats with drafts D_s are selected at a particular wave frequency is therefore

$$D_s \text{ selected} \iff \text{It is the draft for which } \sum_{i=1}^{2} R_{i,i}(D_s) \text{ is smallest.} \tag{6.8}$$

Any drafts for which $\sum_{i=1}^{N} R_{i,i}$ is an invalid entry (NaN) are not included in the range of drafts considered.

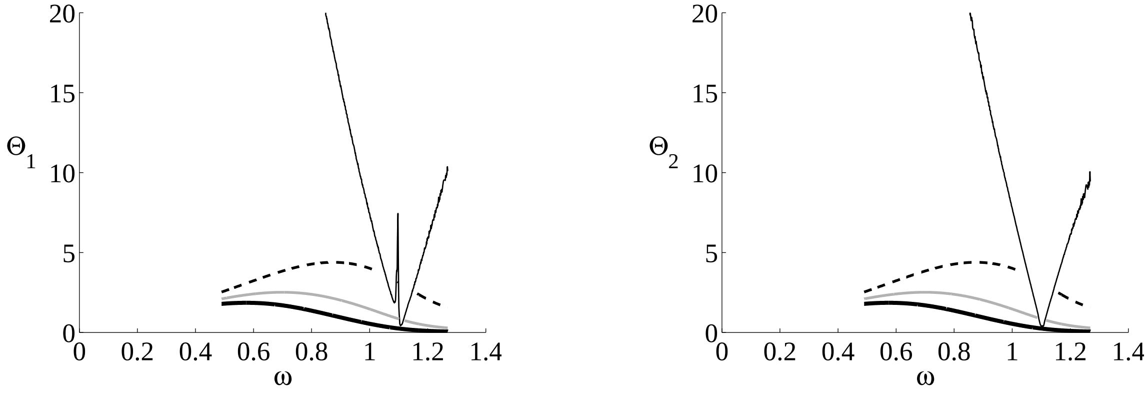

(a) $\Theta < \Omega$, Float 1

(b) $\Theta < \Omega$, Float 2

Figure 6.8: Θ (as given by Equation (6.4)) for pairs of equal draft cylindrical floats of radius a and drafts of $D = 3a$ (thick, solid, black line), $D = 2a$ (grey line) and $D = a$ (Dashed line) at all frequencies where $\Theta < \Omega$, where Ω is given by Equation (6.3) (Thin black line)

The drafts selected using criterion (6.8) are shown in Figure 6.9. At frequencies far from the natural frequency, the shallowest draft pair of floats ($D = a$) are selected as these have the largest radiation damping. As the magnitude of the iteratively selected damping values are reduced closer to the peak frequency, the total radiation damping (Θ) on the shallowest draft pair of floats is greater than the total damping on the base array (Ω). The selected draft is therefore increased to $D = 2a$ in this frequency range. At frequencies very close to the peak, the iteratively selected damping values are less than the radiation damping (Θ) on both of the alternative draft pairs, so the base array ($D = 3a$) is selected.

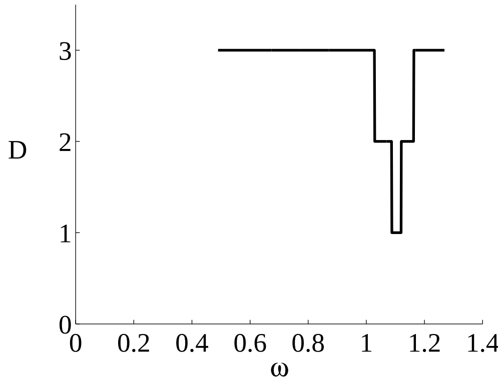

Figure 6.9: Draft D (relative to a) selected to minimise required mechanical damping from the base array without reducing net power (Selected using Criterion (6.8) in which the mechanical damping is determined using Equation (6.6))

The net power absorbed by drafts selected in this way is predominantly greater than or equal to the net power from the base array with the optimum diagonal mechanical damping matrix (Figure 6.10a). At frequencies in the ranges $1.05 \leq \omega \leq 1.055$ rad/sec and $1.88 \leq \omega \leq 1.91$ rad/sec however, the power is reduced by up to 88% compared to the base array by using drafts a and $2a$ respectively which are selected according to condition (6.6). On closer inspection, $R_{i,i}$ of the selected draft, although the least out of the three drafts, are extremely small compared to the equivalent iteratively selected mechanical damping value at these frequencies. A further condition must therefore be included in the selection criteria such that the mechanical damping values of the selected drafts must not only be non-negative, but must be at least 32% of the equivalent iteratively selected mechanical damping values. The draft selection criterion therefore becomes

$$R_{i,i}(D) = \begin{cases} \Omega_i - \Theta_i(D) & \text{where} \quad \frac{\Omega_i - \Theta_i(D)}{R_{i,i}^{[b]}} \geq 0.32 \\ NaN & \text{where} \quad \frac{\Omega_i - \Theta_i(D)}{R_{i,i}^{[b]}} < 0.32 \end{cases} . \tag{6.9}$$

Applying the mechanical damping values calculated using Equation (6.9) within the selection criterion (Equation (6.8)) results in the selection of drafts for which the net power is always at least as great as the base arrays, whilst the mechanical damping is less than or equal to the base array (Figure 6.10b)

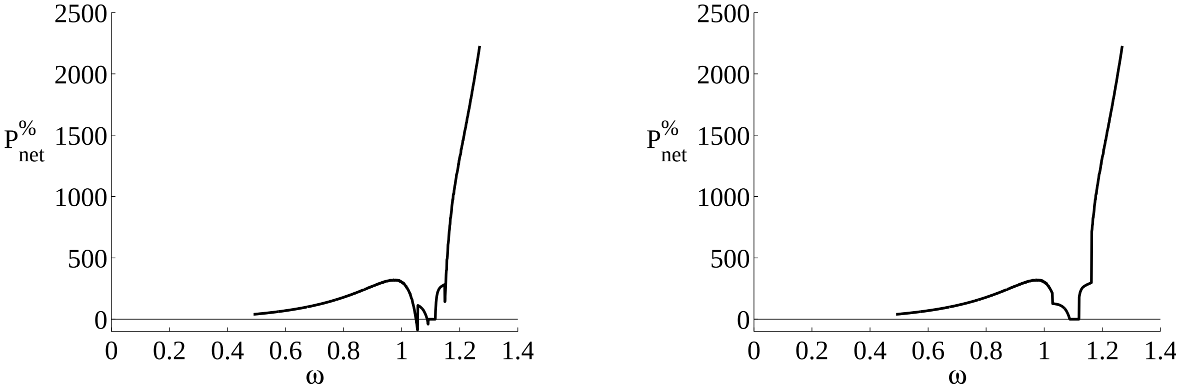

(a) Drafts selected using mechanical damping (6.6)

(b) Drafts selected using mechanical damping (6.9)

Figure 6.10: Percentage increase, $\left(P_{net}^{\%}\right)$, in Net Power of the drafts selected using criterion (6.8) compared to the base array

Where the optimal diagonal mechanical damping matrix is known for a pair of floats at one draft therefore, it is possible at some frequencies to reduce the mechanical damping whilst increasing the net power by varying the draft of the floats. Furthermore, it is possible to select the most appropriate draft for each wave frequency using only knowledge of the base array's optimal diagonal mechanical damping matrix and the radiation damping matrix for each alternative draft.

Further Work

The draft selection for a small array in which both floats have equal draft is considered in this section. A method has been presented to determine which pair of floats would be most appropriate at each wave frequency, where the optimal mechanical damping is known for only one pair of floats. The study has been performed using a choice of only three drafts of floats. It would be beneficial to continue the study to select from a larger range of floats, and a range of floats in which the drafts are not equal within each pair.

The hydrodynamic parameters are determined using WAMIT. In order to allow pairs of floats in which the drafts are not equal, the WAMIT geometry definition file first needs to be modified. Once the study has been extended in this way, the same method can be used to select geometries to be placed within larger arrays using theory of Direct-Neighbour Coupling as discussed in Section 6.1.

Application to a larger array, would require the optimal diagonal mechanical damping matrix to be iteratively determined for a Base Array of equal draft floats. Suppose the floats are numbered with increasing magnitude such that float 1 is the front float, float 2 the float directly adjacent to it and so on. The front float (float 1) could then be fixed so that its draft does not change from the base draft. During the small array study, the mechanical damping matrices for the Alternative Draft Pairs would have been determined for every combination of drafts within a 2×1 array. Based on the Direct-Neighbour Coupling, floats 1 and 2 can then be considered as if they were a 2×1 array. Based on float 1's performance within a 2×1 array, the most appropriate draft for float 2 can be selected. Floats 2 and 3 can then be considered as if they are a 2×1 array, hence float 3's draft selected. The process can be repeated until the drafts of all floats within the array have been selected.

6.5 Chapter Conclusion

Variations in submerged geometry cause variations in added mass, radiation damping and excitation force as well as hydrostatic stiffness if the water-plane area varies between geometries. Application of geometry variation to match the incident wave conditions is best applied through the variation of draft. The masses of the bodies can either be kept constant and independent of mass, or be dependent on draft such as when the floats are neutrally buoyant.

Submerged geometry changes which are closest to the free surface have the most significant effect on the hydrodynamic parameters. A geometry, referred to as ConTop, in which large variations in submerged geometry can be achieved with only small changes in draft is therefore defined and analysed at varying depths in isolation.

The power absorbed by a float at a particular wave frequency is calculated in linear theory as a function of the added mass, excitation force, radiation damping, hydrostatic stiffness, float mass and mechanical damping. Where the water-plane area, hence hydrostatic stiffness remains constant, the variation with draft of radiation damping is much greater than that of the added mass or excitation force. This suggests that where the desired total damping is known, such as the total damping which will result in the greatest power, the radiation damping is the best indicator of which draft is most appropriate.

The free float response accounts for a variation in all of the parameters which are required to calculate the power except for the mechanical damping. It would therefore be desirable to use the free float response as a method to select the drafts which will result in the greatest power without prior knowledge of the mechanical damping values. Where the masses of the floats are draft-dependent, the natural frequency varies significantly and consistently with draft. Where this is the case, the free-float response is a good indicator of the drafts which result in the greatest power at a particular wave frequency, regardless of the mechanical damping value. Where the mass is constant and independent of mass however, there is little correlation between the free-float response and the power absorbed. Where the mass is constant and the mechanical damping value large, the shallower draft floats are found to absorb the greatest power over much of the frequency range.

Where the draft can be varied in accordance with each incident wave frequency, large magnitudes in power can be achieved across a large range of frequencies. The frequency bandwidths over which a large amount of power can be absorbed by each draft can however be small for some drafts. A small variation in incident wave frequency could therefore result in a significant drop in power. A new measure, χ, which combines the magnitude and standard deviation of the power is therefore developed to determine the suitability of a float for power absorption over a specific range of wave frequencies. In certain frequency ranges, χ is found to select a float which achieves a similar power to that which, if floats were selected to achieve the greatest power at each individual wave frequency, would have required a large range of float geometries.

The interactions within an array are found to be most significant between directly adjacent floats for the five element linear array analysed in Section 5. It is therefore possible that float drafts could be varied within an array based only on knowledge of each float's interaction within a two element array with its direct neighbour. This is a theory termed Direct-Neighbour Coupling.

Interactions of three pairs of equal draft cylindrical floats are analysed. As with the isolated bodies, the radiation damping is found to vary more significantly with draft than the added mass or excitation force. Further to this, the diagonal elements of the radiation damping matrix are found to vary significantly with draft and be only slightly smaller in magnitude than the diagonal elements.

Where the optimal diagonal mechanical damping matrix is known for a pair of floats at one draft, it is possible at some frequencies to reduce the mechanical damping whilst increasing the net power by varying the draft of the floats. Furthermore, it is possible to select the most appropriate draft for each wave frequency using only knowledge of the base array's optimal diagonal mechanical damping matrix and the radiation damping matrix for each alternative draft. This method is only valid where the water-plane area and hence the hydrostatic stiffness remain constant.

A study in which this method could be used to select drafts within a large array is proposed. In this study, the first float's draft would be fixed. Based on the first floats performance in a two element array, the directly adjacent float would be selected and fixed. The process would be repeated until the drafts of each element in the array are selected.

Chapter 7

Conclusion

7.1 Overview

This thesis focuses on the modelling of closely spaced groups (arrays) of wave energy devices which each use vertical (heaving) motion to generate electricity. The main aims are to determine the limitations of the applicability of the model, obtain accurate predictions of their behaviour in different sea conditions and determine realistically attainable optimal characteristics.

A mathematical model is presented which combines linear wave theory with a series of linear driven harmonic oscillators to model an array of floating wave energy devices in a train of incident regular waves. Under the assumption of small amplitude waves, the velocity potential is expanded into a perturbation series, of which linear wave theory considers only the terms of the first order. Although it has previously been shown using linear wave theory that large interaction factors may occur at certain combinations of device spacing to the wavelength of regular waves, much of the existing work does not address array configurations or device constraints that are relevant to designers of structure-supported array devices. Specifically, much of the published work addresses relatively large inter-device spacing and optimal mass and damping matrices are typically applied.

The suitability of linear wave theory for application to closely spaced arrays is assessed in this thesis through comparison to small-scale experimental data and to a numerical model in which second-order effects are included. The experimental comparison is performed for the response of a five element array of free-floating hemispherical floats. Power take-off (through the application of a damping force) is not considered in the experimental comparison in order to provide the most stringent test for linear wave theory by permitting large amplitude motions. The second-order comparison is performed for a two element array in which the forces calculated using linear wave theory (first order) are compared to those calculated using terms of the perturbation series up to the second order.

The linear theory model is used to determine the behaviour of a realistic closely spaced array in which float mass cannot change significantly and damping is determined independently of the motion of the other floats within the array and is applied to only the heave oscillation of each float. The maximum power and hence interaction factors that are achievable from fixed geometry arrays in regular seas are thus determined.

Variation of submerged float geometry alters several hydrodynamic parameters at once. The variation of submerged float geometry to manipulate both the power and the magnitude of mechanical damping which needs to be applied to achieve the power is considered. The study is performed through analysis of both simple uniform geometries and a unique complex geometry in isolation, and analysis of the performance of simple uniform geometries at different drafts within a small array.

7.2 Mathematical Conclusions

This section considers the findings from this thesis which are most interesting from a mathematical modelling perspective. The same equation which is commonly used to calculate power for an isolated device is shown to be applicable to arrays of devices provided the mechanical damping matrix is diagonal. This presents a method to determine not only the net power from an array of devices, but also the individual float power outputs.

A new Normalised Interaction Factor, Q, is introduced which gives the power absorbed by devices within an array relative to the maximum power from the same number of isolated devices with set mass and mechanical damping values. This provides a more meaningful measure of performance for the purpose of comparison between devices with different characteristics than the interaction factor q that has traditionally been used to define array performance.

A further new measure, χ, is introduced in this thesis to determine the optimal float (from a selection of floats) for power absorption over a specific range of wave frequencies. This measure considers both the mean and standard deviation of the power over the specified range of wave frequencies. In certain frequency ranges, χ is found to select one float from a range of floats which achieves a similar power to that which, if floats were selected to achieve the greatest power at each individual wave frequency, would have required a large number of different floats from the same range.

A time series of second-order forces is determined from interpolated non-dimensional forces which are made dimensional using wave amplitudes as calculated from a wave spectrum together with random phases. A convergence study is conducted and it is found that second-order wave forces are insignificant within a frequency range specific to the incident wave spectrum, but are greater than or equal to 10 % of the first-order forces at frequencies outside of this range. Quadratic equations for the limit frequencies of this range are presented in this thesis in terms of the significant wave height and the peak period of the incident wave spectrum.

7.3 Engineering Conclusions

This section gives a brief discussion of the main conclusions which are most relevant from the perspective of device developers. Whilst linear theory has been shown to follow the same general trends as experimental results, linear theory models in which a small amount of mechanical damping is included despite the floats being free-floating is found to provide a better fit to experimental data. The magnitude of the damping that is not accounted for in the linear hydrodynamic model could be attributed to a number of physical processes that are typically assumed negligible. These phenomena may include slight differences of geometry between individual floats causing both variations in the hydrodynamic parameters and variations in the scaling (since the scaling factor is based on the float diameter only); the effects of the tank walls causing variations in the radiation damping compared to the open sea case; variations of inter-device spacing that occur in the experiments due to motions in modes which are not included in the numerical model (i.e. in surge); variations in the immersed surface resulting in variations in forcing; and non-linear variations in hydrostatic restoring forces due to non-vertical sides of the floats and large changes in immersed volume during motion. Care must therefore be taken when considering results from both experimental and numerical models, to understand their limitations and assumptions when compared to the final design.

Whilst linear wave theory is applicable to closely spaced arrays in many situations, it excludes all terms of the velocity potential which are higher than first order. The second-order forces are considered in this thesis for a variety of sea states which are determined to be relevant to closely spaced arrays of wave energy devices. Whilst the second-order effects can be significant at low and high frequencies, for most sea states they are insignificant (< 10 % of first order) for much of the range of wave frequencies which closely spaced arrays of wave energy devices are likely to be subjected. Within this important frequency range, it is only at low frequencies when the peak period is large (≥ 11.5 seconds) and at high frequencies when the peak period is small (≤ 7.5 seconds) that second-order effects must be taken into consideration. An increase in significant wave height increases the ratio of second to first-order forces such that second-order forces must also be considered at higher frequencies when the peak period is ≥ 9.5 seconds.

Much published numerical data based on linear wave theory indicates extremely large magnitudes of net power can be absorbed from devices when placed within an array environment compared to when placed in isolation. This data commonly requires highly complex systems to apply the optimal forcing to the devices. A more reasonable system is considered in this thesis in which the floats have a fixed mass and the mechanical damping force is applied to each float independently of the motion of the other floats. For a five element linear array, close to the natural frequency of the devices, where the maximum power is attained for the realistic arrays, the reduction in power compared to the fully optimal arrays is determined to be approximately 3 % in beam seas and 18 % in head seas. Under the restriction that mechanical damping of any one float cannot be dependent on the motion of any other float, the greatest power is achieved by selecting mechanical damping values individually and independently of the radiation damping. For the array in beam seas, power output is found to be greatest when alternate floats are nearly stationary. In head seas, maximum power output is obtained at low wavenumbers if mechanical damping is increased with row number. In contrast, at high wavenumbers, net power output is maximum when damping is greatest on the front float. The peak in net power occurs at a slightly higher wave frequency in head seas than beam seas, with the magnitude of net power at the peak being approximately 4 % greater in head than beam seas. At frequencies below these peaks, the net power is slightly greater in head than beam seas. At frequencies greater than these peaks however, the net power is significantly greater in beam seas.

Application of geometry variation to match the incident wave conditions is best applied through the variation of draft. Submerged geometry changes which are closest to the free surface have the most significant effect on the hydrodynamic parameters. For neutrally buoyant wave energy devices for which float mass is draft dependent, the free-float response can be used to indicate the draft which will result in the greatest power under the application of an unknown quantity of mechanical damping.

Where the mass of the floats is to remain constant (i.e. systems with a counter mass or positively buoyant systems), the radiation damping varies significantly more between drafts than the other hydrodynamic parameters, provided the water-plane area remains constant (i.e. straight-sided axisymmetric floats). When straight-sided axisymmetric floats of fixed mass are placed in isolation, the shallower draft floats are found to absorb the greatest power over much of the frequency range provided the mechanical damping value is large. Where the optimal mechanical damping values are known for an array of straight-sided axisymmetric floats of fixed mass, the required mechanical damping can be reduced at most wave frequencies by varying the draft of individual devices without compromising the net power output.

7.4 Future Work

Several topics addressing the application of linear wave theory to closely spaced arrays and the realistically achievable optimal characteristics of floats within an array have been addressed in this thesis. Whilst each topic is investigated thoroughly and useful findings obtained, they each introduce new topics and questions to be answered. This section gives an overview of several extensions to the thesis which would be interesting to pursue.

The motions noticeable in alternative modes in the wave tank are determined in this thesis to be one of the main contributing factors to the discrepancies between the calculated and experiment magnitudes of response due to the resulting variations in inter-float spacing. A variation of the numerical model in which small motions are permitted in alternative modes would clarify the extent to which these small motions cause these discrepancies. The comparison would be similar in form to the single-mode of motion comparison presented in this thesis, with hydrodynamic parameters obtained from a wave analysis programme (such as WAMIT).

At certain wave frequencies dependent on the sea state, second-order forces are determined in this thesis to be significant within a closely spaced array. The extension to the current model in which multiple modes of motion are permitted could also include second-order response amplitude ratios. The first and second-order non-dimensional response amplitude ratios can also be obtained using a wave analysis programme such as WAMIT and analysed within the model. This more detailed analysis would allow for more precise determination of the frequency ranges over which linear theory is appropriate for use on closely spaced arrays, and offer a more thorough comparison between linear wave theory and experimental data for closely spaced arrays.

The use of free-float response in the comparison between experimental data and linear wave theory in this thesis represents the most extreme test for linear wave theory in terms of amplitudes of float motion and eliminates the need to model a power take-off system. Power values within closely spaced arrays determined using linear wave theory are presented throughout this thesis for different float characteristics. In order to determine the accuracy of these predictions a power take-off system would need to be modelled in the numerical model. Power take-off systems are predominantly non-linear in that they apply mechanical damping for only parts of the wave cycles. In order to include a power take-off system in the numerical calculations, a time-varying model would be required.

The mechanical damping applied in the linear theory calculations in this thesis are the time-averaged values at each wave frequency. The time-varying model could still calculate the float performance in the frequency domain where required through transformation using an FFT. In this way, it could be determined whether a close approximation to the non-linear power take-off system could be made based on time-averaged values in the frequency domain. If a suitable approximation does exist, then a frequency domain model could be used to determine float performance with much higher computational efficiency than a time-domain model. This would also clarify the appropriateness of existing published results in the frequency domain.

The interactions within an array are found to be most significant between directly adjacent floats for a five element linear array. A theory termed direct neighbour coupling is therefore presented in this thesis suggesting that float drafts could be varied within a large array based only on knowledge of each floats interaction within a two element array with its direct neighbour. Where the floats are numbered sequentially from one to N for a linear N-element array such that float 1 is the front float, the geometry of float 1 could be fixed. Based on the most appropriate two-element array in which the front float had the same geometry as float 1, the geometry of float 2 could be selected and fixed. Similarly, based on the most appropriate two element array in which the front float is the same geometry as float 2, float 3 could be determined. This process could be continued until all N elements of the large array have been determined. A procedure would thus be developed in which the optimal geometries to be placed at each position within an array could be determined using only the optimal diagonal mechanical damping matrix for the large array and the knowledge of the interactions of each geometry in a two element array.

In this thesis, drafts are selected from a range of only three drafts (including the original draft) for two element arrays in which both floats within the same array have the same draft. In order to implement the procedure to determine the optimum geometry for each position in a large array, the range of drafts considered should be increased from three to at least ten to improve the accuracy of the results. Every combination of two drafts would need to be analysed to determine the hydrodynamic parameters such that pairs of floats of unequal drafts are also considered. The layout of the array would be linear with fixed, predetermined spacings.

Appendix A

Mathematical Identities

The following are mathematical identities which have been relied upon in this thesis. The symbols, x, y, γ, Z_1 and Z_2 used in this section are arbitrary and do not correspond to any similar symbols used throughout the thesis.

Trigonometric Sum and Product Rules:

$$\cos(x \pm y) = \cos(x)\cos(y) \mp \sin(x)\sin(y) \tag{A.1}$$

$$\cosh(x \pm y) = \cosh(x)\cosh(y) \pm \sinh(x)\sinh(y) \tag{A.2}$$

Exponential Representations:

$$e^{ix} = \cos(x) + i\sin(x) \tag{A.3}$$

Integrals:

$$\int_0^{\pi} \cos(\gamma\cos x)\,\mathrm{d}x = \pi J_0(|\gamma|) \text{ when } \gamma \in \Re \tag{A.4}$$

$$\int_0^{\pi} \sin(\gamma\cos x)\,\mathrm{d}x = 0 \text{ when } \gamma \in \Re \tag{A.5}$$

Infinite Series:

$$J_0(\gamma) = 1 - \frac{\gamma^2}{(1!)^2 \cdot 2^2} + \frac{\gamma^4}{(2!)^2 \cdot 2^4} + \cdots = \sum_{n=0}^{\infty} \frac{(-1)^n \gamma^{2n}}{(n!)^2 \cdot 2^{2n}} \tag{A.6}$$

$$\sinh(\gamma) = \gamma + \frac{\gamma^3}{3!} + \frac{\gamma^5}{5!} + \frac{\gamma^7}{7!} + \cdots = \sum_{n=0}^{\infty} \frac{\gamma^{2n+1}}{(2n+1)!} \tag{A.7}$$

$$\cosh(\gamma) = 1 + \frac{\gamma^2}{2!} + \frac{\gamma^4}{4!} + \frac{\gamma^6}{6!} + \cdots = \sum_{n=0}^{\infty} \frac{\gamma^{2n}}{(2n)!} \tag{A.8}$$

Complex Numbers:

For complex numbers Z_1 and Z_2 with complex conjugates Z_1^* and Z_2^*, if

$$Z_1 = \frac{1}{2}\left(Z_2 + Z_2^*\right) \text{ then } Z_1 = \Re\{Z_2\}. \tag{A.9}$$

Appendix B

Complex Amplitudes

In linear wave theory all oscillations are assumed to be sinusoidal. As a steady state condition is assumed in linear wave theory, there cannot be any transient effects present due to initial conditions. As a result, the linear motions and loads on the body are assumed to oscillate harmonically at the same frequency as the wave loads which excite the body (Faltinsen, 1990, P.39). Using complex representations of these parameters is therefore convenient. The main advantage to using complex amplitudes is that the multiplication of a complex amplitude with $i\omega$ gives the differential of the complex amplitude.

The forces acting on a floating body are assumed to vary sinusoidally with time with an angular frequency of ω with phase constant φ and so can be written as

$$F = |F| \cos \left(\omega t + \varphi \right). \tag{B.1}$$

Using exponential representation (A.3), this can be written as

$$F = \Re \left\{ |F| e^{i(\omega t + \varphi)} \right\} \; = \; \Re \left\{ |F| e^{i\omega t} e^{i\varphi} \right\}. \tag{B.2}$$

Introducing the complex potential of the force, $\hat{F}$, this can be written as

$$F = \Re \left\{ \hat{F} e^{i\omega t} \right\}, \tag{B.3}$$

where

$$\hat{F} = |F| e^{i\varphi} \; = \; |F| \cos(\varphi) + i |F| \sin(\varphi). \tag{B.4}$$

Using the complex number rule given by equation (A.9), the force can alternatively be written as

$$F = \frac{1}{2}\left(\hat{F}e^{i\omega t} + \hat{F}^{*}e^{-i\omega t}\right). \tag{B.5}$$

The displacement, velocity and acceleration of the body can all be written in terms of their complex amplitudes.

It is worth noting that the absolute amplitude of the complex amplitude is equal to the amplitude of the oscillation such that $|\hat{F}| = |F|$.

Appendix C

Defining Geometries in WAMIT

The wave analysis programme, WAMIT, can be used to compute the modulus, phase, real and imaginary parts of various parameters such as the excitation force, added mass, damping, hydrodynamic pressure, and body velocity for specific body geometries in a train of incident waves.

WAMIT contains a lower order method and a higher order method (obtained by setting ILOWH = 0 and 1 respectively in the configuration file). The lower order method involves splitting the body surface into panels. The velocity and the source strength can then be approximated by piecewise constant values on each panel. In the higher order method, the body is represented by 'patches' which are smooth, continuous surfaces in space. The velocity potential on the body is then represented by B-Splines in a continuous manner, and the fluid velocity can be evaluated by analytical differentiation.

When using the higher order method there is an option to use explicit, analytical representation of certain body geometries of the body written in Fortran. This means that the representation of the body geometry is exact and so the only numerical calculation remaining is in the calculation of the velocity potential. For these specific geometries, WAMIT is able to very quickly compute the hydrodynamic parameters. The geometries included in the WAMIT distribution of this geometry definition file include a flat-based circular cylinder, a flat-based elliptical cylinder, a semi-immersed sphere, an ellipsoid, a torus, a Tension Leg Platform, and a ship's hull among others. Each explicitly defined geometry has a small selection of parameters which can be varied, such as the radius and the draught.

Modification of the FORTRAN file in which the geometries are explicitly defined allows for the inclusion of user-defined explicit definitions of alternative geometries. The hemispherical and flat-based-cylindrical floats used throughout this thesis are defined explicitly using the original, WAMIT distribution of the geometry definition file. The more unusual geometries of a hemispherical-based cylinder and ConTop which are studied in Chapter 6 are defined explicitly using patches. The geometry definition file included within WAMIT is modified to include the additional definitions of these geometries at varying depths. The geometry definition is validated by comparison to WAMIT parameters obtained using the lower order method obtained by further definitions of these geometries as lists of panel vertices.

Appendix D

Analytical Froude-Krylov Force

The double integrals in Equation (2.43) can be solved analytically using the Bessel function of the first kind and some well known identities.

The only term in the integrand of Equation (2.43) which includes the variable θ is $\cos(k\,a\sin\psi\cos\theta-\omega\,t)$, which can be expanded using the identity (A.1) to give

$$F_{FK_z}=\frac{\rho\,g\,Ha^2}{2\cosh(k\,d)}\int_0^{\pi/2}\left(\begin{array}{l}\int_0^{2\pi}\left(\begin{array}{c}\cos(k\,a\sin\psi\cos\theta)\cos(\omega\,t)\\+\sin(k\,a\sin\psi\cos\theta)\sin(-\omega\,t)\end{array}\right)\mathrm{d}\theta\\\times\cosh(k(d-a\cos\psi))\cos\psi\sin\psi\end{array}\right)\mathrm{d}\psi.$$

The inner integrand can be solved using identities (A.4) and (A.5) along with the symmetry of the body to give

$$F_{FK_z}=\frac{\rho\,g\,Ha^2}{2\cosh(k\,d)}\int_0^{\pi/2}\left(\begin{array}{l}2\pi J_0\left(k\,a\sin\psi\right)\cos(\omega\,t)\\\times\cosh(k(d-a\cos\psi))\cos\psi\sin\psi\end{array}\right)\mathrm{d}\psi,$$

where J_0 represents the Bessel function of the first kind. As it is the time-averaged force that is of interest, this can be written as

$$F_{FK_z}=\frac{\pi\rho\,g\,Ha^2}{\cosh(k\,d)}\int_0^{\pi/2}\left(\begin{array}{l}J_0\left(k\,a\sin\psi\right)\\\times\cosh(k(d-a\cos\psi))\cos\psi\sin\psi\end{array}\right)\mathrm{d}\psi. \tag{D.1}$$

Using the identity (A.2), the integrand expands to give

$$F_{FK_z}=\frac{\pi\rho\,g\,Ha^2}{\cosh(k\,d)}\int_0^{\pi/2}\left(\begin{array}{l}J_0\left(k\,a\sin\psi\right)\\\times\left(\begin{array}{c}\cosh(kd)\cosh(ka\cos\psi)\\-\sinh(kd)\sinh(ka\cos\psi)\end{array}\right)\cos\psi\sin\psi\end{array}\right)\mathrm{d}\psi.$$

The terms $J_0\left(k\,a\sin\psi\right)$, $\sinh(ka\cos\psi)$ and $\cosh(ka\cos\psi)$ can be expanded to their infinite series using (A.6), (A.7) and (A.8) to give

$$F_{FK_z} = \frac{\pi\rho\,g\,Ha^2}{\cosh(k\,d)}\int_0^{\pi/2}\left(\begin{array}{c} \sum_{n=0}^{\infty}\frac{(-1)^n(k\,a\sin\psi)^{2n}}{(n!)^2\cdot 2^{2n}} \\ \times\left(\begin{array}{c} \cosh(kd)\sum_{n=0}^{\infty}\frac{(ka\cos\psi)^{2n}}{(2n)!} \\ -\sinh(kd)\sum_{n=0}^{\infty}\frac{(ka\cos\psi)^{2n+1}}{(2n+1)!}\cos\psi\sin\psi \end{array}\right)\end{array}\right)\mathrm{d}\psi.$$

Expanding the infinite series to the order of 10 and integrating gives

$$F_{FK_z} = \frac{\pi\rho\,g\,Ha^2}{\cosh(k\,d)}\left(\gamma_2\cosh\left(kd\right)+\gamma_3\sinh\left(kd\right)\right), \tag{2.44}$$

Where

$$\gamma_2 = \left(\begin{array}{c} 1+\frac{a^2k^2}{8}-\frac{a^4k^4}{576}+\frac{a^6k^6}{46080}-\frac{a^8k^8}{5160960}+\frac{a^{10}k^{10}}{796262400}-\frac{29a^{12}k^{12}}{78033715200} \\ +\frac{a^{14}k^{14}}{249707888640}-\frac{53a^{16}k^{16}}{337105649664000}+\frac{a^{18}k^{18}}{6742112993280000}-\frac{a^{20}k^{20}}{148326485852160000} \end{array}\right)$$

and

$$\gamma_3 = \left(\begin{array}{c} -6758061133824000\,ak+39070080\,a^{11}k^{11} \\ -868224\,a^{13}k^{13}+19152\,a^{15}k^{15}-42\,a^{17}k^{17}+a^{19}k^{19} \end{array}\right)\cdot\frac{1}{10137091700736000}.$$

Appendix E

Numerical Froude-Krylov Force

Equation (2.43) can be evaluated numerically using the composite trapezoidal rule twice.

E.1 The Composite Trapezoidal Rule

The composite trapezoidal rule approximates the definite integral of a function, $f(x)$, as the sum of several trapeziums. This is achieved by dividing the domain into $n+1$ discrete points such that $\overrightarrow{x} = x_0, x_1, x_2, \cdots, x_{n-1}, x_n$, where x_0 and x_n are the limits of the integration and $\delta x = x_{i+1} - x_i$ is the increment size, and calculating the function at each. The integral of the function between each adjacent pair in the domain, $\int_{x_i}^{x_i+1} f(x)\mathrm{d}x$, can be approximated by the area of a trapezium with vertices $(x_i, 0)$, $(x_i, f(x_i))$, $(x_{i+1}, 0)$ and $(x_{i+1}, f(x_{i+1}))$ such that

$$\text{Area of Trapezium} = \frac{1}{2}\left(f\left(x_{i+1}\right) + f\left(x_i\right)\right)\delta x.$$

These areas can be summed to approximate the integral between the limits x_0 and x_n:

$$\int_{x_0}^{x_n} f(x)\mathrm{d}x = \left(\frac{1}{2}\left(f(x_0) + f(x_n)\right) + \sum_{i=1}^{n-1} f\left(x_i\right)\right)\delta x. \tag{E.1}$$

E.2 Application to Equation (2.43)

Equation (2.43) contains a double integral whose domain contains both θ and ψ. The angles θ and ψ must be divided into n sections of size $\delta\theta$ and m sections of size $\delta\psi$

respectively such that

$$\begin{aligned} \overrightarrow{\theta} &= [0, \delta\theta, 2\delta\theta, \cdots, (\theta_{n-2})\delta\theta, 2\pi] \\ \text{and} \quad \overrightarrow{\psi} &= [0, \delta\psi, 2\delta\psi, \cdots, (\psi_{m-2})\delta\psi, \frac{\pi}{2}\delta\psi]. \end{aligned}$$

The body surface is thus divided into panels of finite size, $\mathrm{d}S_b = a^2 \sin\psi \delta\theta\delta\psi$. Equation (2.43) can be rewritten as

$$F_{FK_z} = \frac{\rho\, g\, H a^2}{2\cosh(k\, d)} \int_0^{\pi/2} \int_0^{2\pi} I\left(\theta, \psi\right) \mathrm{d}\theta \mathrm{d}\psi,$$

where $I\left(\theta, \psi\right)$ is the integrand given by

$$I\left(\theta, \psi\right) = \cosh(k(d - a\cos\psi)) \cos(k\, a \sin\psi \cos\theta - \omega\, t) \cos\psi \sin\psi.$$

Applying the composite trapezoidal rule twice gives

$$F_{FK_z} = \frac{\rho\, g\, H a^2}{2\cosh(k\, d)} \left(\left(\frac{1}{2} \left(G\left(\theta, \psi_0\right) + G\left(\theta, \psi_n\right) \right) + \sum_{i=1}^{m-1} G\left(\theta, \psi_i\right) \right) \delta\psi \right), \tag{2.45}$$

where

$$G\left(\theta, \psi_i\right) = \left(\frac{1}{2} \left(I\left(\theta_0, \psi_i\right) + I\left(\theta_n, \psi_i\right) \right) + \sum_{j=1}^{n-1} I\left(\theta_j, \psi_i\right) \right) \delta\theta.$$

Appendix F

Derivation of the Full Power Equation (2.49)

The mechanical power, P, of a moving body is a function of the external force, F_{ext}, on the body multiplied by the body's velocity, U:

$$P(t) = F_{ext}(t)U(t).$$

F_{ext} and U can alternatively be written in terms of their complex amplitudes using Equation (B.5) to give

$$\begin{aligned} P(t) &= \frac{1}{4}\left(\hat{F}_{ext}e^{i\omega t} + \hat{F}^*_{ext}e^{-i\omega t}\right)\left(\hat{U}e^{i\omega t} + \hat{U}^*e^{-i\omega t}\right) \\ &= \frac{1}{4}\left(\hat{F}_{ext}\hat{U}e^{i2\omega t} + \hat{F}^*_{ext}\hat{U}^*e^{i2\omega t} + \hat{F}^*_{ext}\hat{U} + \hat{F}_{ext}\hat{U}^*\right), \end{aligned} \tag{F.1}$$

in which the superscript symbol, '$*$', represents the complex conjugate. The first two terms of this expansion, $\hat{F}_{ext}\hat{U}e^{i2\omega t} + \hat{F}^*_{ext}\hat{U}^*e^{i2\omega t}$, represents an oscillating quantity with complex amplitude $\hat{F}_{ext}\hat{U}$ and frequency 2ω which when averaged over time is zero. The time averaged power is therefore given by

$$P = \frac{1}{4}\left(\hat{F}^*_{ext}\hat{U} + \hat{F}_{ext}\hat{U}^*\right). \tag{F.2}$$

Using Equation (B.3) this can be rewritten as

$$P = \frac{1}{2}\Re\left\{\hat{F}^*_{ext}\hat{U}\right\}. \tag{2.47}$$

The external force comes from the waves and so is the sum of the excitation force, F_e, and radiation force, F_r, (see Section 2.2.2). Using Equation (2.34) the power can therefore be written as

$$\begin{aligned}
P &= \frac{1}{2}\Re\left\{\left(\hat{F}_e^* - \hat{U}^*\left(B - i\omega\hat{A}\right)\right)\hat{U}\right\} \\
&= \frac{1}{2}\Re\left\{\hat{F}_e^*\hat{U}\right\} - \frac{1}{2}\Re\left\{\hat{U}^*\left(B - i\omega\hat{A}\right)\hat{U}\right\} \\
&= \frac{1}{2}\Re\left\{\hat{F}_e^*\hat{U}\right\} - \frac{1}{2}\hat{U}^*B\hat{U}. \qquad \text{(F.3)}
\end{aligned}$$

Expanding the complex amplitudes into their real and imaginary parts results in

$$P = \begin{array}{ccc} & \dfrac{1}{2} & \Re\left\{\begin{array}{l} \Re\left\{\hat{F}_e\right\}\Re\left\{\hat{U}\right\} + \Im\left\{\hat{F}_e\right\}\Im\left\{\hat{U}\right\} \\ -i\Im\left\{\hat{F}_e\right\}\Re\left\{\hat{U}\right\} + i\Re\left\{\hat{F}_e\right\}\Im\left\{\hat{U}\right\} \end{array}\right\} \\ - & \dfrac{B}{2} & \left(\begin{array}{l} \left(\Re\left\{\hat{U}\right\}\right)^2 + \left(\Im\left\{\hat{U}\right\}\right)^2 \\ +i\Re\left\{\hat{U}\right\}\Im\left\{\hat{U}\right\} - i\Im\left\{\hat{U}\right\}\Re\left\{\hat{U}\right\} \end{array}\right) \end{array}. \qquad \text{(F.4)}$$

Now consider a set of terms, C_z, which equate to zero when summed together:

$$C_z = \left(\begin{array}{l} \frac{1}{8(B)}\left(\left(\Re\left\{\hat{F}_e\right\}\right)^2 - \left(\Re\left\{\hat{F}_e\right\}\right)^2\right) \\ +\frac{1}{8(B)}\left(\left(\Im\left\{\hat{F}_e\right\}\right)^2 - \left(\Im\left\{\hat{F}_e\right\}\right)^2\right) \\ +i\frac{1}{8(B)}\left(\Im\left\{\hat{F}_e\right\}\Re\left\{\hat{F}_e\right\} - \Im\left\{\hat{F}_e\right\}\Re\left\{\hat{F}_e\right\}\right) \end{array}\right) = 0. \qquad \text{(F.5)}$$

C_z can be added to Equation (F.4) without affecting the value of P, so that the terms can be rearranged to give Equation (2.49):

$$P = \frac{1}{8}\hat{F}_e^*B^{-1}\hat{F}_e - \frac{1}{2}\left(\hat{U} - \frac{1}{2}B^{-1}\hat{F}_e\right)^* B\left(\hat{U} - \frac{1}{2}B^{-1}\hat{F}_e\right).$$

Appendix G

Statistical Measures

In order to mathematically define the statistical measures used in Section 3.4, let the sum over all wave frequencies and all floats be represented by Sum such that

$$Sum = \sum_{i=1}^{N_\omega} \sum_{j=1}^{N}. \tag{G.1}$$

Furthermore, let the experimental and calculated response amplitude ratios be represented by z_E and z_C respectively such that

$$z_E = \left| d_z^{[E]} \left(i, \omega(j)\right) \right| \tag{G.2}$$

$$\text{and} \quad z_C = \left| d_z^{[C]} \left(i, \omega(j)\right) \right|, \tag{G.3}$$

where $\left| d_z^{[E]} \left(i, \omega(j)\right) \right|$ represents the experimental- and $\left| d_z^{[C]} \left(i, \omega(j)\right) \right|$ represents the numerical- response amplitude ratio of body i at frequency $\omega(j)$. Also let a line above a character denote its mean value such that the mean value of the experimental data is given by:

$$\overline{z_E} = \frac{Sum\left(z_E\right)}{N_\omega \cdot N} = \frac{\sum_{i=1}^{N_\omega} \sum_{j=1}^{N} \left| d_z^{[E]} \left(i, \omega(j)\right) \right|}{N_\omega \cdot N}. \tag{G.4}$$

The statistical measures considered in this section can therefore be defined as:
the Mean Absolute Error,

$$MAE = \frac{Sum\left(\left|z_E - z_C\right|\right)}{N_\omega \cdot N}, \tag{G.5}$$

the Root Mean Square Error,

$$RMSE = \sqrt{\frac{Sum\left((z_E - z_C)^2\right)}{N_\omega \cdot N}}, \tag{G.6}$$

the Mean Absolute Percentage Error,

$$MAPE = 100 \times \frac{1}{N_\omega \cdot N} \left(\frac{|z_E - z_C|}{z_E} \right), \tag{G.7}$$

the Root Mean Square Percentage Error,

$$RMSPE = 100 \times \sqrt{\frac{1}{N_\omega \cdot N} Sum \left(\frac{((z_E - z_C)^2)}{z_E} \right)}, \tag{G.8}$$

the Mean Absolute Error as a Percentage of the Experimental Mean,

$$MAEPM = \frac{100}{\overline{z_E}} \times \frac{Sum\left(|z_E - z_C|\right)}{N_\omega \cdot N}, \tag{G.9}$$

the Root Mean Square Error as a Percentage of the Experimental Mean,

$$RMSEPM = \frac{100}{\overline{z_E}} \times \sqrt{\frac{Sum\left((z_E - z_C)^2\right)}{N_\omega \cdot N}}, \tag{G.10}$$

the Coefficient of Residual Mass,

$$CRM = \frac{Sum(z_E) - Sum(z_C)}{Sum(z_E)}, \tag{G.11}$$

the Difference in Variance Ratio,

$$DVR = \frac{Sum\left(z_E - \overline{z_E}\right) - Sum\left(z_C - \overline{z_C}\right)}{Sum\left(z_E - \overline{z_E}\right)}, \tag{G.12}$$

the Maximum Error between any predicted value and its corresponding actual value,

$$ME = \max\left(z_E - z_C\right), \tag{G.13}$$

the Coefficient of Determination,

$$CD = \frac{Sum\left((z_E - \overline{z_E})^2\right)}{Sum\left((z_E - \overline{z_C})^2\right)}, \tag{G.14}$$

and the modelling efficiency,

$$EF = \frac{Sum\,(z_E - \overline{z_E}) - Sum\,(z_C - z_E)}{Sum\,(z_E - \overline{z_E})}. \tag{G.15}$$

The MAE (Mean Absolute Error) gives mean error of the calculated data as a model of the experimental data. The $RMSE$ (Root Mean Square Error) is similar, but considers the squares of the errors, thus making large errors more significant. Both the MAE and the $RMSE$ are given in the same units as the input data, so their values are specific to the case being considered and so useful mainly for comparing similar models. Their values however could not be used to compare the application of models to different variables with different units. It can therefore be useful to give a measure of the error as a percentage of the actual experimental data such as in the $MAPE$ (Mean Absolute Percentage Error), $RMSPE$ (Root Mean Square Percentage Error), $MAEPM$ (Mean Absolute Error as a Percentage of the experimental Mean) and $RMSEPM$ (Root Mean Square Error as a Percentage of the experimental Mean). Care must be taken when considering $MAPE$ and $RMSPE$ as they are sensitive to small experimental values, with singularities given for experimental values of zero. When comparing these four percentage measures of error it is worth considering how, since these represent percentages, a small value at a frequency near the peak frequency can correspond to a large difference between the calculated and experimentally measured values.

The CRM gives the difference between the means of the experimental and calculated values as a ratio of the mean experimental value. Variance indicates the magnitude of the spread of data about its mean value. DVR gives the difference in the variances of the experimental and calculated values relative to the variance of the experimental data. The CD indicates to what extent the spread of the calculated data can explain the variance of the experimental data. EF is suggested to be one of the most important indicators of overall good fit (Mayer and Butler, 1993) with a negative value indicating a model which cannot be recommended as this suggests simply using the mean of the experimental data at all frequencies would be a better model (Loague and Green, 1991).

Together with the statistical values for overall fit of the calculated data to the experimental data it is useful to determine the worst case which is given by ME.

Appendix H

Geometry Specifications of ConTop

It was shown in Section 6.2 that geometry changes close to the free surface cause the greatest effect on the hydrodynamic parameters. For the purpose of draft variation according to the incident wave field, it is therefore desirable to use a shallow draft float for which the hydrodynamic parameters vary greatly with draft. The inclusion of a straight section with a large variation in draft beneath it allows for a large range of parameters to be obtained without varying the hydrostatic stiffness. The inclusion of additional sections in which the water-plane area does vary with draft allows for a large variation in hydrostatic stiffness without a large variation in mass. A float geometry which fits this description is the complex geometry analysed in Stallard et al. (2009b) which is shown in Figure H.1 and is called ConTop from herein.

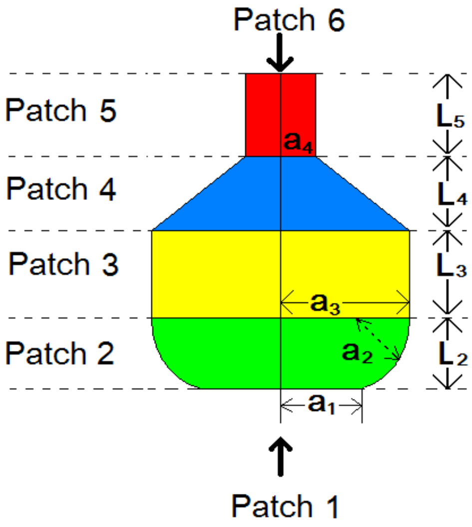

Figure H.1: Diagram of complex geometry called ConTop:
Patch 1 = horizontal circular base of radius $a_1 = 2.21$ m;
Patch 2 = lower outer-quadrant of torus with radius $a_2 = a_3 - a_1 = 2.79$ m and height $L_2 = a_2$;
Patch 3 = vertical circular cylinder of radius $a_3 = 5$ m and height $L_3 = 3.07$ m;
Patch 4 = conical section of height $L_4 = 1.74$ m;
Patch 5 = vertical circular cylinder of radius $a_4 = 1.67$ m and height $L_5 = 3.83$ m;
Patch 6 = horizontal circular lid of radius $a_4 = 1.67$ m

The ConTop geometry consists of a cylindrical section of small radius at the top, below which is a conical section, below which is another cylindrical section of larger radius, below which is the lower outer-quadrant of a torus at the base of which is a flat, circular base. The geometry is defined in WAMIT analytically as a series of patches which are smooth and continuous in space (see appendix C). The specifications (based on an experimental model) and the patches used to define the geometry analytically are shown in Figure H.1. In this thesis the ConTop geometry is analysed at different drafts to determine the effect of the draft variation on different hydrodynamic parameters.

Fifteen drafts of the ConTop geometry are analysed. The drafts are labelled D_X for $X = \alpha$, β, γ, δ, ϵ, ζ, η, A, B, C, D, E, F, G and H as shown in Figure H.2.

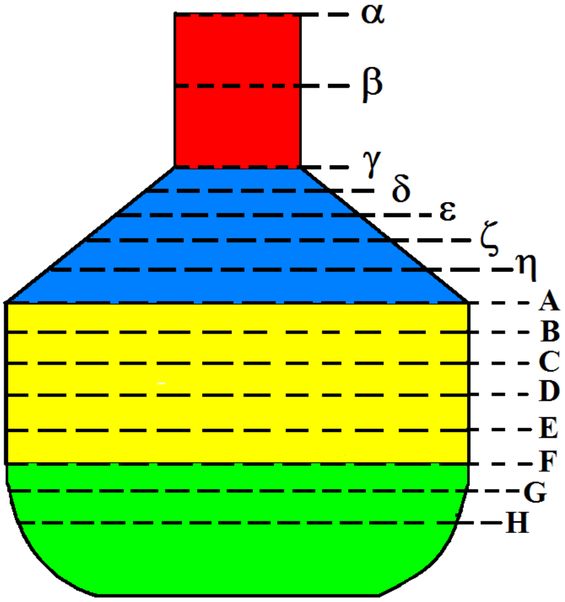

Figure H.2: Diagram of ConTop Geometry with Drafts labelled such that free surface is located along the straight section in still water :
D_α = draft when free surface is located at α: $D_\alpha = L2 + L3 + L4 + L_5$;
D_β = draft when free surface is located at β: $D_\beta = L2 + L3 + L4 + 0.5L_5$;
D_γ = draft when free surface is located at γ: $D_\gamma = L2 + L3 + L4$;
D_δ = draft when free surface is located at δ: $D_\delta = L2 + L3 + 0.8L4$;
D_ϵ = draft when free surface is located at ϵ: $D_\epsilon = L2 + L3 + 0.6L4$;
D_ζ = draft when free surface is located at ζ: $D_\zeta = L2 + L3 + 0.4L4$;
D_η = draft when free surface is located at η: $D_\eta = L2 + L3 + 0.2L4$;
D_A = draft when free surface is located at A: $D_A = L2 + L3$;
D_B = draft when free surface is located at B: $D_B = L2 + 0.8L3$;
D_C = draft when free surface is located at C: $D_C = L2 + 0.6L3$;
D_D = draft when free surface is located at D: $D_D = L2 + 0.4L3$;
D_E = draft when free surface is located at E: $D_E = L2 + 0.2L3$;
D_F = draft when free surface is located at F: $D_F = L2$;
D_G = draft when free surface is located at G: $D_G = 0.8L2$;
D_H = draft when free surface is located at H: $D_H = 0.6L2$

Appendix I

Variation of Hydrodynamic Parameters with Float Draft

Basic hydrodynamic parameters are presented in this section in relation to the geometries considered in Chapter 6. Each geometry is considered at a variety of depths to determine the dependence of each of the hydrodynamic parameters on the draft.

I.1 Isolated Geometries

I.1.1 Flat-Based Cylinder

The first geometry to consider is a flat based cylinder of radius a and draft $3a$, $2a$ or a. As the draft of the flat-based cylinder is increased, the radiation damping and excitation force are decreased, and the added mass is decreased at lower frequencies and increased at higher frequencies.

The maximum ratio of added mass, radiation damping and excitation force from one draft of flat-based cylinder to the next are 1.2, 58.6 and 7.7 respectively. All of these maximum ratios occur at the largest frequency within the specified range ($0.49 \leq \omega \leq 1.4$ rad/sec). The mean across all frequencies of the largest ratios (at each frequency) from one flat-based cylinder to the next are 1.1, 12.1 and 3.1 for the added mass, radiation damping and excitation force respectively.

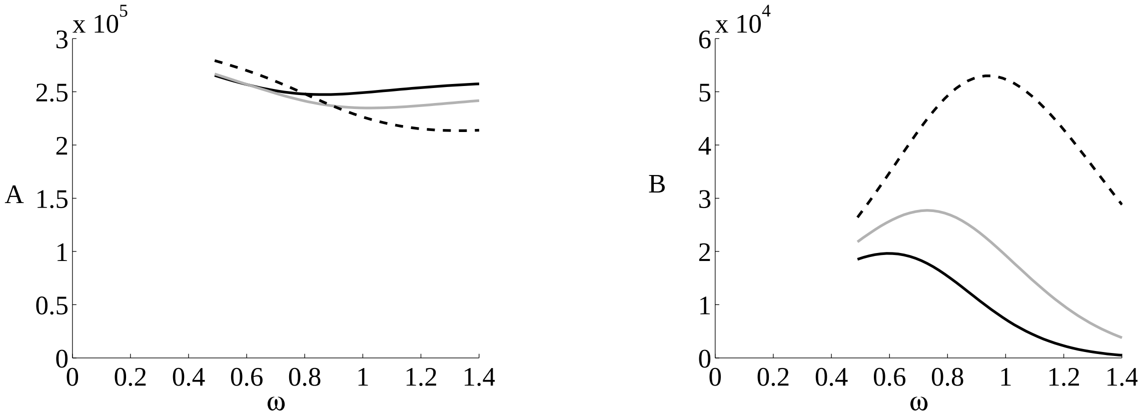

(a) Added Mass

(b) Radiation Damping

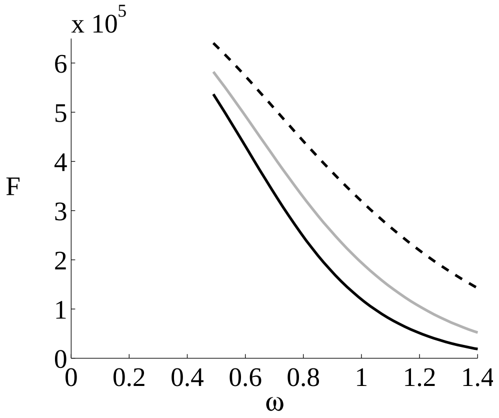

(c) Excitation Force

Figure I.1: Hydrodynamic parameters for a vertical circular cylinder of radius $a = 5$ m with a flat base with length, l:
KEY:
Solid black line, $l = 3a$; Grey line, $l = 2a$; Dashed black line, $l = a$

I.1.2 Hemispherical-Based Cylinder

The hemispherical-based cylinder considered in this section consists of a straight vertical section of radius a and length $l = 3a$, $2a$ or a, and a hemispherical base of radius a. The total drafts considered are therefore $4a$, $3a$ and $2a$.

The general trends of the variation of hydrodynamic parameters with draft are the same as for the flat-based cylinder. The magnitudes of the hydrodynamic parameters are however reduced when compared to the flat-based cylinder whose draft is the same length as the straight section of the hemispherical-based cylinder.

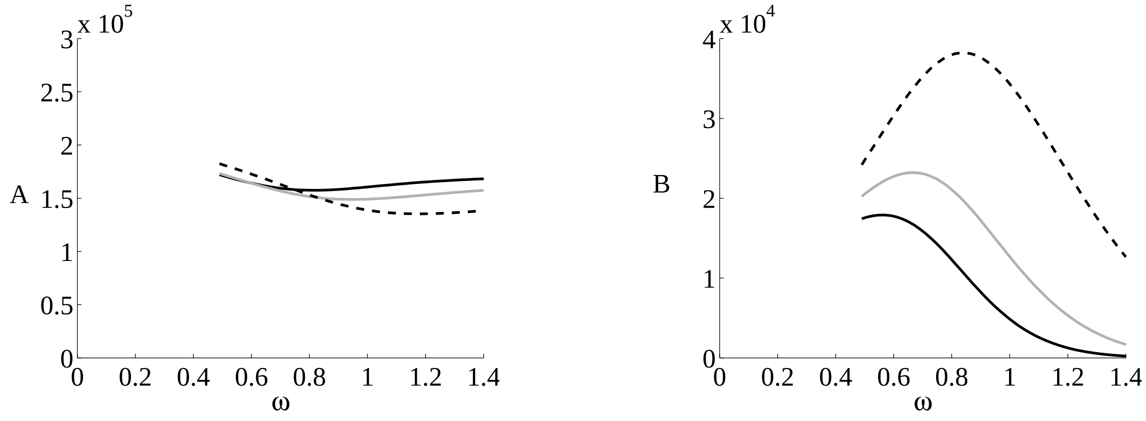

(a) Added Mass (b) Radiation Damping

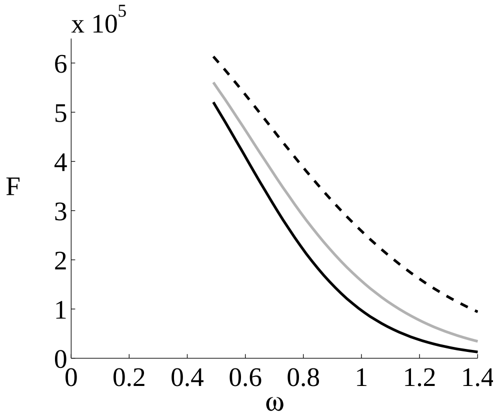

(c) Excitation Force

Figure I.2: Hydrodynamic parameters for a vertical circular cylinder of radius $a = 5$ m with a straight section of length, l and a hemispherical base:
KEY:
Solid black line, $l = 3a$; Grey line, $l = 2a$; Dashed black line, $l = a$

I.1.3 ConTop

The ConTop geometry considered in this section is defined fully in Appendix H.

In Section 6.2 the addition of a hemispherical-base to a cylinder was found to reduce the hydrodynamic parameters whilst preserving the general trends. Drafts D_A to D_F of ConTop are similar in design to the hemispherical-based cylinder, but with a shorter straight section (0 to 3 m) and truncated curved section instead of a hemispherical-base. Like the hemispherical-based cylinder, the hydrodynamic parameters presented in Section I.1.2 for these drafts follow the same trends as the flat-based cylinder.

The variation in parameters between all drafts of ConTop are considered in the following subsections:

Stiffness, Mass and Natural Frequency A variation in area at the water-plane, A_{WP}, results in a variation in hydrostatic stiffness which, under the linear theory assumption of small amplitude, is calculated as $\rho g A_{WP}$ where ρ is the water density and g the acceleration due to gravity (Figure I.3a). The volume and hence displaced mass of fluid, M_m, also varies significantly with draft (Figure I.3b). As with the cylindrical floats, the mass of the float can either be varied with immersed volume (i.e. buoyant) or maintained at a constant value. The natural frequency, ω_0, of each draft is a function of its mass, added mass and hydrostatic stiffness such that $\omega_0 = \sqrt{\frac{S}{M+A}}$. Even when the mass remains constant, the natural frequency varies between drafts due to large differences in hydrostatic stiffness and variations in added mass. When the mass is allowed to vary in relation to the submerged volume, the variations in natural frequency between drafts are large (Figure I.3c).

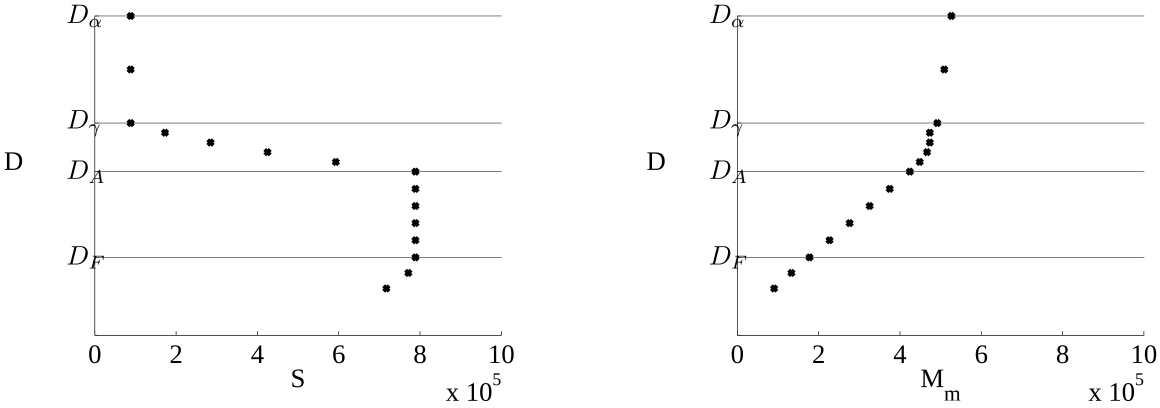

(a) Hydrostatic Stiffness for each draft (b) Displaced mass of fluid for each draft

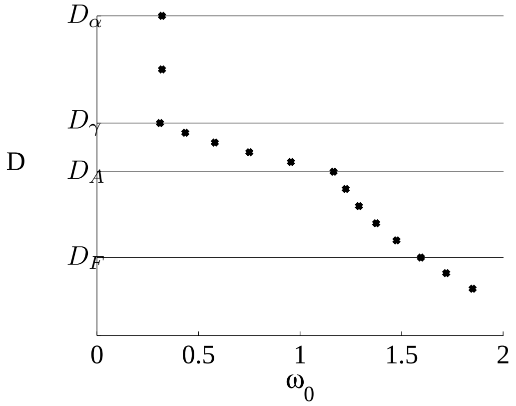

(c) Natural frequency for each draft when ($M = M_m$)

Figure I.3: Hydrostatic stiffness (S), displaced mass of fluid (M_m) and natural frequency (ω_0) when $M = M_m$ for each draft of ConTop

Added Mass (Figure I.4a) When the ConTop is at its deepest draft, D_α, the added mass has a peak at low frequencies, and a trough at high frequencies. As the draft is increased to D_β then D_γ, the magnitude of the values of added mass at the peak and trough are increased. An increase of immersion such that the inclined upper surface is partly immersed (D_γ to D_η), shifts the added mass peaks and troughs towards higher frequencies and reduces their absolute values. Whilst the still water line is located on the middle cylindrical or lower curved sections of float, the frequency variation of added mass is minimal (drafts D_A to D_H). As the draft is reduced along the middle straight section from D_A to D_F, the added mass is however slightly increased at low wave frequencies and decreased at high wave frequencies. Further reductions in draft from D_F to D_H do not significantly change the added mass.

Radiation Damping (Figure I.4b) The radiation damping forms a single peak when plotted against frequency for all ConTop Drafts. As with the added mass, the magnitude of this peak increases with draft from D_α to D_γ, then decreases from D_γ to D_η. The location of the peak is shifted towards increasingly high frequencies as the draft is increased with the free surface located along the upper-inclined section. The peak is located at a frequency higher than 2 rad/sec for draft D_η. A further increase in draft from D_η to D_A (so that the upper-inclined surface is no longer below the free-surface) causes a significant shift in peak to the lower frequencies such that it is located below 1 rad/sec. Any further reductions in draft (from D_A to D_H) cause a slight increase in both magnitude and frequency of the radiation damping peak.

Excitation Force (Figure I.4c) When the free-surface is located along the upper straight section, the excitation force forms a peak when plotted against frequency, with an increase in draft from D_α to D_γ resulting in an increase in magnitude of the peak. As the draft is decreased so that the free surface is located at increasing distances down the upper inclined surface (D_γ to D_η) the peak is shifted toward higher frequencies and decreased in magnitude. A negative excitation force is experienced for an increasing range of lower frequencies for drafts D_ϵ to D_η, such that the magnitude of the excitation force touches zero at one wave frequency. When the draft is decreased with the upper inclined surface above the free surface (drafts D_A to D_H), the excitation force decreases with increasing wave frequency. Only minor increases in excitation force are experienced for all wave frequencies when the draft is increased with the free surface located along the middle straight section (drafts D_A to D_F). Minor decreases of excitation force at low frequencies and increases at high frequencies are obtained due to further decreases in draft from D_F to D_H.

Neutrally Buoyant Free-Float Response Amplitude Ratio (Figure I.4d) Where the upper-inclined surface is completely submerged the $|d_z|_{R=0}$ is small (below

1) with a slight peak in response at low wave frequencies followed by a decrease in neutrally buoyant $|d_z|_{R=0}$ with increasing frequency. An decrease in draft from D_α to D_γ results in an increase in $|d_z|_{R=0}$ at all wave frequencies. Extreme peaks (of 38, 80 and 15 for D_ϵ, D_ζ and D_η respectively) in $|d_z|_{R=0}$ are predicted when the free surface is located at the upper inclined surface, with a decrease in draft corresponding to an increase in the frequency at which the extreme peak is located. For these same drafts $|d_z|_{R=0}$ is zero at a slightly higher frequency than the peak. When the draft is increased so that the upper-inclined surface is completely above the free surface, the peaks in the $|d_z|_{R=0}$ curves are no longer extreme (below 4.5) and do not decrease to zero immediately after the peak frequency. As the draft is decreased from D_A to D_H, the location of the peak is moved to an increasingly high wave frequency, and its magnitude is increasingly reduced.

The extreme peaks predicted when the free surface is located at the upper-inclined surface (drafts D_ϵ to D_η) could be due to motion trapped modes which are coupled oscillations of the body and the fluid which would not decrease with time in the absence of viscosity (McIver and McIver, 2007). The extreme peaks are predicted as a result of the limited radiation damping calculated close to their natural frequencies. In practice, the extreme peaks would not occur however due to the additional forces which would be present for these drafts due to sloshing, wave breaking and viscous effects which are not included within the linear model (Stallard et al., 2009b).

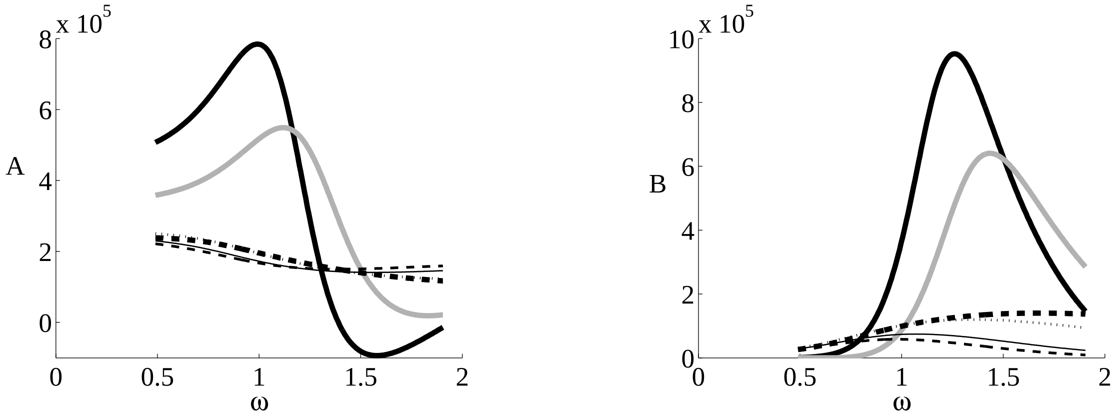

(a) Added Mass

(b) Radiation Damping

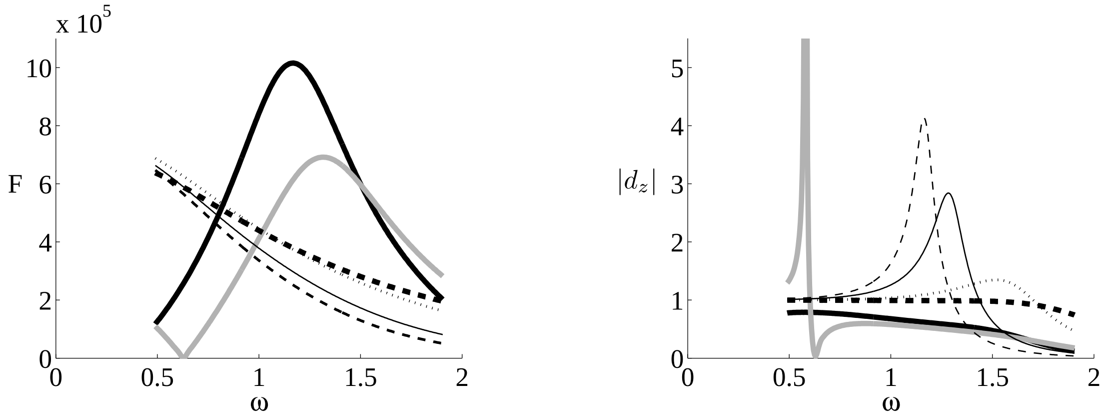

(c) Excitation Force

(d) Neutrally Buoyant Free-Float Response Amplitude Ratio ($\max\{|z_a|\} = 38$)

Figure I.4: Hydrodynamic parameters for ConTop at various drafts defined in Figure H.2:
KEY:
Thick Solid black line, draft D_γ; Solid grey line, draft D_ϵ;
Thin dashed line, draft D_A; Thin Solid black line, draft D_C;
Dotted black line, draft D_F; Thick dashed line, draft D_H

I.2 Array of Flat-Based Cylinders

The hydrodynamic parameters for the cylindrical bodies discussed in Section I.1.1 are presented here within a two-element array. The parameters are given relative to fixed values in Figure I.5, and relative to the equivalent isolated value at the same wave frequency in Figure I.6.

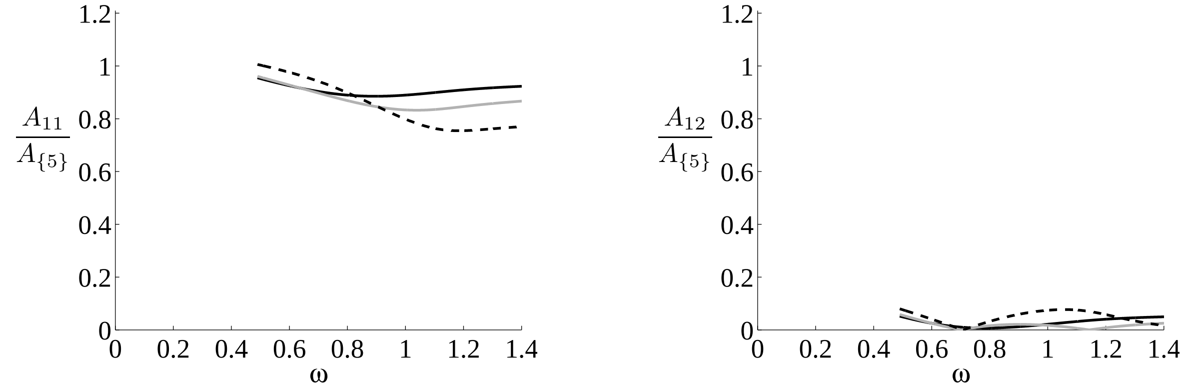

(a) Diagonal Added Mass Elements where $A_{\{5\}} = \max(A_0(D_5))$

(b) Off-Diagonal Added Mass Elements where $A_{\{5\}} = \max(A_0(D_5))$

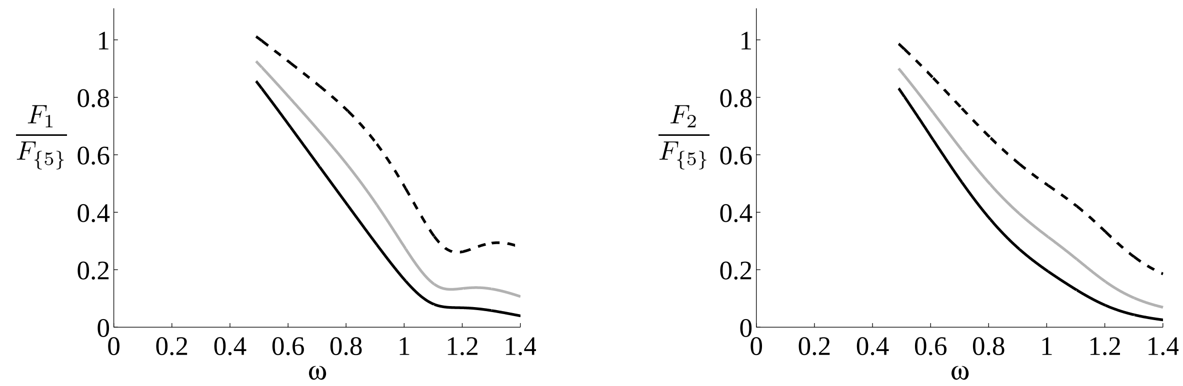

(c) Excitation Force on Float 1 where $F_{\{5\}} = \max(F_0(D_5))$

(d) Excitation Force on Float 2 where $F_{\{5\}} = \max(F_0(D_5))$

Figure I.5: Hydrodynamic parameters for three pairs of identical, cylindrical floats:
KEY:
Solid black line, both flat-based cylindrical floats with drafts $= 3a$;
Grey line, both flat-based cylindrical floats with drafts $= 2a$;
Dashed black line, both flat-based cylindrical floats with drafts $= a$

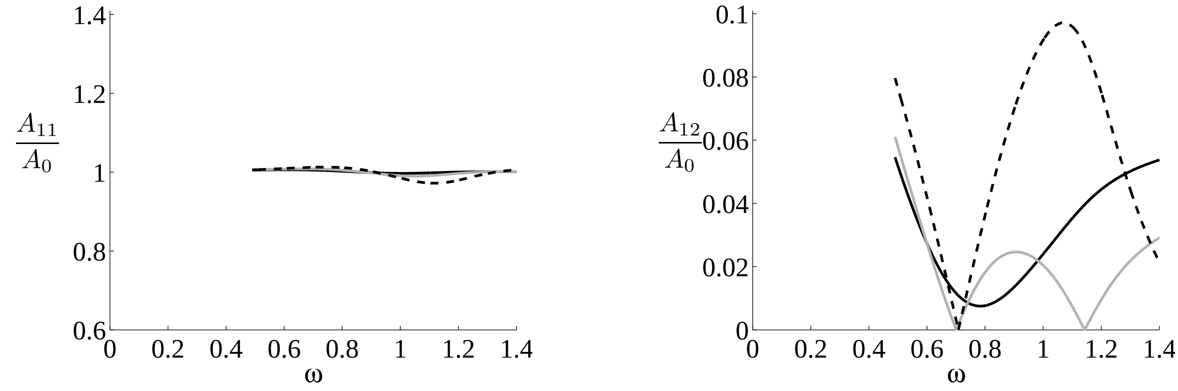

(a) Diagonal Added Mass Elements

(b) Off-Diagonal Added Mass Elements

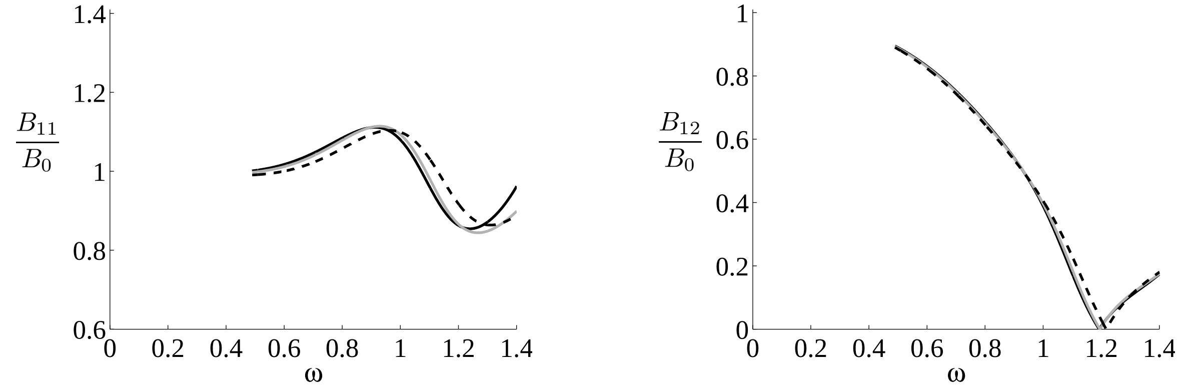

(c) Diagonal Radiation Damping Elements

(d) Off-Diagonal Radiation Damping Elements

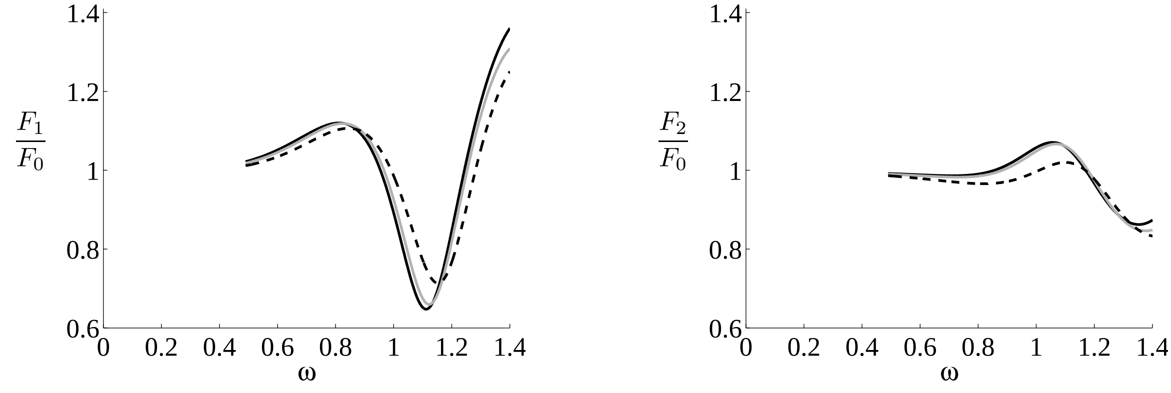

(e) Excitation Force on Float 1

(f) Excitation Force on Float 2

Figure I.6: Hydrodynamic parameters (relative to frequency and draft dependent isolated device parameters) for three pairs of identical vertical circular cylinder of radius $a = 5$ m with a flat base and varying drafts:
KEY:
Solid black line, both drafts = $3a$;
Grey line, both drafts = $2a$;
Dashed black line, both drafts = a;

Appendix J

Relationship Between Response and Power

In this appendix, the free-float response is shown for both flat-based cylinders and ConTop at a variety of drafts. Also shown is the net power which is absorbed by each draft when different values of mechanical damping are applied.

J.0.1 Flat-Based Cylinder

This section considers three drafts of flat-based cylinder with radius a and draft $3a$, $2a$ or a.

Where the mass is allowed to vary according to the draft, the peaks in the power curves for each draft are found close to their natural frequencies, resulting in the range of wave frequencies over which each draft results in the greatest power being very similar to those of greatest free-float response (Figures J.1a and J.1c).

Where the mass is constant, all methods used to calculate the mechanical damping result in the shallower draft floats achieving the greatest power for all frequencies, except very close to the peak when $R = R_{opt}$ (figure J.1d). The same relationship is however not found for the free-float response (Figure J.1b).

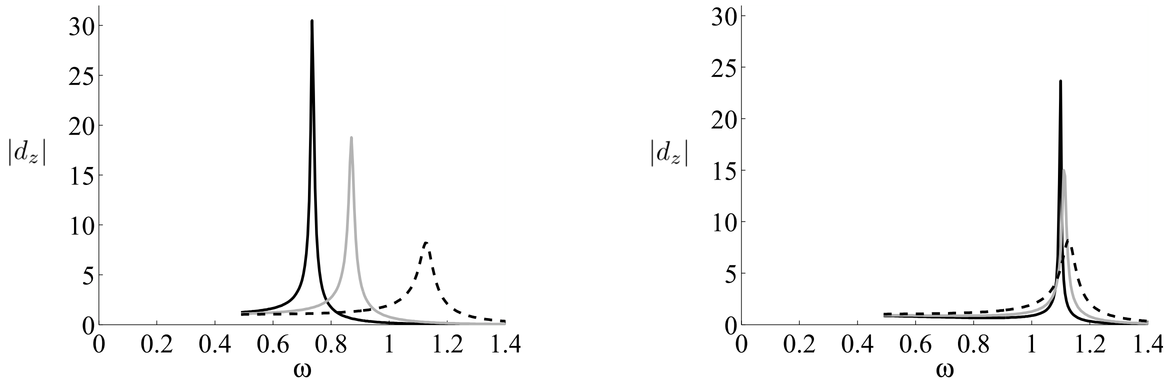

(a) Free-Float Response with $M = M_m$ (b) Free-Float Response with $M = M_5$

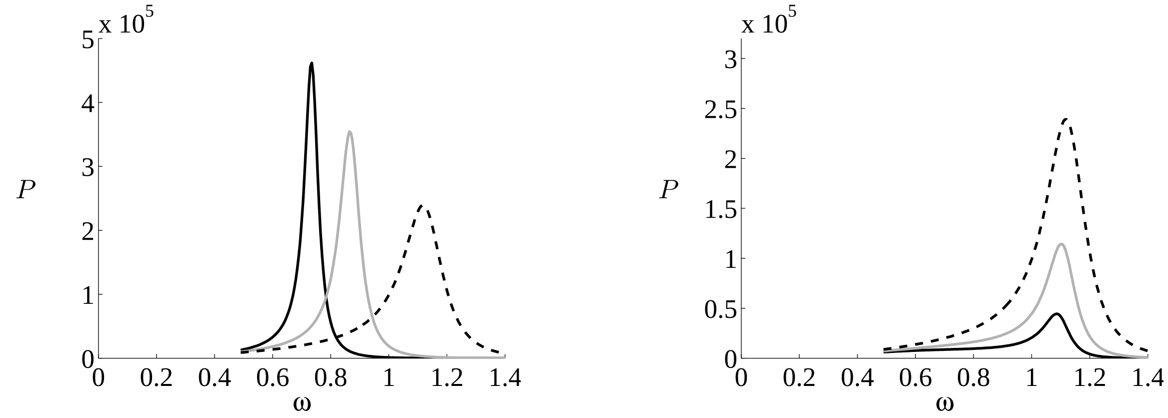

(c) Power with $M = M_m$ and $R = R_5$ (d) Power with $M = M_m\,(5)$ and $R = R_5$

Figure J.1: Free-float response amplitude ratio, $|d_z|_{R=0}$ (simplified to $|d_z|$ in axes labels), and power for a flat-based, vertical, circular cylinder of radius $a = 5$ m and varying draft (see key) with either a draft dependent mass equal to the displaced mass of fluid ($M = M_m$) or a constant draft independent draft equal to the displaced mass of the 5 m draft float ($M = M_m\,(5)$) and mechanical damping either constant and equal to the maximum radiation damping on the 5 m draft float ($R = R_5$) or calculated using Equation (5.2) to be optimised according to the draft and wave frequency ($R = R_{opt}$):
KEY:
Solid black line, draft 15 m;
Grey line, draft 10 m;
Dashed black line, draft 5 m

ConTop Drafts with Constant Stiffness

This section considers drafts of ConTop for which the free surface is located along the middle vertical section. As the water-plane area does not vary between these drafts, the hydrostatic stiffness remains constant.

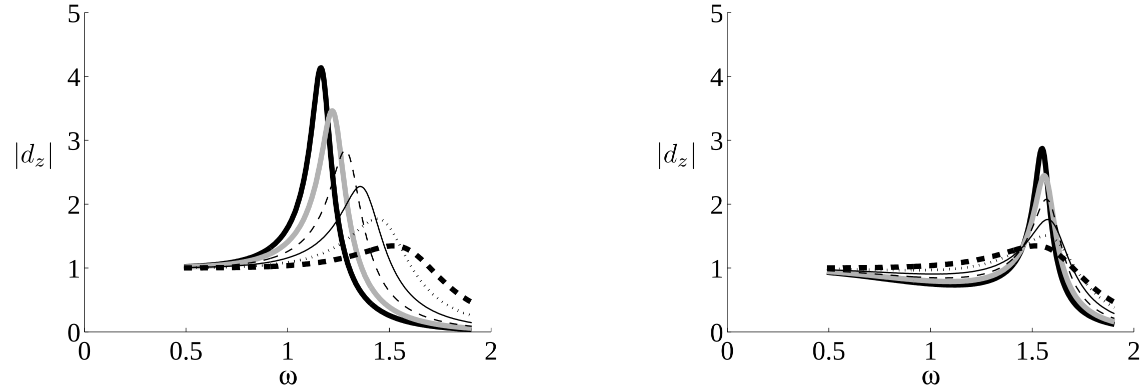

(a) Free-Float Response with $M = M_m$)

(b) Free-Float Response with $M = M_{D_F}$

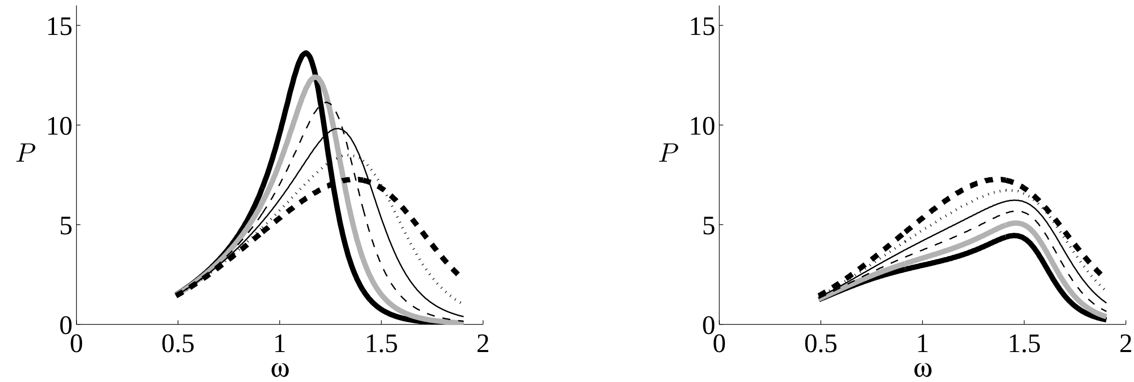

(c) Power with $M = M_m$ and $R = R_{D_F}$

(d) Power with $M = M_{D_F}$ and $R = R_{D_F}$

Figure J.2: Free-float response amplitude ratio, $|d_z|_{R=0}$ (simplified to $|d_z|$ in axes labels), and power for geometry ConTop at drafts D_γ, D_ϵ, D_A, D_C, D_F and D_H (see Figure H.2) with either a draft-dependent mass equal to the displaced mass of fluid ($M = M_m$) or a constant draft-independent mass equal to the displaced mass of the float with draft D_F ($M = M_m(D_F) = M_{D_F}$) and mechanical damping constant and equal to the maximum radiation damping on the float with draft D_F ($R = \max(B(D_F)) = R_{D_F}$):
KEY: Thick Solid black line, draft D_A; Solid grey line, draft D_B;
Thin dashed line, draft D_C; Thin Solid black line, draft D_D;
Dotted black line, draft D_E; Thick dashed line, draft D_F

Whilst the magnitude of the peak in free-float response increases with draft, the bandwidth (that is the range of frequencies over which the free-float response is large) decreases with draft (see Figure J.2b).

At low and high wave frequencies the optimal mechanical damping values for the constant mass floats decrease with decreasing draft, and close to the natural wave frequencies, the optimal mechanical damping values increase with decreasing draft. For any constant mechanical damping value, the larger the draft of the float, the greater the under-damping at low and high wave frequencies (due to the greater difference between the constant and optimal mechanical damping values at those frequencies). A large constant mechanical damping value therefore minimises the under-damping at low and high wave frequencies, but over-damps the deeper draft floats near the peak frequency. This results in the larger draft floats experiencing a larger bandwidth and lower peak power value when the mechanical damping value is large, so that the smaller draft float achieves the greatest power across the whole frequency range. A small constant mechanical damping value however, results in the larger draft floats being even more under-damped at low and high frequencies and closer to their optimum values near the peak frequency, reducing the bandwidth and increasing the peak. The large difference between drafts of both the peaks and bandwidths results in different drafts achieving the greatest power at different wave frequencies.

Drafts with Varying Stiffness

The second set of ConTop drafts is a selection of drafts covering the whole geometry therefore allowing variations in the water-plane area hence stiffness. For this purpose the free-float response and power output for drafts D_γ, D_ϵ, D_A, D_C, D_F and D_H are compared in this section.

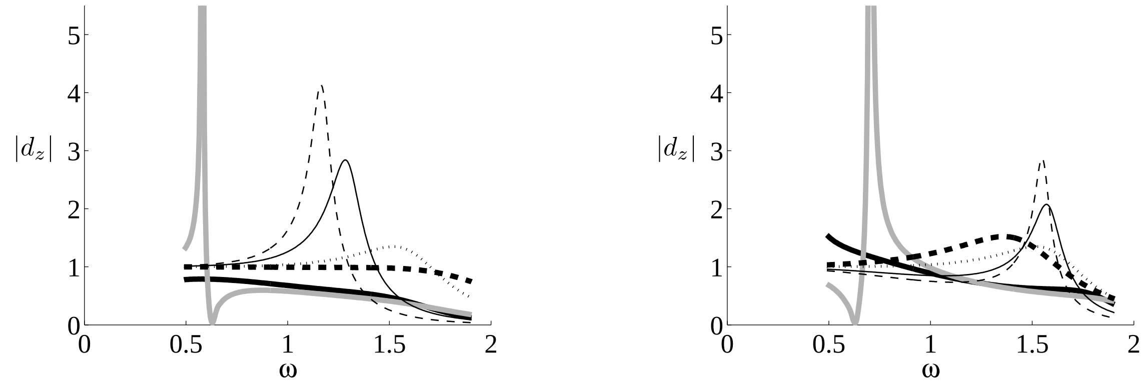

(a) Free-Float Response with $M = M_m$ (b) Free-Float Response with $M = M_{D_F}$

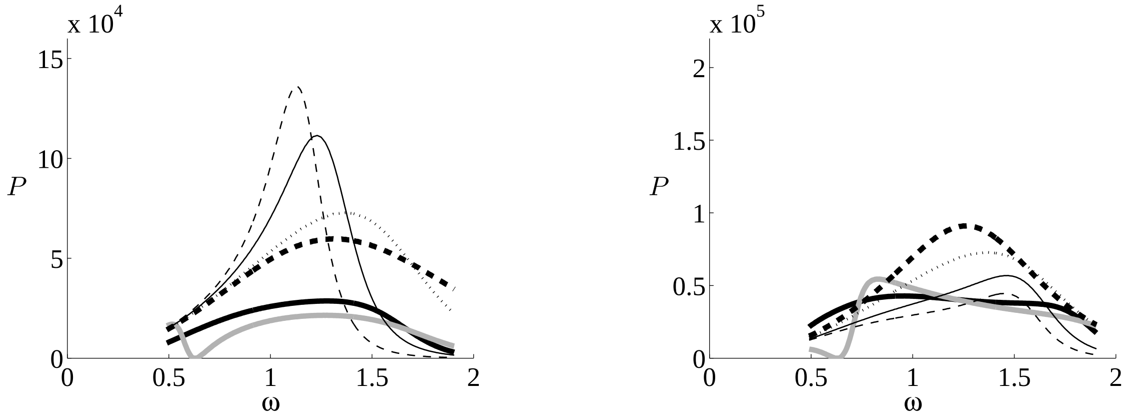

(c) Power with $M = M_m$ and R_{D_F} (d) Power with $M = M_{D_F}$ and R_{D_F}

Figure J.3: Free-float response amplitude ratio, $|d_z|_{R=0}$ (simplified to $|d_z|$ in axes labels), and power for geometry ConTop at drafts D_γ, D_ϵ, D_A, D_C, D_F and D_H (see Figure H.2) with either a draft-dependent mass equal to the displaced mass of fluid ($M = M_m$) or a constant draft-independent mass equal to the displaced mass of the float with draft D_F ($M = M_m(D_F) = M_{D_F}$) and mechanical damping constant and equal to the maximum radiation damping on the float with draft D_F ($R = \max(B(D_F)) = R_{D_F}$) :
KEY:
Thick Solid black line, draft D_γ; Solid grey line, draft D_ϵ;
Thin dashed line, draft D_A; Thin Solid black line, draft D_C;
Dotted black line, draft D_F; Thick dashed line, draft D_H

Bibliography

Abuk-Azm, A. G., Williams, A. N., 1988a. Second-order diffraction loads on truncated cylinders. Journal of Waterways, Port, Coastal and Ocean Division, 436–454.

Abuk-Azm, A. G., Williams, A. N., 1988b. Second-order diffraction loads on two uniform vertical cylinders. In: Proceedings 7th International Offshore Mechanics and Arctic Engineering Conference. Houston, Texas, U.S.A., pp. 131–138.

Abuk-Azm, A. G., Williams, A. N., 1989a. Approximation of second-order diffraction loads on vertical cylinder arrays. Journal of Fluids and Structures, 17–36.

Abuk-Azm, A. G., Williams, A. N., 1989b. Second-order diffraction loads on arrays of semi-immersed cylinders. Journal of Fluids and Structures, 365–388.

Al-Habaibeh, A., Su, D., McCaguec, J., Knight, A., 2010. An innovative approach for energy generation from waves. Energy Conversion and Management 51, 1664–1668.

American Society of Civil Engineers Task Committee on Hydrology Handbook, 1996. Hydrology handbook, 2nd Edition. ASCE Publications.

Aquamarine Power, March 2011. Official website for Oyster wave power device.
URL `http://www.aquamarinepower.com/`

AW-Energy Oy, March 2011. Official website for WaveRoller wave energy converter.
URL `http://www.aw-energy.com/`

AWS Ocean Energy Ltd, March 2011. Official website for Archimedes Wave Swing wave energy converter.
URL `http://www.awsocean.com/home.aspx`

Babarit, A., Clement, A., 2006. Optimal latching control of a wave energy device in regular and irregular waves. Applied Ocean Research 28, 77–91.

Babarit, A., Duclos, G., Clément, A. H., 2004. Comparison of latching control strategies for a heaving wave energy device in random sea. Applied Ocean Research, 227–238.

Bellew, S., Stallard, T., 2010. Linear modelling of wave device arrays and comparison to experimental and second order models. In: Proceedings 25th International Workshop on Water Waves and Floating Bodies. pp. 9–12.

Bellew, S., Stallard, T., Stansby, P., 2009. Optimisation of a heterogeneous array of heaving bodies. In: Proceedings of the 8th European Wave and Tidal Energy Conference. Uppsala, Sweden, pp. 519–527.

Bjarte-Larsson, T., Falnes, J., Moan, T., 2006. Comparison of results from time-domain simulations and model tests of a water-pumping wave-power unit. In: Proceedings of 16th Offshore and Polar Engineering Conference. pp. 417–422.

Boake, C. B., Whittaker, T. J. T., Folley, M., 2002. Overview and initial operational experience of the limpet wave energy plant. In: Proceedings of The Twelfth International Offshore and Polar Engineering Conference. pp. 586–594.

Brito-Melo, A., Neumann, F., Sarmento, A., 2008. Full-scale data assessment in OWC pico plant. International Journal of Offshore and Polar Engineering 18, 27–34.

Brooke, J., 2003. Wave Energy Conversion. Elsevier Science Ltd.

Budal, K., Dec 1977. Theory for absorption of wave power by a system of interacting bodies. JSR 21 (4), 248–253.

Budal, K., Falnes, J., Kyllingstad, Å., Oltedal, G., 1979. Experiments With Point Absorbers. Chalmers University of Technology, Gothenburg, Sweden.

Butler, B. P., Thomas, G. P., 1993. The diffraction of water waves by an array of circular cylinders in a channel. Ocean Engineering 20 (3), 295–311.

Callan, M., Linton, C., Evans, 1991. Trapped modes in two-dimensional wave guides. Journal of Fluid Mechanics 229, 51–64.

Chakrabarti, S. K., Tam, W. A., 29 April-2 May 1973. Gross and wave load on a large vertical cylinder - theory and experiment. In: Proceedings of the 5th Annual Offshore Technology Conference. Houston, Texas.

Chaplin, R. V., Rahmati, M. T., Gunura, K., Ma, X., Aggidis, G. A., 2009. Control systems for wraspa. In: Proceedings of the International Conference on Clean Electrical power. Capri, Italy, pp. 93 – 97.

Chau, F. P., Eatock Taylor, R., 1988. Second order velocity potential for arbitrary bodies in waves. In: Third International Workshop on Water Waves and Floating Bodies.

Chau, F. P., Eatock Taylor, R., 1992. Second order wave diffraction by a vertical cylinder. Journal of Fluid Mechanics 240, 571–599.

Clément, A., McCullen, P., Falcão, A., Fiorentino, A., Gardner, F., Hammarlund, K., Lemonis, G., Lewis, T., Nielsen, K., Petroncini, S., Teresa Pontes, M., Schild, P., Sjöström, B.-O., Sørensen, H. C., Thorpe, T., 2002. Wave energy in europe: Current status and perspectives. Renewable and Sustainable Energy Reviews, 405–431.

Count, B. M., November 1978. On the dynamics of wave-power devices. In: Proceedings of the Royal Society of London. Vol. 363 of A, Mathematical and Physical Sciences. pp. 559–579.

Count, B. M. Jefferys, E. R., Tokyo 1980. Wave power: The primary interface. In: Proceedings of the 13th Symposium on Naval Hydrodynamics. pp. 817–826.

Cruz, J., 2008. Ocean Wave Energy: Current Status and Future Prespectives. Springer.

Cruz, J., Sykes, R., Siddorn, P., Eatock Taylor, R., 2009. Wave farm design: Preliminary studies on the influences of wave climate, array layout and farm control. In: Proceedings of the 8th European Wave and Tidal Energy Conference. pp. 736–745.

de Backer, G., Vantorre, M., Beels, C., De Rouck, J., Frigaard, P., 2009. Performance of closely spaced point absorbers with constrained floater motion. In: Proceedings of the 8th European Wave and Tidal Energy Conference. pp. 806–817.

de Rouck, J., Meirschaert, V., 2009. Sustainable economically efficient wave energy converter (seewec) publishable final activity report. Tech. rep., University of Ghent.
URL `http://www.seewec.org/results/Publishable%20final%20activity%20report.pdf`

Draper, M., 2006. More than just a ripple: Ocean power technologies sets its sights high. Refocus, 54–56.

Eatock Taylor, R., Huang, J. B., 1997a. Second-order wave diffraction by an axisymmetric body in monochromatic waves. In: The Royal Society Proceedings: Mathematical, Physical and Engineering Sciences. Vol. 453. pp. 1515–1541.

Eatock Taylor, R., Huang, J. B., 1997b. Semi-analytical formulation for second-order diffraction by a vertical cylinder in bichromatic waves. Journal of Fluids and Structures 11, 465–484.

Eatock Taylor, R., Hung, S. I., 1987. Second-order diffraction forces on a vertical cylinder. Applied Ocean Research, 19–30.

Eatock Taylor, R., Hung, S. I., Chau, F. P., 1989. On the distribution of second order pressure on a vertical circular cylinder. Applied Ocean Research 11 (4).

Evans, D. V., 1979. Some theoretical aspects of three-dimensional wave-energy absorbers. In: Proceedings of the 1st Symposium on Wave-Energy Utilisation. Gothenburg.

Evans, D. V., Jeffrey, D. C., Salter, S. H., Taylor, J. R. M., 1979a. Submerged cylinder wave energy device: Theory and experiment. Applied Ocean Research 1.

Evans, D. V., Jeffrey, D. H., Salter, S. H., Taylor, J. R. M., 1979b. Submerged cylinder wave energy device: Theory and experiment. Applied Ocean Research 1 (1).

Evans, D. V., Linton, C. M., 1991. Trapped modes in open channels. Journal of Fluid Mechanics 225, 153–175.

Falcão, A. F. d. O., 2008. Phase control through load control of oscillating-body wave energy converters with hydraulic PTO system. Applied Ocean Research, 358–366.

Falcão, A. F. d. O., 2010. Wave energy utilization: A review of the technologies. Renewable and Sustainable Energy Reviews 4, 899–918.

Falcão, A. F. d. O., Justino, P. A., Henriques, J. C., André, J. M. C. S., 2009. Reactive versus latching phase control of a two-body heaving wave energy converter. In: Proceedings of the European Control Conference. Budapest, Hungary, pp. 3731–3736.

Falnes, J., 1980. Radiation impedance matrix and optimum power absorption for interacting oscillators in surface waves. Applied Ocean Research 2, 75–80.

Falnes, J., 2002. Ocean Waves and Oscillating Systems: Linear Interactions Including Wave-Energy Extraction. Cambridge University Press, Cambridge.

Falnes, J., 2007. A review of wave-energy extraction. Marine Structures 20, 185–201.

Falnes, J., Lillebekken, P. M., 2003. Budal's latching-controlled-buoy type wave-power plant. In: Proceedings of the 5th European Wave Energy Conference 2003. pp. 233–244.

Faltinsen, O. M., 1990. Sea Loads on Ships and Offshore Structures. Cambridge University Press, Cambridge.

Fitzgerald, C., Thomas, G., 2007. A preliminary study on the optimal formation of an array of wave power devices. In: Proceedings of the 7th European Wave and Tidal Energy Conference. Porto, Portugal.

Frigaard, P., Lyke Anderson, T., 2008. Effektmålinger på Wave Star i nissum bredning. Tech. Rep. 61, Aalborg University, , Denmark.

Garcia-Rosa, P., Cunha, J., Lizarralde, F., Estefen, S., Costa, P., 2009. Efficiency optimization in a wave energy hyperbaric converter. In: Proceedings of the International Conference on Clean Electrical Power. pp. 68 – 75.

GEOS, F., 2001. Wind and wave frequency distributions for sites around the british isles. Tech. rep., Health and Safety Executive.

Ghalayini, S. A., Williams, A. N., 1991. Nonlinear wave forces on vertical cylinder arrays. Journal of Fluids and Structures 5, 1–32.

Goda, Y., 2000. Random Seas and Design of Maritime Structures, 2nd Edition. World Scientific Publishing Co. Pte. Ltd.

Greenhow, M., Vinje, T., Brevig, P., Taylor, J., 1982. A theoretical and experimental study of the capsize of Salters Duck in extreme waves. Journal of Fluid Mechanics 118, 221–239.

Grue, J., Palm, E., 1984. Wave radiation and wave diffraction from a submerged body in a uniform current. Journal of Fluid Mechanics 151, 257–278.

Havelock, T. H., 1940. The pressure of water waves upon a fixed obstacle on water. In: Proceedings of the Royal Society of London Series A. Vol. 175. pp. 409–421.

Huang, J. B. Eatock Taylor, R., 1996a. Semi-analytical solution for second-order wave diffraction by a truncated circular cylinder in monochromatic waves. Journal of Fluid mechanics 319, 171–196.

Interproject Service AB (IPS) and Technocean (TO) , March 2011. Official website for IPS OWEC Buoy wave energy converter.
URL `http://www.ips-ab.com/`

Jarvis, A. M., 1979. Wave energy report on the electrical aspects of the Edinburgh University wave energy device. Tech. rep., Scottish Offshore Partnership.

Jones, D. S., 1953. The eigenvalues of $\bigtriangledown^2 u + \gamma u = 0$ when the boundary conditions are given on semi-infinite domains. In: Mathematical Proceedings of the Cambridge Philosophical Society. Vol. 49. pp. 668–684, (Have not got a copy).

Justino, P. A. P., Clément, A. H., 2003. Hydrodynamic performance for small arrays of submerged spheres. In: Proceedings of the Fifth European Wave Energy Conference. pp. 266–273.

Kagemoto, H., Murai, M., Saito, M., Molin, B., Malenica, S., 2002. Experimental and theoretical analysis of the wave decay along a long array of vertical cylinders. Journal of Fluid Mechanics 456, 113–135.

Kim, M. H., Yue, D. K. P., 1989. The complete second-order diffraction solution for an axisymetric body. part 1. monochromatic incident waves. Journal of Fluid Mechanics, 235–264.

Kriebel, D. L., 1990. Nonlinear wave interaction with a vertical circular cylinder, part I: diffraction theory. Ocean Engineering 17, 345–377.

Lamb, H., 1924, reprinted 1930. Hydrodynamics, 5th Edition. Cmbridge University Press, London.

Lee, C. H., 1995. WAMIT Theory Manual. Massachusettes Institute of Technology.

Leijon, M., Boström, C., Danielsson, O., Haikonen, K., Langhamer, O., Strömstedt, E., Ståberg, M., Sundberg, J., Svensson, O., Tyrberg, S., Waters, R., 2008. Wave energy from the north sea: Experiences from the Lysekil research site. Surveys in Geophysics 29 (3), 221–240.

Lighthill, J., 1979. Waves and hydrodynamic loading. In: Proceedings of the second international conference on behaviour of offshore structures. Vol. 1. p. 140.

Linton, C. M., Evans, D. V., 1992. Integral equations for a class of problems concerning obstacles in waveguides. Journal of Fluid Mechanics 245, 349–365.

Liu, Z., Teng, B., 2010. Wave-current interactions with three-dimensional floating bodies. Journal of hydrodynamics 22, 229–240.

Liu, Z., Teng, B., Ning, D., Sun, L., 2010. Using a time-domain higher-order boundary element method to simulate wave and current diffraction from a 3-D body. Journal of Marine Science 9, 156–162.

Loague, K., Green, R. E., 1991. Statistical and graphical methods for evaluating solute transport models: Overview and application. Journal of Contaminant Hydrology 7, 51–73.

Malenica, S., Eatock Taylor, R., Huang, J. B., 1999. Second-order water wave diffraction by an array of vertical cylinders. J. Fluid Mech. 390, 349–373.

Maniar, H. D., Newman, J. N., 1997. Wave diffraction by a long array of cylinders. Journal of Fluid Mechanics 339, 309–330.

Marquis, L., 2010. First power production figures from the Wave Star Roshage wave energy converter. In: Proceedings of the 3rd International Conference on Ocean Energy. Bilbao.

Massey, B. S., 1975. Mechanics of fluids. Van Nostrand Reinhold Co.

Masuda, K., Kato, W., Ishizuka, H., 1986. Second-order diffraction loads on plural vertical cylinder with arbitrary cross-sections. In: Proceedings 5th International Offshore Mechanics and Arctic Engineering Conference. Tokyo, Japan, pp. 345–352.

Masuda, K., Kato, W., Sakata, C., 1987. Nonlinear effect of surface waves on wave loads upon the plural vertical cylinder with arbitrary cross-sections. In: Proceedings 6th International Offshore Mechanics and Arctic Engineering Conference. Houston, Texas, U.S.A., pp. 72–81.

Mavrakos, S. A., Chatjigeorgiou, I. K., 2006. Second-order diffraction by a bottom seated compound cylinder. Journal of Fluids and Structures 22, 463–492.

Mavrakos, S. A., Chatjigeorgiou, I. K., 2009a. Second-order hydrodynamic effects on an arrangement of two concentric truncated vertical cylinders. Marine Structures 22, 545575.

Mavrakos, S. A., Chatjigeorgiou, I. K., 2009b. Second-order hydrodynamic effects on an arrangement of two concentric truncated vertical cylinders. Journal of Marine Structures 22, 545–575.

Mavrakos, S. A., McIver, P., 1997. Comparison of methods for computing hydrodynamic characteristics of wave power devices. Applied Ocean Research 19, 283–291.

Mayer, D. G., Butler, D. G., 1993. Statistical validation. Ecological Modelling 68, 21–32.

McCabe, A., Bradshaw, A., Meadowcroft, J., Aggidis, G., 2006. Developments in the design of the PS Frog Mk 5 wave energy converter. Renewable Energy 31, 141–151.

McCamy, R., Fuchs, R., 1954. Wave forces on piles: A diffraction theory. US Army Corps Of Engineers Tech.

McIver, P., 1984. Wave forces on arrays of floating bodies. Journal of Engineering Mathematics 18, 273–285.

McIver, P., Evans, D. V., 1984. Approximation of wave forces on cylinder arrays. Applied Ocean Research 6 (2), 101–107.

McIver, P., McIver, M., 1995. Wave-power absorption by a line of submerged horizontal cylinders. Applied Ocean Research.

McIver, P., McIver, M., 2007. Motion trapping structures in the three-dimensional water-wave problem. Journal of Engineering Mathematics, 67–75.

Molin, B., 1979. Second-order diffraction loads upon three dimensional bodies. Applied Ocean Research 1, 197–202.

Newman, J. N., 1990a. Second-harmonic wave diffraction at large depths. Journal of Fluid Mechanics 213, 59–70.

Newman, J. N., 1990b. The second-order wave force on a vertical cylinder. Journal of Fluid Mechanics 320, 417–443.

Newman, J. N., 2001. Wave effects on multiple bodies. Hydrodynamics in Ship and Ocean Engineering, 326.

Ocean Navitas Ltd, March 2011. Official website for Aegir Dynamo wave energy converter.
URL `http://www.oceannavitas.com/index.html`

Ocean Power Technologies Inc, March 2011. Official website for PowerBuoy wave energy converter.
URL `http://www.oceanpowertechnologies.com`

OceanEnergy Ltd, May 2011. Official website for OE Buoy.

Ohl, C. O. G., Eatock Taylor, P. H., Taylor, P. H., Borthwick, A. G., 2001. Water wave diffraction by a cylinder array. part 1. regular waves. Journal of the Society Of Naval Architects Of Japan 442, 1 – 32.

Pelamis Wave Power Ltd, March 2011. Official website for Pelamis wave energy converter.
URL `http://www.pelamiswave.com/`

Prado, M. G. S., Gardner, F., Damen, M., Polinder, H., 2006. Modelling and test results of the archimedes wave swing. Proceedings of Institute of Mechanical Engineers 220.

Rahm, M., 2010. Ocean wave energy: Underwater substation system for wave energy converters. Ph.D. thesis, Uppsala University, Disciplinary Domain of Science and Technology, Technology, Department of Engineering Sciences, Electricity.

REN21, 2010. Renewables 2010 global status report. Tech. rep., Renewable Energy Policy Network for the 21st Century.

Salcedo, F., Ruiz-Minguela, P., Rodriguez, R., Ricci, P., Santos, M., 2009. Oceantec: Sea trials of a quarter scale prototype. In: Proceedings of the 8th European Wave and Tidal Energy Conference. Uppsala, Sweden, 2009, pp. 460–465.

Salkind, N. J., 2010. Encyclopedia of Research Design. SAGE Publications, Inc.

Salter, S. H., 1982. The use of gyros as a reference frame. In: Proceedings of the Second International Symposium on Wave Energy Utilization. pp. 99–115.

Salter, S. H., Taylor, J. R. M., Caldwell, N. J., 2002. Power conversion mechanisms for wave energy. In: Proceedings of the Institute of Mechanical Engineers. Vol. 216. pp. 1–27.

Sarpkaya, T., Isaacson, M., 1981. Mechanics of Wave Forces on Offshore Structures. Van Nostrand Reinhold Company, New York.

Shifler, D. A., 2005. Understanding material interactions in marine environments to promote extended structural life. Corrosion Science 47 (10), 2335–2352.

Simon, M. J., 1982. Multiple scattering in arrays of axisymmetric wave-energy devices. part 1. a matrix method using a plane-wave approximation. Journal of Fluid Mechanics 120, 1–25.

Stallard, T., Stansby, P. K., Weller, S. D., Williamson, A. C., 2009a. Float design to limit displacement in severe seas. In: Proceedings of the 8th European Wave and Tidal Energy Conference. pp. 601–609.

Stallard, T., Stansby, P. K., Williamson, A., July 2008. An experimental study of closely spaced point absorber arrays. In: Proceedings of the Eighteenth International Offshore and Polar Engineering Conference. Vancouver, BC, Canada, pp. 417–424.

Stallard, T. J., Weller, S. D., Stansby, P., 2009b. Limiting heave response of a wave energy device by draft adjustment with upper surface tension. Applied Ocean Research, 282–289.

Stokes, G. G., 1846. Report on recent researches in hydrodynamics. British Association for the Advancement of Science Report.

Sustainable Economically Efficient Wave Energy Converter Project, March 2011. Official website for FO3 wave energy converter.
URL `http://www.seewec.org/index.html`

Swan, C., Taylor, P. H., Van Langen, H., 1997. Observations of wave-structure interaction for a multi-legged concrete platform. Applied Ocean Research 19, 309–327.

Taghipour, R., Moan, T., 2008. Efficient frequency-domain analysis of dynamic response for the multi-body wave energy converter in multi-directional waves. In: Proceedings of the Eighteenth (2008) International Offshore and Polar Engineering Conference. pp. 357–365.

Tedd, J., Kofoeda, J. P., 2009. Measurements of overtopping flow time series on the Wave Dragon wave energy converter. Renewable Energy 34 (3), 711–717.

The University of Manchester, March 2011. Official website for Manchester Bobber wave energy converter.
URL `http://www.manchesterbobber.com`

Thomas, G. P., Evans, D. V., 1981. Arrays of three-dimensional wave-energy absorbers. Journal of Fluid Mechanics 108, 67 – 88.

Thomas, S. T., Weller, S., Stallard, T., 2008. Float response within an array: Numerical and experimental comparison. In: Proceedings of the 2nd International Conference on Ocean Energy.

Uppsala Univeritat, March 2011. Wave power project - Lysekil.
URL `http://www.el.angstrom.uu.se/forskningsprojekt/WavePower/Lysekilsprojektet_E.html`

Ursell, F., 1987. Mathematical aspects of trapping modes in the theory of surface waves. Journal of Fluid Mechanics 183, 421–437.

Vantorre, M., Banasiak, R., Verhoeven, R., 2004. Modelling of hydraulic performance and wave energy extraction by a point absorber in heave. Applied Ocean Research 26 (1-2), 61 – 72.
URL `http://www.sciencedirect.com/science/article/pii/S0141118704000392`

Vicinanza, D., Frigaard, P., 2008. Wave pressure acting on a seawave slot-cone generator. Coastal Engineering 55 (6), 553–568.

Wacher, A., Neilsen, K., 2010. Mathematical and numerical modeling of the aquabuoy wave energy converter. Mathematics-in-Industry Case Studies Journal.

WAMIT, Inc, 2008. WAMIT User Manual. WAMIT, Inc.

Washio, Y., Osawa, H., Nagata, Y., Fujii, F., Furuyama, H., Fujita, T., 2000. The offshore floating type wave power device “Mighty Whale”: Open sea tests. In: Proceedings of the Tenth International Offshore and Polar Engineering Conference. pp. 373–380.

Wave Star A/S, March 2011. Official website for Wave Star wave energy converter.
URL `http://wavestarenergy.com/`

Wavebob Ltd, March 2011. Official website for Wavebob wave energy converter.
URL `http://www.wavebob.com/`

Weber, J., Mouwen, F., Parish, A., Robertson, D., 2009. Wavebob - research and development network and tools in the context of systems engineering. In: Proceedings of the 8th European Wave and Tidal Energy Conference. Uppsala, Sweden, 2009, pp. 416–420.

Wehausen, J. V., Laitone, E. V., 1960. Surface waves. Handbuch der Physik 9, 446–778.

Weller, S., 2009. Experimental measurements of irregular wave interaction factors in closely spaced arrays. In: Proceedings of the 8th European Wave and Tidal Energy Conference. pp. 952–960.

Weller, S. D., 2010. Wave energy extraction from device arrays: Experimental investigation in a large wave facility. Ph.D. thesis, University of Manchester.

Whittaker, T., Collier, D., Folley, M., Osterried, M., Henry, A., Crowley, M., 2007. The development of Oyster - a shallow water surging wave energy converter. In: Proceedings of 7th European Wave Tidal Energy Conference.

Williams, A. N., Demirbilek, Z., 1988. Hydrodynamic interactions in floating cylinder arrays - I. wave scattering. Ocean Engineering 15 (6), 549 – 583.

Woodroffe, C. D., 2002. Coasts: Form, Process and Evolution. Cambridge University Press.